

**UNIVERSIDADE DE SÃO PAULO
ESCOLA POLITÉCNICA**

JUAN IGNACIO PEREIRA AGUDELO

**ANALYSIS OF THE MICROSTRUCTURE TRANSFORMATION (WEL
FORMATION) IN PEARLITIC STEEL USED IN RELEVANT
ENGINEERING WEAR SYSTEMS**

São Paulo

2018

JUAN IGNACIO PEREIRA AGUDELO

**ANALYSIS OF THE MICROSTRUCTURE TRANSFORMATION (WEL
FORMATION) IN PEARLITIC STEEL USED IN RELEVANT
ENGINEERING WEAR SYSTEMS**

This thesis is submitted for the degree of Doctor
in science at the University of São Paulo.

Supervisor: Prof. Dr. Amilton Sinatora

São Paulo

2018

Este exemplar foi revisado e corrigido em relação à versão original, sob responsabilidade única do autor e com a anuência de seu orientador.

São Paulo, ____ de _____ de _____

Assinatura do autor: _____

Assinatura do orientador:  _____

Catlogação-na-publicação

Pereira Agudelo, Juan Ignacio
ANALYSIS OF THE MICROSTRUCTURE TRANSFORMATION (WEL
FORMATION) IN PEARLITIC STEEL USED IN RELEVANT ENGINEERING
WEAR SYSTEMS / J. I. Pereira Agudelo -- versão corr. -- São Paulo, 2018.
211 p.

Tese (Doutorado) - Escola Politécnica da Universidade de São Paulo,
Departamento de Engenharia Mecânica.

1.Pearlitic steel 2.Abrasive wear 3.Cystallographic orientation 4.Rolling
Contact Fatigue 5.Scratch test I.Universidade de São Paulo. Escola
Politécnica. Departamento de Engenharia Mecânica II.t.

*“¡Pero no digas no puedo ni en broma!
Porque el inconsciente no tiene sentido del
humor, lo tomará en serio, y te lo recordará
cada vez que lo intentes”.*

Facundo Cabral

DECLARATION

This thesis is submitted for the degree of Doctor of Philosophy at the University of São Paulo. The research reported was conducted under the supervision of Professor Dr. Amilton Sinatora in the Department of Mechanical Engineering, University of São Paulo, between September 2013 and March, 2018.

This is my own work and contains nothing that is the outcome of work done in collaboration with others, except where specifically indicated in the text. Neither this, nor any substantially similar work has been or is being submitted for any degree or diploma or other qualification at any other university or institution.

Some part of the chapters 2 and 3 (experimental) of this work has been published (or submitted) in the literature as follows:

- **PEREIRA, J.I.**; TRESSIA, G.; MACHADO, P.C.; FRANCO L.A.; SINATORA, A. Scratch test of pearlitic steels: Influence of normal load and number of passes on the sub-superficial layer formation, **Accepted with revision by Tribology International**, 2017
- **PEREIRA, J.I.**; MACHADO, P.C.; PENAGOS, J.J.; SINATORA, A. Wear characterization from field and laboratory tests of pearlitic steels used for SAG mill liners. *WEAR* **JCR**, v. 376-377, p. 37-45, 2017.

Juan Ignacio Pereira Agudelo
São Paulo, 2018.

ACKNOWLEDGEMENTS

First of all, I would like to express my sincere gratitude to my supervisor, *Abrasivoro* Chief and track and field coach, Prof. Dr. Amilton Sinatora, *Herr* Professor! For offering me the opportunity to pursue my Ph.D. degree, for the patience, the continuous support, the inspiration.

On this long journey, I had the pleasure and the honor to work with, discuss and debate with a wonderful staff of professors. I would like to thank to Prof. Dr. Helio Goldestein and his extraordinary knowledge; Dr. Eduardo Albertin; Prof. Dr. Roberto Martins de Souza who represents the responsibility and hard work; Prof. Dr. Izabel Machado (commitment and discipline).

Another important support group in this journey to whom I am especially grateful is the *abrasivoro* team. The entire subjects discussed in this thesis were the result of many hours of hard work and influenced by these friends. Jimmy Penagos (The original *abrasivoro*, has a special critical eye), Dr. Paulo Machado (The endless discussion doctor and partner in this journey), Dr. Luiz Franco (co-author, co-supervisor. I have so much to thank you, especially when a mechanical- aeronautic and agronomist eye was necessary), MSc. Gustavo Tressia. (*Monsieur* austenitic, college and friend. The recrystallization was our witches hunt), Eng. Marcos Ara (Always willing to give a hand when necessary).

I would like to thank to The Colombian team: MSc. Juan Sebastian, Dr. Alexander Zuleta, MSc. Pablo Correa and MSc. Michael Cano. The VIP team: Dra. Vanessa Seriacopi, Dr. Newton Fukumasu, Eng. Casiano Bernardes, Eng. Arnaldo Lima, Dr. Luiz Lima, MSc. Felipe Carneiro, Eng. Roberto Balarini. A special thanks to MSc. Iramar Tertuliano, MSc. Larissa Lara, MSc. Ana Júlia Tertuliano, Eng. Guido Boidi, MSc. Gustavo Sieber, MSc. Marcionila Santos, Dr. Roberto Oliveira (Bobby), Dr. André Zuin, MSc. Rafael Obara, Dr. Francisco Profito, Silene Carneiro e Sidney Carneiro.

The technician team was an important support in all stages of the process. My eternal gratitude to Raphael Ferreira, Rodney Santos, Carlos Ramires, Cassio Silva, Rafael Melchor.

So many people helped me in all these years and deserve my gratitude. I grew as a human being with the presence of those people in my life: Ginneth Pulido, Sister,

friend, cat sitter, and psychologist. A big gift in a little package; Ana Cecilia Rodrigues, thank you for help me to survive in São Paulo and understand that I am a very annoying person; Pamela Dominutti, many lessons learned. Quentin Lamour, beloved friend. Beatriz Calil, the most colorful woman, always stripping the soul.

I would like to thank to my family for the love, the comprehension, the patience and the understanding of the price of my dreams. My mother, Ana Julia Agudelo, ***En los tiempos difíciles siempre has estado ahí, sos mi inspiración, mi heroína.*** Alvaro Andrés, my younger brother. ***Recuerda que la educación es la clave para dejar huella en los que más queremos.*** Erika Rios, ***gracias por la motivación y el respeto.*** Last but certainly not least, a very special thanks to my partner, MSc. Beatriz Rodrigues, thank you for the patience, for the company, love and most importantly, for the amazing gift. *“Compañera usted sabe puede contar conmigo no hasta dos o hasta diez sino contar conmigo”.*

I also express my gratitude to CAPES (Coordenação de Aperfeiçoamento de Pessoal de Nível Superior) for the scholarship.

I also express my gratitude to VALE for the partnership and the resources provided in this research.

ABSTRACT

In this thesis, the behavior of pearlitic steel was characterized under controlled wear conditions in the laboratory and service conditions in two ore mining stages, comminution and transportation. The thesis consists in three experimental chapters, divided according to the tribosystems analyzed. On all the chapters Electron Microscopy techniques for the microstructural analysis were employed. Scanning Electron Microscopy (SEM), Focused Ion Beam (FIB-SEM), Electron Backscatter Diffraction (EBSD) and Transmission Electron Microscopy (TEM) were used. The first experimental chapter shows the analysis of the pearlite under abrasive wear with loose abrasive particles in multi-events conditions. The sample was taken from Semi-Autogenous Grinding mills (SAG) and experimental simulation was carried out in laboratory using the Dry Sand Rubber Wheel Abrasion Test (DSRW). The results show a polycrystalline layer formation in both cases, characterized by ultra-fine grains of ferrite in the layer closer to the surface. It was also concluded that the DSRW can simulate the wear produced on field (superficial and microstructural features) in conditions of higher normal load than recommended by the ASTM Standard G65. The second experimental chapter explores the characterization of the microstructure after the indenter pass in scratch test using two conditions of normal load applied and five sequences of scratch. The microstructural analysis shows the formation of two sub-superficial layers identified by the level of the microstructural alterations. In the sub-superficial layer (close to the surface), the formation of new ultra-fine grains of ferrite was observed. A second layer was observed deeper in the sample and denominated as layer of the microstructure transition, characterized by the combination of deformed (reduction of the interlamellar spacing) and pearlite colonies not affected plastically by the mechanical loading. On this layer, the crystallographic texture in RD // {111} in samples tested at 4 N (normal load) and one-pass scratch was determined. Later, on this chapter, the microstructure in a ground rail (industrial procedure characterized as a multi-event scratch test) was analyzed. Two grinding conditions were used for the analysis with variation of the grinding linear speed and load on the grinding stones (discs). The combination of low grinding speed and high load promotes a higher deformed layer formation beneath the patch zone and low randomized orientation of the pearlite colonies. Finally, in the third experimental chapter, the pearlitic characterization was concluded with the study of samples of railway wheel and rail

under wear in service and Rolling Contact Fatigue (RCF) in laboratory. The laboratorial simulation was carried out using the twin-disc rolling contact tribometer with a variation of number of cycles. The characterization of railway wheel shows that the WEL is characterized by levels of breaking and aligned cementite and zones with dissolution of the carbon atom in the ferrite to form the supersaturated carbon ferrite. The polycrystalline ferrite formation (ultra-fine grains) in the sub-superficial layer and it was identified a preferential orientation of RD // {111} in the layer of microstructural transition. The results of the laboratory test show surface crack nucleation and propagation at low angle in the more severe deformed layer. The microstructure of the layer consists in polycrystalline ferrite and the cementite dissolution.

Keywords: Pearlite, Abrasive wear, White Etched Layer, crystallographic orientation, Rolling Contact Fatigue, scratch test.

RESUME

Nesta tese foi caracterizado o comportamento do aço perlítico em condições controladas de desgaste em laboratório e em serviço em dois estágios do processo de mineração de minério, cominuição e transporte ferroviário. A tese consiste em três capítulos experimentais divididos segundo o tribosistema analisado. Em todos os capítulos do trabalho foi utilizada a técnica de microscopia eletrônica para análise microestrutural. Foi utilizado Microscopia eletrônica de varredura (MEV), *Focused Ion Beam* (FIB-SEM), *Electron Backscatter Diffraction* (EBSD) e Microscopia eletrônica de transmissão (MET). O primeiro capítulo experimental mostra a análise da perlita in condições de desgaste abrasivo com partículas soltas em eventos múltiplos. As amostras foram tiradas de um moinho semi-autógeno (SAG) e realizada uma simulação experimental do desgaste em condições controladas usando o tribômetro de roda de borracha (RWAT). Os resultados mostraram a formação de camada branca em ambas as condições de análise, consistindo em uma camada poli cristalina caracterizada pela formação de grãos ultrafinos na camada mais próxima da superfície de desgaste. Também foi concluído que a roda de borracha pode simular o desgaste produzido nos moinhos SAG tanto nas características superficiais quanto microestruturais em condições de maior severidade as comumente utilizadas na norma ASTM G65 (procedimento B). O Segundo capítulo experimental explora a caracterização da microestrutura depois da passagem do endentador no ensaio de riscamento (*scratch test*) utilizando duas condições de carga normal aplicada e 5 sequências de riscamento. A análise microestrutural mostrou a formação de duas camadas subsuperficiais identificadas pelo nível de alteração microestrutural. Na camada mais próxima da superfície de desgaste foi observada a formação de grãos ultrafinos de ferrita. A segunda camada identificada mais profundamente na amostra, denominada como camada de transição, é caracterizada pela combinação de colônias deformadas (redução do espaçamento interlamelar) e camadas não afetadas pelos esforços produzidos no contato. Nesta camada foi determinada a texturização em direção RD // {111} nas amostras testadas a 4 N (carga normal aplicada) e uma passada. Posteriormente à análise de riscamento foi caracterizada a microestrutura de uma amostra tirada de um trilho esmerilhado (processo industrial que pode ser considerado como aplicação do ensaio de riscamento). Foram consideradas duas condições de esmerilhamento com variação de velocidade de esmerilhamento

(deslocamento linear do veículo esmerilhador) e potência dos motores dos rebolos usada no procedimento. A combinação de baixa velocidade de esmerilhamento e alta potência nos motores controladores dos rebolos promoveu uma grande deformação nas camadas subsuperficiais na região de contato e uma baixa aleatoriedade das orientações cristalográficas das colônias de perlita. Finalmente, no capítulo três, a caracterização da microestrutura perlítica foi finalizada com o estudo de amostras de roda e trilho em condições de desgaste em campo e de *Rolling Contact Fatigue (RCF)* em ensaios de laboratório. A simulação experimental foi realizada utilizando o tribômetro *twin-disc rolling* (configuração disco-disco) com variação do número de ciclos. A caracterização da roda ferroviária mostrou a formação da camada branca caracterizada por níveis de cementita fraturada e alinhada em direção do movimento de rolamento/deslizamento com áreas de dissolução do átomo de carbono na ferrita formando uma ferrita supersaturada. Foi identificado a formação de policristais de ferrita (grãos ultrafinos) na camada mais superficial e uma orientação preferencial RD // {111} na camada de transição. Os resultados dos ensaios de laboratório mostraram a nucleação de trincas superficiais se propagando a baixo ângulo na camada branca. A transformação microestrutural dessa camada após ensaios de laboratório consiste em policristais de ferrita e dissolução da cementita.

Palavras-chave: Perlita, desgaste abrasivo, camada branca, orientação cristalográfica, Fadiga de contato, ensaio de riscamento

Aim of the thesis

The global aim of this thesis is to validate the assumption of the similarity in the pearlitic steels behavior under controlled wear conditions (laboratory tests) and wear in service condition in relevant engineering systems.

Specific goal

To analyze the microstructural transformation of the pearlitic steel in semi-autogenous grinding mill and the correlation of the behavior in typically abrasive test conditions (laboratory).

To study the correlation between the crystallographic orientation and the microstructural deformation in rail grinding procedure and scratch test.

To compare the microstructure in the subsurface in samples obtained from a wheel (railway) and twin-disc test.

Approach

In the first experimental chapter, the surface and wear micro mechanisms characterization in abrasion wear in natural (field) and laboratory conditions were emphasized.

In the second experimental chapter, a detailed study of the influence of the abrasive particle (scratch test and grinding disc) in the microstructural transformation was carried out. Special attention was put on the crystallographic orientation of the pearlite colonies beneath the contact surface.

In the third experimental chapter, an emphasis was put on the sub-superficial microstructure and the expressive work-hardening, results of RCF conditions.

Delimitations

The studies carried out in this thesis were limited to fully pearlitic steel used in mining (semi-autogenous grinding mill - SAG) and rail transportation industries (fabrication of devices like wheel and rail). The analysis was focused on the interaction of mechanical factors/parameters in the WEL formation beneath the contact zone.

LIST OF FIGURES

Figure 1 Classification of different types of tribological testing	30
Figure 1-1 Schematic representation of tribosystem	31
Figure 1-2 Classification of wear process.....	32
Figure 1-3. Schematic representation of abrasive wear	33
Figure 1-4 Wear mechanisms observed SEM. a) Micro ploughing, b) wedge formation, and c) Micro cutting	34
Figure 1-5 Schematic representation of the evolution in the wear mechanisms as a function of attack angle	37
Figure 1-6 Schematic representation of forces acting in the displacement of the abrasive particle	37
Figure 1-7 Correlation between friction coefficient and wear mechanisms for different attack angle	38
Figure 1-8 Volume loss (accumulate values) as a function of the normal load and the abrasive particle size in ASTM Standard G65 test for AISI 1004	41
Figure 1-9 Schematic representation of the rail fatigue damages. a) Head cracks, b) squats, c) tongue lipping	42
Figure 1-10 Wear rates and regimes for R8T wheel steel tested against UIC60 900A rail steel.....	43
Figure 1-11 Schematic representation of the main steps in ore comminution	45
Figure 1-12 a) High speed camera images of the passage of a ballast stone in the 1st wheel-rail contact-ballast stone, b) Cross-section of a wheel with a third body layer	50
Figure 2-1 Procedure to obtain the sample of the SAG mill liner.....	64
Figure 2-2 DSRW tribometer description.....	65
Figure 2-3 A secondary electron SEM image of the undeformed pearlitic microstructure	67
Figure 2-4 Schematic representation of wear zone in a DSRW sample.....	68
Figure 2-5 Wear scar map of samples at the end of DSRW at 130 N, according with the procedure B of the ASTM Standard G65. A secondary electron SEM image of surface in three deformation regions, b) Entrance zone (correspond the marked region as "I"), c) central zone (region "II") and d) exit zone (region "III").....	69
Figure 2-6 Mass loss as a function of normal load and the worn surface at different abrasive severity	71

Figure 2-7 Granulometric distribution in the determination of the abrasive size particles	72
Figure 2-8 Characterization of the sample in cross- section. a) Schematically representation of the worn surface, b) SEM micrograph of the central region of wear, and c) Secondary electron micrograph of the highlighted contact zone	73
Figure 2-9 The FEG-SEM image of the worn surface cross section of the samples at the end of DSRW with normal load of 220 N.....	75
Figure 2-10 FIB-SEM images of wear central zone for the samples tested at 44 N in DSRW. a) General cross section image, b) a highlighted region with the two-deformed layer, c) region on the right highlighted the deformation around a void space	77
Figure 2-11 FIB-SEM images of wear central zone for the samples tested at 130 N in DSRW, a) general cross section view, showing the presence of an irregular surface, b) highlighted region with the two-deformed layer and c) image with higher magnification (30000x)	78
Figure 2-12 FIB-SEM images of wear central zone for the samples tested at 380 N in DSRW. a) general cross section view, b) highlighted region out of groove showing the two-deformed layer and c) image below the groove caused by an abrasive particle.	79
Figure 2-13 Transmission Electron Microscopy image of the sample lamella	80
Figure 2-14 Microstructure of pearlite steel (non-deformed) observed by High Resolution -TEM. Sequence of amplification images, highlighting the lamellae arrangement.....	80
Figure 2-15 Microstructure transformation observed by TEM in bright and dark field of the severe deformed layer.....	81
Figure 2-16 A macro scale image of lifter exhibiting abrasive wear surface (marked as "A") with detachment of material "B"	84
Figure 2-17 a) macro scale image of the lifter surface worn in service. b) A secondary electron SEM image of the surface showing the abrasive mechanisms using SEM (1000X)	85
Figure 2-18 Cross-section image from a particular fracture region in the SAG liner. b) A cross-sectional secondary electron SEM micrograph of the region identified as "I" and c) SEM micrograph of the microstructure in the region indicated as "II"	87
Figure 2-19 (a) Optical Microscopy image of cross section surface worn in-service. A cross-sectional secondary electron SEM image of the two deformation regions, b) A	

higher magnification view of the region indicated as “I” in (a) indicating a sub-superficial layer	88
Figure 2-20 a) Cross-sectional secondary electron SEM image of sample worn in-service and b) highlighted region using SEM-FEG (180000X)	89
Figure 2-21 Hardness profile of samples worn in-service.....	90
Figure 2-22 IPF + IQ map of a) undeformed pearlite colonies and b) deformed layer	91
Figure 3-1 Cross section and top view of a grinding rail sample	101
Figure 3-2 Schematically representation of scratch test sequence, a) Scratch steps, b) number of passes.....	101
Figure 3-3 Tribômetro Hysitron TriboIndenter 950. a) General view, b) Conical tip indenter (Secondary Electron-SE image)	103
Figure 3-4 Tribometer Bruker UMT-2. a) General view e b) indenter highlighted), c) indenter profile (schematically representation)	103
Figure 3-5 Groove mean profile, highlighting the distance between the pile up, the groove length in the reference plane and the maximum depth.....	104
Figure 3-6 Geometrical characteristics of the groove main profile.....	105
Figure 3-7 SEM and HTEM micrographs of the undeformed pearlite colonies (core)	106
Figure 3-8. In situ gallium (Ga) ion beam etching image of samples tested in Hysitron tribometer. b) one-pass, c) five-passes	107
Figure 3-9. FIB cross section of the groove after one-pass and five-passes scratch test	108
Figure 3-10 SEM micrographs scratches obtained after one-pass scratch at 4 N as normal load.....	109
Figure 3-11 SEM micrographs scratches obtained after five-passes scratch at 4 N as normal load.....	110
Figure 3-12 SEM micrographs scratches obtained after one-pass scratch at 8N....	110
Figure 3-13 SEM micrographs scratches obtained after one-pass scratch at 8 N as a normal load.....	111
Figure 3-14 CCI profile of samples tested at 4 N a) one-pass and five-passes scratch. Samples tested at 8 N, c) one-pass and d) five-passes scratch.....	112
Figure 3-15 Correlation of the contact pressure and energy dissipated with the number of passes of samples in both conditions (in terms of normal load applied).....	114

Figure 3-16 Mean friction coefficient and the its correlation with the contact pressure for all samples	115
Figure 3-17 Friction coefficient for samples tested with macro range.....	116
Figure 3-18 Dry scratch test - AISI 1070, 4 N, mean profile superposition: scratches A (three passes), B (two passes) and C (one pass)	116
Figure 3-19 Scratch images. a) Groove profile image using a secondary electron detector in FIB/SEM and b) Pearlite colonies revealed with Gallium ion beam etching	118
Figure 3-20 A FIB-SEM micrograph for five-passes samples at, a) 4 N and b) 8 N	119
Figure 3-21 Schematic representation of the EBSD plane reference for the microstructure analysis.....	120
Figure 3-22 IPF + IQ map using RD and TD as a reference direction, a) RD (001) and b) TD (100).....	120
Figure 3-23 EBSD analyses of undeformed region of samples. a) IPF map, b) Misorientation curve	121
Figure 3-24 EBSD analysis of sample tested with 4 N as normal load and single-pass. a) IPF + IQ map (Highlighting IPF map), b) sub-superficial layer highlighting by IPF map, c) Misorientation curve	123
Figure 3-25 IPF + IQ and Misorientation map on samples for single and five-passes	125
Figure 3-26 ODF (frequency) for samples tested at single and five-passes.....	126
Figure 3-27 EBSD analysis in sample tested in single-pass scratch. a) Taylor Factor map and b) Kernel Average Misorientation map	127
Figure 3-28 Kernel Misorientation map on samples at test conditions	129
Figure 3-29 Taylor factor distribution.....	130
Figure 3-30 Taylor factor map on samples at test condition.....	132
Figure 3-31 IPF + IQ of specimen using TD as the reference plane	133
Figure 3-32 ODF (frequency) for samples tested at single and five-passes.....	134
Figure 3-33. Rail cross-section image and the schematic representation of the strips in the rail head	135
Figure 3-34. Secondary electron micrograph of the microstructure on the interior (bulk) of the pearlite rail.....	136
Figure 3-35. SEM micrographs showing the microstructure (cross section) of a rail without grinding process in: a) region near to the worn surface, b) material detachment	

highlighted, c) area A of interest showing a pearlite highly deformed layer and d) area B of in interest	138
Figure 3-36. SEM micrographs of the rail showing in cross-section the regions with material detachment and WEL formation	139
Figure 3-37. Optical Microscopy micrographs (OM) from the strip I highlighting facets A and B1 of the rail.....	140
Figure 3-38. Microstructure in cross-section of the facet A in the sample from the rail under the first grinding condition. a) SEM micrograph of a region with WEL formation and material detachment, b) FEG-SEM micrographs of the region with WEL formation and highly deformed microstructure	141
Figure 3-39. Secondary electron micrograph of the microstructure (cross-section) in facet A from two regions showing the WEL formation and the deformed layer. The samples were taken from the rail under the second grinding condition	142
Figure 3-40. Secondary electron micrograph of the microstructure (cross-section) in facet B1 of the sample take from the rail under the first grinding condition	143
Figure 3-41. Secondary electron micrograph of the microstructure (cross-section) in facet B1 of the sample taken from the rail under the second grinding condition.....	144
Figure 3-42. EBSD micrographs of the facet A of the sample take from the rail under the first grinding condition.....	147
Figure 3-43. EBSD micrographs of the facet B of the sample taken from the rail under the first grinding condition.....	148
Figure 4-1 Rolling/sliding wear rate of a few pearlitic and bainitic steels with varying hardness.....	156
Figure 4-2 Schematics diagram of the twin-disc tribometer	158
Figure 4-3 Image of the generic wheel-rail contact and the configuration in the twin-disc tribometer.....	159
Figure 4-4 A secondary electron SEM image of the undeformed pearlitic microstructure	160
Figure 4-5 Secondary Electron micrographs of the W4 surface (25000 cycles). a) Area without contact between discs, b) transition area corresponding with the lateral zones of the contact and c) center of the worn surface.....	161
Figure 4-6 SEM images of the worn surface from the W9 specimen (650000 cycles)	162
Figure 4-7 OM micrograph of the microstructure in cross section of specimen W4.	163

Figure 4-8 SEM micrograph of the microstructure in cross-section showing the sub-surface layers distribution.....	164
Figure 4-9 FEG-SEM micrographs of the microstructure beneath the rolling band in two regions of the sample highlighting the morphology in the layer A. Sample of interest: 25.0000 cycles (W4).....	165
Figure 4-10 FEG-SEM micrographs showing the microstructure transformation in the layer A of samples W4 and W9, respectively.	166
Figure 4-11 FIB-SEM micrograph of the microstructure of the grinding sample (sample preparation for disc-disc contact)	167
Figure 4-12 FIB-SEM micrograph of the microstructure of the W4 in the end of the rolling band (beneath of the material removed from the surface)	168
Figure 4-13 FIB-SEM micrographs of the microstructure of the sub-superficial layer in W4 and W9.....	169
Figure 4-14 Micro-hardness profile of samples after disc-disc test.....	170
Figure 4-15 Crystallographic orientation of the microstructure beneath the rolling band shows by EBSD. a) SEM micrograph of the microstructure highlighting the layers A and B. IPF maps of specimen W9. a) Layer A and c) layer B.....	172
Figure 4-16 Taylor Factor analysis of the W9 specimen in a) layer A and b) layer B.....	173
Figure 4-17 Transmission Electron Microscopy image of the samples W. a) Sample preparation, b) Bright field image, c) Dark field image.....	174
Figure 4-18 High resolution - TEM micrograph and SAED diffraction patterns at 100 μm from the worn surface.....	175
Figure 4-19 Wheel sample used in the microstructural characterization, corresponding with the severely deformed section	176
Figure 4-20 A secondary electron SEM image of the undeformed pearlitic microstructure.....	176
Figure 4-21 Microstructural characterization in cross-section using SEM	177
Figure 4-22 FEG-SEM micrographs of the microstructure in cross-section from the deformed layer	178
Figure 4-23 Microstructural characterization beneath the running band in the more severe region.....	180
Figure 4-24 Hardness profile of the wheel in the cross-section of the running band (strip II) and severe plastic deformation zone (strip I).....	181
Figure 4-25 FIB-SEM micrograph in the center of the running band	182

Figure 4-26 Sub-surface EBSD plots after wheel-rail contact, a) inverse pole figure (IPF) , b) pattern quality plot combined with grain boundaries (red lines for LAGBs of 2–5°, green lines for LAGBs of 5 –15° and blue for > 15° HAGBs)	183
Figure 4-27 Transmission Electron Microscopy image of the samples W (disc-disc). a) Sample preparation, b) HRTEM image	184
Figure 4-28 High Resolution - TEM micrograph of the deformed layer used by the SAED analysis. SAED diffraction patterns obtained in different spots.....	185
Figure 5-1 Schematic representation of the microstructural transformation beneath the worn surface.....	193

LIST OF TABLES

Table 1 Chemical composition (wt. %) of pearlitic devices used in the mining industry	29
Table 2-1 Dry Sand Rubber Wheel Abrasion Test parameters	65
Table 3-1 Scratch test parameters	102
Table 3-2. Parameters used in the grinding process	102
Table 3-3 Geometrical dimension of grooves for all test conditions	113
Table 4-1 Steel grade specified by AAR.....	157
Table 5-1 Main characteristics of the samples tested in the different wear conditions	197

NOMENCLATURE

A	:	Area
CCI	:	Coherence Correlation Interferometry
COF	:	Friction Coefficient
DSRW	:	Dry sand Rubber Wheel
EBSD	:	Electron Backscatter Scanning Diffraction
FEG	:	Field Emission Gun
FIB	:	Focused Ion Beam
GND	:	Geometrically Necessary Dislocations
HSS	:	High Strength Steels
HAGBs	:	High Angle Grains Boundaries
HRTEM	:	High Resolution Transmission Electron Microscopy
IPF	:	Inverse Pole Figure
KAM	:	Kernel Average Misorientation
LAGB	:	Low Angle Grain Boundaries
LFS	:	Laboratório de Fenômenos Superficiais
ILS	:	Interlamellar space
ODF	:	Orientation Distribution Function
OM	:	Optical Microscopy
r	:	Hardness ratio (material hardness/abrasive particle hardness)
r_c	:	Critical value of hardness ratio
RCF	:	Rolling Contact Fatigue
RD	:	Rolling/Reference Direction

RWAT	:	Rubber Wheel Abrasion Test
SAED	:	Selected Area Electron Diffraction
SEM	:	Scanning Electron Microscopy
SPHT	:	Sphericity
T	:	Tractive force
TF	:	Taylor Factor
TEM	:	Transmission Electron Microscopy
TTS	:	Tribological Transformed Surfaces
XRD	:	X-Ray Diffraction
WEL	:	White Etched Layer

TABLE OF CONTENTS

INTRODUCTION	28
1 – LITERATURE REVIEW: CLASSIFICATION OF WEAR AND WHITE ETCHED LAYER FORMATION IN RELEVANT ENGINEERING WEAR SYSTEMS	31
1.1 WEAR: definition and classification	31
1.2 Abrasive wear	32
1.3 Rolling Contact Fatigue (RCF)	41
1.4 Abrasive and RCF wear systems	44
1.4.1 Abrasion in the mining process	44
1.4.2 Wear in the wheel-rail interface	47
1.5 TRANSFORMED/DEFORMED LAYER FORMATION IN STEELS	49
1.5.1 Microstructure transformation under abrasive wear conditions	49
1.5.2 Microstructural transformation under RCF conditions	51
1.6 REFERENCES	54
2 – SURFACE AND MICROSTRUCTURAL CHARACTERIZATION OF PEARLITIC STEEL UNDER ABRASIVE WEAR: CORRELATION BETWEEN SEMI-AUTOGENOUS GRINDING MILL - SAG AND DRY SAND RUBBER WHEEL ABRASIVE TEST - DSRW	62
2.1 – ABSTRACT	62
2.2 INTRODUCTION	63
2.3 MATERIALS AND SAMPLES PREPARATION	64
2.4 WEAR PROCEDURE (LABORATORY TEST)	65
2.5 MICROSTRUCTURAL CHARACTERIZATION AND THE SURFACE ANALYSIS	66
2.6 RESULTS AND DISCUSSION	67
2.6.1 WEAR CHARACTERIZATION IN DSRW ABRASIVE TEST (LABORATORY RANGE)	67
2.6.1.1 Microstructure characterization	67
2.6.1.2 Wear micro mechanisms analysis	68

2.6.1.3	Microstructural analysis of the sub-superficial layer	73
2.6.1.4	Microstructural analysis using Transmission Electron Microscopy	79
2.6.2	WEAR CHARACTERIZATION OF THE SEMI-AUTOGENOUS GRINDING MILLS	84
2.6.2.1	Wear micro mechanisms analysis	84
2.6.2.2	Microstructural analysis of the sub-superficial layer	85
2.6.2.3	Crystallographic orientation analysis using EBSD	90
2.7	CONCLUSION	92
2.8	REFERENCES	94
3	CHARACTERIZATION OF THE MICROSTRUCTURAL TRANSFORMATION IN SAMPLES UNDER ABRASIVE WEAR IN LABORATORY CONDITIONS (SCRATCH TEST) AND FIELD CONDITIONS (RAIL GRINDING PROCEDURE)	97
3.1	ABSTRACT	97
3.2	INTRODUCTION	98
3.3	EXPERIMENTAL APPROACH	100
3.3.1	MATERIALS AND SAMPLE PREPARATION	100
3.3.1.1	Laboratory tests (scratch test)	100
3.3.1.2	Rail grinding procedure (wear on field)	101
3.3.2	EXPERIMENTAL PROCEDURE	101
3.3.2.1	Scratch test sequence	101
3.3.2.2	Rail grinding conditions	102
3.3.2.3	Tribometer specifications	102
3.3.2.3.1	Micro range	102
3.3.2.3.2	Macro range	103
3.3.2.4	Groove geometrical dimensions	104
3.3.2.5	Microstructural analysis	105
3.4	RESULTS AND DISCUSSION	106

3.4.1	SCRATCH TEST: INFLUENCE OF THE TEST PARAMETERS IN THE WEL FORMATION	106
3.4.1.1	Microstructural characterization before the test	106
3.4.1.2	The influence of the number of passes on the formation of sub-superficial layer	107
3.4.1.2.1	Micro range scratch test	107
3.4.1.2.2	Macro range scratch test	109
3.4.1.3	Friction coefficient analysis	115
3.4.1.4	Microstructural characterization of the sub-superficial layer	117
3.4.1.5	Crystallographic orientation analysis using EBSD	119
3.4.2	RAIL GRINDING PROCEDURE: APPLIED MULTI-PASS SCRATCH TEST	135
3.4.2.1	Microstructural Characterization	135
3.4.2.2	Microstructural analysis after grinding process	139
3.4.2.3	Crystallography orientation using EBSD	145
3.5	CONCLUSION	149
3.6	REFERENCES	151
4-	ANALYSIS OF THE ROLLING CONTACT FATIGUE (RCF) IN PEARLITIC STEEL UNDER CONDITIONS OF LABORATORY TEST (TWIN-DISC ROLLING CONTACT TRIBOMETER) AND FIELD (WHEEL)	155
4.1	ABSTRACT	155
4.2	INTRODUCTION	155
4.3	EXPERIMENTAL PROCEDURE	157
4.3.1	MATERIALS AND SAMPLE PREPARATION	157
4.3.1.1	Laboratory test	157
4.3.1.2	Wheel-rail contact	158
4.3.2	ANALYSIS OF THE MICROSTRUCTURE BENEATH THE CONTACT ZONE	159

4.4	RESULTS AND DISCUSSION	160
4.4.1	TWIN-DISC ROLLING CONTACT TRIBOMETER	160
4.4.1.1	Microstructural Characterization	160
4.4.1.2	Characterization of the worn surface	160
4.4.1.3	Microstructural characterization beneath the rolling contact	163
4.4.1.3.1	Characterization by Scanning Electron Microscopy	163
4.4.1.3.2	Characterization by Focused Ion Beam (FIB-SEM)	167
4.4.1.4	Micro-hardness profile analysis	169
4.4.1.5	Crystallographic orientation analysis by EBSD	171
4.4.1.6	Microstructural characterization by Transmission Electron Microscopy	173
4.4.2	WHEEL-RAIL CONTACT (CHARACTERIZATION ON FIELD)	176
4.4.2.1	Microstructural characterization in the initial condition	176
4.4.2.2	Microstructural characterization of the sub-superficial layer	177
4.4.2.3	Micro-hardness profile determination	181
4.4.2.4	Characterization by Focused Ion Beam (FIB-SEM)	182
4.4.2.5	Crystallographic orientation analysis by EBSD	182
4.4.2.6	Microstructural characterization by Transmission Electron Microscopy	183
4.5	CONCLUSION	186
4.6	REFERENCES	188
5	FINAL DISCUSSION	190
5.1	Wear Mechanisms	190
5.2	Microstructure features	190
6	COMPLEMENTARY REFERENCES	200
7	CONCLUSIONS	201
8	<i>FUTURE WORK</i>	202
	LIST OF PUBLICATIONS	203

CONFERENCE PRESENTATIONS

204

ANNEX

205

INTRODUCTION

The pearlitic steels are employed in the manufacturing of devices in the mining industry in different stages, such as liners and lifters in semi-autogenous grind mill (SAG) in the comminution process and wheel and rail in the ore transportation (railway). On the development of more resistant materials to the specific demands of abrasion and impact on those devices, pearlitic steels had prevailed the attempt of replacement by other type of steels with microstructures like martensite and bainitic (ALDRICH, 2013; BAKSHI et al., 2014; BAKSHI; SHIPWAY; BHADESHIA, 2013; POWELL et al., 2006).

The pearlitic steel has been used in the manufacturing of railway wheel and rail since the development of the railway transportation. They are manufactured by roller-straightening which introduces residual stress, influencing the local roll-rail contact and bending on the final profile. Residual stresses contained in railway rails are known to affect the growth rate of fatigue cracks that lead to rail failure. In particular, longitudinal tensile stress in the head accelerates the growth rate of transverse flaws (TALAMINI et al. 2004).

On the railway, defects produced by Rolling Contact Fatigue (RCF) and the sliding wear are the main demands for wheel and rail. In the case of the rail, the RCF is responsible for the most part of the rail change, while the sliding wear is notably the main damage mechanisms in the lateral of the rail head. On the other hand, the presence of “new” elements in the contact wheel-rail promotes the reduction of the rail life service. Abrasive particles as contaminants (from the environment) or in the application of the rail grinding procedure makes the abrasive wear an important type of wear for this device. For wheels, the RCF defects are observed in the patch contact, sliding wear in the flange and, additionally, abrasion wear due the grinding procedure by the wheel re-profiling.

In this work, Rolling Contact Fatigue and abrasion wear were characterized in both devices, wheel and rail. The sliding wear effect was not analyzed. This last wear mechanism is part of the scope of the *Catedra roda-trilho* and the results are shown by CHAVES, 2017 and NISHIKAWA 2018 (CHAVES, 2017; NISHIKAWA, 2018).

Another important factor to analyze, besides the economical and technological relevance, is the interest in the comparison between the demands of the SAG and

railway devices. The demand of impact is a common factor in SAG and railway devices. The impact in the SAG is extremely high due the rotation and the “jump” of the charge. In the SAG and railway devices the pearlitic microstructure is obtained at low price by the high volumes of material used in the manufacturing. This microstructure is the result of carbon and manganese content mainly. The Ni, Cu and Cr can be present as a result of controlled additions or by the employment of scrap or the use of electric furnace in the case of the rails. The **Table 1** summarizes the element content (wt. %) of the devices.

Table 1 Chemical composition (wt. %) of pearlitic devices used in the mining industry

Steel grade	C content (%)	Mn content (%)	Ni content (%)	Cu content (%)	Cr content (%)	Hardness HB
Class C*	0.67 – 0.77	0.60 – 0.90	< 0.25	< 0.35	-	321 – 363
Class D*					-	341 – 415
Standard**	0.67 - 0.77	0.70 – 1.00	< 0.1	-	0.7	300 – 340
Mill liner	0.5 – 0.78	0.75 – 0.95	< 0.082	-	2.0 – 2.17	320 – 360

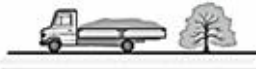
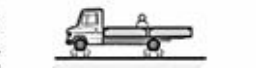
*From ARR M-107/M-208

**From ASTM-A-1

In general terms, the content of carbon and manganese (wt. %) is between 0.6 – 1.2 and 0.6 – 1, respectively. To reduce the possibility of pro-eutectoid cementite formation, the C and Mn contents require strict control during the welding process by thermite railroad welding or flash butt welding.

In this work, the SAG mill liners and the railway wheels were submitted to laboratory tests in controlled conditions of wear to simulate the phenomenon observed in service. The current methodology for the development of solution by friction and wear is based in the schematic representation shown in **Figure 1**. On this representation there is the assumption that the proper selection of the laboratory test provides valuable information about the material behavior and is able to give a hierarchy of materials in the same wear resistance sequence observed on field.

Figure 1 Classification of different types of tribological testing

TYPE OF TEST Test Conditions	TEST SYSTEM
FIELD TRIAL - Normal Operating Conditions - Extended Operating Conditions	
TEST LABORATORY WITH COMPLETE VEHICLE (EQUIPMENT) OR PLANT - Close to Normal Operating Conditions - Extended Operating Conditions	
TEST LABORATORY WITH PLANT OR CONSTRUCTION ELEMENTS - Close to Normal Operating Conditions - Extended Operating Conditions	
EXPERIMENT WITH STANDARD CONSTRUCTION ELEMENT OR SCALED DOWN PLANT	
EXPERIMENT WITH TEST EQUIPMENT OPERATING CLOSE TO NORMAL CONDITIONS	
EXPERIMENT WITH SIMPLE LABORATORY TEST EQUIPMENT (BENCH TEST)	

Adapted from (ZUM GAHR, 1987)

For the selection of the laboratory test and its set up was considered the geometry and the type of contact, relevant factors to establish the representativeness with the on-field phenomena (e.g. twin-disc tribometer in the wheel-rail contact).

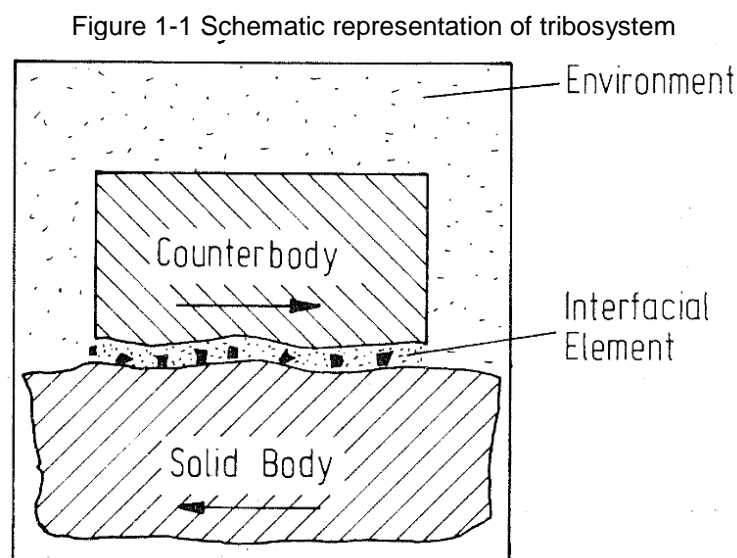
In this work, the damage mechanisms in the surface and the correlation with the sub-superficial microstructure will be compared in samples taken from devices tested in field and samples tested in laboratory. The aim of this work is to validate if the assumption of the similarity of the wear micro mechanisms in both scales allows the development of solution in the engineering.

1 – LITERATURE REVIEW: CLASSIFICATION OF WEAR AND WHITE ETCHED LAYER FORMATION IN RELEVANT ENGINEERING WEAR SYSTEMS

1.1 WEAR: definition and classification

The wear is defined by ASTM International as "damage to a solid surface (generally involving progressive loss of material), caused by the relative motion between surfaces in different situations (agriculture, crushers, ball bearing, brakes, etc.). Material removal in most cases takes place gradually due to a repetitive motion, but wear is a complicated process and influenced by several parameters. Among these are the following: Contact geometry, length of exposure, environments conditions, material compositions and hardness, interacting material surfaces, mechanical factors (load applied, sliding speed). The identification of all factors that interact in the contact allows recognizing the different wear mechanisms and the classification of the type of wear process.

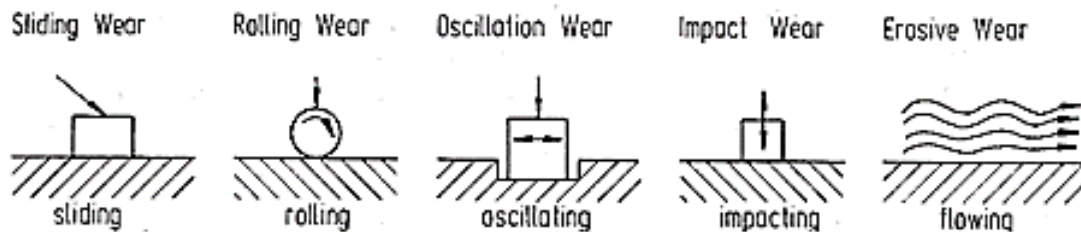
The physical characteristics and the environmental conditions in the interaction of mechanical pairs that are in contact or in relative movement are denominated as tribosystem. The structure of the tribosystem is determined by the elements, their properties and the interaction between them. Usually, the elements are a solid body, a counter body, interfacial element and the environment. **Figure 1-1** shows the schematic representation of elements involved in the interaction.



Adapted by (ZUM GAHR, 1987)

The action of external factors on the interaction of elements of the tribosystem could be generally classified as shown in Erro! Fonte de referência não encontrada..

Figure 1-2 Classification of wear process



Adapted from (ZUM GAHR, 1987)

The most common types of interaction between surfaces are classified as sliding, rolling, impact and erosion in accordance with the motion. On the other hand, the wear process is defined as a function of the kinematics of the system, such as sliding wear, rolling wear, impact wear and erosion wear. The detailed classification of wear is related to the interfacial element and is called dry or lubricated systems, and two or three body wear depending on the presence of hard particles.

The wear modes responsible for surface detachment are classified as adhesion, abrasion, surface fatigue and tribological reaction. In this thesis, the literature review is focused on the definition of wear mechanisms observed in tribosystems classically under abrasive wear and RCF conditions.

1.2 Abrasive wear

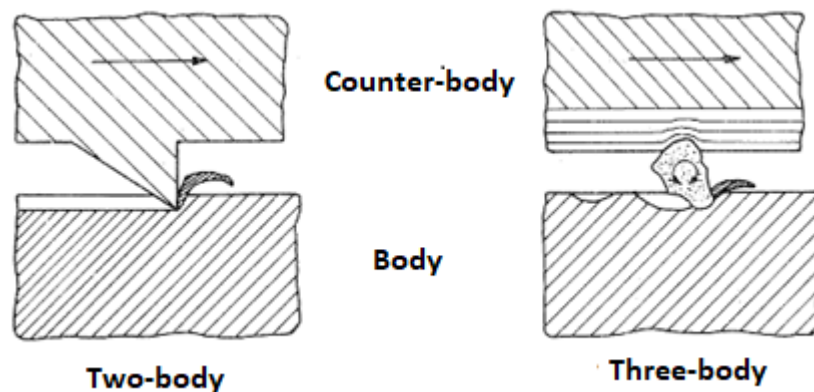
The ASTM standard G40-01 (ASTM INTERNATIONAL, 2014), define the abrasive wear as the loss of mass (or material detachment) as the result of the interaction of hard particles or asperities forced against a surface in relative motion. The hard particles may be the product of processing, a work-hardened fragment or a contaminant (particle). The abrasive wear depends on different physical factors from the wearing surface to the particle characteristics, such as size, type, roundness, etc.

The interaction between the particles and the body is classified as two or three-body abrasion according to the level of motion of the hard particle. The two-body abrasion is defined as a system in which the hard particles or the asperities are fixed in one of the bodies and the motion over the material surface is partially controlled. In three-

body abrasion, the particles act as an interfacial element and are free to move over the surface. Additionally, in these two types of contact, MISRA and FINNIE, describes another one as a function of velocity with the hard particle hitting the surface, being denominated as abrasion by erosion (MISRA; FINNIE, 1981a).

In tribosystem with three-body abrasion wear, the abrasive particles cause wear in small proportion due to the variation of angle attack (change in the wear micro mechanisms), since the particles could roll and slide, producing mass loss one or two order of magnitude smaller than two-body abrasion wear (HUTCHINGS, 1992). **Figure 1-3** shows a schematic representation of the abrasive wear.

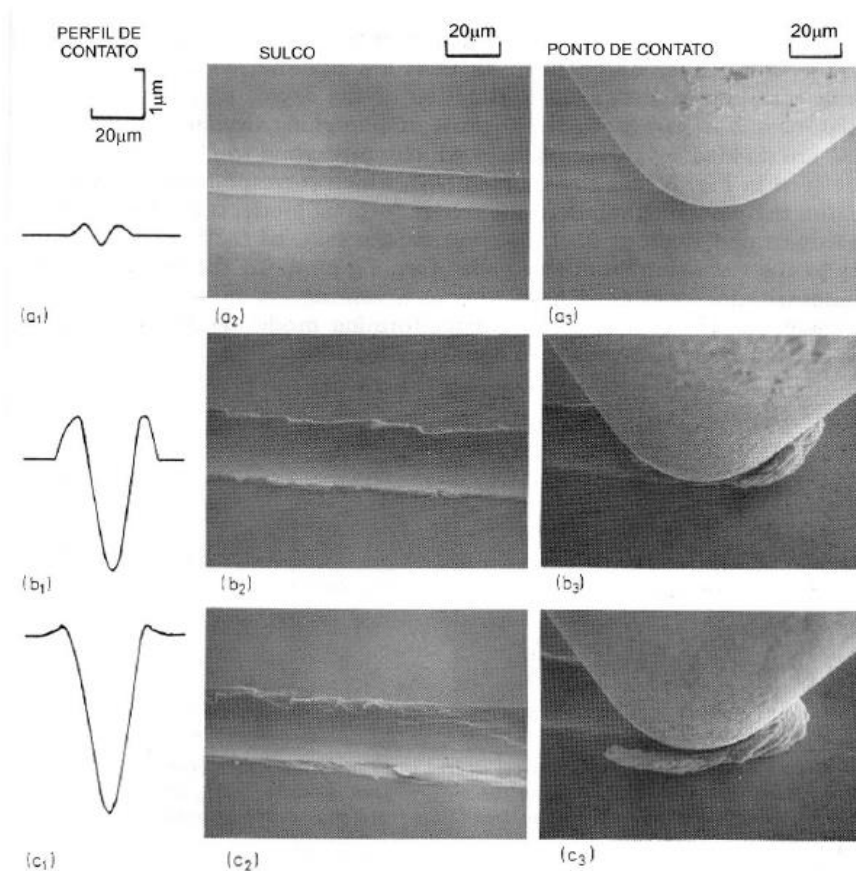
Figure 1-3. Schematic representation of abrasive wear



From (ZUM GAHR, 1987)

(GATES, 1998) discussed the classification of abrasive wear in two and three-body abrasion wear using the Dry Sand Rubber Wheel Abrasion tribometer (DSRW) (according to ASTM Standard G65). The discussion is based on the fact that this abrasive test is widely classified as a three-body abrasion test, but the author calls attention to the cases in which some abrasive particles are trapped in the rubber by the effect of its morphology (roundness) and the normal load applied in the system acting like two-body abrasion wear. In this case, a change in wear is observed, characterized by the simultaneous presence of cutting (predominant wear mechanism in two-body abrasion) and ploughing (predominant wear micro mechanism in three-body abrasion) as the predominant wear mechanisms. (HOKKIRIGAWA; KATO; LI, 1988; KATO, 1990) presented an analysis of the wear mechanisms as evidenced in **Figure 1-4**.

Figure 1-4 Wear mechanisms observed SEM. a) Micro ploughing, b) wedge formation, and c) Micro cutting



From (HOKKIRIGAWA; KATO; LI, 1988)

The difference between the wear mechanisms is defined by the severity of the damage. Ploughing is characterized by a ridge of deformed material is pushed along of the particle (pile up formation) without material removal from the surface. The other extreme case, in the cutting the material is deflected through a shear zone and flows up the front face of the particle to form a chip. In this mode, there is material removal from the surface. This mechanism is observed especially in ground tools, with the material removed as debris. The mechanisms are associated with moderate and severe regimes of wear, respectively, once the material removal for each mode are very different. On the other hand, wedge formation is characterized by the distribution of material in front and below the indenter and associated with the transition moderate-severe of the wear.

In the industry, there are some examples of simultaneous presence of the two and three abrasion wear. In the ore transportation (e.g. gutter), typically classified as two-

body abrasion (gutter and mineral ore), although the abrasive particles are in free motion, and could roll, characterizing a three-body tribosystem. Despite the discussion presented by GATES, the classification of wear in two and three-body is intuitive and can help to understand the phenomenon involved in the contact.

Besides the type of the interaction between the abrasive particle and the bodies surfaces, the interaction of the variables involved (characteristics of the material and the abrasive, the wear conditions) in the tribosystems has a strong influence in the results in different levels, being observed in the value of wear rates, types of wear mechanisms and the microstructural deformation or transformation beneath the worn surface.

The influence of the worn surface which has plastic deformation is commonly ignored, and the hardness is greater than that of the bulk. According to (KHRUSCHOV, 1974) abrasive wear resistance is linearly proportional to the hardness of wearing material (in pure metals). When the worn surface is strain-hardened and taken in account for the analysis, the results is that the flow stress of the deformed surface may be two or three times that of the bulk and the tendency of the curves does not follow the reported by KHRUSCHOV. The strain-hardness is the results of a competition between dislocation accumulation and the loss dislocation length) promoting an increase of hardness and the strength caused by plastic deformation at a temperature lower than the recrystallization temperature (HUTCHING, 1987).

EVERY showed a literature review about the work hardening nature presenting the results obtained by EMBURY, KEH and FISHER (1966) discussing the description of the cellular sub-structure formation during the initial stages of working in the several materials studied by the authors above mentioned. The dimension of those substructures is related with the spacing of cell walls which act as dislocation barriers in a manner analogous to grain boundaries (EVERY, 1974).

SUNDSTROM *et al.* showed for low alloyed steels (ferrite–pearlitic, ferrite–pearlitic-bainite, martensitic, bainitic) under laboratory test conditions (impeller-tumbler test equipment) that the wear resistance of the steels was found to be dependent on the microstructure and chemical composition. Steels with a similar type of microstructure show a linear decrease in mass loss with decreasing grain size and increasing carbon

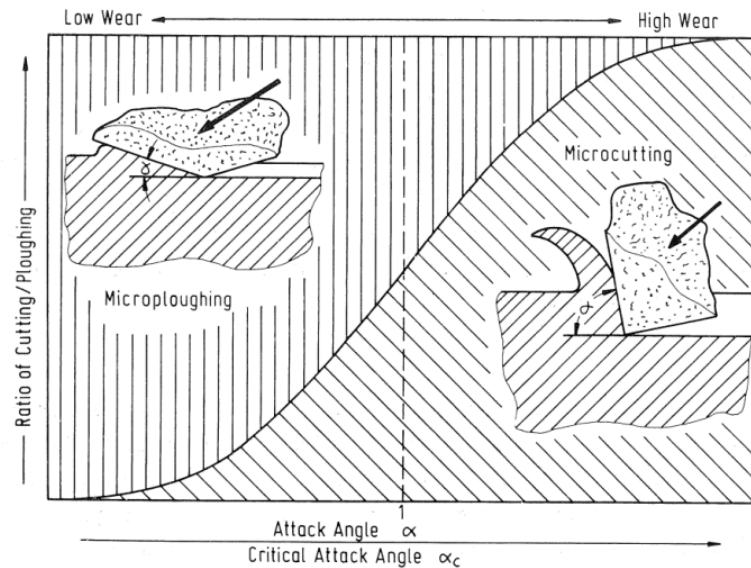
content. The softer non-martensitic steels work-harden to a higher extent than the harder martensitic steels during the wear process, i.e. steels with different microstructure showing different bulk hardness may show similar worn surface hardness values during the wear process (SUNDSTRÖM; RENDÓN; OLSSON, 2001).

The influence of the main characteristics of the abrasive particles in the wear has been widely studied in the literature (HUTCHINGS, 1992; MISRA; FINNIE, 1981b; ZUM GAHR, 1987).

MISRA e FINNIE showed that the abrasive particle size effect in abrasive and erosive wear is also influenced for the damage of the abrasive grits, elastic contact, rake angle. When small particles abrade the surface, they influence of work hardening and thus encounter much harder material than do larger particles which will also deform the material below the hard layer and thus abrade more. After some critical particle size, the influence of the work hardening layer will be slight and there will be no increase in wear rate for a further increase in particle size (MISRA; FINNIE, 1981c).

Abrasive wear in ductile materials is characterized by the presence of micro cutting and micro ploughing as the predominant wear mechanisms controlled by the morphology of the abrasive particle and the angle in the contact particle-surface (attack angle). The predominance of micro ploughing as a wear mechanism is observed for low angle (MULHEARN; SAMUELS, 1962). The correlation between the wear mechanism and the wear rate is schematically represented by (ZUM GAHR, 1987) in **Figure 1-5**Erro! Fonte de referência não encontrada..

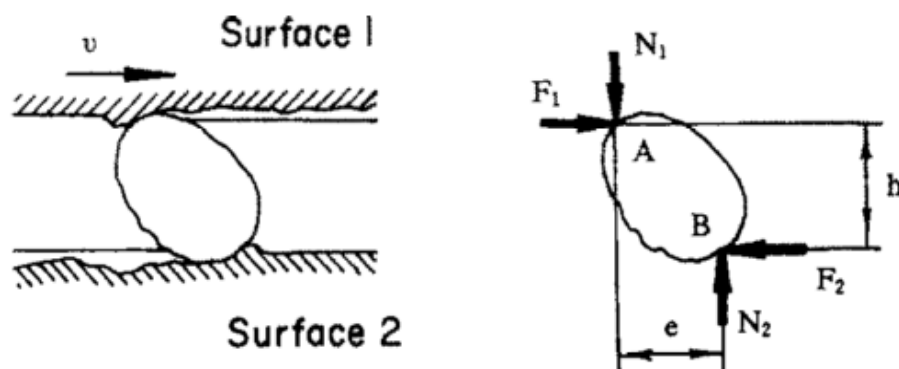
Figure 1-5 Schematic representation of the evolution in the wear mechanisms as a function of attack angle



From (ZUM GAHR, 1987)

FANG *et al.* highlighted the importance of the abrasive morphology in the determination of wear mechanisms in abrasive wear. The authors studied the patterns of movement of abrasive particles in three-body abrasion. The results of single-particle abrasion tests (**Erro! Fonte de referência não encontrada.** Figure 1-6) show that the movement patterns of the particles can be mainly divided into sliding and rolling (FANG *et al.*, 1993).

Figure 1-6 Schematic representation of forces acting in the displacement of the abrasive particle

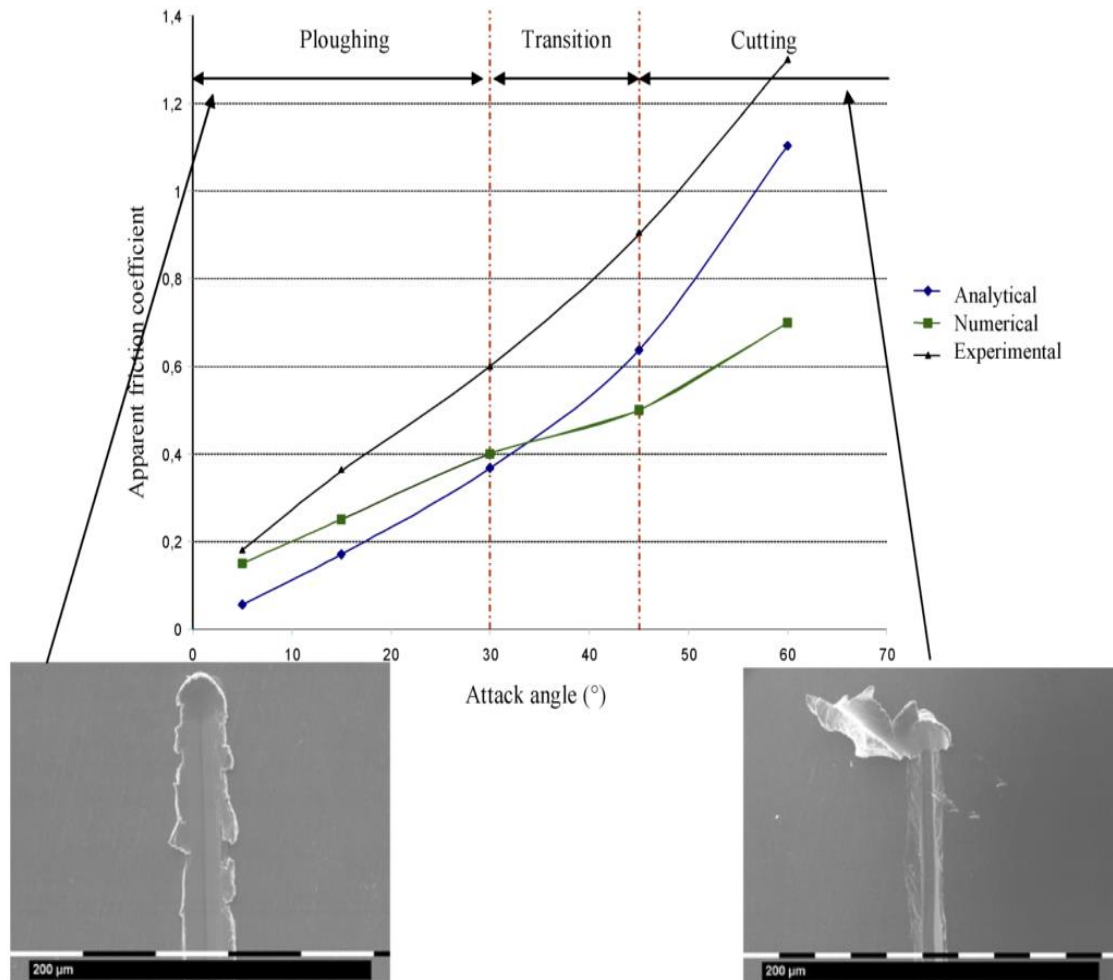


From (FANG *et al.*, 1993)

MEZLINI *et al.* studied the effect of particle geometry on wear mechanisms and the friction coefficient using scratch abrasion test (MEZLINI *et al.*, 2005). A numerical and analytical simulation (Bowden and Taylor model) was compared with experimental

results on a flat surface of aluminum alloy (Al-Mg). Different attack angles were tested. The results showed that the increase of the attack angle promotes the transition of the wear mechanisms (ploughing to cutting) and the increment of the friction coefficient as shown in the **Figure 1-7** Erro! Fonte de referência não encontrada..

Figure 1-7 Correlation between friction coefficient and wear mechanisms for different attack angle



From (MEZLINI *et al.*, 2005)

Later, NAHVU *et al.* using the mode developed by Fang *et al.* showed in the analysis of particle motion and modes of wear under DSRW abrasion test that the movement patterns are influenced by the applied load and the hardness of the material under test (NAHVI; SHIPWAY; MCCARTNEY, 2009).

In the study development by RONG *et al.* in hard-metal using sand/steel wheel test under wet/dry conditions (ASTM Standard B611), the correlation of applied load with the severity of wear as a function of the changes in the morphology of the abrasive particle was discussed. In order to describe the morphology in the abraded surface,

the authors divided the surface in three areas according to abrasive concentration in the specimen at the test. These areas were denominated as starting area, middle area and ending area. A change was found in the morphology in the abraded surface as a function of forces acting in the contact, which have a variation along the abraded surface. The abrasive characteristics and the wear conditions, i.e. the hardness of abrasive, their mass fraction in the slurry and the duration of the test, respectively, affect the morphology of the abrasive particle (RONG et al., 2011).

RATIA *et al.* analyzed some steels and hard metals under three body high-stress abrasive wear, used in the manufacturing of machinery devices in mining and earthmoving processes. The authors observed that in steels with relatively homogeneous microstructure, there is not a clear correlation between the wear and the studied abrasive properties. The wear in this kind of material depends not only on the abrasive but also on the wearing material (RATIA et al., 2014).

The effect of the force applied in the tribosystems under abrasive wear conditions has been widely studied and discussed in the literature. Authors such as (MISRA; FINNIE, 1981a; MOORE, [s.d.]; MOORE; DOUTHWAITE, 1976; STEVENSON; HUTCHINGS, 1996) showed that increasing the load applied in laboratory tests intensifies the severity, producing high wear rate.

In the mineral processing industry, the high stress conditions create a challenging environment for the wear protection steels. LINDROOS *et al.* studied the wear resistance of steels used commonly in abrasive conditions with the aim to get more precise insight into the material behavior in the abrasive service conditions. The authors used the single and multiple scratch test configuration in the analysis of material loss, surface work hardening, and wear mechanisms. The results show that in cyclic abrasion experiments, the abrasion resistance of the steels was improved noticeably from the initial state due to surface hardening. However, the highest surface hardening rate did not result in the highest wear resistance. Moreover, when the surface loading was sufficiently increased, the transition to a high wear rate mechanism was observed (LINDROOS et al., 2015)

DUBE *et al.* analyzed the influence of fracture behavior and the motion of abrasive particles in abrasive wear tests. The authors describe that systems under high stress

conditions produce breakage of the particles, develop new planes and surfaces, changing the angularity in the particles, and an opposite behavior occurs under low stress condition, which produces rounded particles. The results allow establishing that high stress systems are 10 times more severe (wear rate) than low stress conditions. The new angle attack produced with the particles fragmentation contribute to the simultaneous presence of cutting and indentation as the wear mechanisms, both obtained by abrasive rolling (DUBE; HUTCHINGS, 1999).

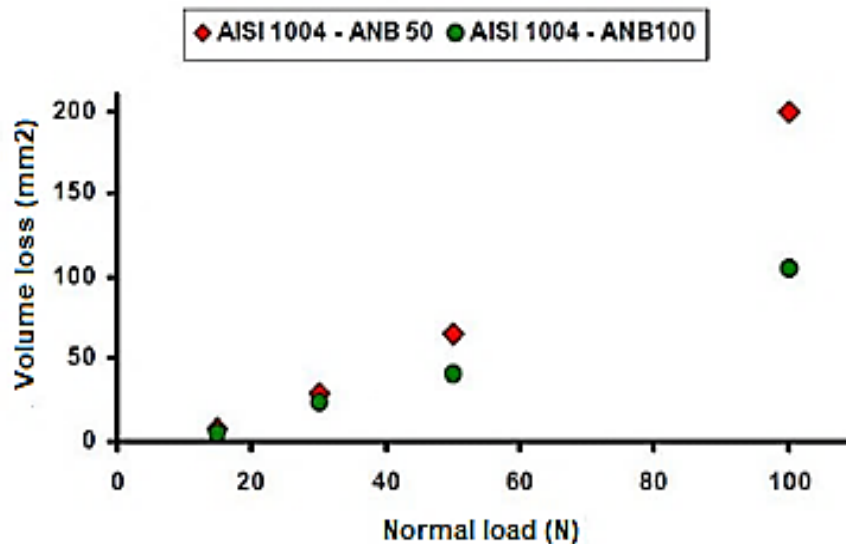
HOSSEINI *et al.* studied the correlation between abrasive breakage and wear in condition, enabling the simulation of a harsh environment as observed in comminution devices, especially in tumbling mills. The authors selected the DSRW (ASTM G65) Test as the critical test based on the observation founded by (RADZISZEWSKI, 2002) about the abrasive nature in mining processes. The type of contact and the wear regimes found in ball mill devices are both simulated using this type of laboratory test. The results show that variables in the system, such as wheel motion speed and normal load affect the level of wear severity, since the abrasive motion and the breakage or the abrasive particles are related to rotation speed and the applied force, respectively (HOSSEINI; RADZISZEWSKI, 2011).

RADZISZEWSKI *et al.* developed an abrasive test based on the ASTM Standard G65 for the analysis of wear of a tumbling mill steel (1018 and 1045) as a function of the energies/forces acting in a mill. The authors used the laboratory tests over a range of applied forces, wheels rotation speeds and wheel torque (for the analysis of the friction coefficient). The results reported by the authors shows that for a given ore (abrasive flow), the wear mechanisms have a dependency of the applied load in both tested steels. Unfortunately, no particle breakage data was collected by the authors and the analysis of the correlation between wear and friction and breakage was not carried out (RADZISZEWSKI *et al.*, 2005).

VILLABON studied the correlation between the volume loss of low carbon steel and the normal load applied in the laboratory test (ASTM standard G65). The results (**Figure 1-8**) showed that in low normal load conditions, the abrasive particle size does not influence the steels response; however, an increase in the load applied promotes differences in the behavior. Samples tested with bigger abrasive particles could break

once the applied load is increase, changing the wear mechanisms acting in the process, confirmed in the difference of tendency in the curves (VILLABON, 2005).

Figure 1-8 Volume loss (accumulate values) as a function of the normal load and the abrasive particle size in ASTM Standard G65 test for AISI 1004



Adapted From (VILLABON, 2005)

1.3 Rolling Contact Fatigue (RCF)

Rolling-contact fatigue (RCF) is defined as a failure or material removal driven by crack propagation caused by the near-surface alternating stress field. It is also commonly observed in gears, camshaft mechanisms, and rail-wheel contacts and is considered the most unavoidable failure in the rolling contacts.

The main mechanisms in RCF in railway are subsurface originated spalling and/or surface originated pitting and the prevalence of one of them depends on a number of factors, e.g., surface quality, lubricant cleanliness, material quality. Spalling occurs due to propagation of microcracks originated below the surface. The microcracks develop at material heterogeneities (like inclusions) and propagate towards the surface. Smooth surfaces, abundance of the nonmetallic inclusions in the material, and absence of surface shear are the key factors to favor this failure mode. On the other hand, pitting occurs due to surface roughness which acts as a stress raiser and facilitates the crack initiation. Further it propagates at a shallow angle 15–30 degrees to the surface and afterwards back towards the surface (SADEGHI et al., 2009).

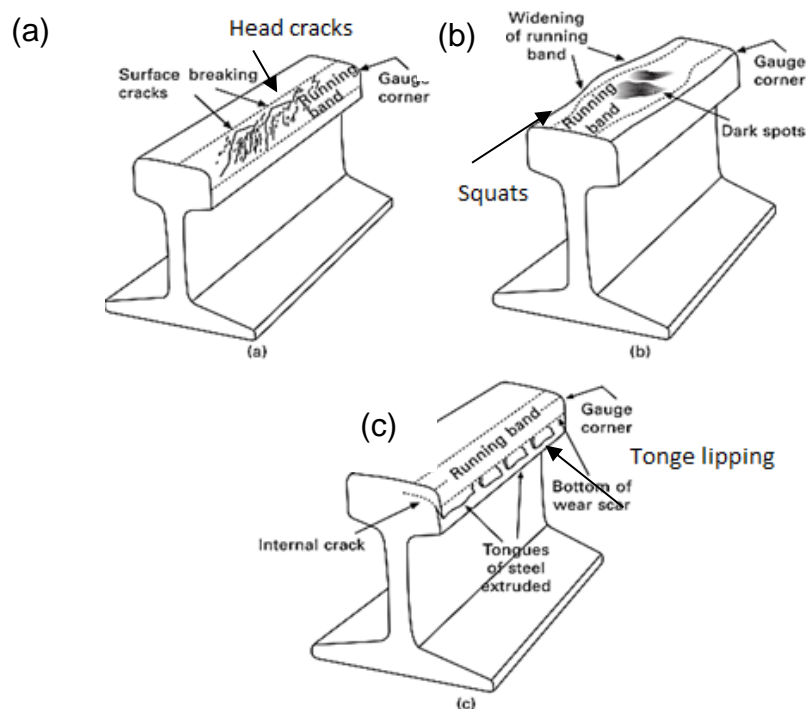
The main RCF damages are commonly define as follows:

Head checks (Shallow cracks): are the results of the accumulation of plastic strain increments (ratcheting) and denominated as small and fine cracks on the rail surface also known as “gauge corner cracking”. With the progression, these cracks can cause rail break or promote spalling on rail surface (**Figure 1-9a**).

Squats: occur on straight tracks on the surface of the rail head. It is known as the combination of the darkening of the rail surface and the widening of the running band. It is observed that the material flows sideways on the rail producing a surface depression promoting the contaminant material deposition to become a corroded surface leading to the characteristic shadow. They can initiate as a result of ratcheting and fluid pressurization and also from white etching layers (WELs) which result from modification of the microstructure of the rail surface material from pearlite to martensite (PYZALLA et al., 2001). When rails are ground, in fixed cycles, such defects are removed in an early stage and therefore in principle do not give rise to catastrophic failures (**Figure 1-9b**).

Tongue lipping: Identified by the formation of thin slivers or tongues of material from the running band of the rail (**Figure 1-9c**).

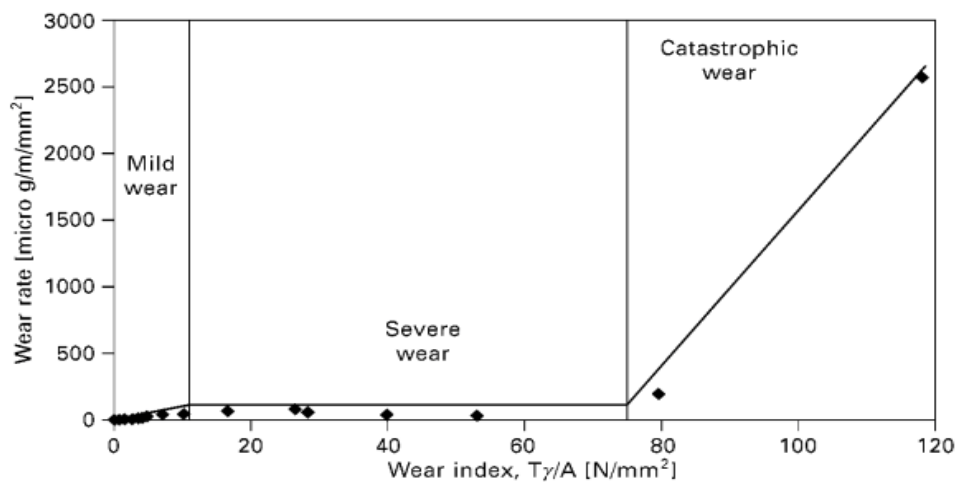
Figure 1-9 Schematic representation of the rail fatigue damages. a) Head cracks, b) squats, c) tongue lipping



From (FLETCHER; FRANKLIN; KAPOOR, 2009)

In laboratory conditions, the slip ratio (i.e. creepage) has an important effect on the wear and RCF damage of wheel and rail materials (BOLTON; CLAYTON, 1984; SATO ANDERSON, P.M., RIGNEY, D.A., 1993; SEO et al., 2016). Three wear regimes have been identified based on the variation of loading, sliding speed, bulk temperature: mild regime (type I) resulting in extremely smooth surfaces (often smoother than the original) and debris typically with diameter down to 100 nm; severe regime (type II) and debris with diameter up to 0.01 mm. adhesive and thermal mechanisms are associated with severe regime; catastrophic regime (type III) associated with the increase of the temperature in the contact resulting in thermal softening (BOLTON; CLAYTON, 1984). The wear regimes are shown in **Figure 1-10** in terms of wear rate (μg material lost/m rolled/ mm^2 contact area) against an index based on work done in the contact, $T\gamma/A$, where T is tractive force (normal load divided by friction coefficient), γ is slip and A is contact area (BRAGHIN; BRUNI; LEWIS, 2009).

Figure 1-10 Wear rates and regimes for R8T wheel steel tested against UIC60 900A rail steel



From (BRAGHIN; BRUNI; LEWIS, 2009)

Garnham *et al.* in the study of the early detection of rolling-sliding contact fatigue cracks describes that in rail-wheel contact, the creepages below 4% (susceptibility to fatigue cracking) do not show a simple relationship with creepage. Small changes in low rates of creepage can result in large differences in fatigue life. It is important, therefore, to have close control over creepage during a laboratory test (GARNHAM; BEYNON, 1991; GARNHAM; DAVIS, 2011).

1.4 Abrasive and RCF wear systems

1.4.1 Abrasion in the mining process

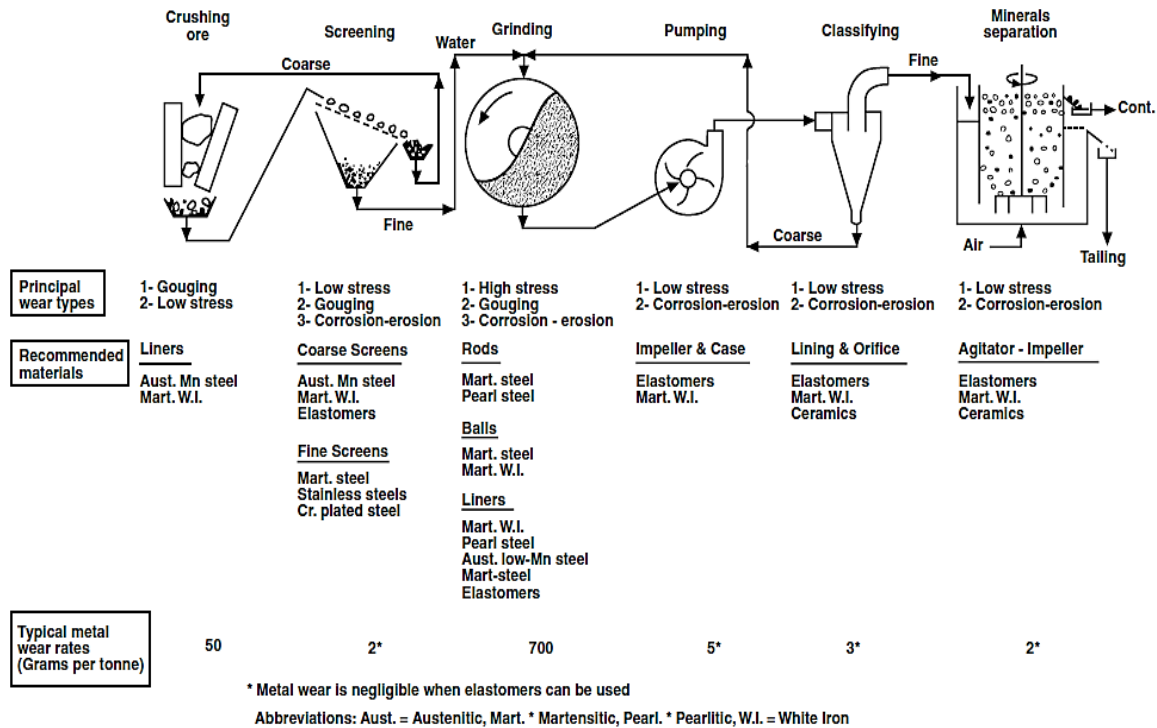
Earthmoving, mining, and mineral processing involve frequent severe, mechanical interactions between metals, and between metals and abrasive nonmetallic and metallic materials (i.e., mineral bearing ores).

The mechanisms by which metal-to-metal and abrasive wear occur, and the relationships between material properties and wear behavior, are reasonably well-understood in general terms (DURMAN, 1988; KHRUSCHOV, 1974; RICHARDSON, 1968). However, the specific wear mechanisms/wear material interactions that occur during earthmoving, digging and the processing of ore are more complex and depend on conditions and characteristics of material like worn material and the nature of abrasion. The process conditions have a strong influence in the wear process, such as the type of loading and the comminution environment (HAWK; WILSON, 2001).

In general, the wear behavior of materials used in these operations is determined by a number of factors, which can be grouped into three main categories: (1) the properties of the wear material (microstructure); (2) the properties of the abrasive material (morphology, size); and (3) the nature and severity of the interaction between the metal-to-metal wear surfaces and between the abrasive and the wear materials (wear conditions) (HAWK; WILSON, 2001).

Figure 1-11 depicts generic ore processing operations in schematic form with the materials used for the particular wearing surfaces and some typical wear rates (Norman, 1980).

Figure 1-11 Schematic representation of the main steps in ore comminution



From (HAWK; WILSON, 2001)

On this thesis, the abrasive wear in the comminution process is focused in the grinding stage, which in several cases has the compounds fabricated in pearlitic steels as shown in the **Figure 1-11**.

Grinding process (SAG/AG mills)

The dominant wear modes in grinding are high-stress abrasion and erosion-corrosion for ball mill and additionally, high impact and gouging abrasion in autogenous and semi-autogenous mills. During grinding (usually in wet conditions), the ore is ground from a maximum 20-mm diameter down to about 0.3 mm or less. The wear of grinding media (balls or rods), plus the wear of grinding mill liners, accounts for a major portion of the wear in an ore processing plant (AVERY, 1974).

The performance of grinding mills and the consumption of grinding media and wear liners are influenced to a great degree by liner design. Grinding of the crushed ore is almost always performed in cylindrical rotating mills, which are filled about half full of grinding medium (steel or iron balls, steel rods). In semi-autogenous grinding, steel balls about 125 mm in diameter are charged into the mill to occupy approximately 8 to

10% of the mill volume and supplement the grinding produced by the large pieces of ore in the mill.

The wear of these liners, as well as the wear of the grinding balls and rods, is a major item of expense in most ore processing operations. The crushed ore fed into the grinding mills is almost always mixed with water so that the grinding is done in slurry containing about 75% solids (IMHOFF et al., 1985).

The dominant abrasive wear conditions that exist in earthmoving, mining and minerals processing equipment can be described using the following broad classifications (AVERY, 1961).

- Gouging abrasion
- High-stress, or grinding, abrasion
- Low-stress, or scratching, abrasion

Gouging abrasion occurs under conditions where abrasive particles indent and move over the wear surfaces under high stress levels. It involves both cutting and tearing types of wear, in which small chips of metal are removed from the wearing surface by the movement of the sharp points of rock, under considerable pressure, over the wearing surface.

High-stress, or grinding, abrasion occurs when abrasive particles are compressed between two solid surfaces, as for example, between grinding rods or balls. The high-stress abrasion that occurs in grinding mills takes place over a very small contact region, where the ore particles are caught between the grinding balls, or between grinding balls and the mill liner. High-stress abrasion is sometimes referred to as three-body abrasion, although two-body, high stress conditions can sometimes exist. High-stress abrasion implies that the abrasive particle is fractured and broken apart during the wear process.

Low-stress or scratching abrasion occurs when lightly loaded abrasive particles impinge upon, and move across, the wear surface, cutting and plowing it on a microscopic scale. In aqueous or other liquid environments, corrosion may also contribute to the overall wear rate, in which case erosion-corrosion is the operative wear mechanism.

1.4.2 Wear in the wheel-rail interface

The contact wheel-rail is not spread over the whole rail and wheel surface. The contact area can be divided into stick (no slip) and slip regions. Longitudinal creep and tangential (tractive) forces arise due to the slip that occurs in the trailing region of the contact patch. With increasing tractive force, the slip region increases and the stick region decreases, resulting in a rolling and sliding contact.

LEWIS AND OLOFSSON, defined for sliding bodies, that the friction force, and thereby the coefficient of friction (friction force divided by normal force), depends on three different mechanisms: deformation of asperities, adhesion of the sliding surfaces and ploughing caused by hard particles/asperities. For the steel wheel-steel rail contact, the rolling coefficient of friction is of the order of 1×10^{-4} (LEWIS; OLOFSSON, 2009).

The high energy efficiency of railway transportation is made possible by the favorably low losses in the rolling contact between the hard surfaces of the wheel and rail. However, several undesired phenomena may occur in this contact. High vertical contact forces, but also lateral and longitudinal forces, induce stresses that may cause material yielding and fatigue. Rolling contact forces combined with friction induce wear. Traction and braking may lead to wheel sliding, resulting in rail burns and wheel flats, unfavorable material phase transformations and thermal cracks.

Due to its complicated working conditions, the wheel suffers various damages, such as tread wear, flange wear, polygon wear and rolling contact fatigue (RCF). There are two typical wheel/rail contact types, wheel tread/rail head contact and wheel flange/rail gauge contact, which result in quietly different slip ratios between the wheel and rail.

The wheel-rail interface involves a number of research fields. The 'traditional' fields deal with the physical phenomena in the interface itself. Additional fields are indirectly related since they strongly affect the conditions in the wheel-rail interface.

- *Contact mechanics* involving forces and relative motion in the wheel-rail rolling contact.
- *Material mechanics* is central to modeling and understanding material behavior under contacting surfaces with severe plastic strains often combined with strong anisotropy.

- *Fracture mechanics* deals with the strength of cracked components. It can be employed to predict final fracture, e.g. of a rail. Further, fracture mechanics-based models can be employed to predict the rate of crack growth.
- *Tribology* is central to understanding and optimizing the wheel-rail interface. Both dry and lubricated friction are important in the understanding of vehicle dynamics and traction and at braking.

In terms of potential to cause wear, sliding motion (motion tangential to the surface) is more severe than motion perpendicular to the surface, such as occurs with impact or rolling. Oxidative wear occurs in mild contact conditions (low load and sliding velocity - typical of rail head-wheel tread contacts). On the other hand, adhesive or galling wear (possible in curves, where the rail gauge corner and wheel flange contact) is observed in more severe conditions. The presence of particles in the interface leads to abrasive wear. Very severe sliding conditions can lead to seizure and high heat generation in the contact (this has been observed in very tight curves) (LEWIS; OLOFSSON, 2009).

Rail grinding procedure

Grinding is a common practice in the railway industry to maintain the profile and remove wear marks (fatigue cracks, head checks, etc.) from the rail surface. Those marks are observed when the rail is subjected to high dynamic forces or when the loaded zone is comparatively small (FLETCHER; FRANKLIN; KAPOOR, 2009).

SATOH *et al.* in the analysis of effect of rail grinding on RCF observed that the rail grinding directly removes the surface layer with accumulated rolling contact fatigue, removing the micro cracks, plastic deformation or high strain accumulated in the surface of rail (SATOH; IWAFUCHI, 2005).

The rail grinding process is essentially the process of material removal in the rail surface to eliminate irregularities in the longitudinal plane (corrugation) and fatigued material. The rail standard maintenance reduces the presence of excessive stresses, removing the rolling contact fatigue layer on the running surface and preventing spalling and/or shelling damage (CUERVO; SANTA; TORO, 2015).

1.5 TRANSFORMED/DEFORMED LAYER FORMATION IN STEELS

Grain refinement prevents the dislocations movement into the microstructure and has been associated with the increase of wear resistance. However, in real conditions, contact between surfaces can be more complex and the compounds could be subjected to different wear mechanism as simultaneous processes impact and abrasion.

The microstructure transformation of materials under wear condition is widely called White Etched Layer (WEL). WEL owes its name to the white appearance after etching with Nital reagent. There are mainly two approaches to explain its development (STEENBERGEN; DOLLEVOET, 2013). The first theory assumes that severe plastic deformations at temperatures below the austenitisation temperature cause the formation of WEL (friction-martensite). The second one supposes that WEL develops due to heating above austenitisation temperature followed by rapid cooling (thermal-martensite) (PYZALLA et al., 2001; TAKAHASHI; KAWAKAMI; UEDA, 2010).

LOJKOWSKI *et al.* presented a third hypothesis based in the analysis of pearlitic steels in the analysis of the surface of railways tracks. The authors conclude that the WEL formed on the surface corresponds to nanocrystalline α -Fe-C alloy, as the result of a solid-state process analogous to mechanical alloying (LOJKOWSKI; DJAHANBAKHS; BU, 2001).

Even with an extensive information in the literature, the nature of the WEL formation has not been successfully described, especially in devices under abrasive wear conditions.

1.5.1 Microstructure transformation under abrasive wear conditions

DOLLAR *et al.* observed in the analysis of the deformed layer in pearlitic steels that the work hardening is controlled by the dislocation movements in ferrite between the cementite (DOLLAR; BERNSTEIN; THOMPSON, 1988; MERCER; HUTCHINGS; BOX, 1989).

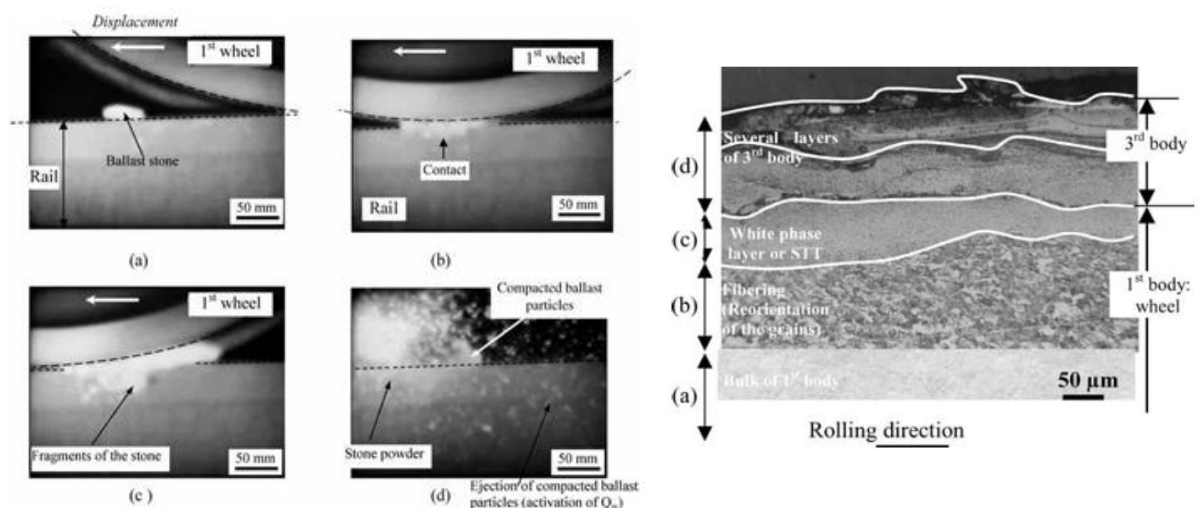
PRASAD *et al.* in the analysis of the abrasion-induced microstructural changes during low stress abrasion of a plain carbon steel, it was observed that the material removal mechanisms during abrasion of steels are controlled by the properties of a layer

beneath the abraded surface. The properties of this layer are in turn governed by the bulk microstructure (PRASAD; PRASAD, 1991).

MODI *et al.* studied the abrasive behavior under low stresses using DSRW abrasion test. The SEM results revealed that microstructural changes and deformation lead to work hardening controlling the material removal mechanisms. The resulting microstructure consists in the formation of ultrafine martensite (50-100 μm) due to fast re-austenitization under the conditions of high rates. Broken pearlitic structures and flow lines in the regions close to the abraded surface were also observed (MODI *et al.*, 1994).

In a particular analysis of WEL formation, Descartes *et al.* studied the interaction of contaminant particles in the wheel–rail contact. The wear was characterized by massive indentations. The results showed the presence of a natural third body, initially composed of particles stemming from wheels and rails (DESCARTES; DESRAYAUD; BERTHIER, 2008). The sliding between wheel and rail allows the absorbing of fluid contaminants into the contact as shown in **Figure 1-12**.

Figure 1-12 a) High speed camera images of the passage of a ballast stone in the 1st wheel-rail contact-ballast stone, b) Cross-section of a wheel with a third body layer



From (DESCARTES; DESRAYAUD; BERTHIER, 2008)

Figure 1-12b shows the longitudinal section (in the rolling direction) of an area of the running surface revealing the layer formation on the wheel characterized by unchanged metallographic structures in the bulk (bottom), a reorientation of grains by

sliding in the near-surface (350 μm), and white phase layer generally called Tribological Transformed Surface.

BAKSHI *et al.* in the analysis of the microstructure (pearlite, bainite and martensite) under three-body abrasion reported contradictory results as shown by (XU *et al.*, 1995) in the WEL formation. The results presented by the authors established the formation of WEL on the surface of all three microstructures. Unfortunately, the subsurface analysis was not the scope of the work. The authors observed that the cementite lamellae were plastically deformed in the abrasion direction and some differences in the morphology and thickness in the deformed layer. The white-etching layer on the nanostructured bainite is thinner than that in the pearlitic sample. For the martensite, an extensive fragmentation was observed and hence the remaining WEL is considerably thinner than in the other samples (BAKSHI; SHIPWAY; BHADESHIA, 2013).

1.5.2 Microstructural transformation under RCF conditions

It is generally believed that increasing rail hardness and strength increases rail wear resistance. KALOUSEK *et al.* in the study of the wear resistance in rail steel microstructures (pearlite, bainite and tempered martensite) under contact fatigue (disk-on-disk tribometer configuration) showed that dry wear rates decreased significantly with increasing hardness in high rails with tempered martensite or bainite microstructures but were almost independent of hardness for pearlite in the range tested. The superior performance of pearlite in dry wear appears to be due to a very pronounced work hardening near the wearing surface, characterized by refinement in the pearlite microstructure near the wearing surface. TEM examination of worn surfaces shows a considerable refinement of the interlamellar spacing of pearlite and the formation of very fine polycrystalline ferrite grains. Diffraction patterns show that a strong possibility of texture formation exists (KALOUSEK; FEGREDO; LAUFER, 1985).

Based on experimental investigations, the basic hardening mechanisms of corrugated rails may be stated as follows: (a) Hardening by reduced interlamellar spacing, (b) grain boundary hardening, (c) particle hardening, (d) metallurgical transformation hardening and (e) work hardening. The structure below the white layer exhibits

deformed and broken cementite lamellae. The hardening process is caused by the decreased interlamellar spacing and can be described in accordance with the Hall-Petch relation. A decrease of the grain size from 5-10 μm in the unaffected microstructural zone to less than 50 nm in the area of the white layer could be noticed by the TEM analysis. There is no indication that a lamellar structure still exists in the WEL (BAUMANN; FECHT; LIEBELT, 1996).

According to BAUMANN *et al.* the transformation of the surface layer in rails starts with the formation of stripes, parallel to the travel direction. Two mechanisms for the formation of white etching layers in rail steels are: the dissolution of cementite during severe plastic deformation; formation of a nanocrystalline structure in the surface layer and after advanced corrugation, the transformation of the supersaturated $\alpha\text{-Fe}$ into a austenitic-martensitic structure. In other words, grain refinement plays a significant role in the formation of nanocrystalline WEL on a rail surface under cold deformation with cyclic shear conditions (BAUMANN; FECHT; LIEBELT, 1996; BAUMANN; ZHONG; FECHT, 1996).

The study of WEL formation by metal-metal contact has been widely developed for the rail transportation industry. Traditionally, in the manufacture of devices (wheels and rails) pearlitic steels have been used, in spite of, in the literature some authors discussed the tribological behavior of bainitic alloys in relation with pearlite microstructures in fatigue contact conditions (CLAYTON, 1980; DANKS; CLAYTON, 1987; ZAPATA; JARAMILLO; TORO, 2011).

The results obtained by ZAPATA *et al.* in the rolling contact fatigue for bainitic and pearlite steels indicated that the mass losses were similar regardless of the fact that difference in wear mechanisms. The behavior of pearlitic samples are influenced by the occurrence of ratcheting with and without creepage and the bainitic samples the adhesive wear also act as a significant mechanism in creepage conditions (ZAPATA; JARAMILLO; TORO, 2011).

As previously established, several authors considered WEL as a martensitic transformation, to be caused by thermal energy in the contact. STEEMBERGEN *et al.* discussed WEL formation as of the significance of subsurface layer in the formation of squat defects on train rails. On the rails surfaces the presumption of purely martensitic

microstructure and the exclusion of mechanisms (as showed by Baumann *et al.*) do not present a conclusive answer. On high friction levels and slip rates such as high legs of sharp curves, in zones of high traction such as stations, this behavior may be different. The authors made two remarks on the early nucleation of white etching material in relation to rail grinding. The freshly ground surface consists of hard and brittle martensitic peaks (with magnitude in the order of tens of microns) and a second aspect considers that the severe local plastic deformation on the surface rail (facets depending of the curvature profile) play a role in WEL nucleation (STEENBERGEN; DOLLEVOET, 2013).

STEENBERGEN, in the analysis of rolling contact fatigue (RCF) in rail grinding, showed two mechanisms that lead to the formation of a hard-white brittle etching surface layer. The first one occurs due to storage of potential (or strain) energy in the material; the second due to addition of thermal energy (STEENBERGEN, 2016).

The main factor for the discrepancy in the literature about the wear mechanisms predominant in the contact and the WEL formation relates with the difficulty in the interpretation of the influence in the phase transformation of thermal and mechanical processes.

As shown in the literature review, the most part of the works are focused in the determination of the wear mechanisms responsible for the material removal, and WEL formation is a topic that has acquired importance in the last decades. The characterization techniques used restricted the detailed analysis, being necessary the application of higher resolution techniques, as proposed in this thesis.

1.6 REFERENCES

AAR. Manual of Standards and Recommended Practices Section C - Part II, 2007.

AVERY, H. S. The measurement of wear resistance. *Wear*, v. 4, p. 427–449, 1961.

AVERY, H. S. Work hardening in relation to abrasion resistance. Materials for the mining industry. *Anais*.1974

BAKSHI, S. DAS; SHIPWAY, P. H.; BHADESHIA, H. K. D. H. Three-body abrasive wear of fine pearlite, nanostructured bainite and martensite. *Wear*, v. 308, n. 2013, p. 46–53, 2013.

BAUMANN, G.; FECHT, H. J.; LIEBELT, S. Formation of white-etching layers on rail treads. *Wear*, v. 191, n. 1–2, p. 133–140, 1996.

BAUMANN, G.; ZHONG, Y.; FECHT, H. J. Comparison between nanophase formation during friction induced surface wear and mechanical attrition of a pearlitic steel. *Nanostructured Materials*, v. 7, n. 1–2, p. 237–244, 1996.

BEYNON, J. H.; GARNHAM, J. E.; SAWLEY, K. J. Rolling contact fatigue of three pearlitic rail steels. *Wear*, v. 192, n. 1–2, p. 94–111, 1996.

BHUSHAN, B. *Modern Tribology Handbook*. 2000.

BOLTON, P. J.; CLAYTON, P. Rolling-sliding wear damage in rail and tyre steels. *Wear*, v. 93, n. 2, p. 145–165, 1984.

BORCHERS, C.; KIRCHHEIM, R. Cold-drawn pearlitic steel wires. *Progress in Materials Science*, v. 82, p. 405–444, 2016.

BRAGHIN, F.; BRUNI, S.; LEWIS, R. Railway wheel wear. In: R. LEWIS; OLOFSSON, U. (Eds.). *Wheel-rail interface handbook*. WOODHEAD PUBLISHING LIMITED, 2009. p. 172–210.

CHEN, H. et al. Assessment of lubricant applied to wheel/rail interface in curves. *Wear*, v. 314, n. 1–2, p. 228–235, 2014.

CLAYTON, P. The relations between wear behaviour and basic material properties for

pearlitic steels. *Wear*, v. 60, n. 1, Apr. 1980, p. 75–93, 1980.

CUERVO, P. A.; SANTA, J. F.; TORO, A. Correlations between wear mechanisms and rail grinding operations in a commercial railroad. *Tribology International*, v. 82, n. PB, p. 265–273, 2015.

DANKS, D.; CLAYTON, P. Comparison of the wear process for eutectoid rail steels: field and laboratory tests. *Wear*, v. 120, p. 233–250, 1987.

DESCARTES, S.; DESRAYAUD, C.; BERTHIER, Y. Experimental identification and characterization of the effects of contaminants in the wheel-rail contact. *Journal of Rail and Rapid Transit*, v. 222, n. 2, p. 207–216, 2008.

DOLLAR, M.; BERNSTEIN, I. M.; THOMPSON, A. W. Influence of deformation substructure on flow and fracture of fully pearlitic steel. *acta*, v. 36, n. 2, p. 311–320, 1988.

DUBE, N. B.; HUTCHINGS, I. M. Influence of particle fracture in the high-stress and low-stress abrasive wear of steel. *Wear*, v. 233–235, p. 246–256, 1999.

DURMAN, R. W. Progress in Abrasion - Resistant Materials for use in Comminution Processes. *International Journal of Mineral Processing*, v. 22, p. 381–399, 1988.

EMBURY, J. D.; FISHER, R. M. The structure and properties of drawn pearlite. *Acta Metallurgica*, v. 14, n. 2, p. 147–159, 1966.

EYRE, T. S. The Mechanisms of wear. *Tribology International*, p. 91–96, 1978.

FANG, L. et al. Movement patterns of abrasive particles in three-body abrasion. *wear*, v. 164, p. 162–164, 1993.

FARGAS, G.; ROA, J. J.; MATEO, A. Influence of pre-existing martensite on the wear resistance of metastable austenitic stainless steels. *Wear*, v. 364, p. 40–47, 2016.

FELLER, H. G.; WAIF, K. Surface analysis of corrugated rail treads. *Wear*, v. 144, p. 153–161, 1991.

FLETCHER, D. I.; FRANKLIN, F. J.; KAPOOR, A. Rail surface fatigue and wear. In:

Wheel-Rail Interface Handbook. Woodhead Publishing Limited, 2009. p. 280–310.

FREITAS, I. M. Análise de propriedades e mecânica da fratura de rodas ferroviárias microligadas fundidas e forjadas. 70º Congresso Anual da ABM. Anais.2015

GARNHAM, J. E.; BEYNON, J. H. The early detection of rolling-sliding contact fatigue cracks. *Wear*, v. 144, n. 1–2, p. 103–116, 1991.

GARNHAM, J. E.; DAVIS, C. L. Very early stage rolling contact fatigue crack growth in pearlitic rail steels. *Wear*, v. 271, n. 1–2, p. 100–112, 2011.

GATES, J. D. Two-body and three-body abrasion: A critical discussion. *Wear*, v. 214, n. 1, p. 139–146, 1998.

HAWK, J. A.; WILSON, R. D. Tribology of Earthmoving, Mining and Minerals Processing. In: *Modern Tribology Handbook, Two Volume*. p. 1331–1368, 2001.

HILLERT. Growth of lamellar eutectics and eutectoids in binary and ternary systems. *ACTA METALLURGICA*, v. 19, p. 769–778, 1971.

HOKKIRIGAWA, K.; KATO, K.; LI, Z. Z. The effect of hardness on the transition of the abrasive wear mechanism of steels. *Wear*, v. 123, n. 2, p. 241–251, 1988.

HOSSEINI, P.; RADZISZEWSKI, P. Combined study of wear and abrasive fragmentation using Steel Wheel Abrasion Test. *Wear*, v. 271, n. 5–6, p. 689–696, 2011.

HUTCHINGS, I. M. *Tribology: Friction and Wear of Engineering Materials*. First edit ed. London: Edward Arnold, 1992.

IHHA. *Guidelines to Best Practices for Heavy Haul Railway Operations: Management of the Wheel and Rail Interface*. Simmons-Boardman Books, IC, 2015.

IMHOFF, C. H. et al. *A review of tribological sinks in six major industries (Pacific Northwest Laboratory, Ed.)*. Richland, WA, 1985.

ISO/FDIS. *Metallic materials — Instrumented indentation test for hardness and materials parameters International Standard*, 2002.

KALOUSEK, J.; FEGREDO, D. M.; LAUFER, E. E. The wear resistance and worn metallography of pearlite, bainite and tempered martensite rail steel microstructures of high hardness. *Wear*, v. 105, n. 3, p. 199–222, 1985.

KATO, K. Wear mode transitions. *Scripta Metallurgica*, v. 24, n. c, p. 815–820, 1990.

KHRUSCHOV, M. M. Principles of abrasive wear. *Wear*, v. 28, p. 69–88, 1974.

KRUMEICK, F. Properties of electrons, their interactions with matter and applications in electron microscopy. [microscopy.ethz.ch](http://www.uni-ulm.de/physchem-praktikum/media/literatur/SEM-interaction-ETHZ.pdf), 2011. Disponível em: <<http://www.uni-ulm.de/physchem-praktikum/media/literatur/SEM-interaction-ETHZ.pdf>>

L'HOSTIS, B. et al. Influence of lubricant formulation on rolling contact fatigue of gears – interaction of lubricant additives with fatigue cracks. *Wear*, v. 382–383, p. 113–122, 2017.

LEWIS, R.; OLOFSSON, U. Basic tribology of the wheel-rail contact. In: *Wheel-Rail Interface Handbook*. Woodhead Publishing Limited, 2009. p. 34–57.

LINDROOS, M. et al. Wear behavior and work hardening of high strength steels in high stress abrasion. *Wear*, v. 322–323, p. 32–40, 2015.

LOJKOWSKI, W.; DJAHANBAKHS, M.; BU, G. Nanostructure formation on the surface of railway tracks. *Materials Science and Engineering*, v. A303, p. 197–208, 2001.

MAKINO, T.; KATO, T.; HIRAKAWA, K. The effect of slip ratio on the rolling contact fatigue property of railway wheel steel. *International Journal of Fatigue*, v. 36, n. 1, p. 68–79, 2012.

MERCER, A. P.; HUTCHINGS, I. M.; BOX, P. O. The deterioration of bonded abrasive papers during the wear of metals. *Wear*, p. 77–97, 1989.

MEZLINI, S., ZIDI, M., ARFA, H., TKAYA, M.B., KAPSA, P. Experimental, numerical and analytical studies of abrasive wear: correlation between wear mechanisms and friction coefficient. *C.R. Mecanique*, v. 333, p. 830–837, 2005.

MISRA, A.; FINNIE, I. Correlations between two-body and three-body abrasion and

erosion of metals. *Wear*, v. 68, p. 33–39, 1981a.

MISRA, A.; FINNIE, I. On the size effect in abrasive and erosive wear. *Wear*, v. 65, p. 359–373, 1981b.

MISRA, A.; FINNIE, I. Some observations on two-body abrasive wear. *Wear*, v. 68, p. 41–56, 1981c.

MODI, O. P. et al. Abrasive wear behaviour of an ISI 5132 steel under low stress. *Materials Transaction, JIM*, v. 1, p. 67–73, 1994.

MOORE, M. A. The relationship between the abrasive wear resistance, hardness and microstructure of ferritic materials. *Wear*, v. 28, n. 1974, p. 59–68.

MOORE, M. A. A preliminary investigation of frictional heating during abrasive wear. *Wear*, v. 7, n. 1971, p. 51–58, 1970.

MOORE, M. A.; DOUTHWAITE, R. M. Plastic deformation below worn surfaces. *Metallurgical Transactions A*, v. 7, n. 11, p. 1833–1839, 1976.

MULHEARN, T.; SAMUELS, L. E. The abrasion of metals: A model of the process. *Wear*, v. 5, p. 478–498, 1962.

NAHVI, S. M.; SHIPWAY, P. H.; MCCARTNEY, D. G. Particle motion and modes of wear in the dry sand – rubber wheel abrasion test. *Wear*, v. 267, p. 2083–2091, 2009.

NAPIER-MUNN, T. Grinding Mills. In: *Mineral Processing Design and Operation*. p. 146–185, 2005.

NEWCOMB, S. B.; STOBBS, W. M. A transmission electron microscopy study of the white-etching layer on a rail head. *Materials Science and Engineering*, v. 66, n. 2, p. 195–204, 1984.

OKOLO, B. et al. Focused ion beam study of the effects of shot peening on the subsurface microstructure of normalized pearlitic steel. *Journal of Materials Processing Technology*, v. 183, n. 2–3, p. 160–164, 2007.

OLOFSSON, U. et al. Tribology of the wheel-rail contact-aspects of wear, particle

emission and adhesion. *Vehicle System Dynamics*, v. 51, n. 7, p. 1091–1120, 2013.

PALADUGU, M.; LUCAS, D. R.; SCOTT HYDE, R. Effect of lubricants on bearing damage in rolling-sliding conditions: Evolution of white etching cracks. *Wear*, v. 398–399, n. December 2017, p. 165–177, 2018.

PRASAD, B. K.; PRASAD, S. V. microstructural changes during low stress abrasion of a plain carbon (0.5 %C) steel. *wear*, v. 151, p. 1–12, 1991.

PYZALLA, A. et al. Changes in microstructure, texture and residual stresses on the surface of a rail resulting from friction and wear. *Wear*, v. 250–251, p. 901–907, 2001.

RABINOWICZ, E.; MUTIS, A. Effect of abrasive particle size on wear. *Wear*, v. 8, p. 381–390, 1965.

RADZISZEWSKI, P. Exploring total media wear. *Minerals Engineering*, v. 15, n. 12, p. 1073–1087, 2002.

RADZISZEWSKI, P. et al. Tumbling mill steel media abrasion wear test development. *Minerals Engineering*, v. 18, p. 333–341, 2005.

RATIA, V. et al. Effect of abrasive properties on the high-stress three-body abrasion of steels and hard metals. *Finnish Journal of Tribology*, v. 32, n. 1, p. 3–18, 2014.

RENDÓN, J.; OLSSON, M. Abrasive wear resistance of some commercial abrasion resistant steels evaluated by laboratory test methods. *Wear*, v. 267, p. 2055–2061, 2009.

RICHARDSON, R. C. D. The wear of metals by relatively soft abrasives. *Wear*, v. 11, p. 245–275, 1968.

RONG, H. et al. Dependence of wear behaviors of hardmetal YG8B on coarse abrasive types and their slurry concentrations. *Wear*, v. 271, n. 7–8, p. 1156–1165, 2011.

SADEGHI, F. et al. A Review of Rolling Contact Fatigue. *Journal of Tribology*, v. 131, n. 4, p. 41403, 2009.

SATO, M., ANDERSON, P.M., RIGNEY, D.A., M. Rolling-sliding behaviour of rail

steels. *Wear*, v. 162–164, p. 159–172, 1993.

SATOH, Y.; IWAFUCHI, K. Crystal orientation analysis of running surface of rail damaged by rolling contact. *Wear*, v. 258, n. 7–8, p. 1126–1134, 2005.

SEO, J. W. et al. Rolling contact fatigue and wear of two different rail steels under rolling-sliding contact. *International Journal of Fatigue*, v. 83, p. 184–194, 2016.

STEENBERGEN, M. Rolling contact fatigue in relation to rail grinding. *Wear*, v. 356–357, p. 110–121, 2016.

STEENBERGEN, M.; DOLLEVOET, R. On the mechanism of squat formation on train rails - Part I: Origination. *International Journal of Fatigue*, v. 47, p. 361–372, 2013.

STEVENSON, A. N. J.; HUTCHINGS, I. M. Development of the dry sand/rubber wheel abrasion test. *Wear*, v. 195, p. 232–240, 1996.

SUNDSTRÖM, A.; RENDÓN, J.; OLSSON, M. Wear behaviour of some low alloyed steels under combined impact/abrasion contact conditions. *Wear*, v. 250, n. 251, p. 744–754, 2001.

TAKAHASHI, J.; KAWAKAMI, K.; UEDA, M. Atom probe tomography analysis of the white etching layer in a rail track surface. *Acta Materialia*, v. 58, n. 10, p. 3602–3612, 2010.

TAKAKI, S. et al. Deformation Behavior of Ultrafine Grained Iron. *Materials Science Forum*, v. 503–504, p. 317–322, 2006.

THIAGO GOMES VIANA. Estudo comparativo do comportamento de aços (trilhos) premium na tenacidade à fratura e na propagação de trinca por fadiga, de aplicação ferroviária. REDEMAT, 2015.

VILLABÓN, L.R. Construção e instrumentação de abrâsometro do tipo roda-de-borracha para o estudo do comportamento tribológico de aços. Dissertação de mestrado na Escola Politécnica da Universidade de São Paulo, Departamento de Engenharia Mecânica, 2015

XU, L. et al. Laboratory assessment of the effect of white layer on wear resistance for digger teeth. *Wear*, v. 183, n. 94, p. 112–117, 1995.

ZAPATA, D.; JARAMILLO, J.; TORO, A. Rolling contact and adhesive wear of bainitic and pearlitic steels in low load regime. *Wear*, v. 271, n. 1–2, p. 393–399, 2011.

ZHANG, X. et al. Microstructure and strengthening mechanisms in cold-drawn pearlitic steel wire. *Acta Materialia*, v. 59, n. 9, p. 3422–3430, 2011.

ZHOU, Y., PENG, J.F., WANG, W.J., JIN, X.S., ZHU, M.H. Slippage Effect on Rolling Contact Wear and damage behavior of pearlitic steels. *Wear*, 2016.

ZHU, W. T. et al. Wear and damage transitions of two kinds of wheel materials in the rolling-sliding contact. *Wear*, v. 398–399, n. October 2017, p. 79–89, 2018.

ZHU, Y.; LYU, Y.; OLOFSSON, U. Mapping the friction between railway wheels and rails focusing on environmental conditions. *Wear*, v. 324–325, p. 122–128, 2015.

ZUM GAHR, K. *Microstructure and wear of materials*. Amsterdam, The Netherlands: Elsevier Science Publishers B.V., 1987.

2 – SURFACE AND MICROSTRUCTURAL CHARACTERIZATION OF PEARLITIC STEEL UNDER ABRASIVE WEAR: CORRELATION BETWEEN SEMI-AUTOGENOUS GRINDING MILL - SAG AND DRY SAND RUBBER WHEEL ABRASIVE TEST - DSRW

2.1 – ABSTRACT

In this work, the wear behavior of a pearlitic SAG Mill liner was studied. Initially, the surface and the microstructure were characterized in samples taken from a mill liner used in ore comminution. The Dry Sand Rubber Wheel Abrasion Test (DSRW) in accordance to the ASTM G65 was selected as the critical laboratory test, being carried out by applying different normal loads (from 22 N to 380 N). The samples for the laboratory tests were obtained from the same mill liner in a region without plastic deformation (core). Electron microscopy techniques (FEG-SEM, FIB-SEM, EBSD and TEM) were used for microstructural and wear micro mechanisms characterization. The samples worn in field showed scratches and micro-indentations along the surface. For laboratory tests, a transition of the wear micro mechanisms was observed and the predominance was defined as a function of the interaction between the abrasive particles flow and the surface. The change in the normal load affects the ploughing/cutting ratio: for lower loads, micro-ploughing prevailed as the predominant wear micro mechanism, accompanied by micro-indentations as the complementary wear micro mechanism. On the other hand, with the increase of the normal load (up to 130 N), the micro cutting was promoted as the predominant micro mechanism. Cross sections analysis of both types of samples revealed the presence of a deformed layer below the contact zone. This work shows that typical operational conditions in grinding mining process promote the work hardening below the worn surface, increasing the micro-hardness from 360 HV₁₀ measured in the undeformed pearlite (core) to 580 HV₁₀ in the sub-surface layer. The thickness of the deformed layer was determined to be approximately 300 µm and 3 µm for mill liners and laboratory samples, respectively. It was shown that the variation of normal load in DSRW does not affect the thickness of the deformed layer significantly. It remains constant in 3 µm. The electron diffraction (SAED) pattern obtained in the TEM analysis indicates that the microstructure is composed of polycrystalline ferrite. The grains are not completely randomly oriented because the intensity of the ring patterns is not uniform. Based on the observations, it is possible to establish that the DSRW represents a suitable alternative to simulate the

abrasive wear observed in SAG Mill devices applying normal load up to the recommended by the ASTM Standard G65 in their different procedures. The normal load recommended in this work was defined between 200 N and 280 N. The results show the existence of microstructural features within the 300 μm thick severe deformed layer, i.e. a nanocrystalline layer and a deformed pearlite comprised (reduction of the interlamellar spacing) and fragmented cementite.

2.2 INTRODUCTION

The mining industry consumes large amounts of abrasion resistance materials due to the high wear rates observed in service (RENDÓN; OLSSON, 2009) or large tonnage per hour in some equipment. Traditionally, pearlitic steels have been used in the manufacturing of liners for Autogenous and Semi-Autogenous (AG/SAG) Mills where operational conditions promote wear processes such as abrasion, impact, and corrosion.

The surface structures formed on a number of ferrous materials after a range of wear treatments are usually called either hard or white layers. The White Etching Layer (WEL) is associated with high etching resistance to Nital etchant (2-10 vol. % HNO_3 in ethanol). This layer has been systematically studied due to its presence in different deformation processes, from mechanical milling to heating processes which involve heat treatment.

The mechanisms of WEL formation have been widely studied in wheel-rail contact and associated to martensitic transformation by cyclic shear deformation (NEWCOMB; STOBBS, 1984); transformation from pearlite to a nanostructured Fe-C alloy layer (LOJKOWSKI; DJAHANBAKHSI; BU, 2001) and austenization (by flash temperature in the contact) with a subsequent martensitic transformation, with the presence of retained austenite (PYZALLA et al., 2001; TAKAHASHI; KAWAKAMI; UEDA, 2010).

The current study presents the characterization of the sub-surface deformed layer (of a pearlitic steel) resulting from two abrasive wear processes: in service (SAG Mill Liner) and laboratory (DSRW) (ASTM, 2008). The relationship between normal load and wear mechanism and also with microstructure transformation in RWAT was analyzed.

2.3 MATERIALS AND SAMPLES PREPARATION

All the samples used in this work were obtained from a Semi-Autogenous Grinding mill - SAG used in ore comminution (copper ore). Pearlitic steel (0.75 %C, 2.00 %Cr, 0.76 %Mn, 0.76 %Si) was analyzed. **Figure 2-1** shows the SAG mill liner used for the samples preparation. All samples analyzed in laboratory tests were prepared following the procedure:

- The cutting of the samples was carried out using cutting machine *Discotom-65*[®] fabricated by Struers[®].
- Metallographic polishing
 - Subsequently, the samples were mounted with Phenolic conductive resin;
 - Grinding with sandpaper (# 220 SiC) in the first step of the samples polishing. A sequence of polishing cloths was used following steps. It was used diamond paste with abrasive size from 10 μm up to 1 μm .
 - The microstructure was revealed using 5% Nital reagent (2 ml de HNO₃ in 98 ml de ethyl alcohol).

Figure 2-1 Procedure to obtain the sample of the SAG mill liner



2.4 WEAR PROCEDURE (LABORATORY TEST)

Abrasive wear tests were carried out according to the procedure described in ASTM standard G65, Dry Sand Rubber Wheel Abrasion Test - DSRW. A variation of the normal load in a range of 22 N to 380 N was used in the experimental procedure, with the other test parameters (time, speed rotation, abrasive flow) remaining constant. The tribometer and the test conditions are shown in details in the **Figure 2-2** and **Table 2-1**.

Figure 2-2 DSRW tribometer description

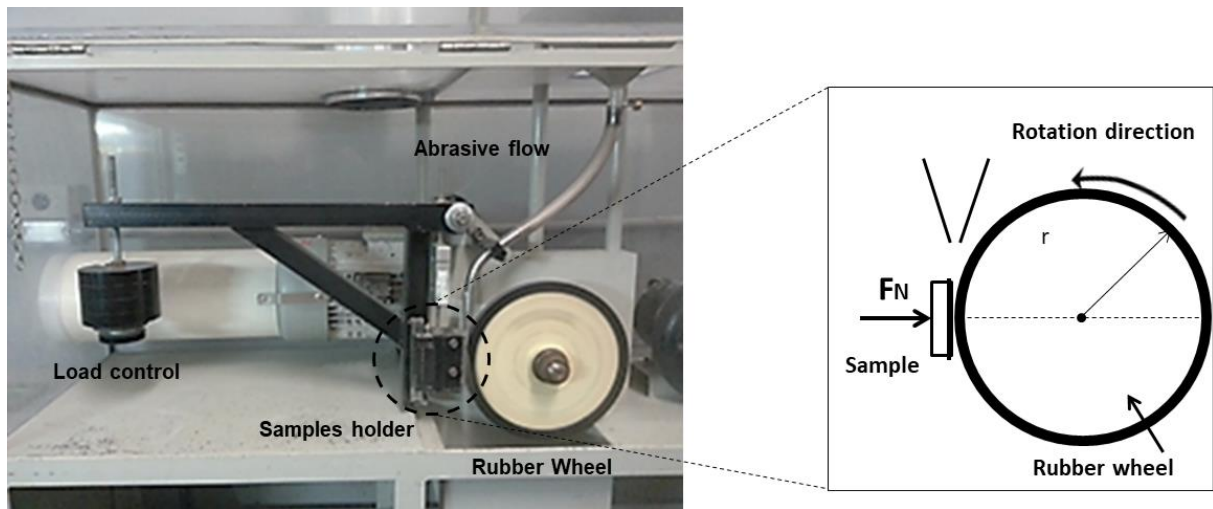


Table 2-1 Dry Sand Rubber Wheel Abrasion Test parameters

Number of samples	Three for each normal load
Hardness of rubber	Shore A-60
Abrasive used	Silica Sand
Abrasive size (mean)	0.20 ± 0.07 mm
Abrasive sphericity (SPHT = $4\pi A/P^2$)	0.790
Abrasive Aspect ratio (b/l)	0.701
Load	22, 35, 50, 75, 105, 130, 150, 180, 200, 250, 320 and 380 N
Sand Flow rate	200 g min^{-1}
Total sliding distance	1436 m
Test time	10 Min

2.5 MICROSTRUCTURAL CHARACTERIZATION AND THE SURFACE ANALYSIS

The Techniques of Scanning Electron Microscopy (SEM), Field Emission Gun Scanning Electron Microscopy (FEG-SEM), Focused Ion Beam (FIB-SEM), Electron Backscatter Scanning Diffraction (EBSD) and Transmission Electron Microscopy (TEM) were used for the microstructural characterization and the surface analysis of the samples worn on field and in laboratory.

- SEM: JEOL JSM-6010LA – Surface Phenomenal Laboratory – USP.
- FEG-SEM: FEI Quanta 450 FEG – Laboratório de Microscopia Eletrônica e de Força Atômica – USP.
- FIB-SEM: FEI QUANTA 3D FEG – Instituto de Pesquisas Tecnológicas - IPT

The FIB technique was performed using the FEI - Quanta 3D FEG/FIB microscope. The milling process was operated at 30 kV and 30 nA to open a cavity of 30 μm x 20 μm . The finishing proceeded in two steps:

- I. 30 kV and 5 nA, and
- II. 30 kV and 3 nA.

The images were captured using 30 kV and 30 pA.

- EBSD: FEI INSPECT 50 – EDAX - Laboratório de Microscopia Eletrônica e de Força Atômica – USP.
- TEM: JEOL 3010 – Brazilian Nanotechnology National Laboratory – LNNano

The sample preparation was divided in steps as follows:

- Deposition of the pt (2.4 nA – 5 kV)
- Opening of the cavities (30 nA – 30 kV)
- Cleaning/reduction of the lamella (5 nA - 30 kV, 3 nA – 30 kV)

Fixation of the lamella in the Omniprobe equipment

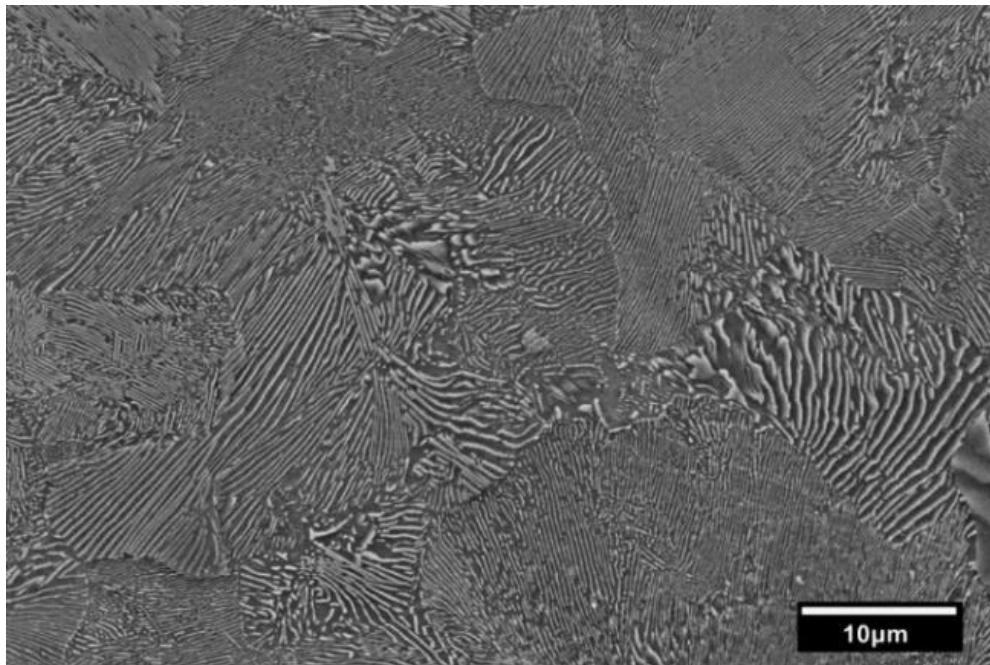
2.6 RESULTS AND DISCUSSION

2.6.1 WEAR CHARACTERIZATION IN DSRW ABRASIVE TEST (LABORATORY RANGE)

2.6.1.1 Microstructure characterization

Figure 2-3 shows the SEM micrograph of the sample in an undeformed region. The microstructure corresponds to lamellar arrangement of ferrite (α -Fe) and cementite (Fe_3C). The Interlamellar space (ILS) was determined as $0.18 \pm 0.02 \mu\text{m}$, value that represent the average of 10 regions and 10 measures each using the lines intercept.

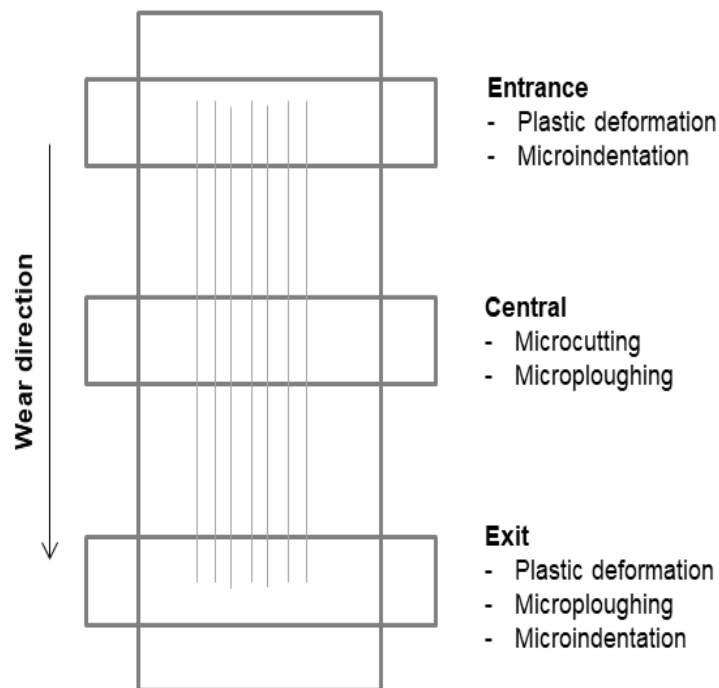
Figure 2-3 A secondary electron SEM image of the undeformed pearlitic microstructure



2.6.1.2 Wear micro mechanisms analysis

In **Figure 2-4** shows three wear zones identified in the DSRW sample after the test according with DUBE and HUTCHINGS and HOSSEINI (DUBE; HUTCHINGS, 1999; HOSSEINI; RADZISZEWSKI, 2011). The wear zones are characterized by the predominant presence of wear micro mechanisms, resulting in difference in the rate wear.

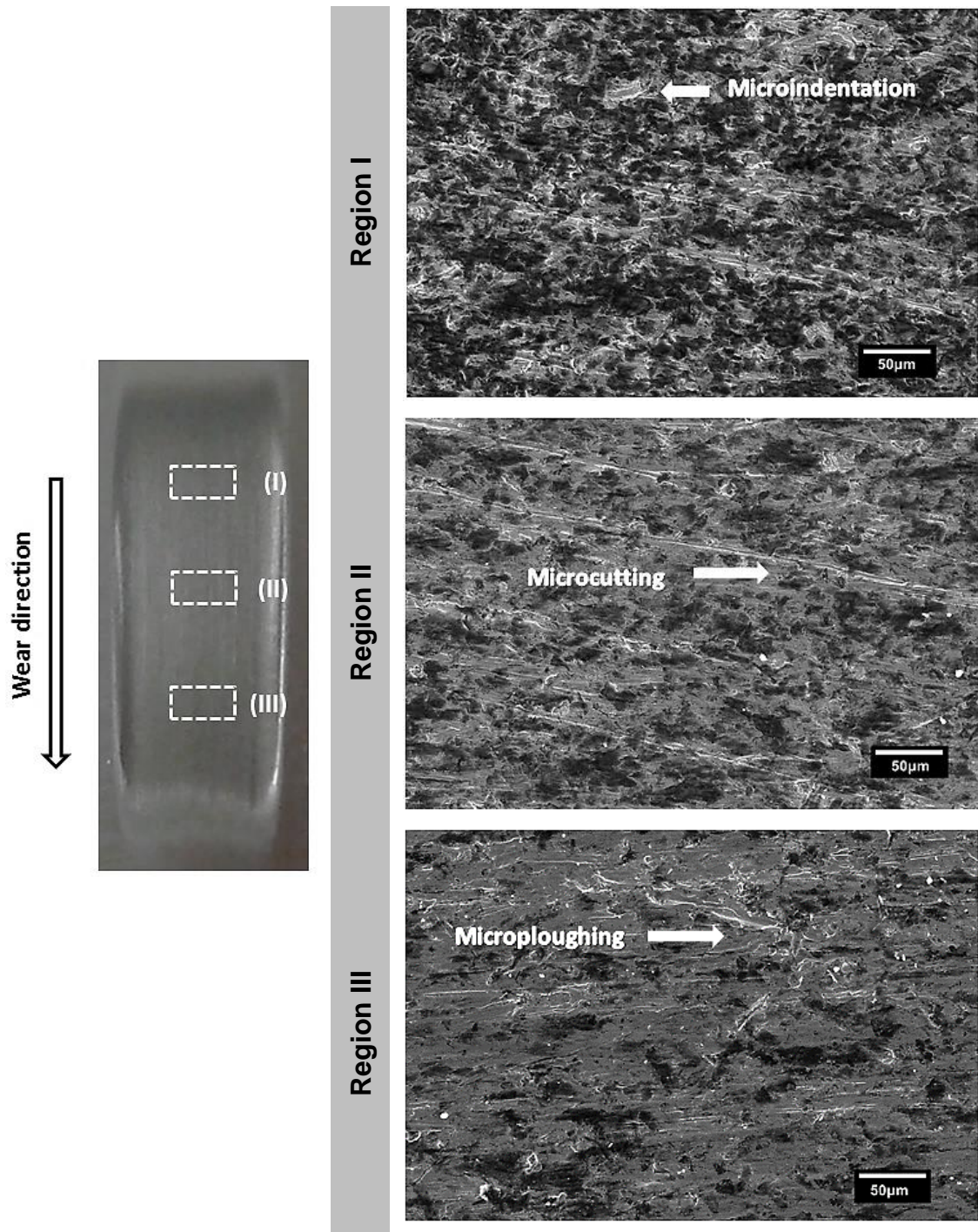
Figure 2-4 Schematic representation of wear zone in a DSRW sample



Adapted from (DUBE; HUTCHINGS, 1999)

The identification of the wear mechanisms predominant in the samples surface after the abrasive test was performed according to the DUBE and HUTCHINGS classification and shown in **Figure 2-5**.

Figure 2-5 Wear scar map of samples at the end of DSRW at 130 N, according with the procedure B of the ASTM Standard G65. A secondary electron SEM image of surface in three deformation regions, b) Entrance zone (correspond the marked region as "I"), c) central zone (region "II") and d) exit zone (region "III")



The acting force could be expressed as a function of the angle between the normal load and the vector between the two perpendicular coordinate axes (horizontal and vertical). Initially, in the first stage of interaction identified as the entrance zone of abrasive particle in the interface and representing in **Figure 2-5** as region I, the loose

particles reach the surface of sample with high tangential force which allows the rotation of particles which are free to roll. The presence of micro indentation was observed as the predominant wear micro mechanisms accompanied by the formation of superficial grooves and low mass loss (micro ploughing). In sequence, the abrasive particles are moving to the central zone (Region II), where the normal load exerts a large influence and most of the particles are trapped in the interface. Micro cutting and micro indentation were observed as the predominant wear mechanisms. Finally, in the exit zone of the particles and the end of contact with surface, the forces acting in the particles are influenced by the normal load applied on the system and the particles are free to roll again; thus, obtaining micro indentations and micro ploughing as observed in the entrance zone to the DSRW.

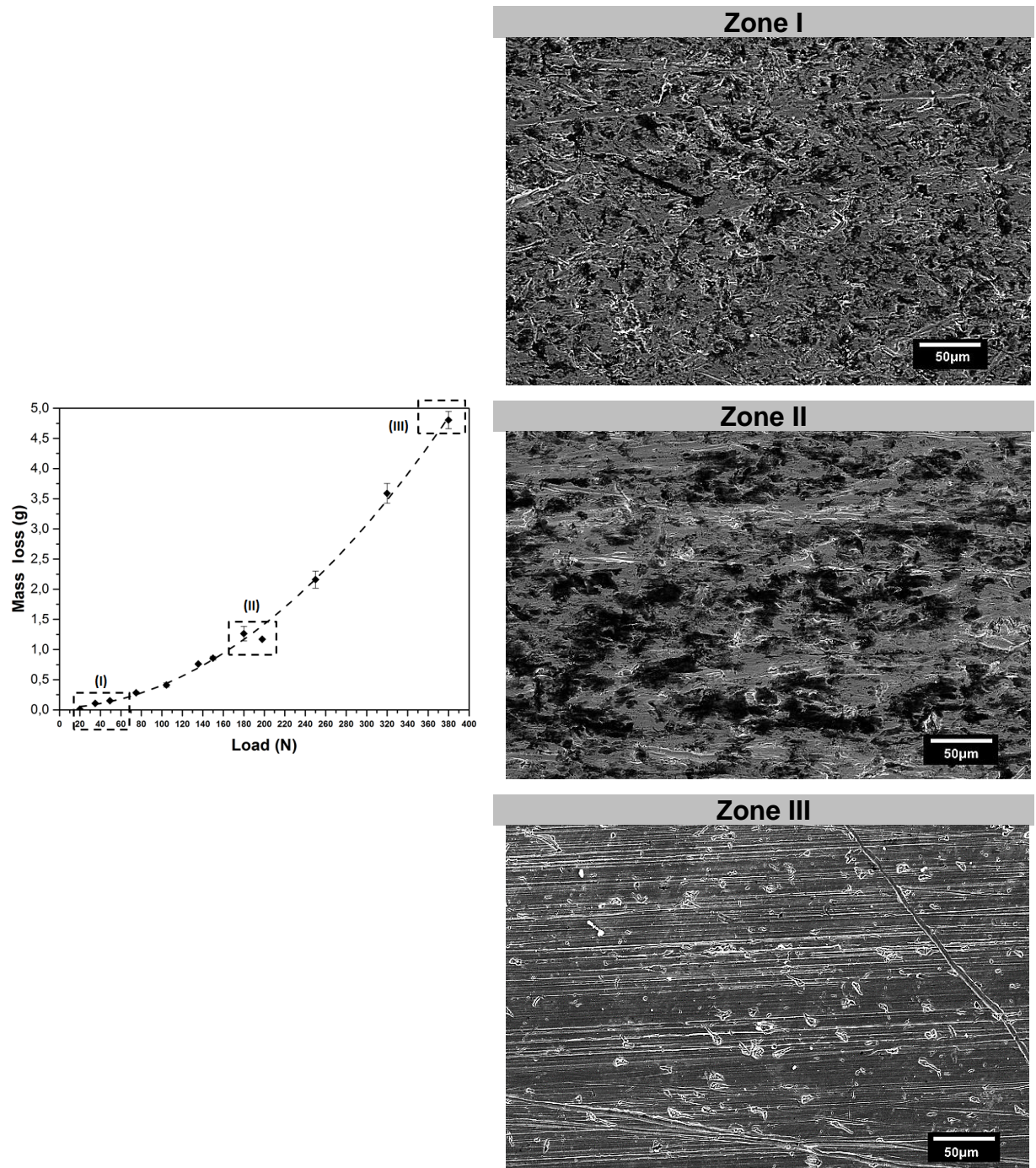
Preliminary DSRW tests were performed in the samples for the analysis of the wear micro mechanisms and mass loss as a function of the severity level (changing the normal load applied).

The mass loss increased with normal load as is shown in **Figure 2-6**. The increase of the wear rate as a function of the load is in agreement with results reported in the literature (HOSSEINI; RADZISZEWSKI, 2011; MISRA; FINNIE, 1981c; NAHVI; SHIPWAY; MCCARTNEY, 2009; STEVENSON; HUTCHINGS, 1996).

The difference in the wear rate can be associated with changes in the particle-surface interaction as a function of the normal load increment. The surface in the central zone in each sample was analyzed due to the simultaneous presence of ploughing and cutting as the predominant micro mechanisms. The samples under low normal loads showed plastic deformation with less difference in the micro-indentation and micro-cutting proportion. The increment of the normal load leads the reduction of micro-indentation events and promotes micro-cutting and micro-ploughing (II and III). In the more severe test, it was observed that micro cutting was the prevailing wear micro mechanism.

The results obtained in these preliminary tests allow the determination of the normal load influence in the wear micro mechanisms. This information will be useful by the identification of wear condition, which promotes the worn surface with similar characteristics to the worn surface in service.

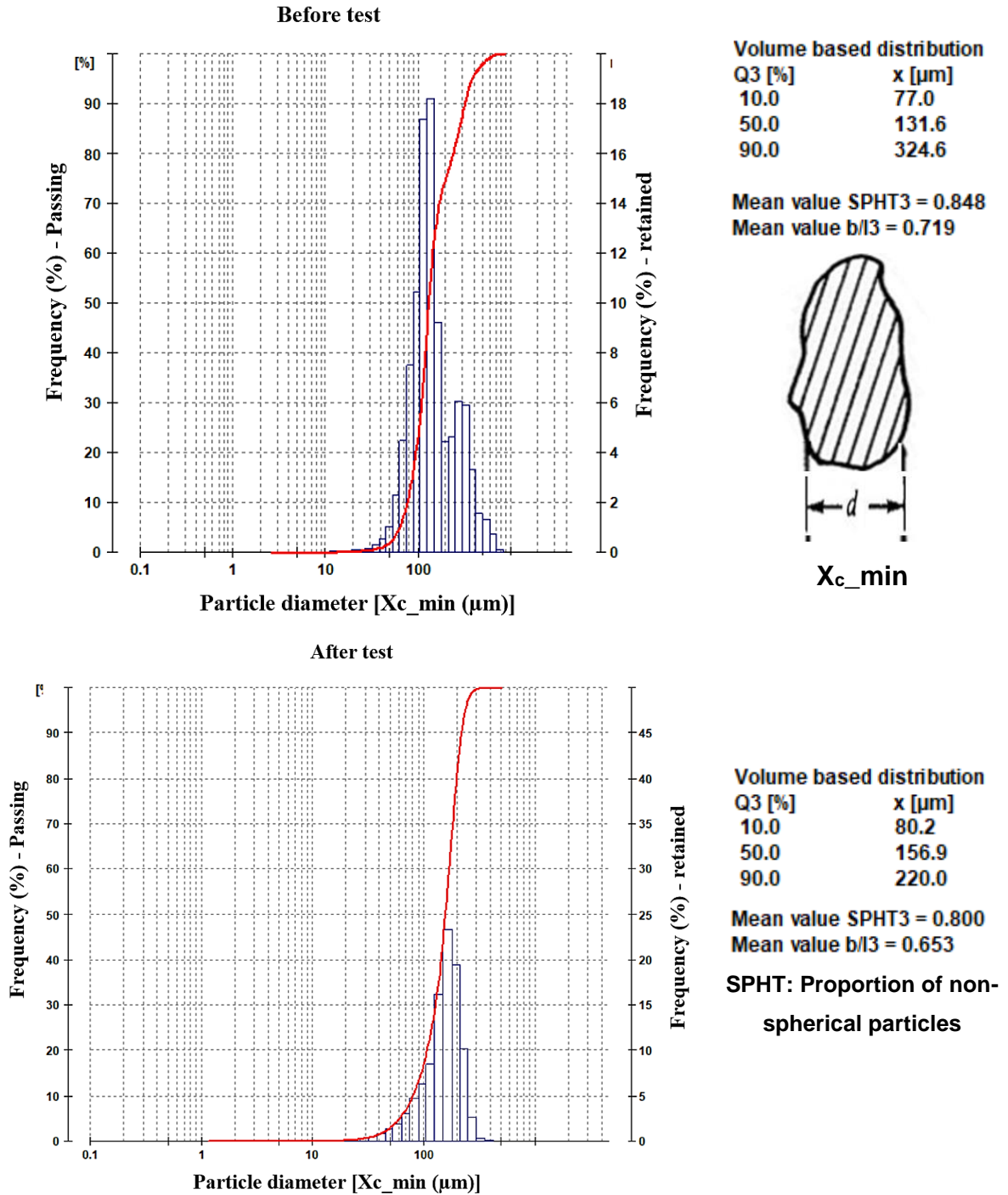
Figure 2-6 Mass loss as a function of normal load and the worn surface at different abrasive severity



In the analysis of the abrasive particles after the test, substantial differences were not observed in terms of morphology and size when normal load up to 220 N (**Figure 2-7**). This information was collected using the ISSO 133222-2, Particle size analysis Image analysis methods, in which is based the operation of the CAMSIZER particle analyzer. The sample is transported to the measurement field via a vibratory feeder where the particles drop between a planar light source and two CCD cameras. The projected particle shadows are recorded at a rate of more than 60 images per second and

analyzed. **Figure 2-7** shows the comparison in morphology of the abrasive particles before and after DSRW test at 220 N. Volume distribution was measured using the diameter value (x_{c_min}), the sphericity average (SPHT) and the aspect ratio (b/l).

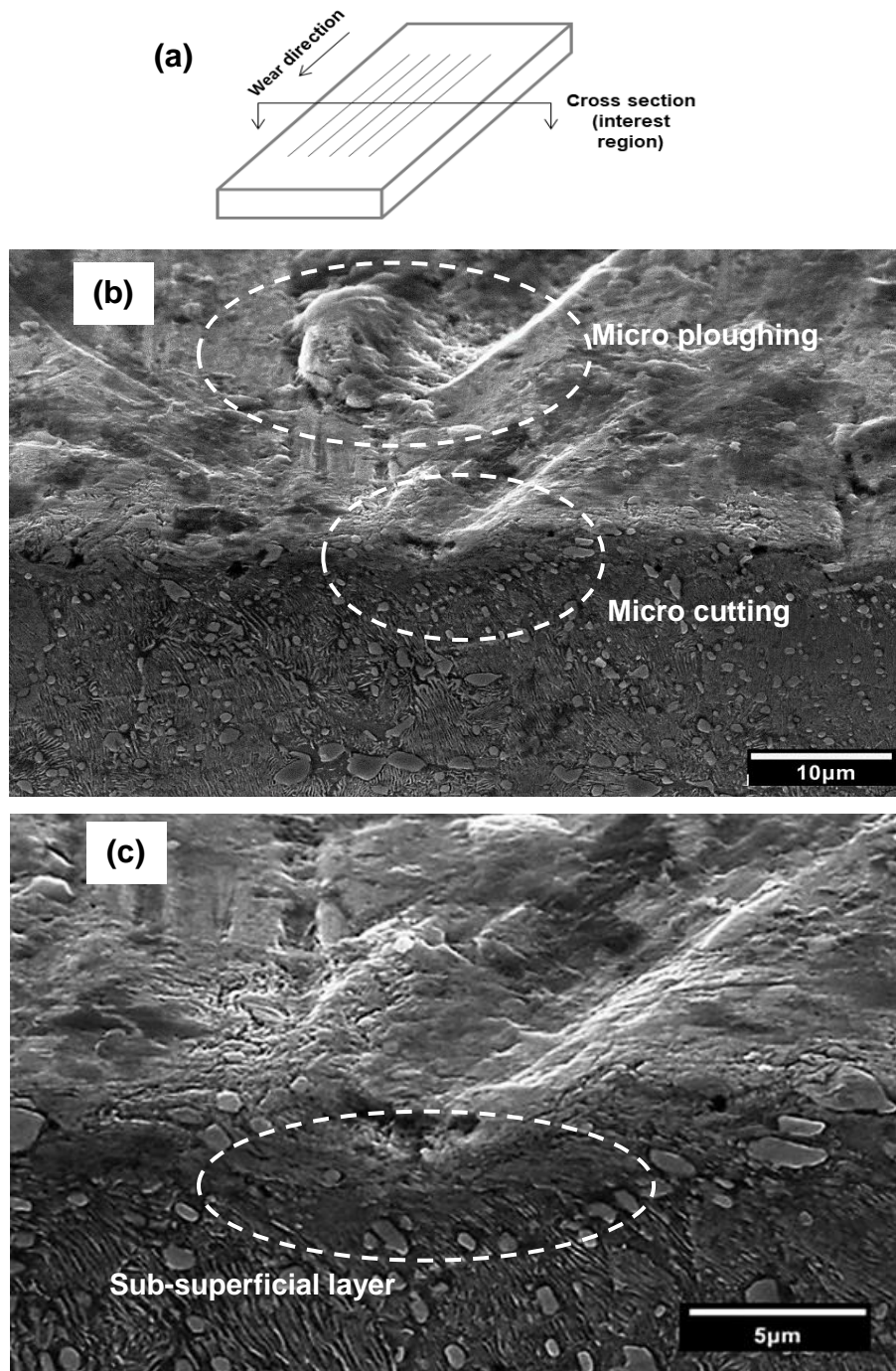
Figure 2-7 Granulometric distribution in the determination of the abrasive size particles



2.6.1.3 Microstructural analysis of the sub-superficial layer

A cross section of central zone of the worn surface, which presents the higher rate wear as previous discussion, was used by analysis. **Figure 2-8** shows the results in samples tested at 220 N.

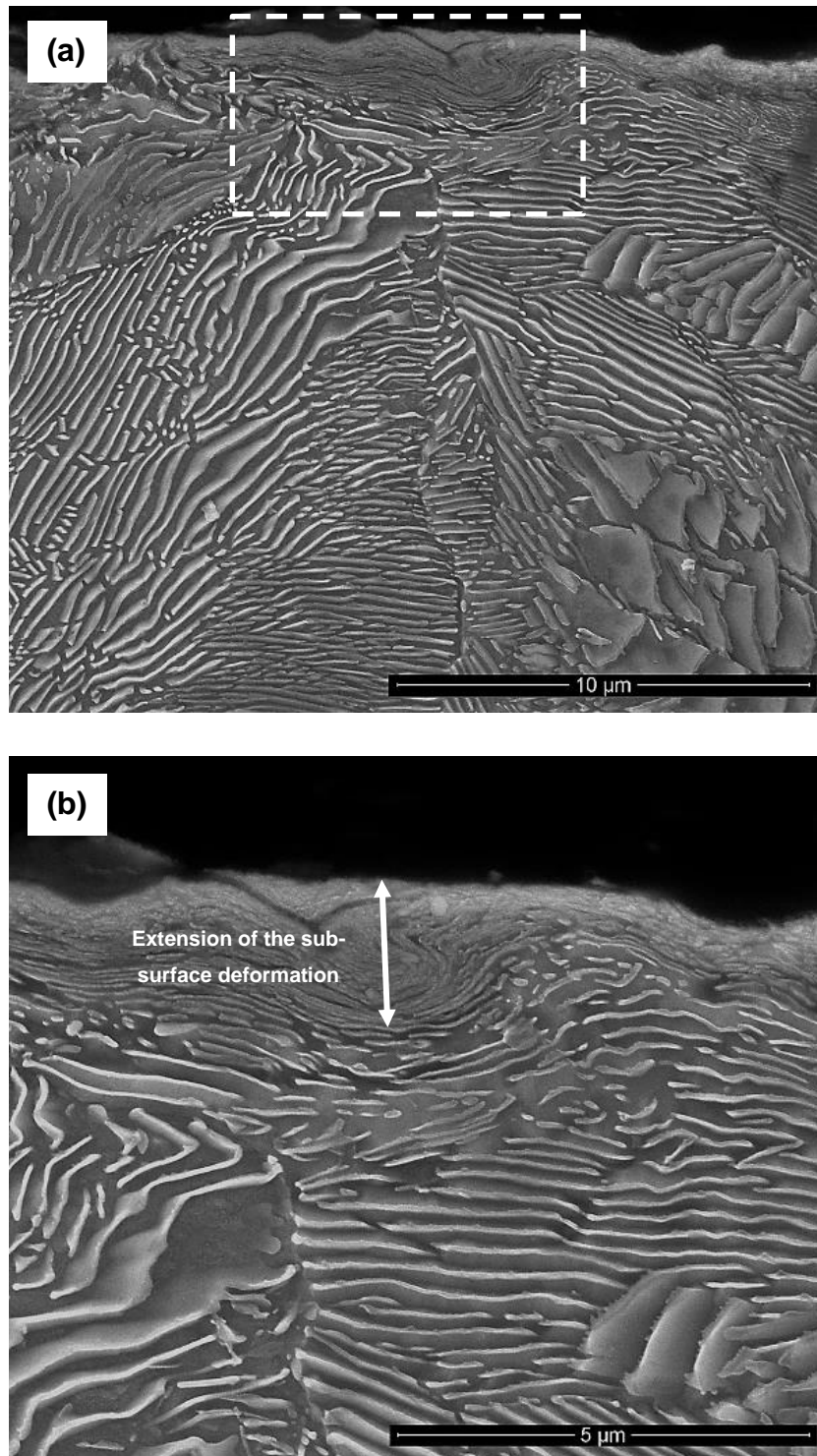
Figure 2-8 Characterization of the sample in cross- section. a) Schematically representation of the worn surface, b) SEM micrograph of the central region of wear, and c) Secondary electron micrograph of the highlighted contact zone



The secondary electron SEM image indicates damage by successive abrasive events in the surface, highlighting the grooves produced by abrasive particles (**Figure 2-8b**). It was observed that the width of grooves was larger than the fine microstructure. It is concluded that the refined microstructure cannot resist the passing of abrasive particle, even in presence of some pro-eutectoid cementite precipitating in the pearlite which increments the microstructure hardness, making it difficult for mass loss (as a function of wear rate). The conventional SEM, i.e. the use of low resolution was not effective in the identification of the sub-superficial layer nature, although a fine lamellar deformation was observed as shown in **Figure 2-8c**. The next step in the analysis requires higher resolution than used until now, deeming the use of the FEG-SEM technique necessary.

The analysis of cross section in the central zone of wear is shown in **Figure 2-9**. It is possible to observe a continuous sub-superficial deformed layer with a thickness between 1-3 μm . Eyre defined the formation of this layer as fine grain microstructure associated with a surface heating and cyclic deformation combination and a friction-induced shear stress (EYRE, 1978). Under abrasive wear conditions, the wear micro mechanisms could be affected by the rise of temperature at the contact area, playing an important role in the behavior of metal surface and leaving to the microstructure changes as a recrystallization as reported by (A; MOORE, 1971). In pearlitic steels, temperature peaks could be high enough to cause ferrite to austenite transformation and in cooling rate fast conditions, the austenite would transform in martensite.

Figure 2-9 The FEG-SEM image of the worn surface cross section of the samples at the end of DSRW with normal load of 220 N



The formation of deformed layer was analyzed as a function of normal load (i.e. 44 N, 220 N and 380 N). The thickness average of the deformed layer was measured using FIB/SEM cross-sectional image in the Image J Software. **Figure 2-10-11** shows the

cross section of the samples. As of information obtained using SEM-FEG, the two-deformed layer in the microstructure was designed as follows:

- (1) A layer closer the worn surface characterized by high deformed layer. FARGAS *et al.* define this arrangement as nanostructured, with ultrafine grains (FARGAS; ROA; MATEO, 2016);
- (2) A second layer deeper in the sample, denominated as transition layer, characterized by the combination of deformed colonies (reduction of the interlamellar spacing) and undeformed pearlite colonies. The material-Galium beam allows to observe a sheared and more finely structured than bulk material. The lamellae of the colonies in this layer are mainly oriented in parallel direction to the direction of sand flow, characteristic also described by OKOLO *et al.*(OKOLO *et al.*, 2007).
- (3) the core of the samples, characterized by undeformed pearlite colonies.

An influence of the normal load was observed in the thickness of the deformed layer and the pearlite colonies orientation (related with the worn surface) of the transitional layer. In the sample tested at 40 N as the normal load, a range of 0.26 μm to 0.78 μm of thickness was determined. This range is related with the colonies' orientation, orthogonal and parallel orientation in the transitional layer, respectively as shown in **Figure 2-10b**. In samples at 220 N and shown in **Figure 2-11b**, the thickness of the deformed layer in an orthogonal orientation of pearlitic lamellae was 0.46 μm , while in the parallel orientation the value was 0.76 μm . Finally, in severe conditions of wear, i.e. 380 N as normal load, the deformed layer exhibits a thickness of 0.39 μm for orthogonal orientation of pearlitic lamellae and 0.59 μm for parallel orientation as shown in **Figure 2-12b**.

In the analysis of the transitional zone marked as (2), the mean values of thickness increased from 0.64 to 1.53 μm with the normal load increased.

Figure 2-10 FIB-SEM images of wear central zone for the samples tested at 44 N in DSRW.
a) General cross section image, b) a highlighted region with the two-deformed layer, c) region on the right highlighted the deformation around a void space

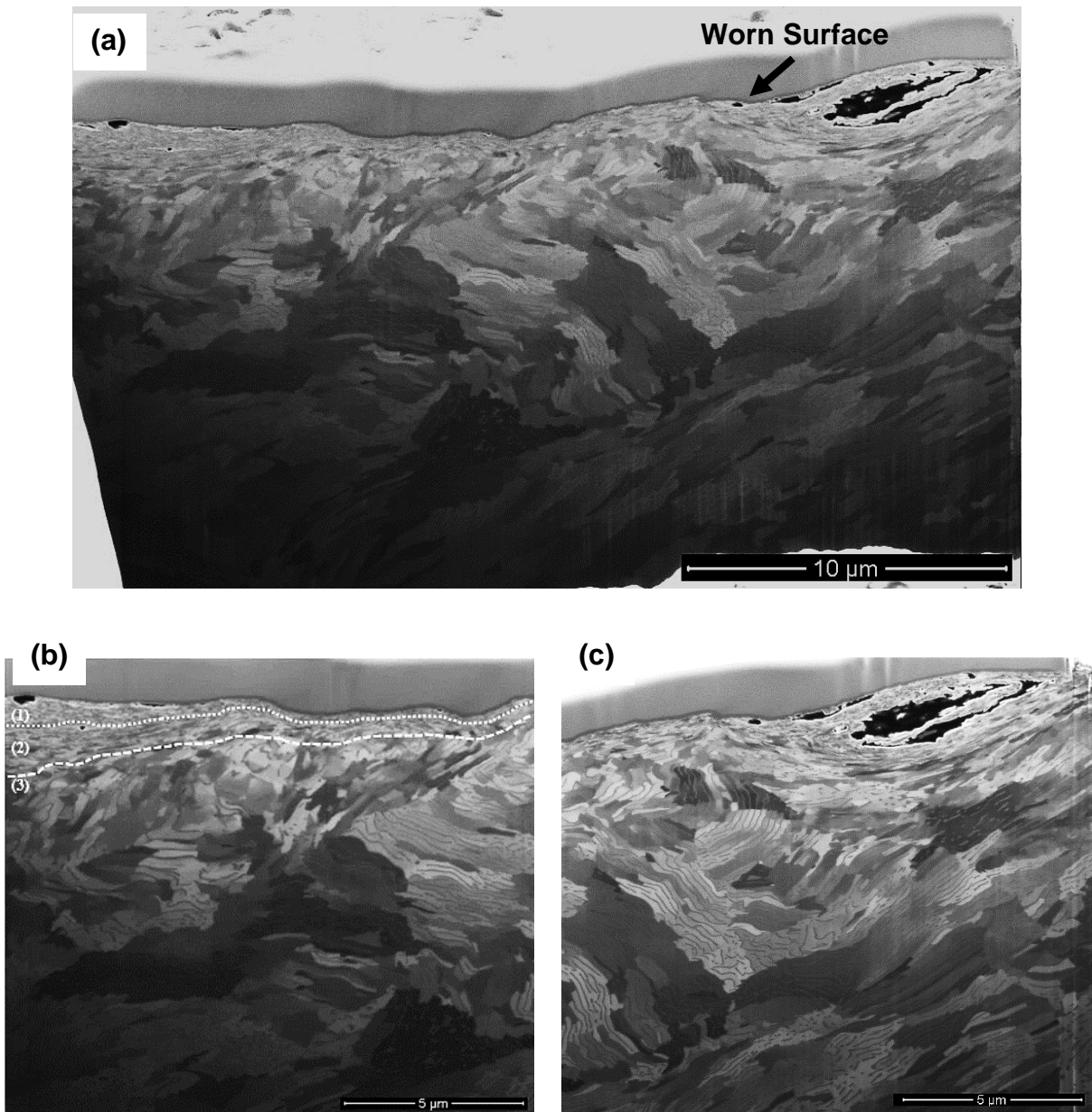


Figure 2-11 FIB-SEM images of wear central zone for the samples tested at 130 N in DSRW, a) general cross section view, showing the presence of an irregular surface, b) highlighted region with the two-deformed layer and c) image with higher magnification (30000x)

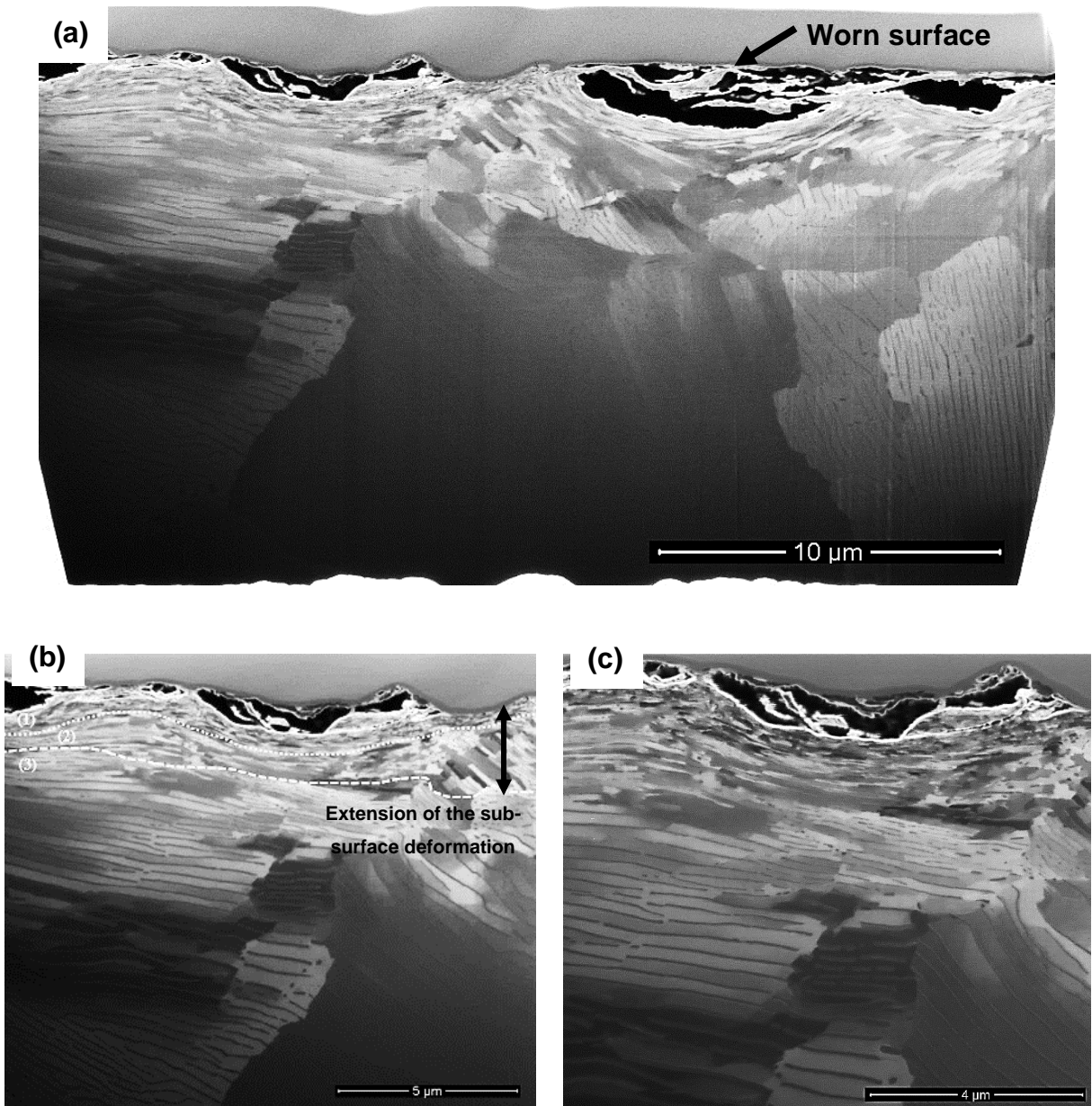
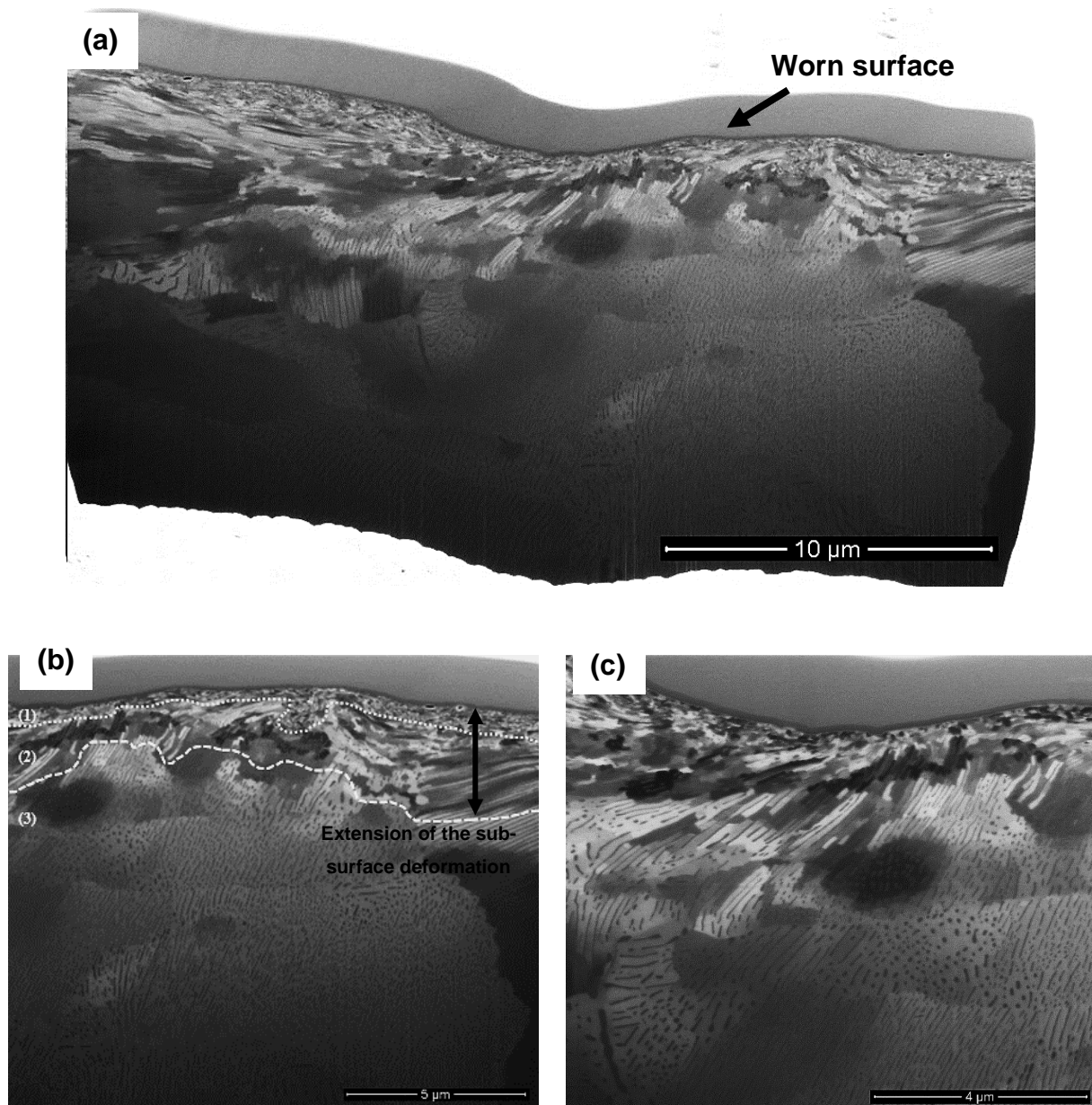


Figure 2-12 FIB-SEM images of wear central zone for the samples tested at 380 N in DSRW. a) general cross section view, b) highlighted region out of groove showing the two-deformed layer and c) image below the groove caused by an abrasive particle



2.6.1.4 Microstructural analysis using Transmission Electron Microscopy

TEM was used for the analysis of the microstructure transformation after laboratory tests. The region analyzed corresponds to the deformed layer. **Figure 2-13** shows the sample obtained via FIB/SEM and used for the analysis.

Figure 2-13 Transmission Electron Microscopy image of the sample lamella

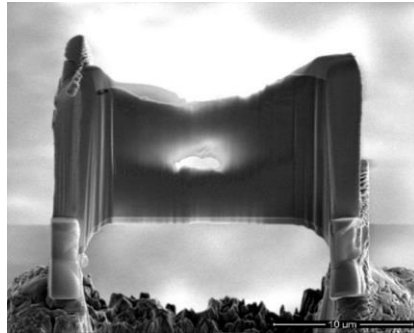


Figure 2-14 shows the microstructure in a region without influence of the wear phenomena approx. 3 μm below the worn surface. It consists in micron sized pearlite nodules each containing the interlocking single crystal of ferrite and cementite. Cementite lamellae are 20 - 30 nm in width and the interlamellar spacing remains about 150 – 170 nm.

Figure 2-14 Microstructure of pearlite steel (non-deformed) observed by High Resolution -TEM. Sequence of amplification images, highlighting the lamellae arrangement

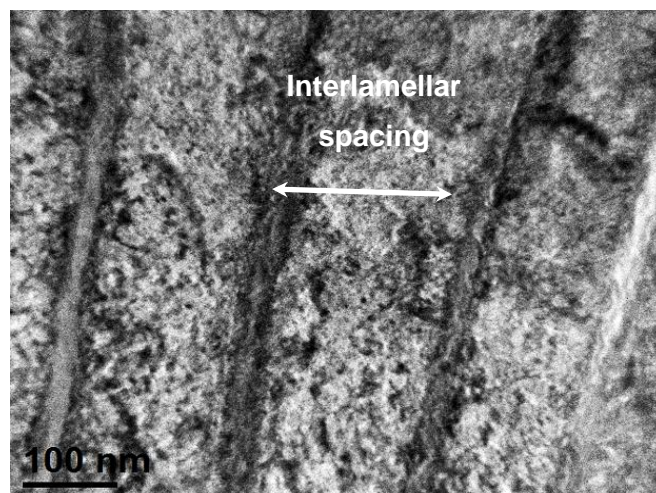
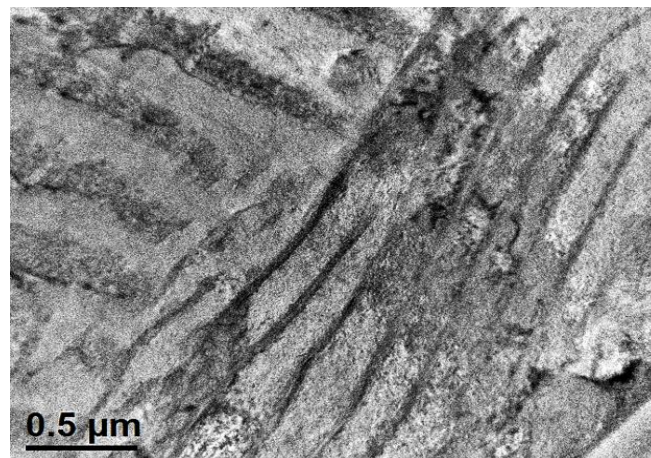
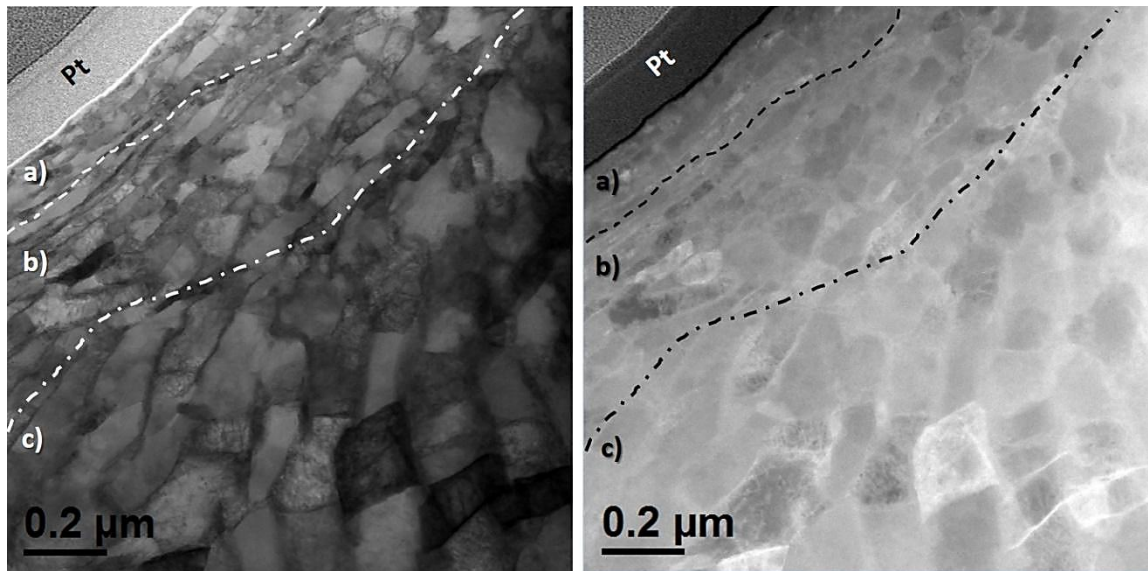


Figure 2-15 shows the microstructure in the deformed layer and the affected area by the worn process. Three layers were observed, characterized by the difference in size and orientations of the new grains. Regular lamellae arrangement in the new cell was not observed.

Figure 2-15 Microstructure transformation observed by TEM in bright and dark field of the severe deformed layer



The results obtained in this work show the fragmentation of cementite as described by the authors previously mentioned. There is a different description of the arrangement of the dislocations inside the ferrite lamellae. Takaki observed that for the yielding of polycrystalline metals, a competitive relationship exists between grain refinement strengthening and dislocation strengthening (TAKAKI et al., 2006). The larger number of dislocations crossing the cementite from the ferrite lamella to the adjacent one changes the slip system as discussed by (BORCHERS; KIRCHHEIM, 2016; ZHOU et al., 2016). Under high strains, there is the formation of continuous cementite plates or deformation, resulting in dislocation production at the ends of the cementite particles and subsequent formation of cell walls containing complex arrangements of dislocations and fragmented carbides (EMBURY; FISHER, 1966).

The mechanical properties of deformed metal are dominated by dislocations storage and for the understanding of the strain hardening, establishing the dislocation density in ferrite lamella as an important factor required. The contribution of cementite lamellae to the strength is estimated based on the Hall–Petch equation relating the yield stress

(σ_y) to the distance between barriers which can act as obstacles to dislocation gliding. Dislocations stored in ferrite-cementite interfaces can eject segments through the ferrite lamella to an adjacent interface (ZHANG et al., 2011).

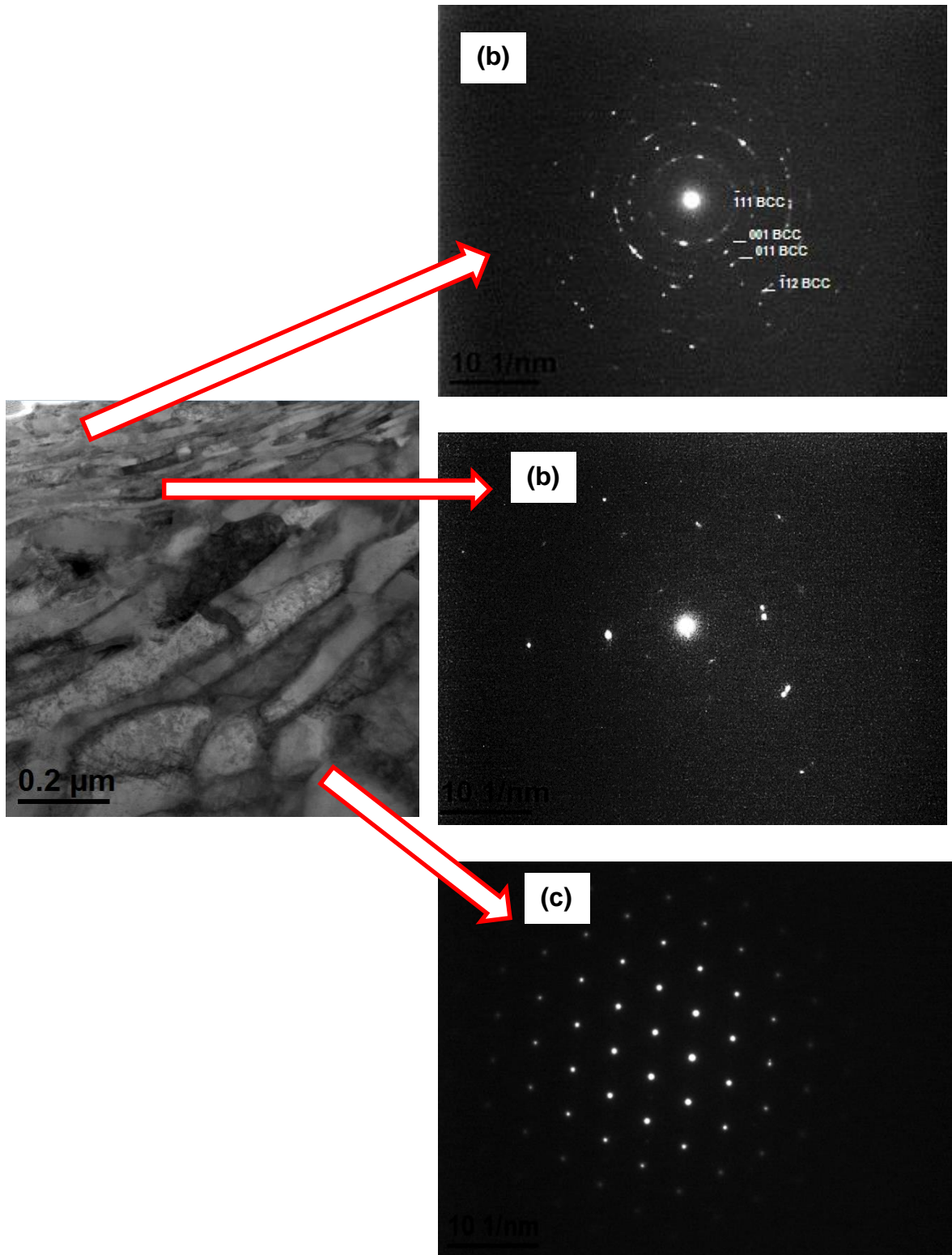
Figure 2-16 shows the electron diffraction (SAED) pattern using TEM from different positions in the topmost surface. The diffraction pattern shown in Figure 2-16b indicates that the microstructure is composed of polycrystalline ferrite (KRUMEICK, 2011). The grains that are not completely randomly oriented can be identified because the intensity of the ring patterns is not uniform. The density of dislocations within the ferrite lamellae is lower than in the deformed layer; the residue of the lamellar structure at the topmost surface layer.

Figure 2-16c shows the undeformed pearlite with a structure characterized by a dislocation density within the ferrite lamellae much lower than the deformed layer. The formation of austenite or martensite was not observed.

Even in abrasive wear, the temperature in the contact zone plays an important role in the wear resistance of a metal surface. The surface will affect in one or more of three ways: producing microstructural changes (recrystallization or melting), increasing the rate of diffusion of elements or producing changes in the mechanical properties of the heated zone (MOORE, 1970).

The results illustrate the existence of microstructural features within the 300 nm thick WEL, i.e. a nanocrystalline layer and a deformed pearlite comprised of deformed ferrite.

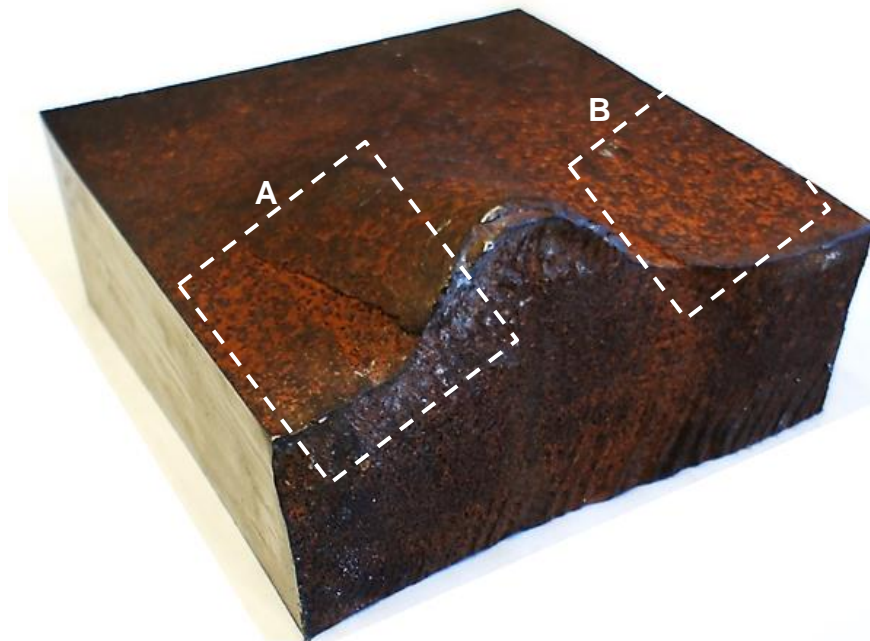
Figure 2-16 SAED diffraction patterns from sample DSRW at 220 N in different distances from the top surface



2.6.2 WEAR CHARACTERIZATION OF THE SEMI-AUTOGENOUS GRINDING MILLS

The milling process occurs from the landing of larger rocks on smaller ore, with energy that might then be sufficient to fracture the rocks. **Figure 2-16** shows the in service worn surface of SAG lifter. The region marked as “A” and “B” corresponds to analysis areas of abrasive wear and of a particular event of material fracture, respectively.

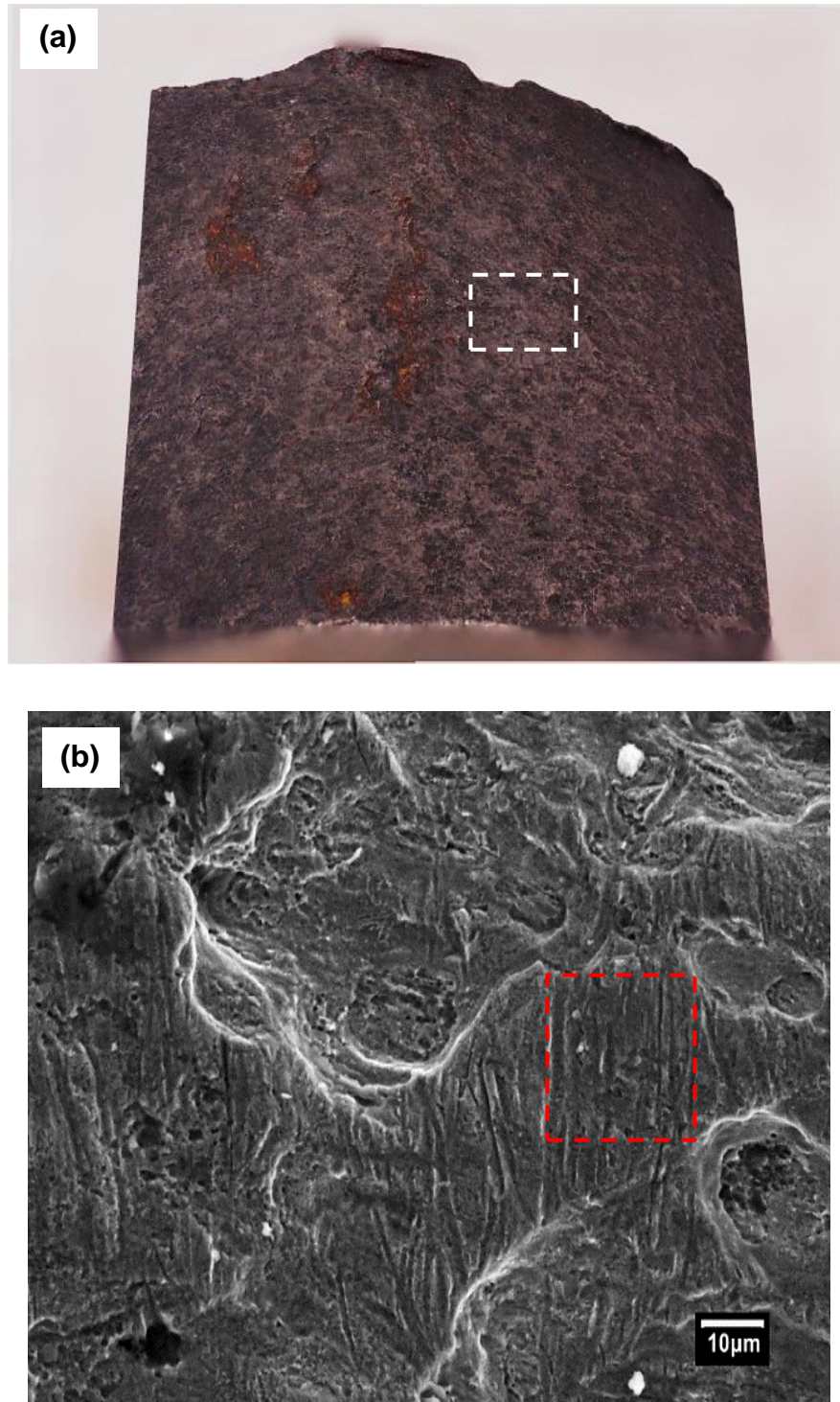
Figure 2-16 A macro scale image of lifter exhibiting abrasive wear surface (marked as “A”) with detachment of material “B”



2.6.2.1 Wear micro mechanisms analysis

The typical abrasion surface is shown in **Figure 2-17**, being possible to observe grooves and indentations (indicated by the dashed red box) as a result of mill charge impact. According to NAPIER-MUNN *et al.* lifter damages caused by ball and rocks impact are essentially the same, but the impact forces for the latter are lower and therefore less detrimental (NAPIER-MUNN, 2005).

Figure 2-17 a) macro scale image of the lifter surface worn in service. b) A secondary electron SEM image of the surface showing the abrasive mechanisms using SEM (1000X)



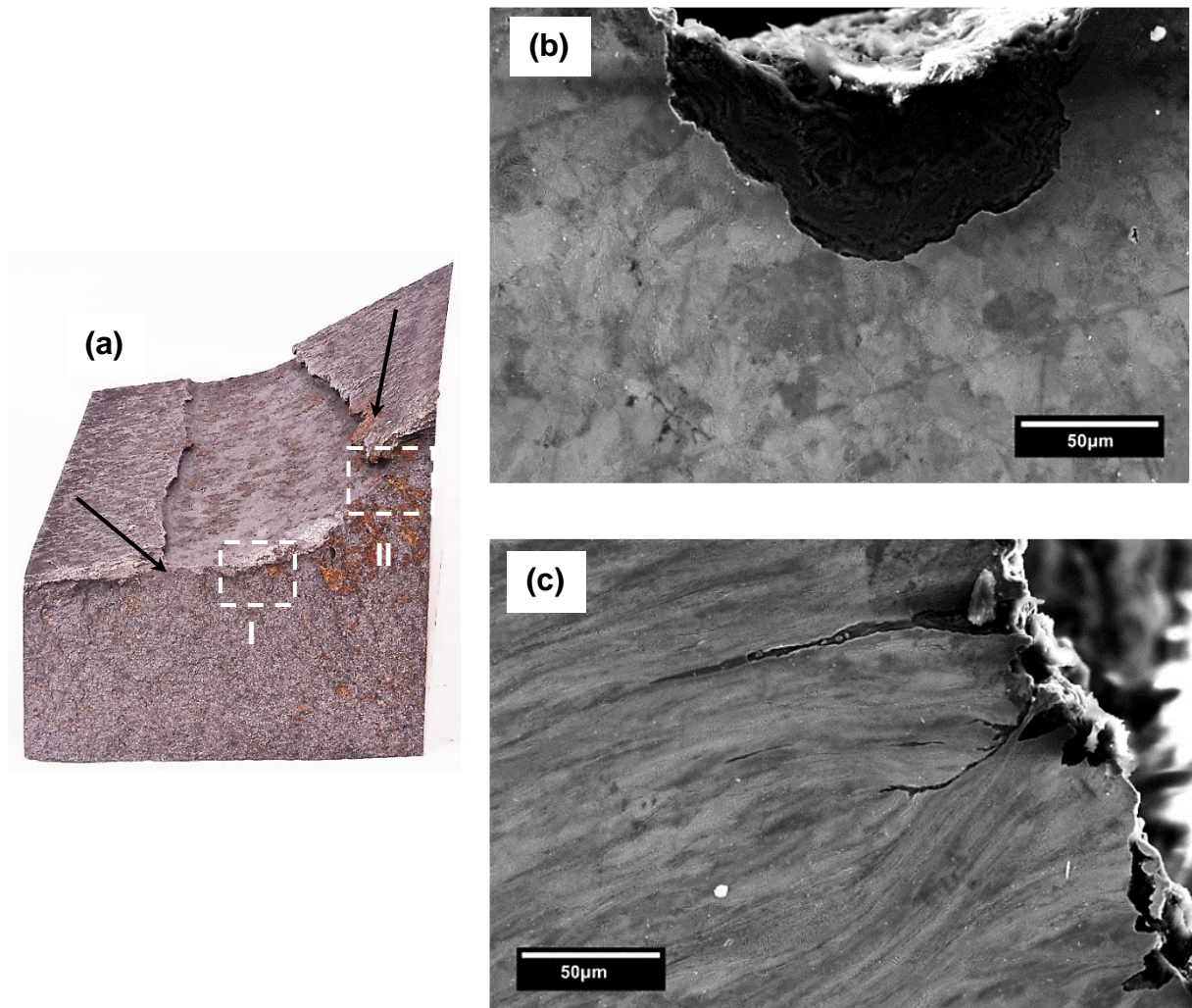
2.6.2.2 Microstructural analysis of the sub-superficial layer

The detachment of material from **Figure 2-17** and marked as “A” corresponds to the particularity in the abrasive wear surface. This specific region was analyzed using cross-sectional images as shown in **Figure 2-19**. The microstructural analysis shows

that in the region selected in the sample and marked by the black arrows in **Figure 2-19a**, the behavior in two ways can be observed. **Figure 2-18b** shows a region located in the middle of the fracture (indicated as “I”), characterized by pearlitic colonies with the typical arrangement. No deformation was observed. **Figure 2-19c** shows the lateral side of the fracture, indicated as “II” and showing an intense deformation of the pearlite, accompanied by cracks spreading to the interior of the sample. This observation suggests that the material removal process is the result of the reduction of the ability to deform in successive wear processes. Once the nucleation and the crack propagation are complete, the deformed material is removed and the pearlite colonies without deformation are highlighted.

The material detachment is a response of material to particles-surface interaction and promoted by operational factors as the rotation speed of mill and the volume of charge (ore and grinding media). This particular event was not analyzed with more detail in this work.

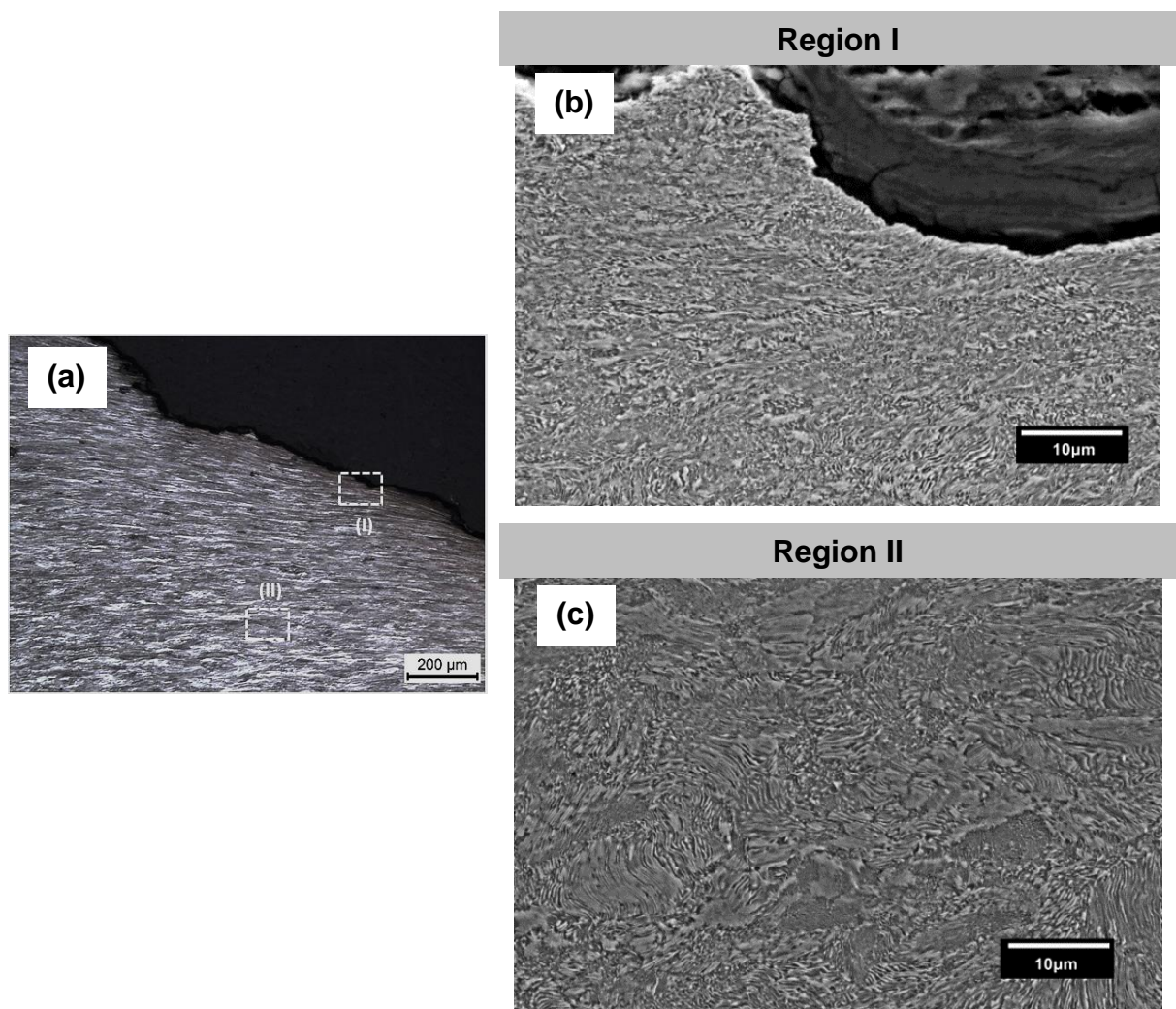
Figure 2-18 Cross-section image from a particular fracture region in the SAG liner. b) A cross-sectional secondary electron SEM micrograph of the region identified as "I" and c) SEM micrograph of the microstructure in the region indicated as "II"



The cross-section analysis in the region "B" from **Figure 2-17** shows the microstructural profile characterized by the deformation levels from the worn surface (**Figure 2-19a**). **Figure 2-19b** shows a sub-superficial layer with a thickness approximately of 300 μm and characterized by a microstructural high deformation and the breakage of the cementite lamellae. These results were observed by FELLER and WALF (FELLER; WAIF, 1991). Deeper in the sample (follow the deformed profile) a second layer (transition layer) was observed, characterized by the combination of deformed colonies with a reduced interlamellar spacing in comparison with the not deformed region (core) and the typical lamellae arrangement as shown in **Figure 2-19c**.

In the work of XU *et al.*, the author identified the microstructure deformation (called WEL by authors and attributed to the abrasion mechanisms) with a thickness of 20 μm in materials used in digger tooth, more than 10 times less than the values reported in the present work. The authors also reported that the influence of this induced layer on the wear rate is negligible due to abrasive particles being harder than the layer, exceeding the wear resistance of the microstructure (XU *et al.*, 1995).

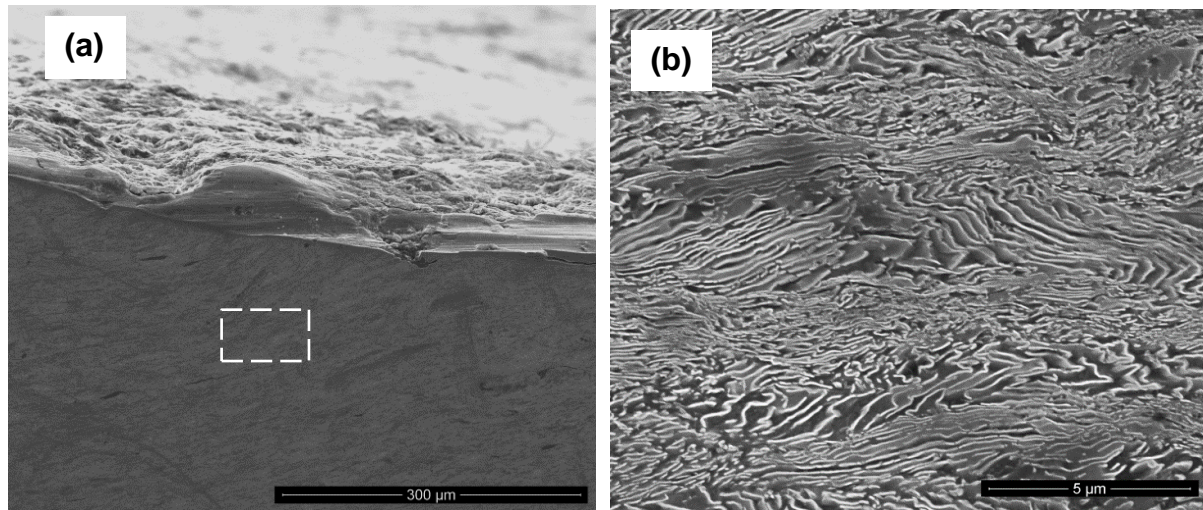
Figure 2-19 (a) Optical Microscopy image of cross section surface worn in-service. A cross-sectional secondary electron SEM image of the two deformation regions, b) A higher magnification view of the region indicated as "I" in (a) indicating a sub-superficial layer



A detailed analysis of microstructural deformation (high resolution) is presented in **Figure 2-20** in a region selected at 150 μm from worn surface (in the cross section) and performed using FEG-SEM. The cross-sectional image showed the deformation of cementite carbides without breaking of the lamellae. A possible reduction of

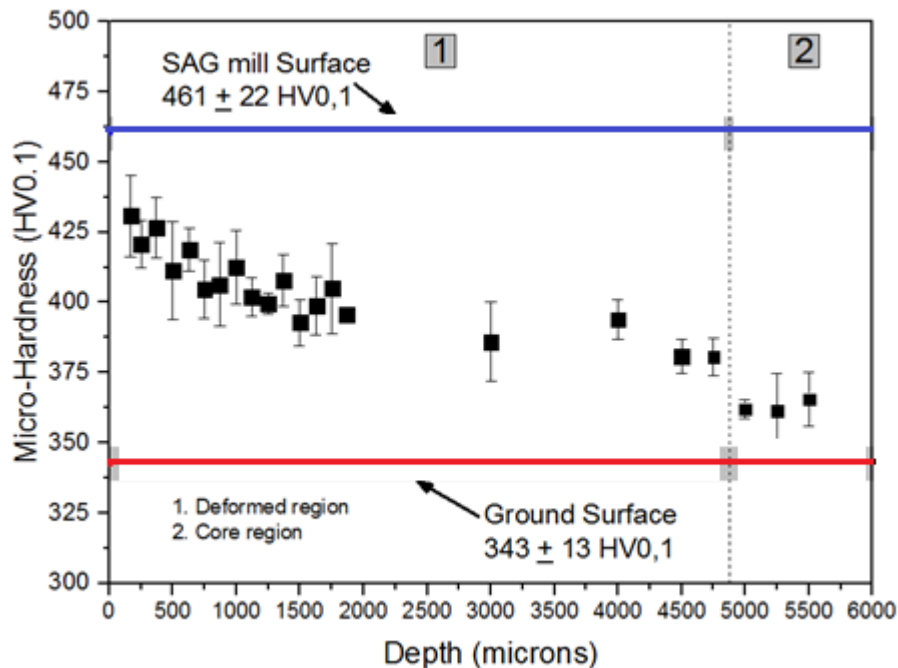
interlamellar spacing was not confirmed by ILS method due to the difficulty to develop a proper procedure. However, the breaking and the spheroidized of cementite were discarded and martensitic transformation was not evidenced.

Figure 2-20 a) Cross-sectional secondary electron SEM image of sample worn in-service and b) highlighted region using SEM-FEG (180000X)



The effect of the microstructural deformation was evaluated by work-hardening profile as shown in **Figure 2-22**. The lines parallel to X-axis (blue and red lines) represent the micro-hardness average value in the surface due to wear process and the metallographic preparation of samples. The curve shows a difference of 219 HV points between the surfaces metallographic prepared and the surface worn in-service. In the closer layer to the surface, a higher hardness value corresponding to the deformed layer was observed. A second region (between 750 and 5000 μm) in the curve had a hardness value slightly higher than measured in the polished surface. Finally, a region undeformed was observed with lower hardness values ($343 \pm 13 \text{ HV}_{0,1}$).

Figure 2-21 Hardness profile of samples worn in-service



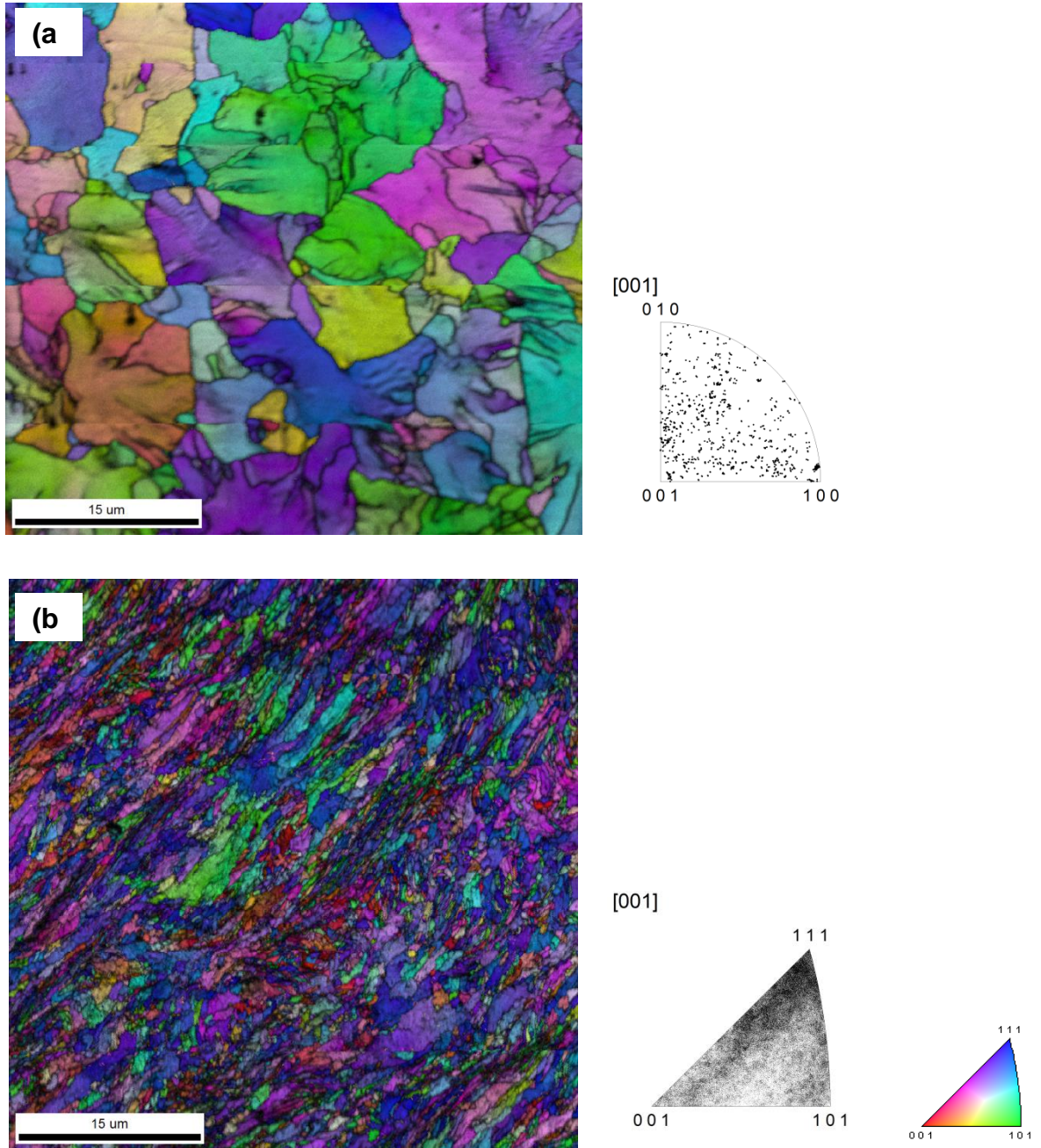
It is important to notice the simultaneous presence of different wear micro mechanisms (indentation and cutting) during the milling process. The milling process promoted therefore a greater deformation and an increment of hardness in the surface in comparison to those evaluated for the grinding process that involves predominantly only cutting. The prevalence of cutting in the grinding process could be associated with the reduced ability to promote work hardening resulting in the formation of negligible hardened layer.

2.6.2.3 Crystallographic orientation analysis using EBSD

For this work, RD direction (Rolling/Reference direction) was selected as the reference direction (which corresponds to the conventional arrangement in the microscopy chamber). **Figure 2-22a** shows the microstructure orientation using inverse pole figure (IPF) of an undeformed sample (core). Each preferential orientation was delimited by the grain boundaries (HAGBs), identified by the thin black lines. Also, low-degree values were observed (with 10° as the highest angle) through the pearlite colony indicating a low lamellar orientation difference. There was not a preferential orientation observed in the IPF map for the pearlite colonies in the core as expected. **Figure 2-22b** shows the IPF map of the deformed layer (sub-surface layer). The preferential orientation of the colonies and the size reduction of the new pearlite colonies are clearly

observed. Supported in the orientation distribution function (ODF), it is possible to indicate that the grinding mill process produces a crystallographic texture in the RD // $\{111\}$.

Figure 2-22 IPF + IQ map of a) undeformed pearlite colonies and b) deformed layer



2.7 CONCLUSION

The analysis of the worn surface in samples of SAG liner allows establishing the simultaneous presence of micro cutting and micro-ploughing as the main abrasion wear mechanism.

The milling process produced a bigger sub-superficial deformed layer than reported in another abrasive process. This layer is characterized by the reduction of interlamellar spacing without cementite lamellae breakage.

Massive material detachment was observed in some regions, following the progressive plastic deformation with the interlamellar spacing reduction, promoting the increment of the local work hardening.

Nucleation and propagation of cracks in the sub-superficial layer are the main mechanisms observed in the massive material detachment.

The grinding mill process does not produce the crystallographic texture in the region below the contact. The sub-superficial layer observed in SAG mill shows a crystallographic texture in $RD // \{111\}$.

The classification in three zones of the worn surface in the DSRW abrasive test is consistent with the literature and allows the observation of the particular interaction between the abrasive particle and the specimen surface. This interaction shows the predominant wear mechanisms in the specific spot.

The predominant presence of micro-indentation and micro ploughing were the dominant mechanisms for entrance and exit zones of the abrasive flow in the specimen and rubber wheel interface, resulting in low wear rate and mass loss. On the other hand, in the central zone of the interface, the micro cutting and micro-indentation were identified as the micro mechanisms responsible for abrasive wear.

The presence of these three zones of analysis does not depend on the abrasive condition (normal load applied), since they were observed for all normal loads. However, the normal load affects the relative frequency of those wear micro mechanisms. Higher normal load results in the micro cutting increased over micro-indentation.

The cross-section analysis by Scanning Electron Microscopy (SEM-FEG-FIB) of the samples tested with DSRW showed the influence of the simultaneous abrasive passes in the interface characterized by changes in the microstructure below the worn surface.

The increase of the normal load in the DSRW has no influence in the thickness of the deformed layer below the contact area.

The sub-superficial microstructure is characterized by the polycrystalline ferrite with a high dislocation density and fragmented cementite. The orientation of the new grains formation is not completely randomized and the formation of martensite was not observed.

The wear mechanisms predominance has a strong dependence of the wear conditions (normal load, abrasive size, and contact area) and influence the material microstructural behavior for laboratory tests and grinding process.

Even though the procedure B of ASTM Standard G65 (i.e. normal load of 130 N) is widely used as the typical test conditions, it does not reproduce the micro mechanisms observed at the samples of mill SAG. A better reproduction of the wear micro mechanisms and the microstructural "transformation" observed at the in service worn samples was achieved with normal loads higher than recommended by the ASTM, in the range of 200 N and 280 N.

2.8 REFERENCES

BORCHERS, C.; KIRCHHEIM, R. Cold-drawn pearlitic steel wires. *Progress in Materials Science*, v. 82, p. 405–444, 2016.

DUBE, N. B.; HUTCHINGS, I. M. Influence of particle fracture in the high-stress and low-stress abrasive wear of steel. *Wear*, v. 233–235, p. 246–256, 1999.

EMBURY, J. D.; FISHER, R. M. The structure and properties of drawn pearlite. *Acta Metallurgica*, v. 14, n. 2, p. 147–159, 1966.

EYRE, T. S. The Mechanisms of wear. *Tribology International*, p. 91–96, 1978.

FARGAS, G.; ROA, J. J.; MATEO, A. Influence of pre-existing martensite on the wear resistance of metastable austenitic stainless steels. *Wear*, v. 364, p. 40–47, 2016.

FELLER, H. G.; WAIF, K. Surface analysis of corrugated rail treads. *Wear*, v. 144, p. 153–161, 1991.

HILLERT. Growth of lamellar eutectics and eutectoids in binary and ternary systems. *ACTA METALLURGICA*, v. 19, p. 769–778, 1971.

HOSSEINI, P.; RADZISZEWSKI, P. Combined study of wear and abrasive fragmentation using Steel Wheel Abrasion Test. *Wear*, v. 271, n. 5–6, p. 689–696, 2011.

KRUMEICK, F. Properties of electrons, their interactions with matter and applications in electron microscopy. microscopy.ethz.ch, 2011.

LOJKOWSKI, W.; DJAHANBAKHSH, M.; BU, G. Nanostructure formation on the surface of railway tracks. *Materials Science and Engineering*, v. A303, p. 197–208, 2001.

MISRA, A.; FINNIE, I. Some observations on two-body abrasive wear. *Wear*, v. 68, p. 41–56, 1981.

MOORE, M. A. A preliminary investigation of frictional heating during abrasive wear. *Wear*, v. 7, n. 1971, p. 51–58, 1970.

NAHVI, S. M.; SHIPWAY, P. H.; MCCARTNEY, D. G. Particle motion and modes of wear in the dry sand – rubber wheel abrasion test. *Wear*, v. 267, p. 2083–2091, 2009.

NAPIER-MUNN, T. Grinding Mills. In: *Mineral Processing Design and Operation*. p. 146–185.

NEWCOMB, S. B.; STOBBS, W. M. A transmission electron microscopy study of the white-etching layer on a rail head. *Materials Science and Engineering*, v. 66, n. 2, p. 195–204, 1984.

OKOLO, B.; PÉREZ-WILLARD, F.; HAWECKER, J.; GERTHSEN, D.; WANNER, A. Focused ion beam study of the effects of shot peening on the subsurface microstructure of normalized pearlitic steel. *Journal of Materials Processing Technology*, v. 183, n. 2–3, p. 160–164, 2007.

PYZALLA, A.; WANG, L.; WILD, E.; WROBLEWSKI, T. Changes in microstructure, texture and residual stresses on the surface of a rail resulting from friction and wear. *Wear*, v. 250–251, p. 901–907, 2001.

RENDÓN, J.; OLSSON, M. Abrasive wear resistance of some commercial abrasion resistant steels evaluated by laboratory test methods. *Wear*, v. 267, p. 2055–2061, 2009.

STEVENSON, A. N. J.; HUTCHINGS, I. M. Development of the dry sand/rubber wheel abrasion test. *Wear*, v. 195, p. 232–240, 1996.

TAKAHASHI, J.; KAWAKAMI, K.; UEDA, M. Atom probe tomography analysis of the white etching layer in a rail track surface. *Acta Materialia*, v. 58, n. 10, p. 3602–3612, 2010.

TAKAKI, S.; KAWASAKI, K.; FUTAMURA, Y.; TSUCHIYAMA, T. Deformation Behavior of Ultrafine Grained Iron. *Materials Science Forum*, v. 503–504, p. 317–322, 2006.

XU, L.; CLOUGH, S.; HOWARD, P.; STJOHN, D. Laboratory assessment of the effect of white layer on wear resistance for digger teeth. *Wear*, v. 183, n. 94, p. 112–117, 1995.

ZHANG, X.; GODFREY, A.; HUANG, X.; HANSEN, N.; LIU, Q. Microstructure and strengthening mechanisms in cold-drawn pearlitic steel wire. *Acta Materialia*, v. 59, n. 9, p. 3422–3430, 2011.

ZHOU, Y., PENG, J.F., WANG, W.J., JIN, X.S., ZHU, M.H. Slippage Effect on Rolling Contact Wear and damage behavior of pearlitic steels. *Wear*, 2016.

3 – CHARACTERIZATION OF THE MICROSTRUCTURAL TRANSFORMATION IN SAMPLES UNDER ABRASIVE WEAR IN LABORATORY CONDITIONS (SCRATCH TEST) AND FIELD CONDITIONS (RAIL GRINDING PROCEDURE)

3.1 ABSTRACT

The rail grinding process is essentially the process of material removal in the rail surface to eliminate irregularities in the longitudinal plane (corrugation) and fatigued material. Scratch testing is a method of mechanically testing a specimen surface using a hard-scratching element (indenter) to generate a groove in the specimen surface. Both processes, grinding and laboratory tests, are considered abrasive wear mechanisms. This chapter characterizes WEL formation under wear condition in field and laboratory tests (controlled conditions). The multi-pass scratch test was selected as a critical test, analyzing the influence of test parameter (the numbers of passes and the normal load applied) in the formation of a sub-superficial layer (WEL). For the conditions of wear in field, two grinding rail conditions were selected (changing speed of grinding) and the analysis of the sub-superficial layer was carried out. The microstructure characterization was performed using Electron Microscopy (FIB/SEM and EBSD). The average COF for all the samples was determined and the grooves were characterized using Coherence Correlation Interferometry (CCI) and Scanning Electron Microscopy (SEM). The EBSD results suggest that the pearlite colonies orientation influence in the plastic deformation due to the relationship between the crystal orientation and the stored energy. Crystallographic texture can be found in samples tested with the lower normal load (4 N) and its relationship with the number of passes was determined as a function of the reference plane selected. Using the traditional microscopy arrangement (RD) crystallographic texture was found in the less severe condition of passes, while in the TD as a reference plane, a high concentration of pearlite colonies oriented at $\langle 111 \rangle$ was determined. The rail grinding process promotes microstructure alterations represented in the change of the pearlite colony size and preferential orientation in the region near to the contact zone. The combination of a lower grinding speed and high engine power is related with multiple contact grinding disc/deformed surface events, producing a severe plastic deformation, accumulation and a microstructure evolution.

3.2 INTRODUCTION

Abrasion is generally marked by several passages of abrasive particles over a given region, making it difficult to understand and to follow the evolution of the microstructural phenomena, associated with the deformation generated by the process.

Many works reported in the literature simulate the abrasive process using single-pass scratch tests: Kato (KATO, 1990) observed that the differences in the microstructure and the non-uniform mechanical properties are established as of hardness distribution on the worn surface. The author used micro-model experiments for the analysis of the wear micro mechanisms. The study of sliding wear procedures allows defining the main parameters in the wear mechanisms predominance at critical conditions. (XU et al., 1995; XU; ZWAAG; XU, 2015) usually focused on surface damage mechanisms (micro ploughing, micro cutting, micro cracking and micro fatigue) and the material removal factor (f_{ab}).

More recently, in studies with multi-pass scratch tests, da Silva et al. (DA SILVA; DE MELLO, 2009; DA SILVA; COSTA; DE MELLO, 2011) proposed the use of well-controlled indentation and scratch tests to simulate the interaction of a single abrasive particle and the analysis of its influence on the abrasive wear. The authors established the relationship between wear mechanisms, the increment in the hardness profile and the material removal with the level of superimposition of scratches.

SATOH AND IWAFUCHI examined the crystal orientation in the surface of a ground rail using EBSD and TEM, thereby demonstrating a crystallographic texture in the specimens related with the distance (depth) from the running service (worn surface) (SATOH; IWAFUCHI, 2005).

Nowadays, high resolution Techniques like Transmission Electron Microscopy (TEM) and Electron Backscatter Diffraction (EBSD) are employed in the metallurgical characterization of WEL in nanometric scale especially in dry sliding wear. Zhang *et al.* (ZHANG et al., 2006) used TEM to observe the formation of a nanostructured layer close to the worn surface and subsequently the formation of a deeper layer with an interlamellar spacing reduction in samples obtained from rail.

Cheng *et al.* (CHEN et al., 2016) studied the WEL evolution in steels used in rolling and sliding conditions. The authors reported nano-crystal formation in a sub-superficial

layer with a severe decomposition of carbon atoms of cementite and their migration to the new ferrite grains.

The influence of plastic deformation distributions across the thickness and the influence of microstructure and local texture through the material were studied using the EBSD technique (GEE; MINGARD; ROEBUCK, 2009). An unstrained, undamaged grain will have a uniform orientation that can be represented by a unique homogeneous color that indicates the crystallographic orientation: deformation will distort the crystal structure, leading to a range of orientations within a single grain and thus a range of colors.

The use of Taylor Factor (TF) in EBSD analysis allows predicting how favorable the orientation of the crystal to accommodate the deformation is, wherein; small TF values indicate the crystal predisposition to high deformation (SARMA; DAWSON, 1996). Large TF values corresponding to crystals with high deformation resistance may undergo plastic deformation under larger stress, because of the higher yield strength of these regions (STOUDT et al., 2011; LI; HUANG; HUANG, 2017).

Kernel Average Misorientation is another important tool in the analysis of dislocation density distribution in different grains. As a rule, Kernel average misorientation is high ($>1^\circ$) in deformed grains due to the high density of dislocations. In contrast, Kernel average misorientation is low ($<1^\circ$) in recrystallized grains (LI et al., 2008).

3.3 EXPERIMENTAL APPROACH

3.3.1 MATERIALS AND SAMPLE PREPARATION

3.3.1.1 Laboratory tests (scratch test)

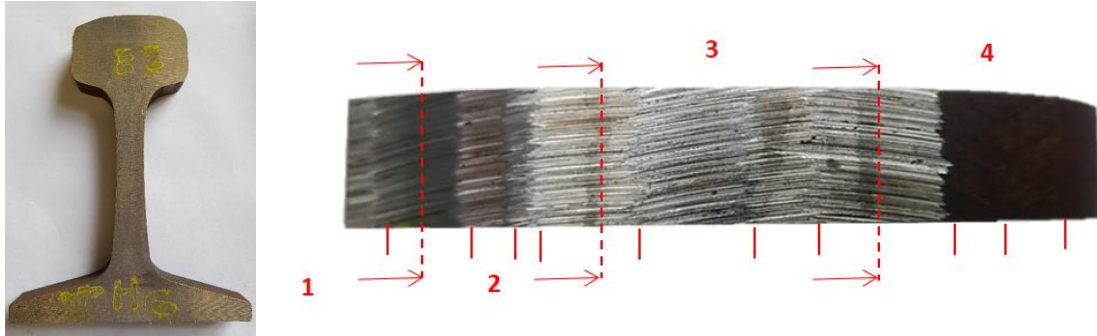
A pearlitic steel (0.75 %C, 2.00 %Cr, 0.76 %Mn, 0.76 %Si) was used in this study. All samples analyzed in this chapter were prepared following the procedure:

- The cutting of the samples was carried out using cutting machine *Discotom-65*[®] fabricates by Struers[®]. The cutting was performed in cooling conditions.
- Metallographic polishing
 - Subsequently, the samples were mounted with Phenolic conductive resin Aka-Resin[®] from Akasel Industry using the Simplimet 3000[®] Mounting Press, fabricated by BUEHLER.
 - The *Labopol-1* polisher system with grinding sandpaper (# 220 SiC) was used in the first step of the samples polishing. A sequence of polishing cloths was used in the following steps in the *TegraPol-25*[®] automatic polisher system. Diamond paste was used with abrasive sizes of 10 μm (MD-Largo), 3 μm (MD-Mol) and 1 μm (MD-Nap).
 - The microstructure was revealed using 5% Nital reagent (2 ml de HNO₃ in 98 ml the ethyl alcohol)
 - For EBSD analysis, one more polishing step was necessary in a suspension of Colloidal Silica. The final step was performed in the MiniMet 1000 semi-automatic grinder/polisher (BUEHLER).

3.3.1.2 Rail grinding procedure (wear on field)

Figure 3-1 shows the top view of the rail sample after grinding process. The red lines correspond to the specimens taken from this sample.

Figure 3-1 Cross section and top view of a grinding rail sample

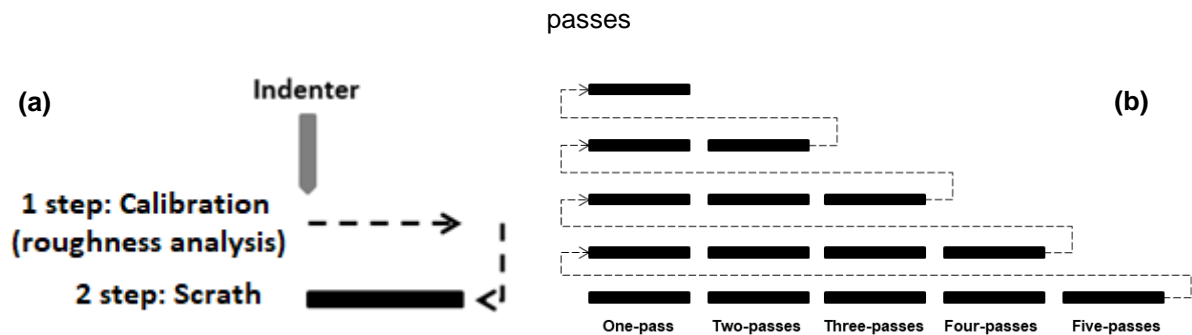


3.3.2 EXPERIMENTAL PROCEDURE

3.3.2.1 Scratch test sequence

The scratch test was performed with constant normal loads. These loads were 0.05 N (micro range) and 4 N and 8 N (macro range), according with the description of the ISO 14577 (ISO/FDIS, 2002). **Figure 3-2** shows the schematic representation of the scratch sequences and the **Table 3-1** shows the parameters used in the test.

Figure 3-2 Schematically representation of scratch test sequence, a) Scratch steps, b) number of passes



Adapted from (FRANCO, 2015)

- Calibration (analysis of initial roughness)
- Scratching (**Figure 3-2a**)
- Number of passes: 1 - 5 (**Figure 3-2b**)
- Each sequence of scratching has three repetitions.

Table 3-1 Scratch test parameters

Conditions	Macro range	Micro range
Indenter tip	Vickers	Conical
Displacement velocity (mms ⁻¹)	0.1	0,0052
Groove length (µm)	1000	500
Normal Load (N)	Two levels: 4, 8	0,05

3.3.2.2 Rail grinding conditions

The analysis presented in this chapter was performed on rail samples from two sections of rail JFE 2014 THC6542 R105, which has been in service under real traffic conditions (ore transportation) in a straight line of the railway of VALE in the region of Valadares-ES – Brazil. It was used the machine Speno[®] with 16 grinding stones type 6V with an attack angle of 1.3°. The main characteristics of the procedure are shown in **Table 3-2**.

Table 3-2. Parameters used in the grinding process

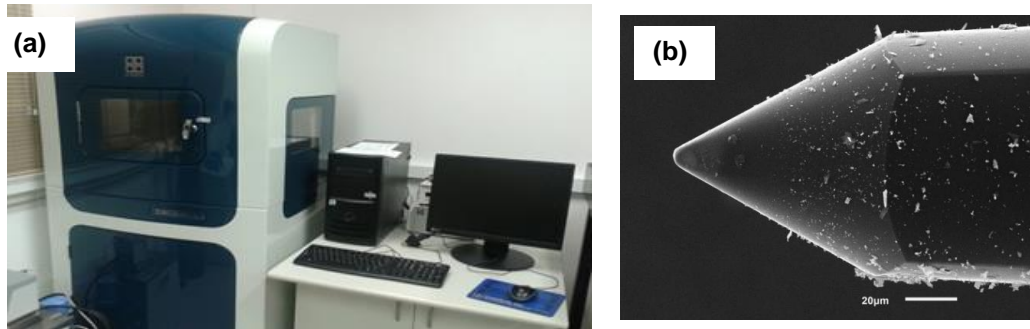
Parameter	Condition 1	Condition 2
Linear grinding vehicle	8 km/h	12 km/h
Engine Power applied in the grinding stones	100 %	70 %

3.3.2.3 Tribometer specifications

3.3.2.3.1 Micro range

- Commercial reference: Nano-indentador 950 Tribo-Indenter designed by Hysitron, headstocks D OmniProbe.
- Indenter tip: Diamond with conical indenter (60°) with a spherical tip of 5 µm.
- Acquisition rate: up to 30 kHz.
- Normal load: 0.05 N

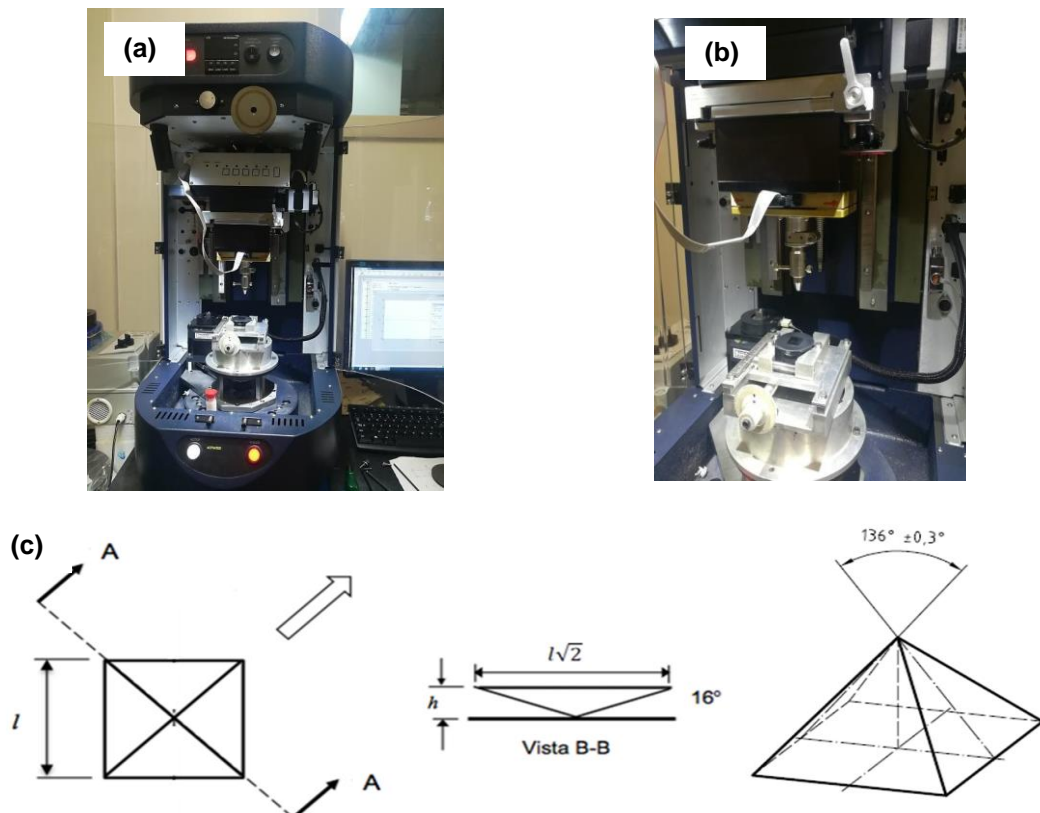
Figure 3-3 Tribômetro Hysitron TribolIndenter 950. a) General view, b) Conical tip indenter (Secondary Electron-SE image)



3.3.2.3.2 Macro range

- Commercial reference: Bruker UMT-2 (Figure 3-4);
- Sensor type: DFH-10;
- Indenter tip: Square pyramid (136°) (Figure 3-4c);
- Normal load applied resolution: 5 mN.
- Normal load applied: 4 n and 8 N.

Figure 3-4 Tribometer Bruker UMT-2. a) General view e b) indenter highlighted), c) indenter profile (schematically representation)



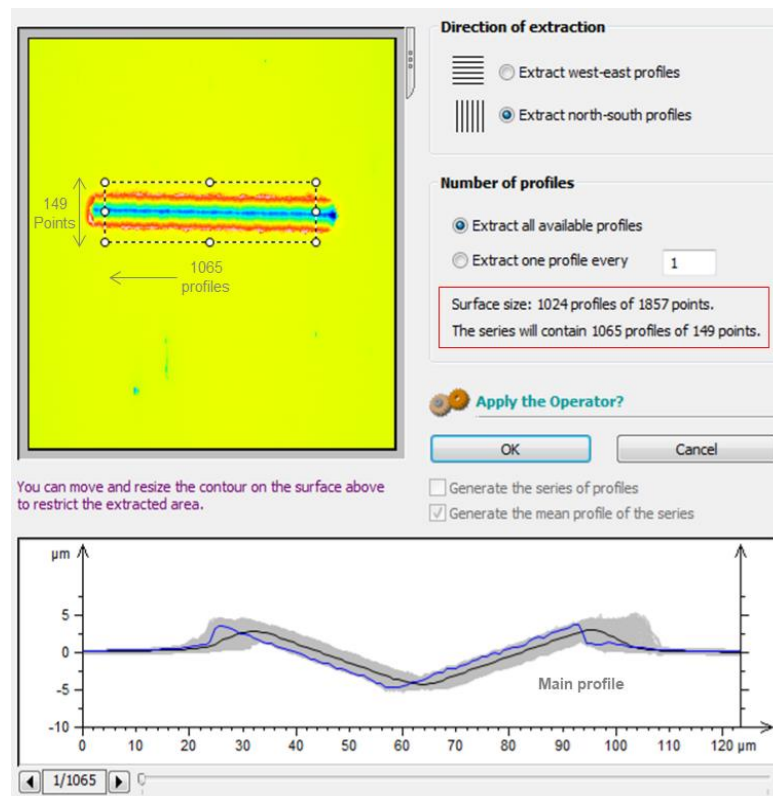
3.3.2.4 Groove geometrical dimensions

The analysis of surface (after polishing) and the geometrical characterization after the scratch test in macro scale was performed by Coherence Correlation Interferometry (CCI), using the Taylor Hobson CCI-MP optical interferometer.

The arithmetic mean height after the manual polishing corresponding to the original surface was measured as $0.006 \pm 0.001 \mu\text{m}$. The geometrical characteristic after the scratch test was determined for the samples tested in macro scale due to resolution limitations of the equipment.

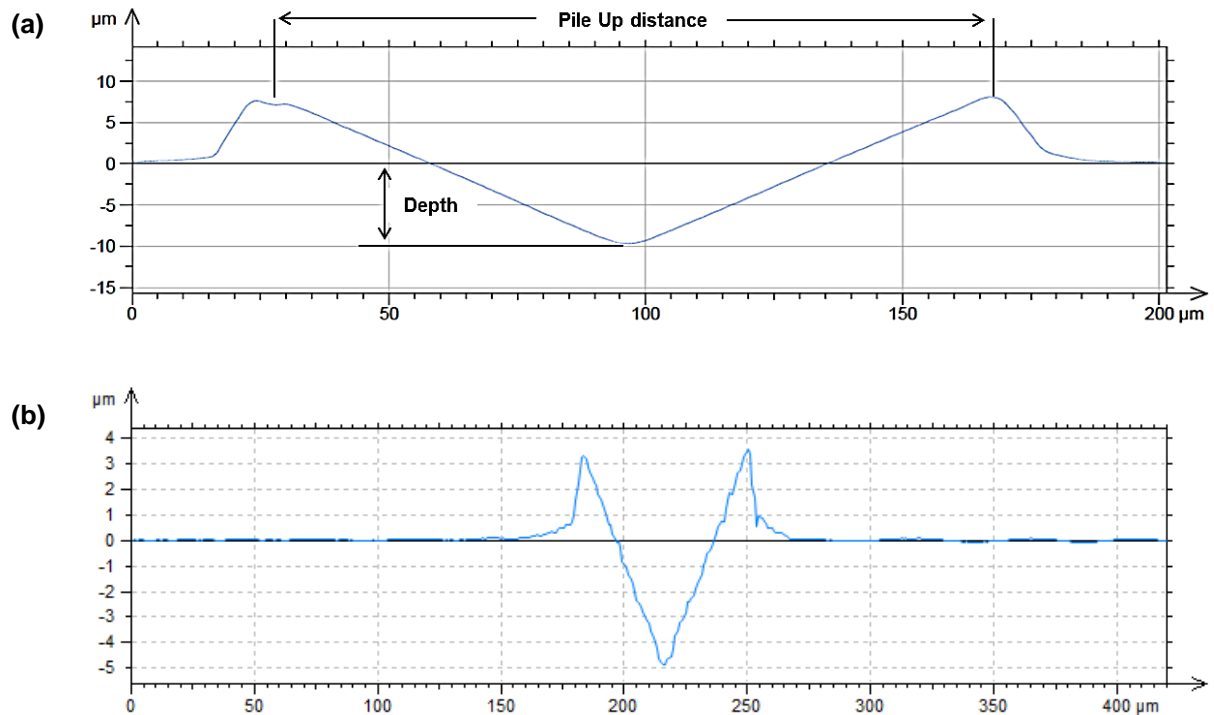
The geometrical parameters (width and depth) were obtained from the average profile of the groove, corresponding with the graphic representation of a cross section as shown by Franco (FRANCO, 2015). The average profile for all conditions were obtained using a surface size of 1065 single profiles with a variation of number of points according with the normal load (149 points for 4 N and 255 for 8 N) due to the increment of the deformed area (**Figure 3-5**).

Figure 3-5 Groove mean profile, highlighting the distance between the pile up, the groove length in the reference plane and the maximum depth



The measurement of pile-up distance (horizontal distance) and depth were performed using the tool “distance measured” of the software Talymap as shown in [Erro! Fonte de referência não encontrada.](#) According to (FRANCO, 2015), the determination of the groove width requires an average profile extension, highlighting in the groove size as a function of a reference plane ([Erro! Fonte de referência não encontrada.](#)**b**).

Figure 3-6 Geometrical characteristics of the groove main profile



3.3.2.5 Microstructural analysis

The Techniques of Focused Ion Beam (SEM/FIB) and Electron Backscatter Diffraction (EBSD) were used for the microstructural characterization below the scratch (cross section).

The FIB technique was performed using the FEI - Quanta 3D FEG/FIB microscope. The milling process was operated at 30 kV and 30 nA to open a cavity of 30 μm x 20 μm . The finishing proceeded in two steps: i. 30 kV and 5 nA, and ii. 30 kV and 3 nA. The image was captured with 30 kV and 30 pA.

The EBSD technique was selected to identify the mean crystallographic planes of the pearlite colonies using a FEI-Inspect 50 FEG with an EDAX camera and the analysis was carried out with a step size of 0.1 μm .

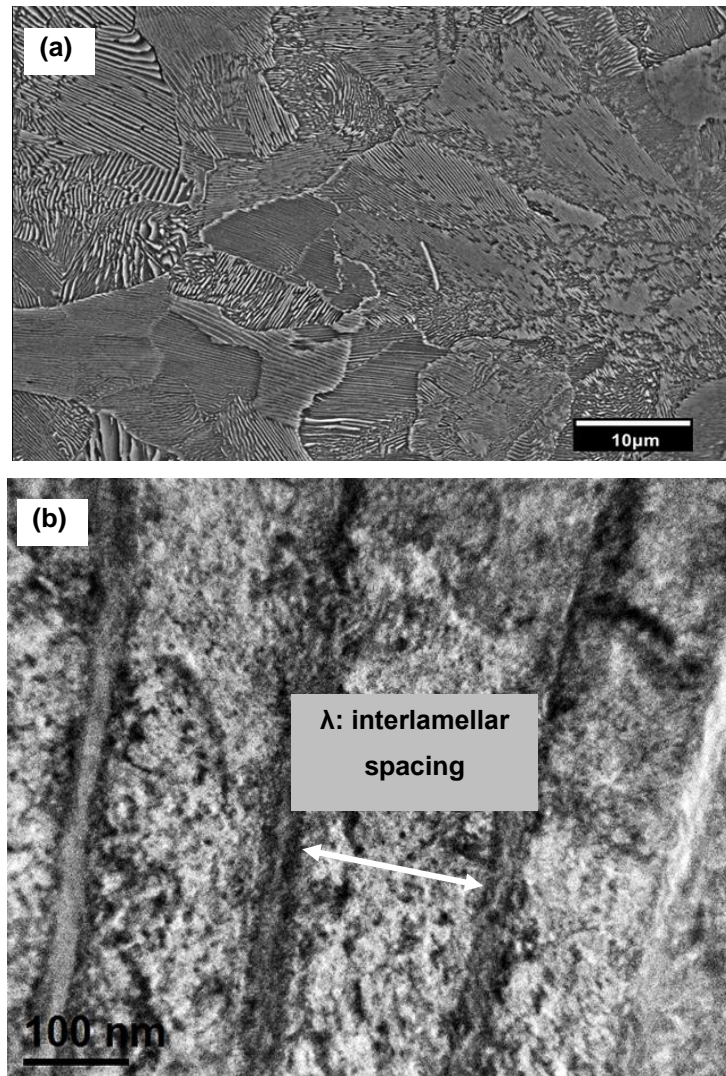
3.4 RESULTS AND DISCUSSION

3.4.1 SCRATCH TEST: INFLUENCE OF THE TEST PARAMETERS IN THE WEL FORMATION

3.4.1.1 Microstructural characterization before the test

Figure 3-7a shows a lamellar arrangement of ferrite (α -Fe) and cementite (Fe_3C) in the undeformed region, corresponding to a pearlite microstructure. The High-Resolution Transmission Electron Microscopy (HRTEM) image in **Figure 3-7b** shows a fine microstructure with a lamellar spacing of $0.15 \pm 0.02 \mu\text{m}$ and high-density dislocations.

Figure 3-7 SEM and HTEM micrographs of the undeformed pearlite colonies (core)



3.4.1.2 The influence of the number of passes on the formation of sub-superficial layer

3.4.1.2.1 Micro range scratch test

The analysis of the microstructure below the indenter track was carried out using FIB/SEM. **Figure 3-8** shows the image of top of view of two grooves obtained with one-pass and five-passes scratch, at 0.05 N. The microstructure was revealed with an *in situ* gallium etching (Ga). An increment in the plastic deformation represented as lateral deformation (pile up) was observed in the sample with a successive indenter pass (five-passes).

Figure 3-8. In situ gallium (Ga) ion beam etching image of samples tested in Hysitron tribometer. b) one-pass, c) five-passes

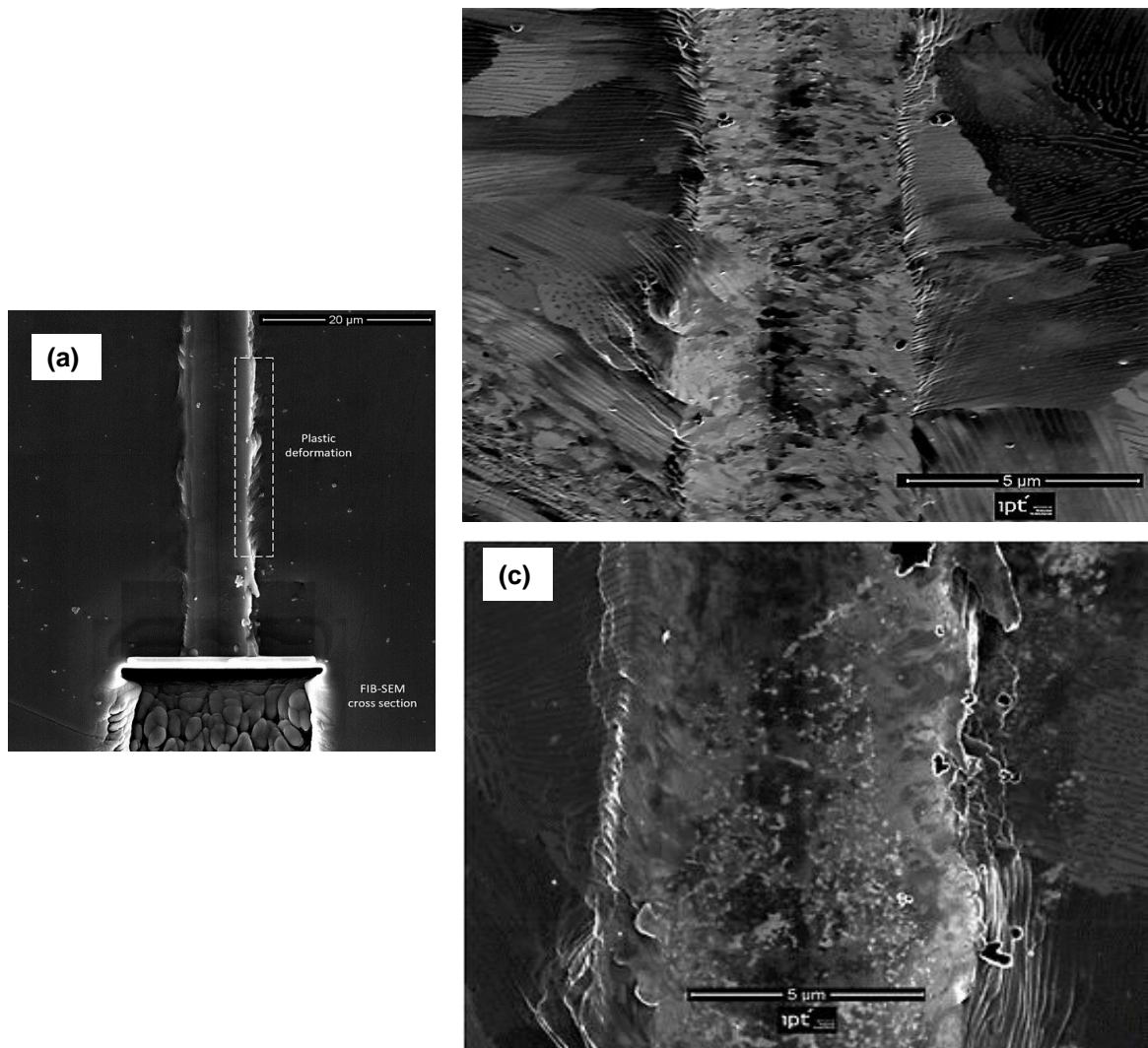
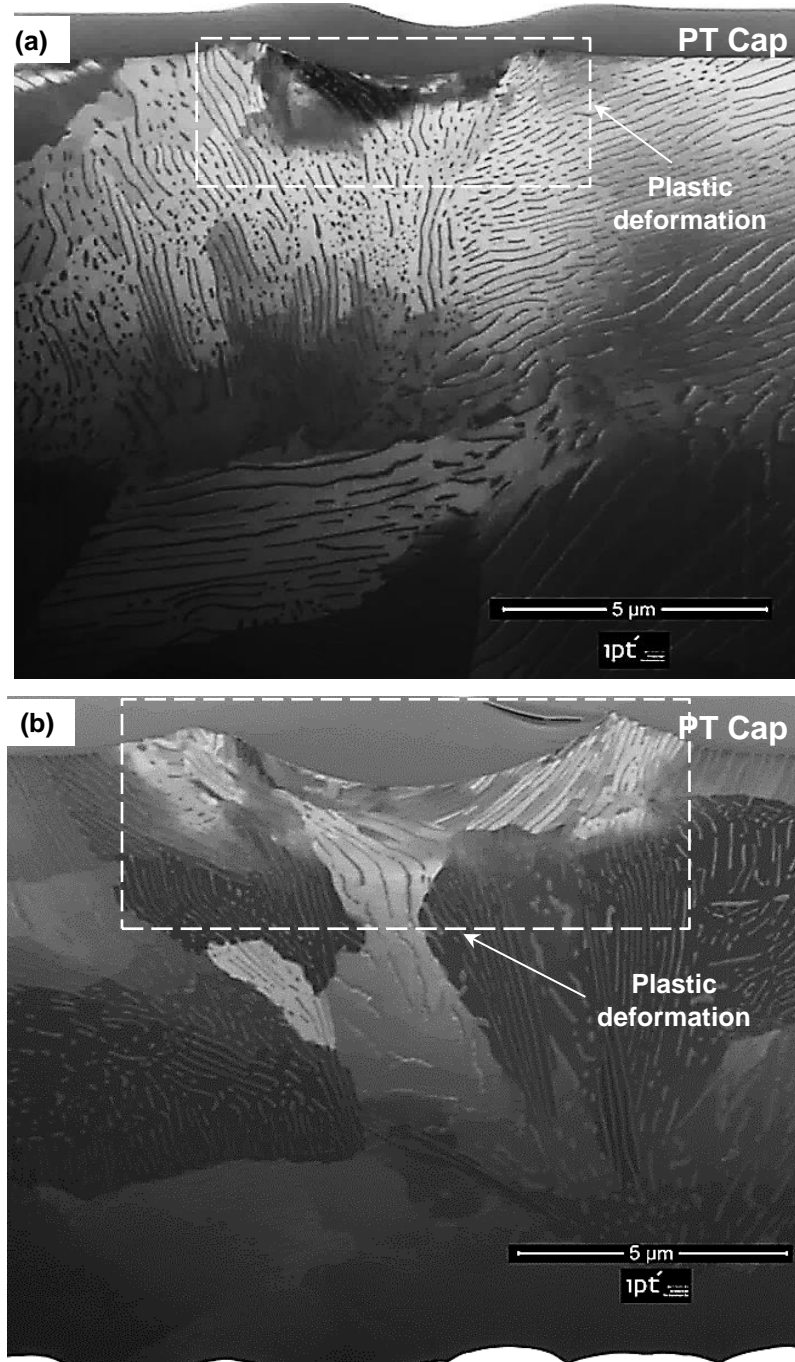


Figure 3-9 shows the microstructure of samples under the test surface after the scratch test at one-pass and five-passes. The typical pearlitic arrangement with a fine

interlamellar spacing can be observed in both cases. The number of passes has influence on the width and the depth of groove. A difference of 25% in the width and 40% in the depth between both conditions was determined.

Figure 3-9. FIB cross section of the groove after one-pass and five-passes scratch test



Plastic deformation was observed in both conditions, being clearer in the sample tested at five-passes scratch (**Figure 3-9b**). Furthermore, this sample exhibited the formation of lateral deformation (pile up). None of the samples (even at intermediate conditions

of test) show ultrafine grain formation or a possible microstructure transformation (annex 1).

3.4.1.2.2 Macro range scratch test

Figure 3-10 shows the groove generated by the indenter in the sample tested in conditions of one-pass test (single scratch) and 4 N of normal load. The deformed material was pushed along ahead of the indenter producing a discontinuous lateral material displacement and raised prow of material at the end of the groove. Two regions of the groove denominated A and B were highlighted exhibiting this behavior.

Figure 3-10 SEM micrographs scratches obtained after one-pass scratch at 4 N as normal load

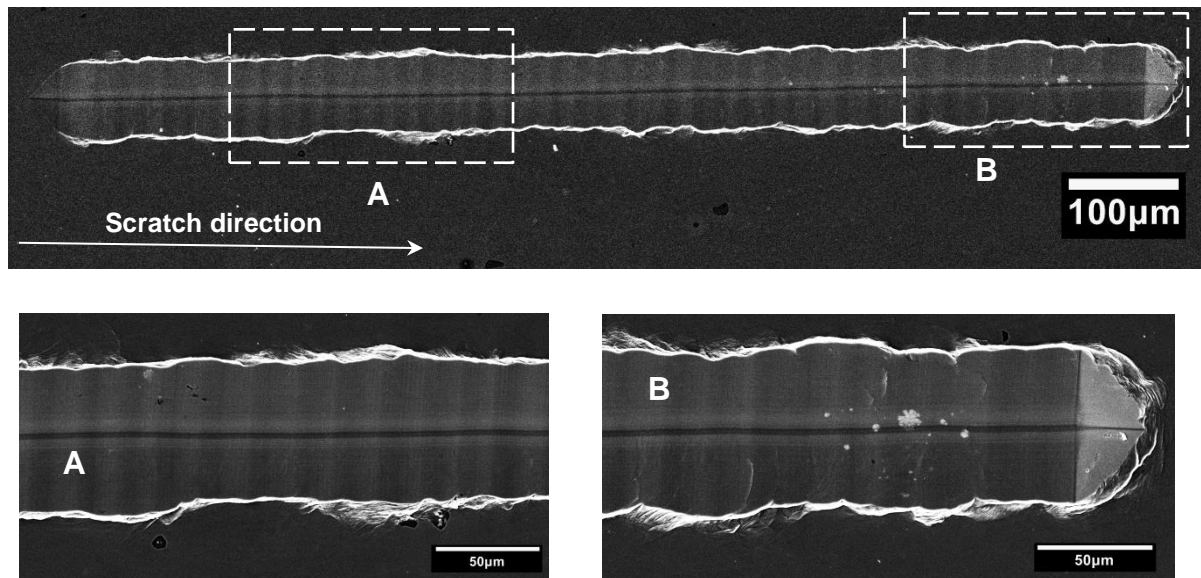
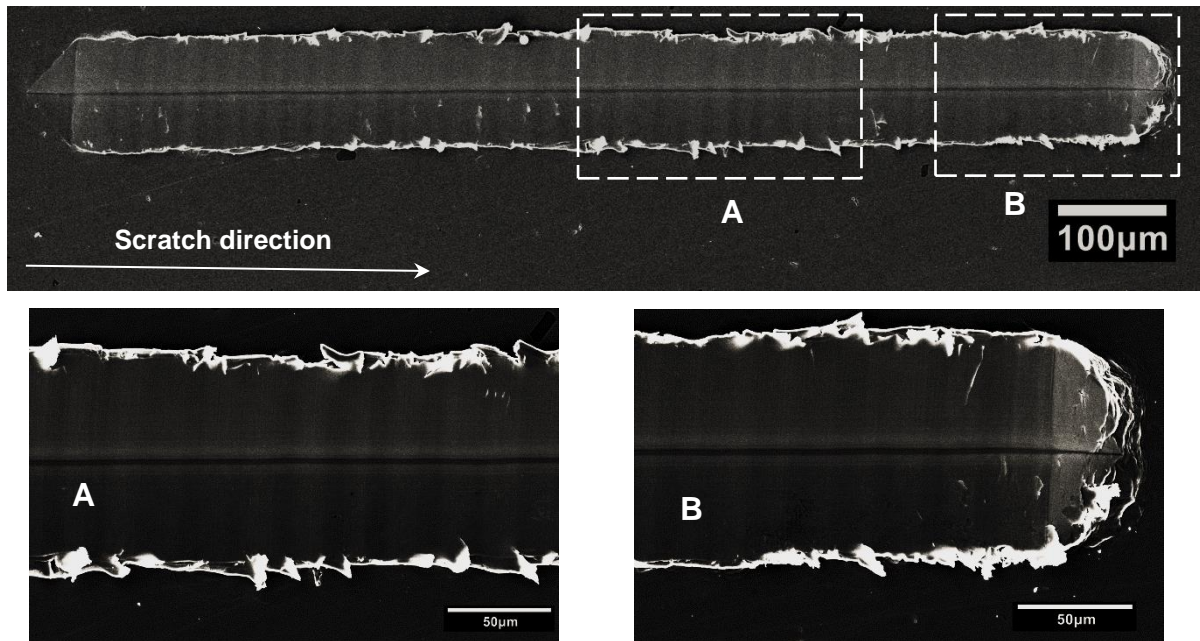


Figure 3-11 shows the SEM image of the groove in the samples tested at 4 N of normal load and five-passes sequence. Once again two regions were selected for the highlighting of the specific phenomena detected. The lateral displacement material was followed by material detachment. The prow formation was identified in the region B.

Figure 3-11 SEM micrographs scratches obtained after five-passes scratch at 4 N as normal load



The grooves of samples tested at 8 N of normal load, one-pass and five-passes scratch sequences are shown in **Figure 3-12** and **Figure 3-13**, respectively. The increase in the geometrical dimensions (width, depth and distance between the piles up) with the increment of number of passes was measured. Material detachment was observed in the groove in the sample tested with the five-passes sequence evidenced in the highlighted images.

Figure 3-12 SEM micrographs scratches obtained after one-pass scratch at 8N

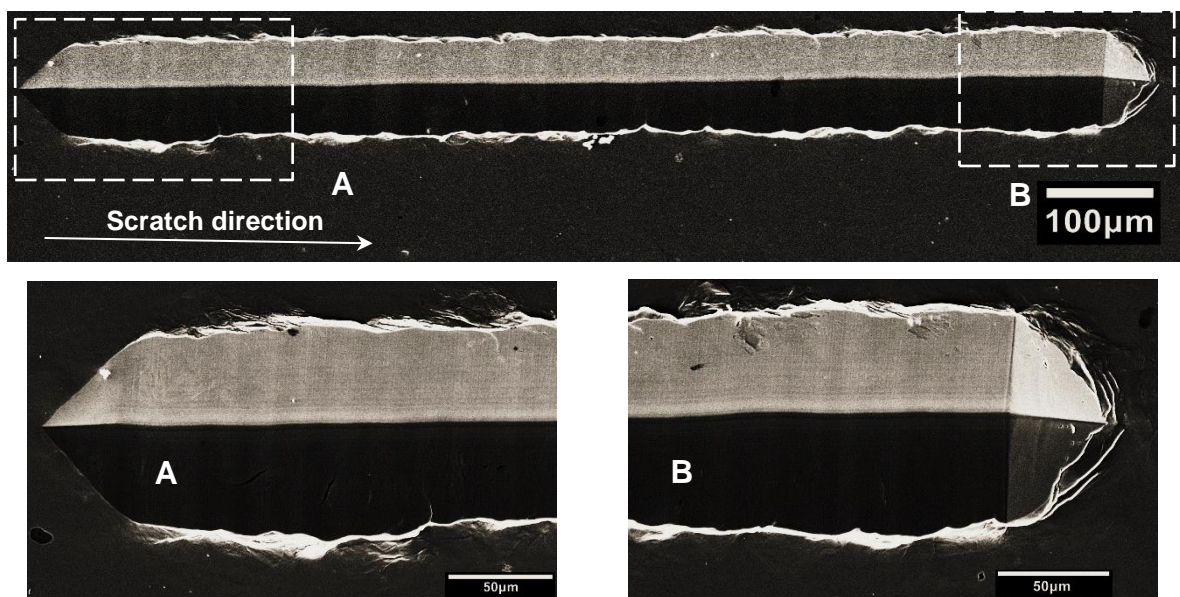


Figure 3-13 SEM micrographs scratches obtained after one-pass scratch at 8 N as a normal load

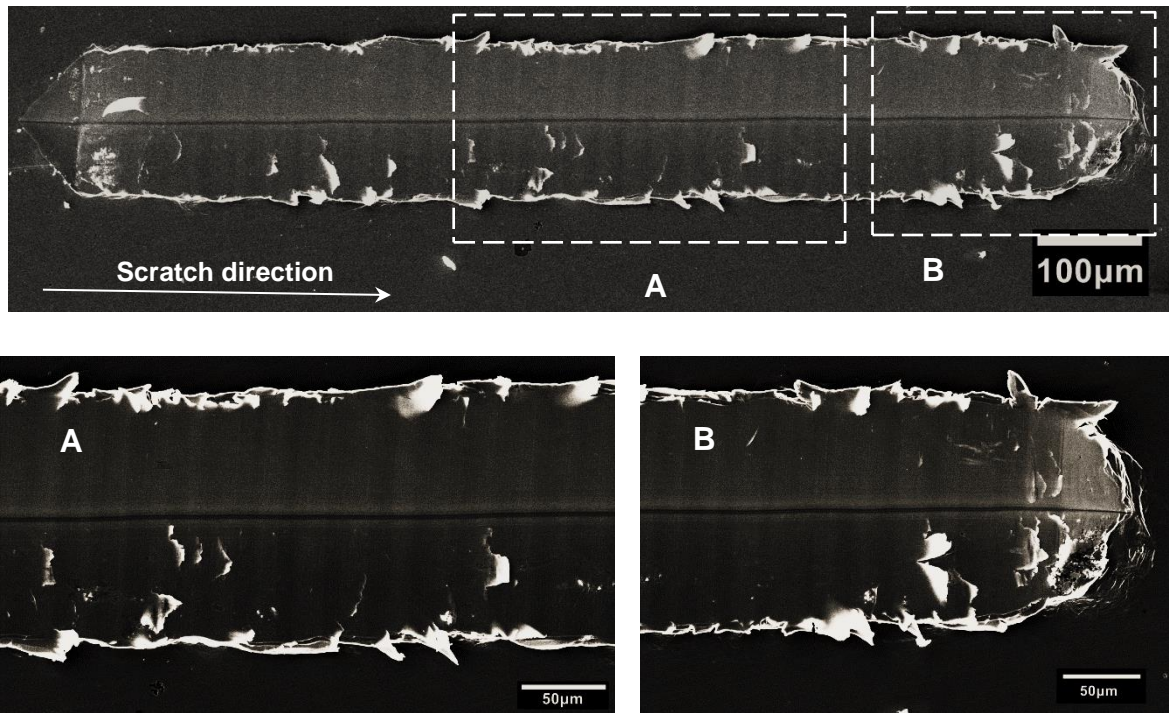


Figure 3-14 shows the groove profile obtained after the scratch test using the CCI interferometer. For all the samples, the geometrical parameters as distance between the average lines of the pile up (black lines) and the depth of the groove (red lines) were measured. **Figure 3-14a-b** shows the results of the samples tested at 4 N of normal load (constant load). **Figure 3-14c-d** shows the profiles of samples tested at 8 N of normal load. It was observed that the number of passes and the increase of the normal load influence the changes in the groove profile in similar ways.

Figure 3-14 CCI profile of samples tested at 4 N a) one-pass and five-passes scratch. Samples tested at 8 N, c) one-pass and d) five-passes scratch

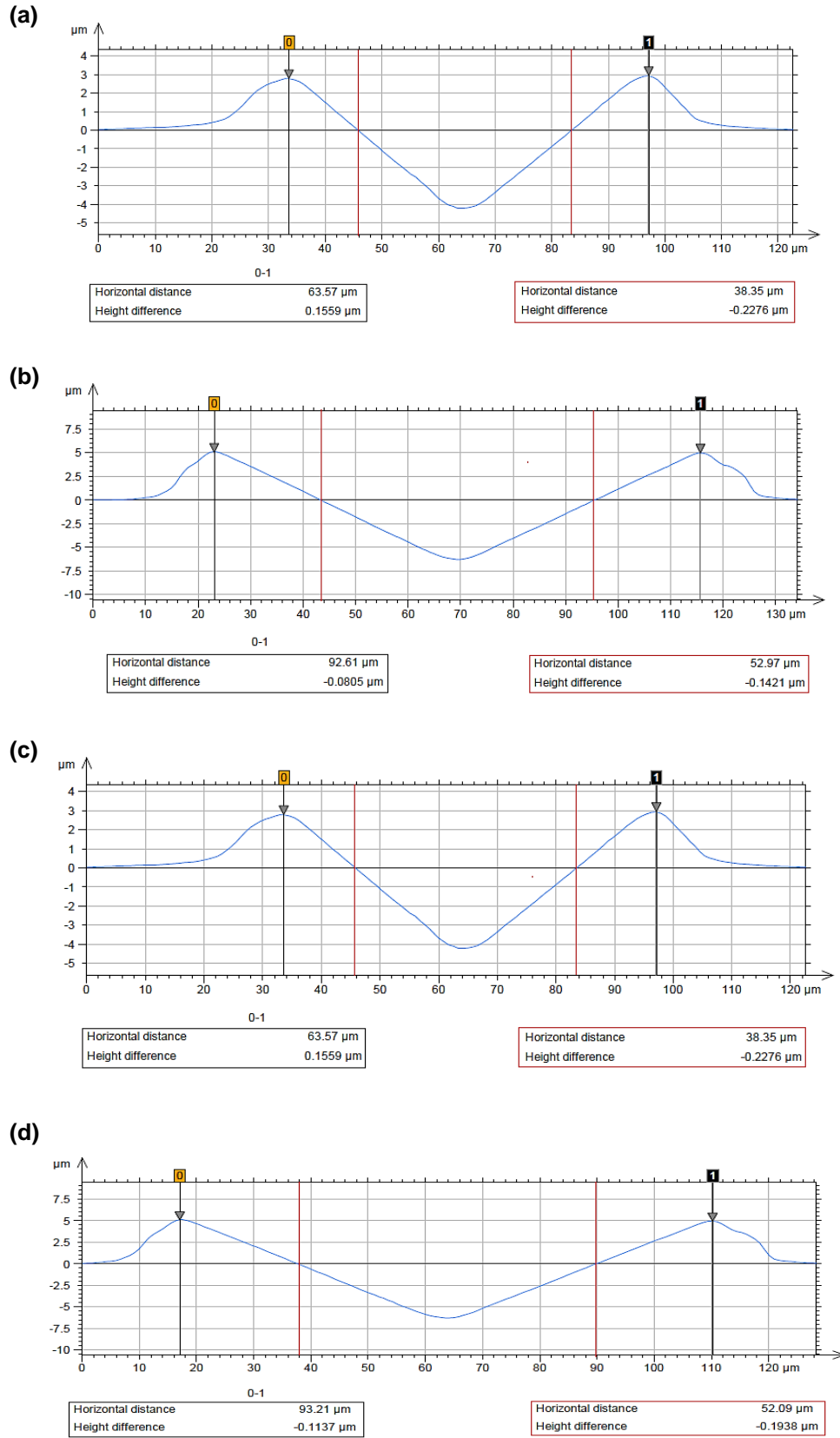


Table 3-3 shows the progressive change of geometrical dimensions in the samples analyzed in terms of depth, width and distance between the lateral displacements materials (pile-up). In samples tested at 4 N it was determined the increase of 36 % in the depth from the one-pass to five-passes sequence. The difference of number of passes had a lower influence in the change of the depth in samples tested at 8 N an increment of 31%.

Table 3-3 Geometrical dimension of grooves for all test conditions

Normal load	Number of passes	Depth (µm)		Width (µm)		Pile up distance (µm)	
		Average	Standard Deviation	Average	Standard Deviation	Average	Standard Deviation
4 N	1	4,31	0,16	37,99	0,16	63,59	0,41
	2	5,35	0,09	43,30	0,37	76,11	0,69
	3	5,76	0,04	47,28	0,33	82,28	1,24
	4	6,23	0,06	50,56	0,38	91,02	1,03
	5	6,73	0,11	52,84	0,22	95,38	14,15
8 N	1	6,68	0,18	54,63	0,88	93,83	0,82
	2	7,71	0,27	63,56	0,57	109,27	0,86
	3	8,75	0,15	70,06	0,59	123,07	1,38
	4	9,20	0,09	73,22	0,55	131,50	0,35
	5	9,73	0,13	77,30	1,26	139,50	1,25

Figure 3-15 shows the correlation of the contact pressure with number of passes (indenter) for all samples tested in both conditions (in terms of normal load applied). The initial contact pressure between the indenter and the surface of the material subjected to the scratch test was calculated according to:

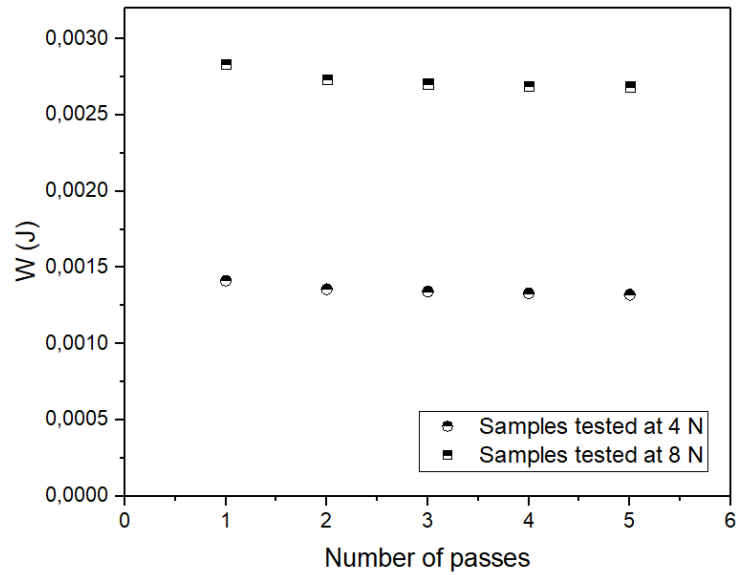
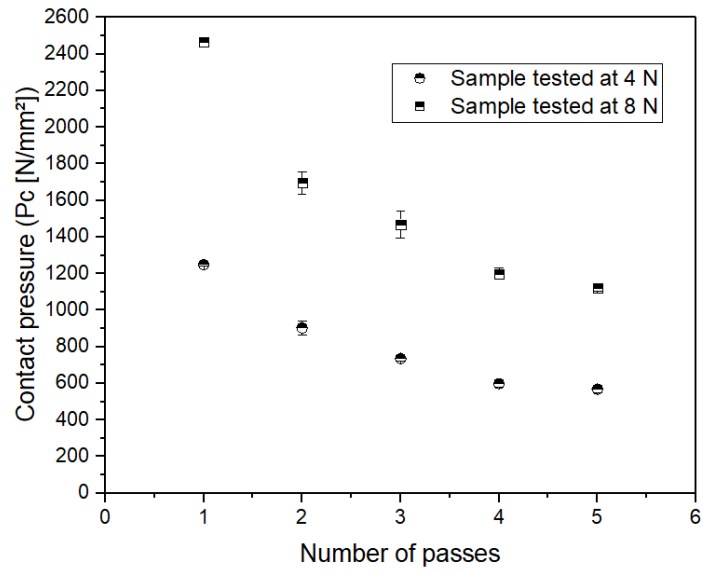
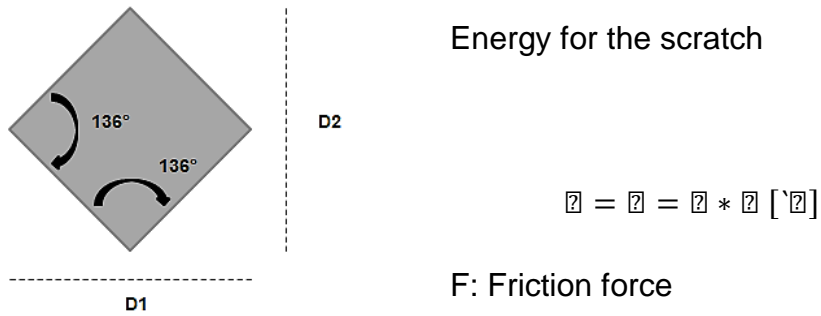
$$P_c = \frac{N}{A} \quad \text{Equation 1}$$

Where, the terms “N” and “A” correspond to the normal load applied (4 N and 8 N) and the contact area, respectively. In the determination of the contact area it was considered the width of the groove (after the indenter pass). The measurements were performed by optical interferometry, considering the average diagonal of the printing and thus calculate the contact area by means of equation 2.

$$A = \frac{d^2}{2 \cdot \sin \frac{136}{2}} \quad \text{Equation 2}$$

Where, “d” correspond to average of the diagonals and 136 ° the angle between opposing faces of the indenter.

Figure 3-15 Correlation of the contact pressure and energy dissipated with the number of passes of samples in both conditions (in terms of normal load applied)



For both test conditions (normal load) it was observed the decrease of the contact pressure with the increase of the indenter passes. This phenomenon is the result of

the increase of the groove area. On the other hand, the alteration of the energy dissipated by friction was not observed since the friction force remained constant.

3.4.1.3 Friction coefficient analysis

Figure 3-16 shows the average friction coefficient for the tests carried out at all test sequence at 4 N and 8 N of normal load, respectively. The mean COF was obtained after the running-in period until 0.9 mm of groove length.

The COF remains stable for all samples with slightly higher values for the first pass. In both cases, it was observed that samples tested with one-scratch show curves with higher values of COF and their apparent reduction with the increment of number of passes.

Figure 3-16 Mean friction coefficient and the its correlation with the contact pressure for all samples

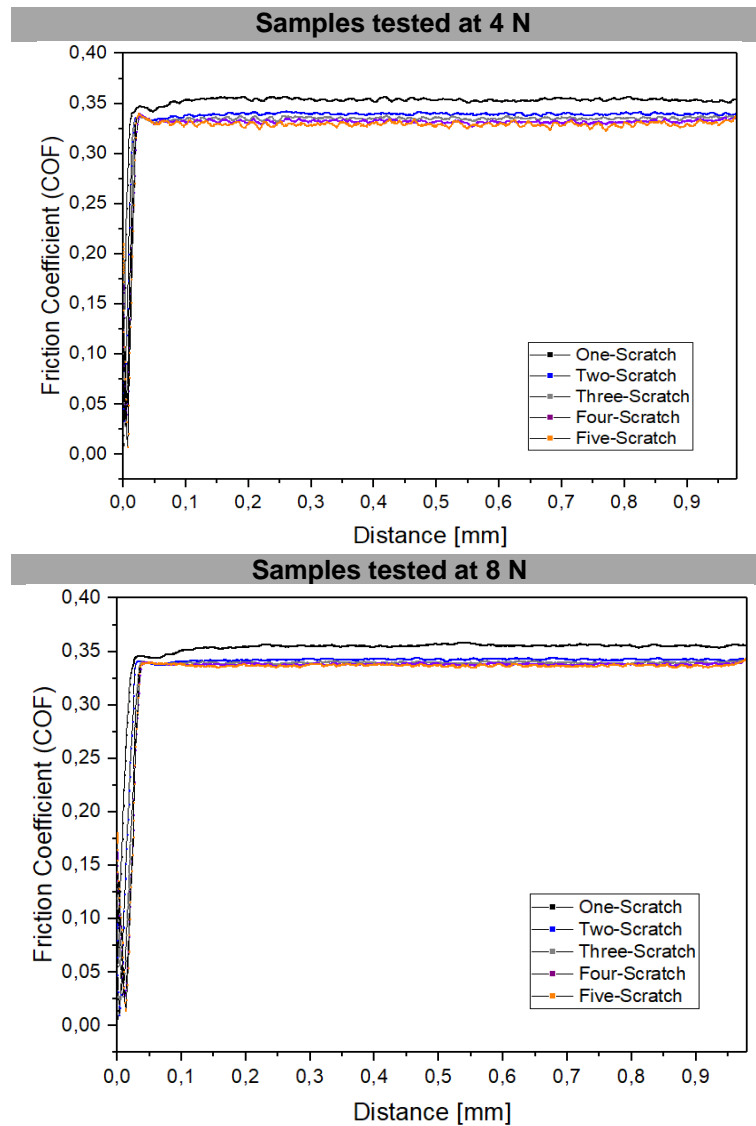
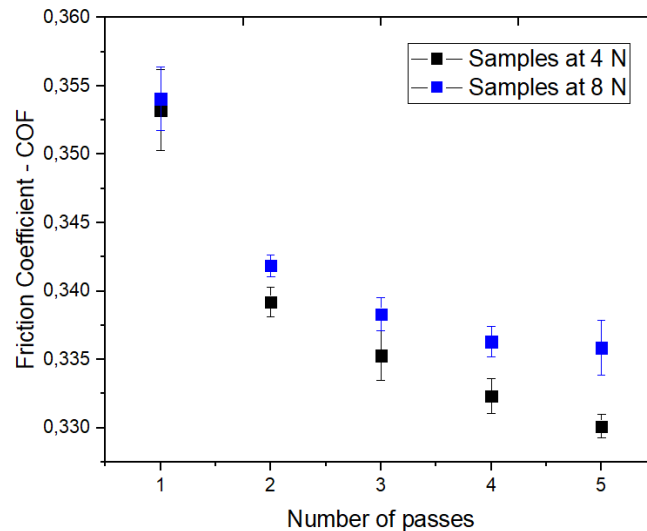


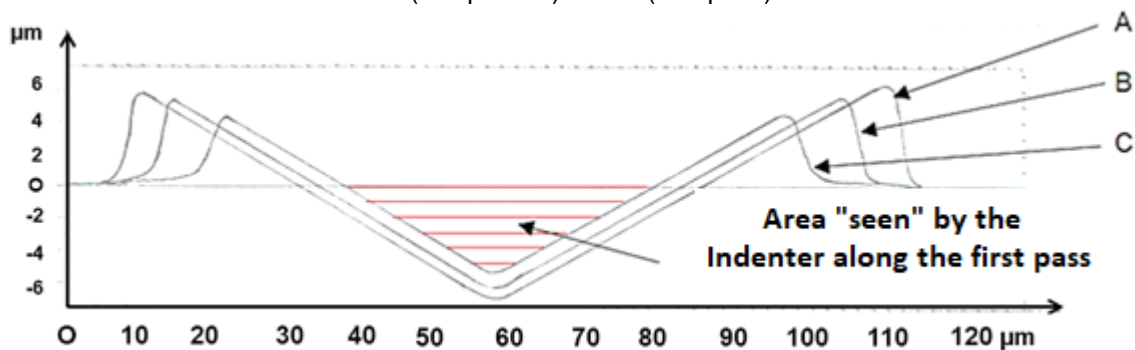
Figure 3-17 shows the individual values (average value) for all conditions. It was observed that samples tested with one-pass scratch show similar values of COF for both normal loads applied. For the subsequent passes, a difference was determined. A relationship between the COF and the number of passes was established. The COF was reduced with the increment of the number of passes, notwithstanding such difference can be particularly high.

Figure 3-17 Friction coefficient for samples tested with macro range



The small difference between the COF value along the first pass and the similar values of the remaining passes were analyzed by Franco (FRANCO, 2015). The area "seen" by the indenter at three successive passes was estimated by considering the grooves of three scratches submitted to one (C), two (B) and three passes (A), as shown in **Figure 3-18**.

Figure 3-18 Dry scratch test - AISI 1070, 4 N, mean profile superposition: scratches A (three passes), B (two passes) and C (one pass)



From (FRANCO, 2015)

It was not possible to measure groove geometry after each pass since test conditions did not offer a very precise relocation procedure. Mean groove profiles were obtained after the tests and in order to compare profiles originating from scratches after different number of passes it was necessary to rely on the regularity of the scratches and their proximity within the samples. Under the circumstances, comparisons refer to different but close scratches.

According to **Figure 3-18** and within the stated assumptions, areas "seen" by the indenter were calculated from the superposition of mean profiles with the following results:

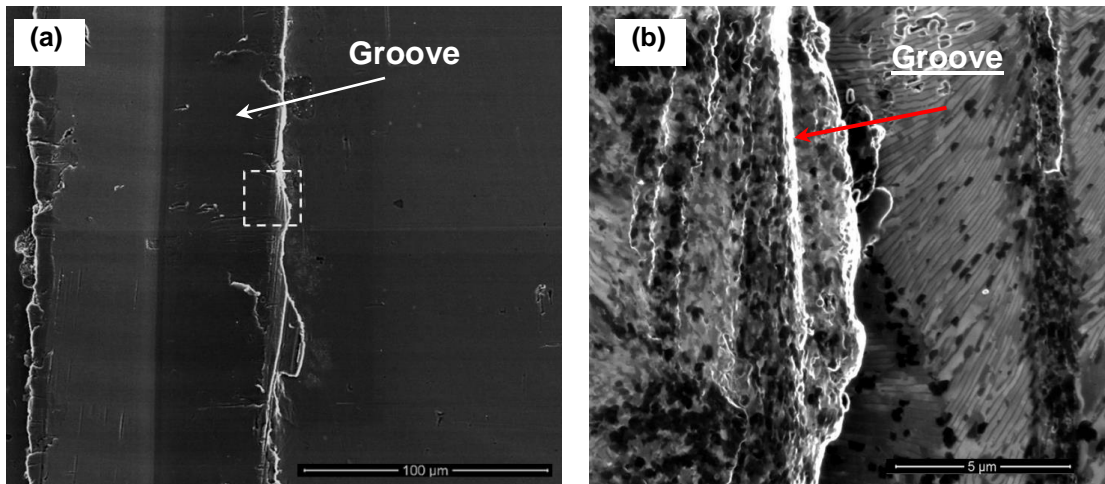
- $S_1 = 121 \text{ m}^2$ (for the first pass)
- $S_2 = 68 \text{ m}^2$ (thin lateral slices seen by the indenter along the second pass)
- $S_3 = 63 \text{ m}^2$ (thin lateral slices seen by the indenter along the third pass).

The hypothesis that work hardening is responsible for the lack of difference between COF values along successive passes cannot be ignored. On the other hand, it seems necessary to consider other factors, since it is hard to imagine that it could, alone, make for an exact compensation of the above indicated area variations: approximately 44% reduction from the first to the second pass and 7% from the second to the third pass (FRANCO, 2015).

3.4.1.4 Microstructural characterization of the sub-superficial layer

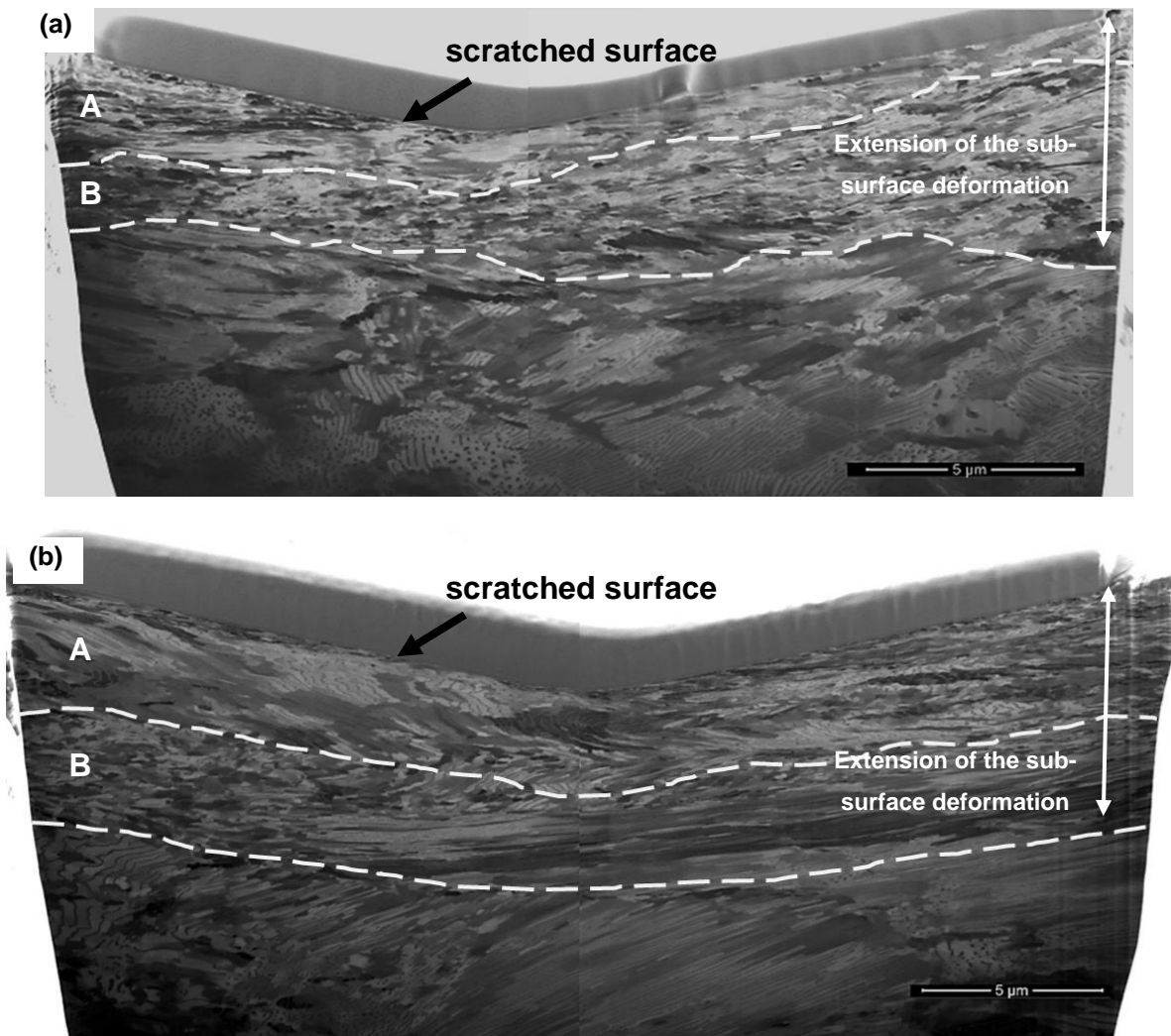
The microstructural analysis in the region below the worn surface was carried out using FIB-SEM following the same parameters described previously. The specific area of the groove is highlighted with secondary electron detector and shows in **Figure 3-19a**. The *in-situ* gallium (Ga) ion beam etched image is shown **Figure 3-19b**. Pile up formation and the typical pearlite arrangement was observed out of the groove.

Figure 3-19 Scratch images. a) Groove profile image using a secondary electron detector in FIB/SEM and b) Pearlite colonies revealed with Gallium ion beam etching



The formation of a deformed layer as analyzed as a function of normal load is shown in **Figure 3-20**. For all the samples, microstructural layers were observed below the worn surface and classified by the deformation level as, (A) ultrafine grain (nanostructured) zone in agreement with Fargas *et al.* and Pereira *et al.* (FARGAS; ROA; MATEO, 2016; PEREIRA *et al.*, 2017); (B) a transition layer characterized by a sheared and more finely structured arrangement (interlamellar spacing) than bulk material with pearlite colonies oriented following the wear direction as reported by OKOLO *et al.* (OKOLO *et al.*, 2007). Deeper in the sample, undeformed pearlite colonies were observed. The number of passes and the normal load applied on the test influenced the thickness of the layer.

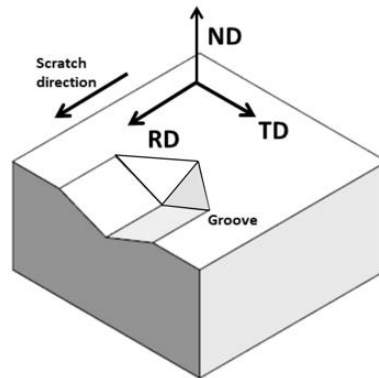
Figure 3-20 A FIB-SEM micrograph for five-passes samples at, a) 4 N and b) 8 N



3.4.1.5 Crystallographic orientation analysis using EBSD

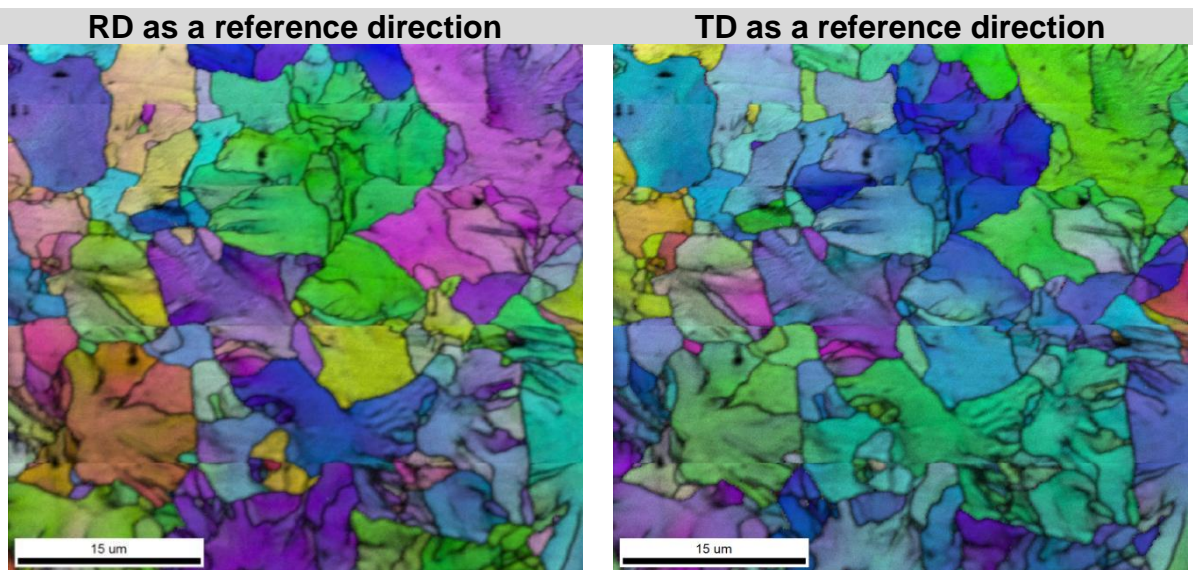
The EBSD allows sample analysis using different a reference plane (analysis surface) according to the research interest. For this work, the RD direction (Rolling/Reference direction) was selected as the reference direction which corresponds to the conventional arrangement in the microscopy chamber. The comparison with the results obtained using the TD (transversal direction) as reference direction will be also present. **Figure 3-21** shows a schematic representation of EBSD analysis in the conventional arrangement.

Figure 3-21 Schematic representation of the EBSD plane reference for the microstructure analysis



In an initial approach, the results obtained in an undeformed sample using both reference direction (RD) and TD, were compared. The **Figure 3-22** shows the difference in the color distribution of the pearlite colonies as indicated in the inverse pole figure map (IPF) for a specific reference direction.

Figure 3-22 IPF + IQ map using RD and TD as a reference direction, a) RD (001) and b) TD (100)



In a sequence, as described previously, the RD was selected as reference direction and the undeformed sample was analyzed as shown in **Figure 3-23**. High angle grain boundaries (HAGBs) with misorientation greater than 15° are marked as thick black lines. The IPF map showed a random orientation of grains; for instance, the grains oriented along $\{001\}$, $\{110\}$ and $\{111\}$ parallel to the reference direction are indicated in red, green and blue, respectively. It is well known that the grains oriented with the $\{110\}$ crystallographic planes correspond to close-packed planes, which can facilitate dislocation movements inside the grains and can decrease crack growth rate (HUMPHREYS; M. HATHERLY, 2004).

Figure 3-23a shows the microstructure orientation using inverse pole figure (IPF) of an undeformed sample (core). Each preferential orientation was delimited by the grain boundaries (HAGBs), identified as the thin black lines. **Figure 3-23b** shows the analysis of low angle grain boundaries - LAGBs (point-to-point misorientation less than 15°) into the one-color gradient which represents the lamellar arrangement in a pearlite colony. Also, low degree values (with 10° as the highest angle) were observed along the dashed arrow through the pearlite colony, indicating a low lamellar orientation difference, characterizing one single colony.

Figure 3-23 EBSD analyses of undeformed region of samples. a) IPF map, b) Misorientation curve

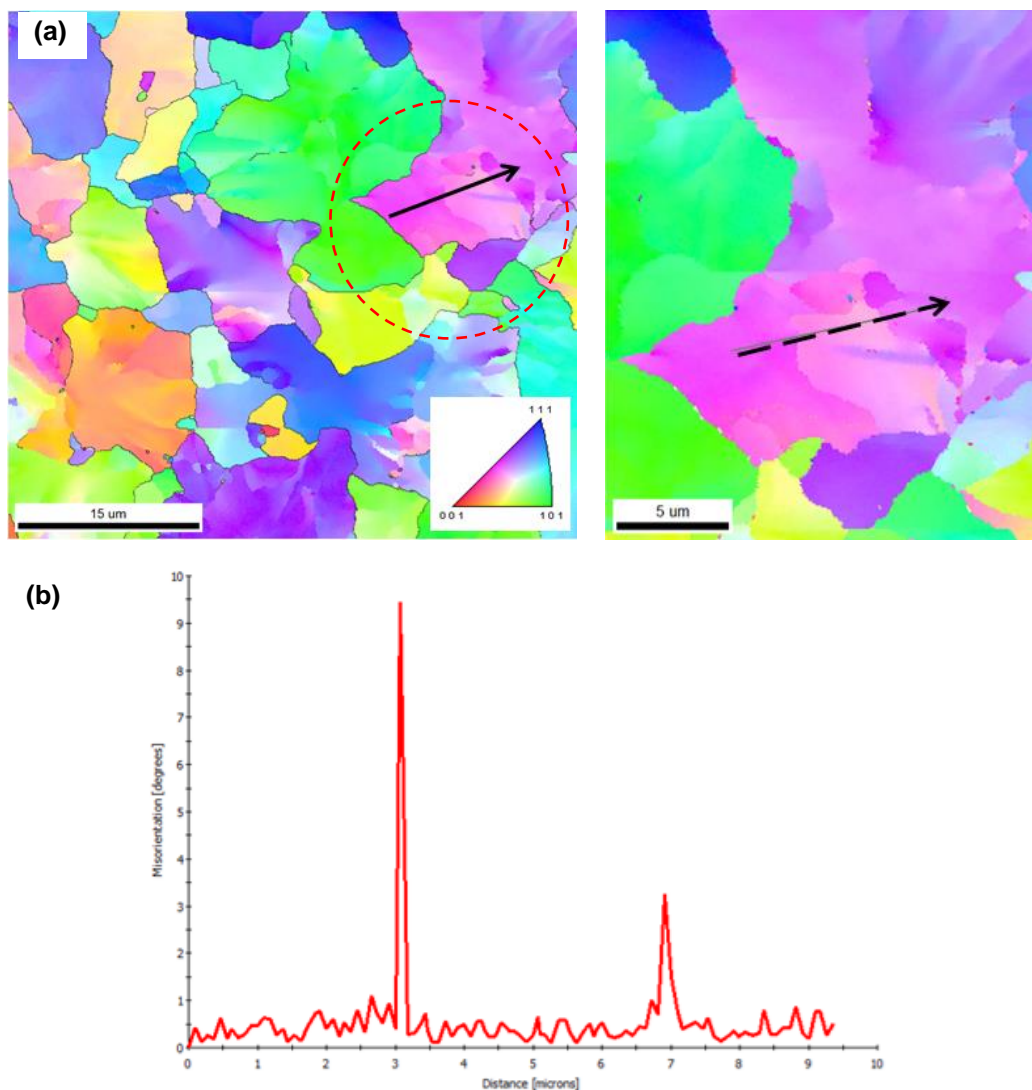


Figure 3-24 shows the IPF map in a sample tested with 4 N (normal load) and single-pass scratch sequence. The color distribution in the IPF map shows pearlite colonies mainly oriented in RD // $\{111\}$. It was identified two regions below the groove (indenter

passing) characterized by color distribution and shown in **Figure 3-24b**. The region near the worn surface was denominated as Region A, in which was not fully identified the pearlite colony size due to the fact that the microstructure broken down into grains was smaller than the resolution of EBSD method, a result reported by MEYER *et al.* and FACCO (MEYERS *et al.*, 2003; FACCO, 2013). Another possible explanation for this phenomenon was presented by GEE *et al.* in the discussion of the reduction in band contrast and indexing proportion by severe deformation (GEE; MINGARD; ROEBUCK, 2009). The region B corresponds to the second layer located deeper in the sample and is characterized by a color gradient denoted in the formation of pearlite colonies. It was observed that the colonies are oriented mainly in RD // {101}. The formation of those two regions in the sub-superficial layer was observed for all test conditions.

Figure 3-24c shows the correlation of the angles grains boundaries along of the three pearlite colonies, identified by the dashed white arrow (**Figure 3-24a**). It was observed the change of the angle from LAGB in the interior of the colonies to HAGB corresponding to the passing of one colony to other (grain boundary). This observation established that the color distribution (changes) is the feature of a particular crystallographic orientation, which identified a colony without distortion in the lattice.

Figure 3-24 EBSD analysis of sample tested with 4 N as normal load and single-pass. a) IPF + IQ map (Highlighting IPF map), b) sub-superficial layer highlighting by IPF map, c) Misorientation curve

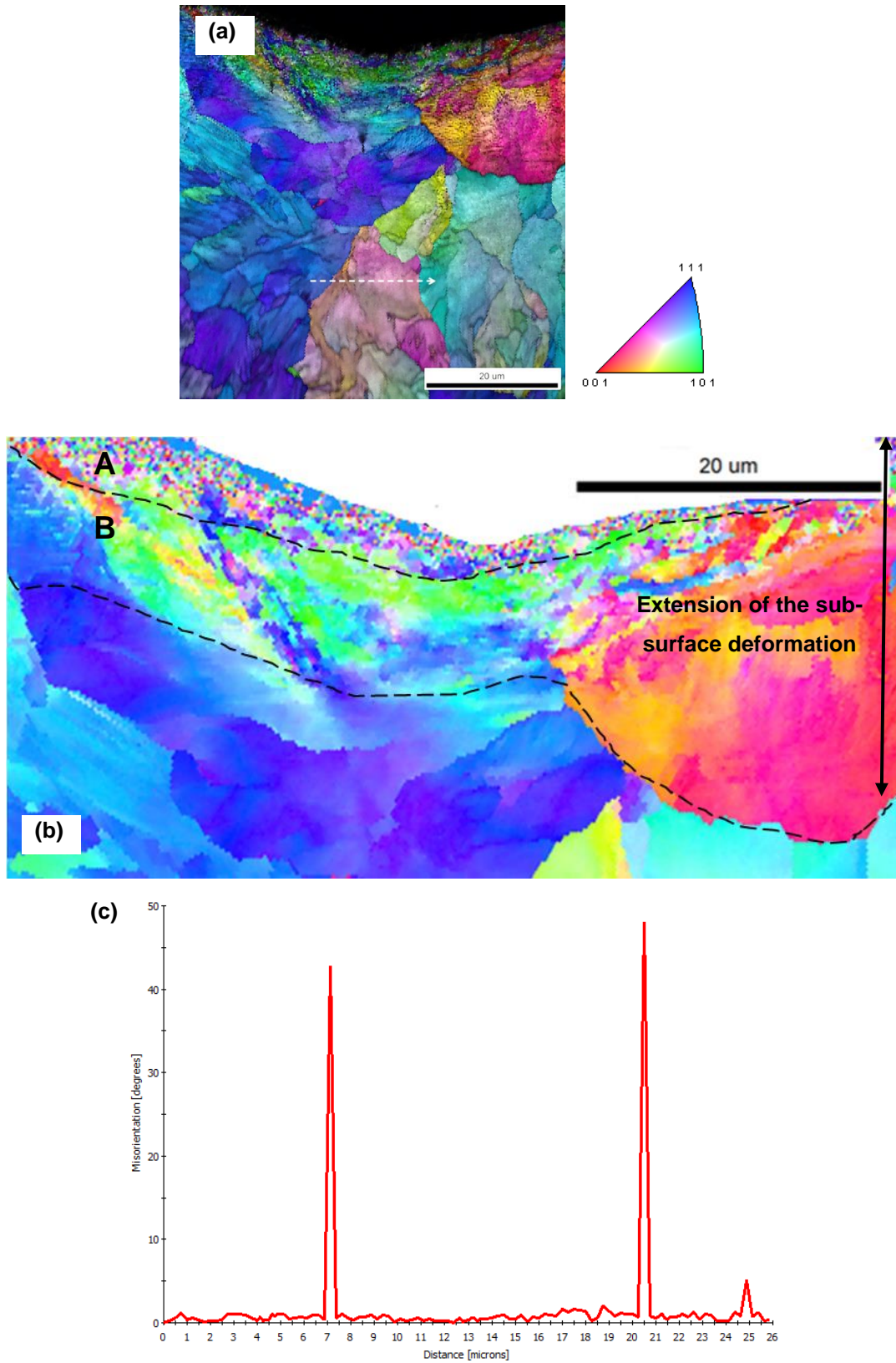
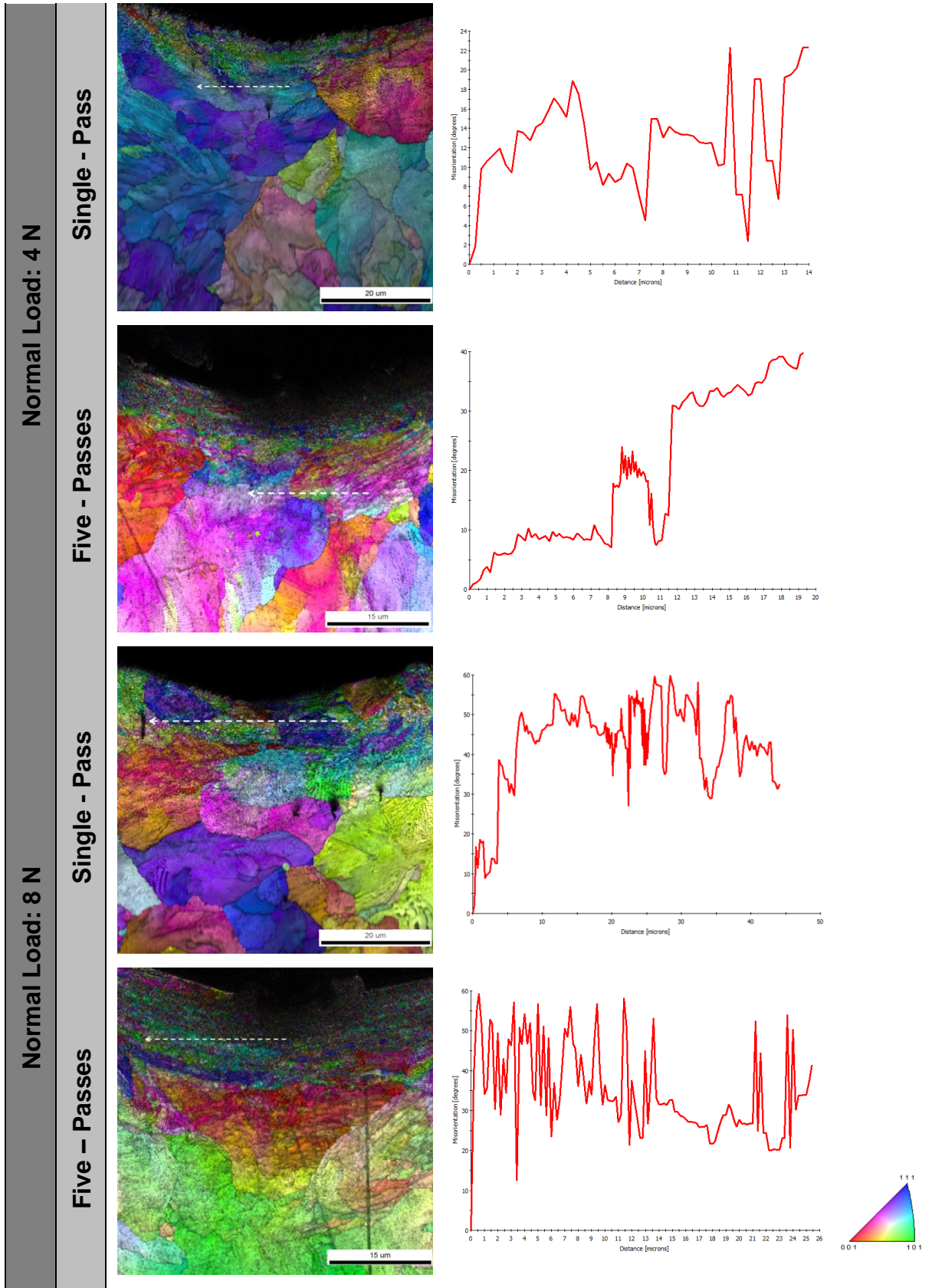


Figure 3-25 shows the IPF maps for samples tested in sequences of one-pass and five-passes scratch and normal loads of 4 N and 8 N. The analysis of misorientation shows HAGBs (higher than 15°) in all samples indicated by the black arrows. The analysis was performed in the region near the groove. High angle orientations were observed for all samples in the deformed layer, indicating that in those regions new grains (or colonies) were formed with a random orientation.

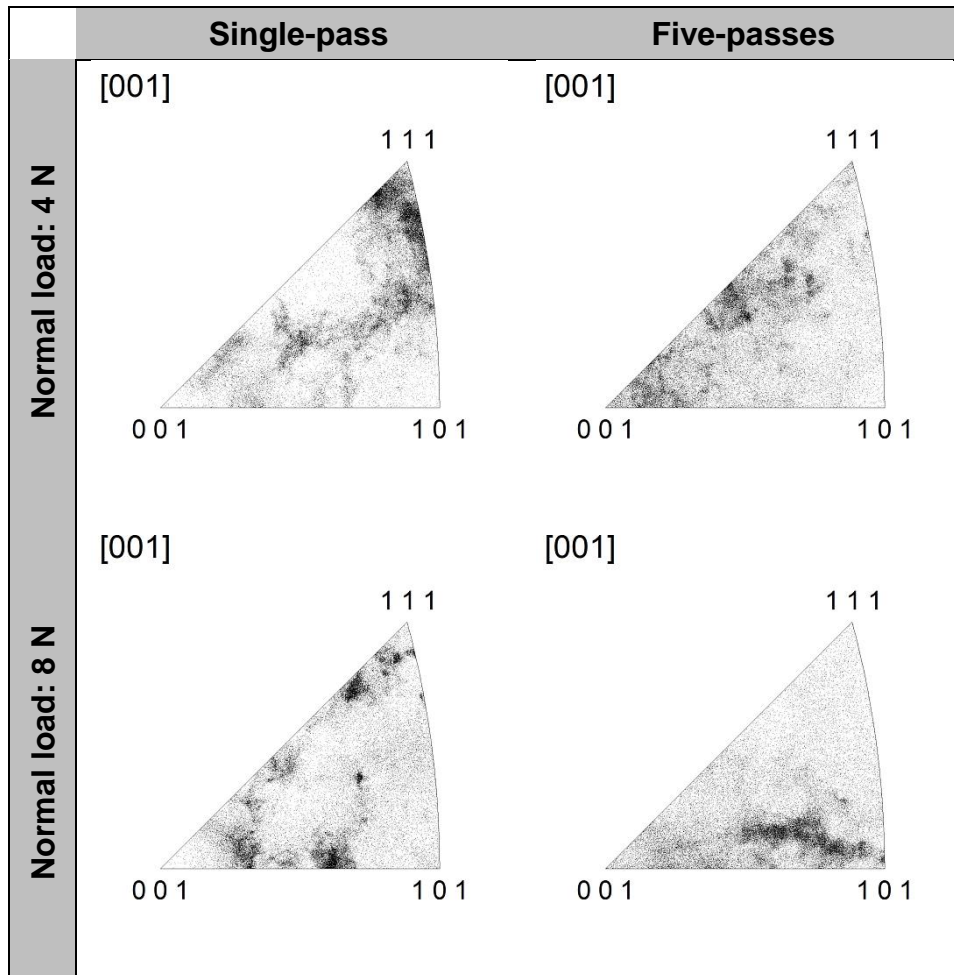
Based on the IPF map, two hypotheses about the crystallographic orientation beneath the scratched surface can be discussed: The orientation corresponds to a random arrangement of the microstructure as result of the metallurgical process of manufacture of the sample; the microstructure orientation in the deformed layer (regions A and B) was influenced by the normal load applied. The pearlite colonies in the samples tested at one-pass scratch remain mainly oriented in RD // $\{111\}$ for 4 N. The sample at 8 N shows a random crystallographic orientation, representing by the color distribution on its colonies. On the other hand, samples tested at five-passes scratch show orientation mainly in RD// $\{001\}$ and RD// $\{101\}$, for 4 N and 8 N, respectively.

Figure 3-25 IPF + IQ and Misorientation map on samples for single and five-passes



For a detailed description of the orientation distribution, the central concept in texture analysis and anisotropy (OD – Orientation distribution) was used, an additional EBSD tool showing that each point in the orientation distribution represents a single specific orientation or texture component. A mathematical function is always available to describe the (continuous) orientation density; this is known as an “orientation distribution function” (*ODF*). Properly speaking, any texture can be described by an OD but “ODF” should only be used if a functional form has been fitted to the data. **Figure 3-26** shows the Orientation Density Function (ODF) for the samples analyzed in this work.

Figure 3-26 ODF (frequency) for samples tested at single and five-passes



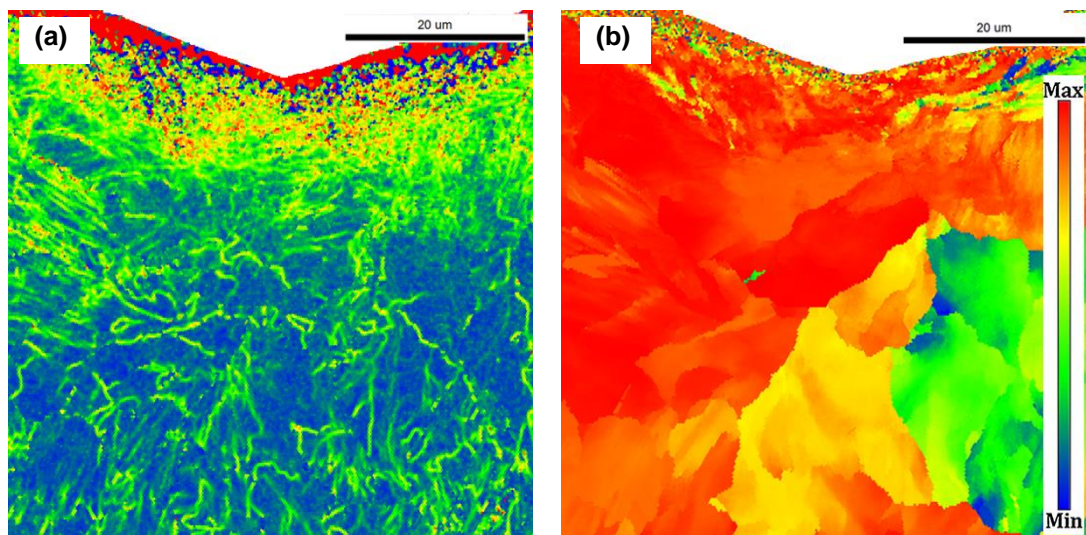
For samples tested with one-pass scratch, the ODF shows the RD// {111} as the preferential orientation, represented by the point concentration, especially for 4 N, while the sample with five-passes scratch was not a preferential orientation. The samples at 8 N (one-pass scratch) exhibited a homogeneous distribution with a

concentration in RD// {111}. Once again, the ODF map shows that the sample tested at 8 N and five-passes scratch shows the RD// {111} as the preferential orientation.

A correlation between yield stress and crystal orientation in metals can be observed by the distribution of grain orientation (KOCKS; MECKING, 2003; SHEN; LI; WEI, 2013). For that analysis, a complementary analysis of the microstructure was performed using EBSD tools as Taylor factor (TF) and Kernel Misorientation Map (KAM), as follows.

The level of stress induced into the grains can be analyzed based on the family of slip systems using the Kernel Average Misorientation (**Figure 3-27a**) and the Taylor Factor analysis (**Figure 3-27b**), both tools found in the EBSD analysis software. In the case of the Taylor Factor map, the color distribution was obtained using the preferential slip system for BCC metals {110} <111> (DELANNAY; JACQUES; KALIDINDI, 2006). A correlation between predominant pearlite colonies orientation after scratch sequences and level of stress was observed. The pearlite colonies located closely to the more deformed layer showed a high concentration of energy (represented by KAM map). On the other hand, the colonies mainly oriented in RD // {111} shown higher deformed resistance (TF > 3).

Figure 3-27 EBSD analysis in sample tested in single-pass scratch. a) Taylor Factor map and b) Kernel Average Misorientation map



Takahashi *et al.* (TAKAHASHI; PONGE; RAABE, 2007) observed the presence of sub-boundaries usually characterized as low angle boundaries. A new pearlite colony does not necessarily have to be formed as an individual colony by a nucleation process, but

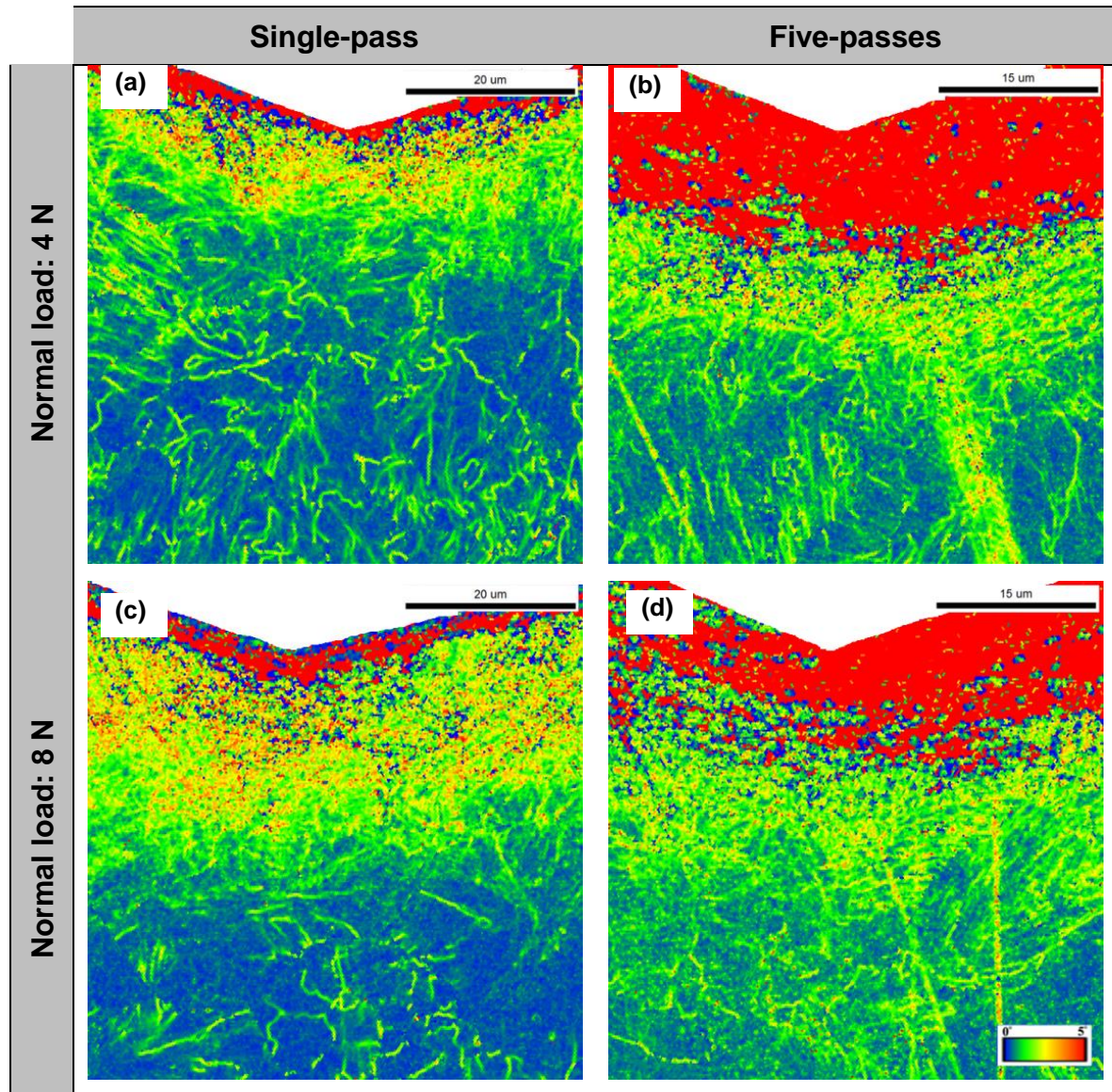
it may also be created by changing the lamellar direction during the growth process. According to the authors, the existence of dislocation inside the pearlite colonies promotes the continuous changes in the orientations.

TAKAYAMA and SZPUNAR (TAKAYAMA; SZPUNAR, 2004) showed that stored energy increases with an increase in the TF. Yet, according to the authors, the misorientation reflects the stored strain energy and the recommended parameter to evaluate the stored energy is Kernel Average Misorientation, useful tool in EBSD technique by representation of the dislocation density distribution in different grains.

Figure 3-28 shows the KAM or local misorientation map for the main test conditions, representing the numerical misorientation average between a given pixel and its nearest neighbors and cut-off level of 5° was used to characterize the local misorientation gradient. Therefore, the KAM histogram was used to assess the local plastic strain in the specimens. In this EBSD tool, the lowest and highest dislocation density areas are marked in blue and red, respectively. The high KAM values were observed in grain near to groove regions, which indicate that the deformation is more concentrated on the areas close to the scratch.

As observed, the thickness of the two regions identified in the sub-superficial layer using FIB/SEM, can be determined with more detail by KAM technique, since the color gradient is more concentrated by the deformation concentration. A relationship was established between the number of passes for each normal load applied. The samples tested at 4 N the sub-superficial layer (representing in red color) show a change in the thickness of $1.44 \mu\text{m}$ to $11.32 \mu\text{m}$ (87.3 %) when the test was carried out with one to five passes. The transitional layer remains stable in $10 \mu\text{m}$ (**Figure 3-28a-b**). On the other hand, samples tested at 8 N reported lower difference. For one-pass, the thickness of the more deformed layer was $4.11 \mu\text{m}$, while sample at five-passes exhibited a layer with $13.8 \mu\text{m}$, representing a difference of 70% (**Figure 3-28c-d**). A significant difference was not found in the thickness of the more deformed layer as a function of the normal load applied in the tests. In contrast, a variation of almost 55% in the thickness was observed in the transition layer with the increment of normal load.

Figure 3-28 Kernel Misorientation map on samples at test conditions

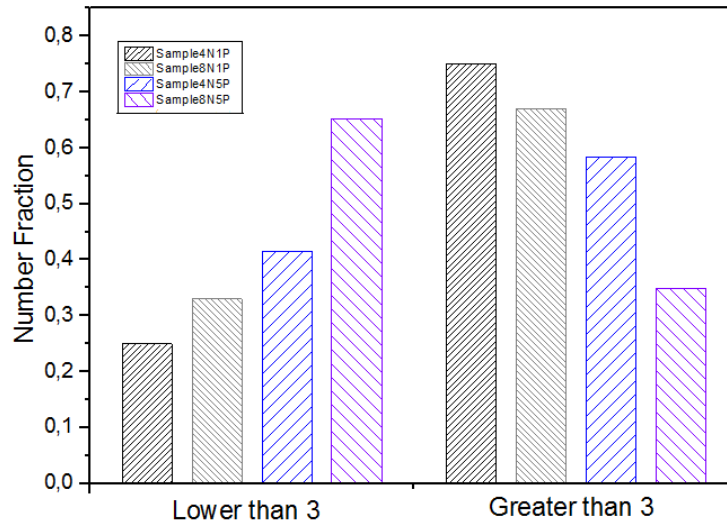


The distribution of the magnitude of the Kernel Average Misorientation is not uniform throughout the pearlitic region, but shows pronounced patterning, in accordance with Takahashi *et al.* (TAKAHASHI; PONGE; RAABE, 2007) who had showed that in the analysis of pearlite gradient orientation.

The frequency distribution of TF values is presented in **Figure 3-29**. A high influence of the number of passes was observed on the stress level in the samples. In a sample tested at 4 N single-pass, 25% of the pearlite colonies had low-moderate TF value, while maintaining the normal load and increasing the number of passes to five, the TF value rose to 41%. This is equivalent with a difference of 40% in the frequency of colonies with less rotation to the preference slip system. On the other hand, samples

analyzed after applying a normal load of 8 N show the increase of the frequency of moderate Taylor values, being 33% for single-pass and 65% for five-passes, corresponding with a difference of 49%.

Figure 3-29 Taylor factor distribution



The behavior observed in the samples at successive passes was strongly influenced by the increment of normal load. Increasing the number of passes reduced the frequency of colonies with preferential crystal orientation in the slip system. In tests at 4 N, the difference in the frequencies of pearlite colonies with high TF values obtained after single and five-passes test was 22%, while a difference of 48% between samples tested at 8 N was reported.

Two hypotheses about the relationship between the Taylor Factor and the crystallographic orientation were proposed in this work, as follows:

1. The TF values correspond to a combination of colonies orientated to the preferential slip system of BCC crystal (not affected by the indenter pass) and the new colonies, resulting of a crystal rotation (plastic deformation).

This hypothesis was not entirely demonstrated in this work since the presumption of grains (colonies) not deformed after the scratch test with a prior orientation preferential was not confirmed. On the other hand, the Taylor Map indicates that pearlite colonies oriented mainly in $\{101\}$ shows TF values lower than 3.0, indicating that those regions (in particular) can be easily deformable. The main microstructure involving the groove

attains the maximum level of deformation leading to the nucleation and propagation of cracks promoted by successive sequences of loading (LIU et al., 2016).

2. The TF is related to the stored energy on the microstructure after plastic deformation.

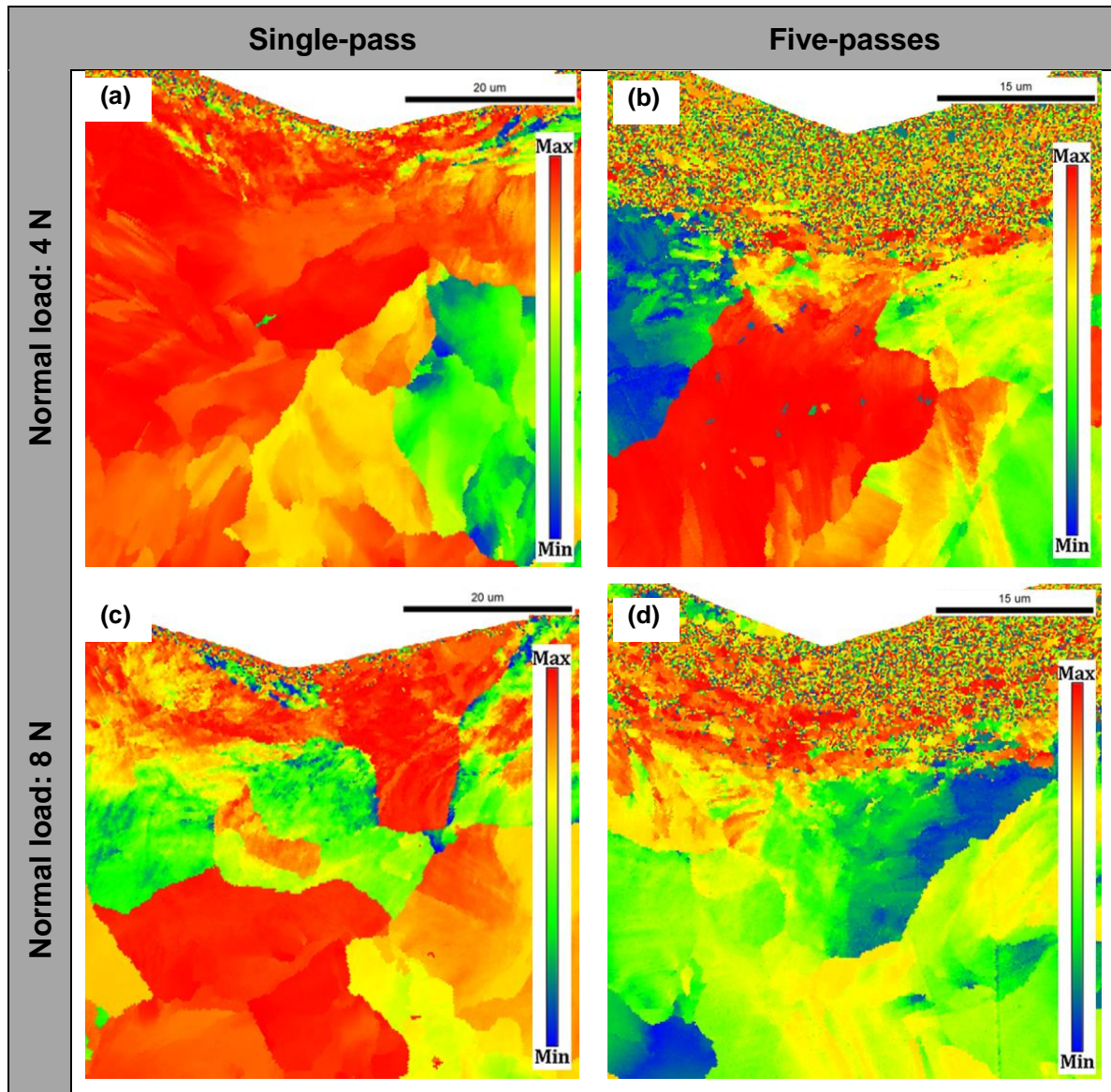
TAKAYAMA *et al.* showed that the stored energy increased during the deformation of a grain in a specific orientation, corresponding with high TF values. The results showed some exceptions and a lot of scatter attributed to the rotation of the grain orientation and a non-homogeneous deformation. Low TF grains are not difficult to deform and require only a small amount of the total slip on all active slip systems. Actually, non-homogeneity of strain within the grain is caused by differences in deformability of grains of different orientation in a given stress state. This means that the actual deformation needs local stress equilibrium between differently oriented grains, which is assumed by the Sachs model (TAKAYAMA; SZPUNAR, 2004).

Under the same amount of deformation, the energy stored in the grains depends not only on the TF but also on other factors such as crystal lattice rotation and work hardening behavior (PARK et al., 2010).

Besides this, the energy stored by the slip system activation, an anisotropic effect requires special attention. As shown in the analysis of the microstructure using EBSD (IPF, KAM and TF), especially in **Figure 3-25**, the indenter in some cases presented the same size scale as the pearlite colonies in the undeformed region. The behavior of the colonies will be restricted with the phenomenon.

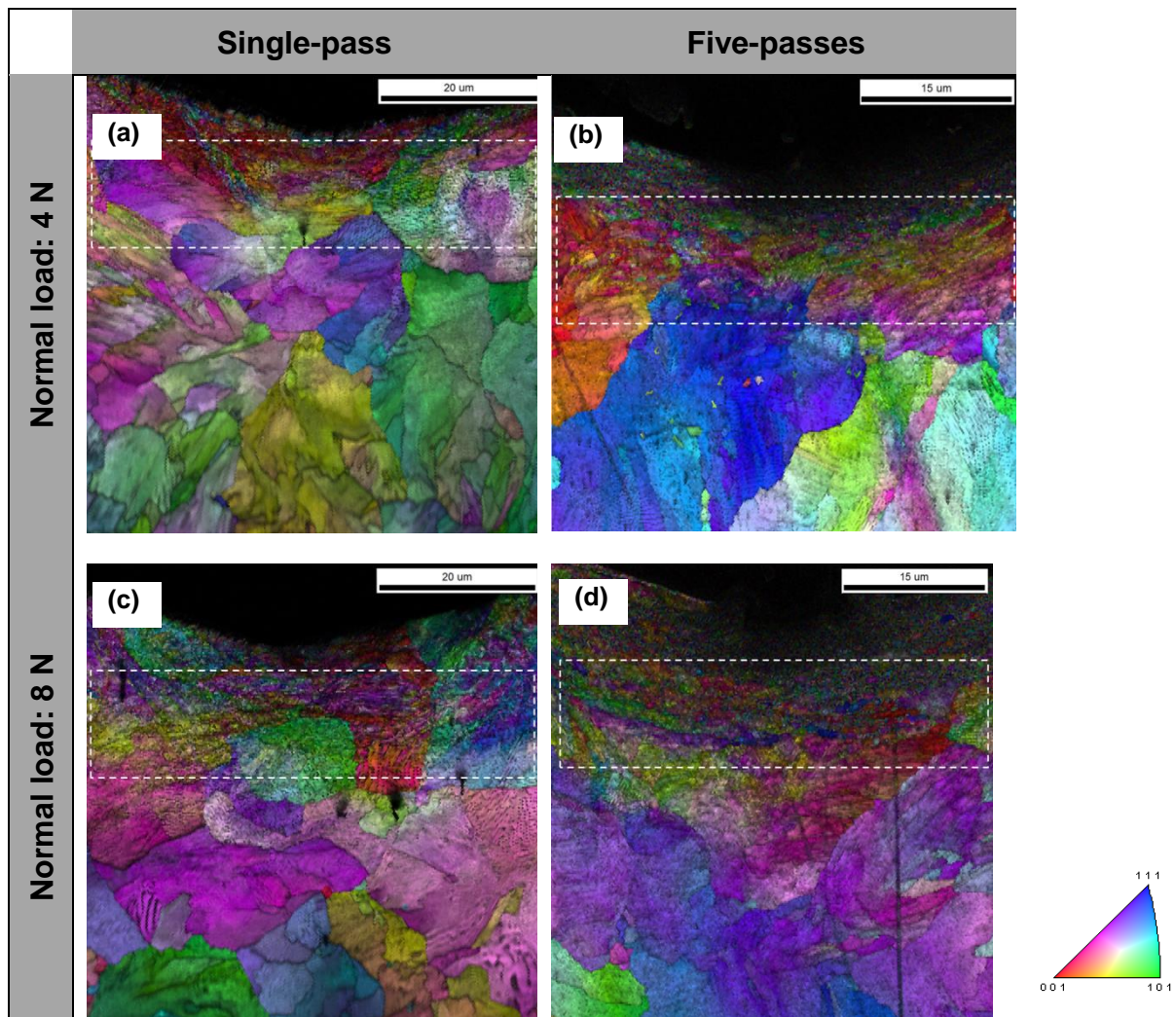
Figure 3-30 shows the level of plastic deformation using Taylor Factor. The colonies indicated in blue present a low deformed resistance whereas those colonies in red offer high deformation resistance. The transition layer shows the highest level of TF, characteristic of colonies with low capacity of deformation. Those colonies can act as a barrier to plastic deformation propagation, especially in samples tested with high loading which exhibited a thicker layer. As shown in **Figure 3-30**, the colonies below the transitional layer present a wide gap in the TF (moderate values) corresponding with non-preferential crystallographic orientation in the IPF map i.e. {101}. Those colonies cannot rotate to the appropriate slip systems.

Figure 3-30 Taylor factor map on samples at test condition



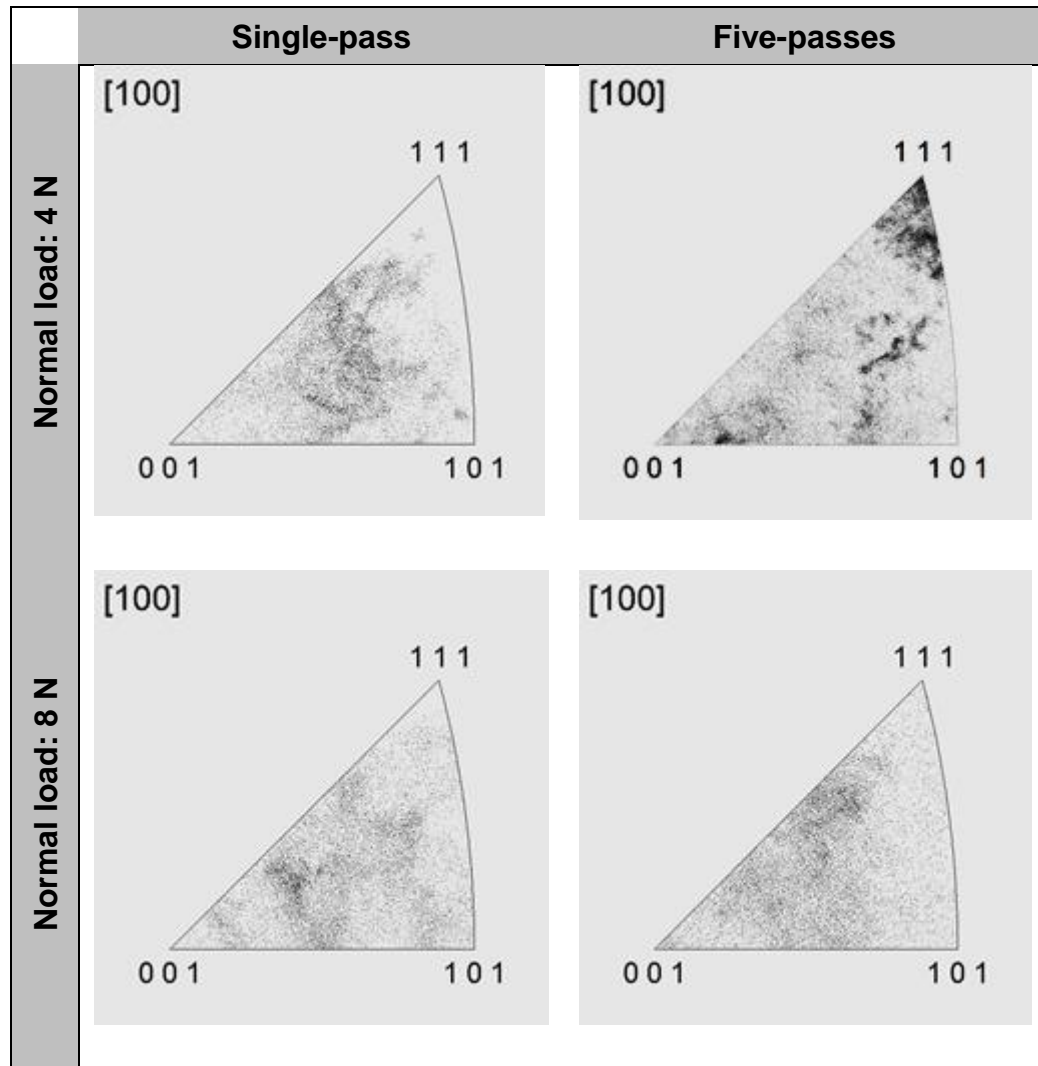
A final sample analysis using EBSD was performed changing the reference plane (i.e. normal direction) in the EBSD configuration (as described previously) evaluating the crystallographic orientation. SATOH and IWAFUCHI used this configuration in the analysis of texture formation in a rail after successive rolling contact. The authors reported a colony reorientation to TD // $\{111\}$, thereby referring a crystallographic texture (SATOH; IWAFUCHI, 2005). Those results suggest that those crystallographic plane results in small grains which become parallel to the running surface. The results obtained in this new analysis are shown in **Figure 3-31**. The microstructure orientation is shown using IPF + IQ for all samples. The **Figure 3-31a-c** show the colonies mainly oriented to TD // $\{123\}$, while in five-passes scratch samples a tendency in the distribution of colonies oriented to TD // $\{111\}$ was observed (**Figure 3-31b-d**).

Figure 3-31 IPF + IQ of specimen using TD as the reference plane



For the orientation frequency analysis, the region of transition (previously identified by KAM) was selected. In **Figure 3-32**, the colonies preferential orientation in this layer was confirmed. The sample tested at 4 N and five-passes scratch was the only showing the TD // {111} as a preferential. For the other samples, a heterogeneous distribution without a preferential orientation was observed.

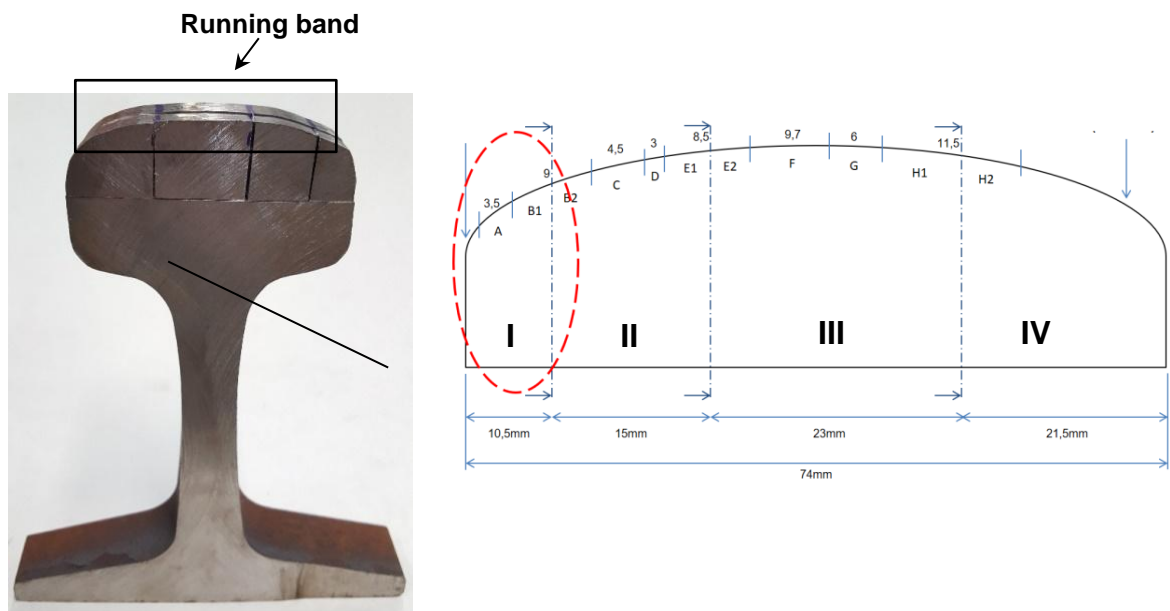
Figure 3-32 ODF (frequency) for samples tested at single and five-passes



3.4.2 RAIL GRINDING PROCEDURE: APPLIED MULTI-PASS SCRATCH TEST

Two grinding conditions were used in the analysis of WEL formation, characterized by the changing in the grinding speed (linear speed of the grinding vehicle) and the rate of material removal by the grinding stone power (i.e. contact pressure). **Figure 3-33** shows the rail profile (cross section photo) highlighting the area of interest (rail head). The rail head was divided in four strips (denominated I, II, III, IV) and shows in the schematic representation. In this work, only strip I was analyzed. The denomination of A to H2 corresponds to the facet obtained by the grinding disc pass. For this chapter, only the facets A and B1 were studied.

Figure 3-33. Rail cross-section image and the schematic representation of the strips in the rail head

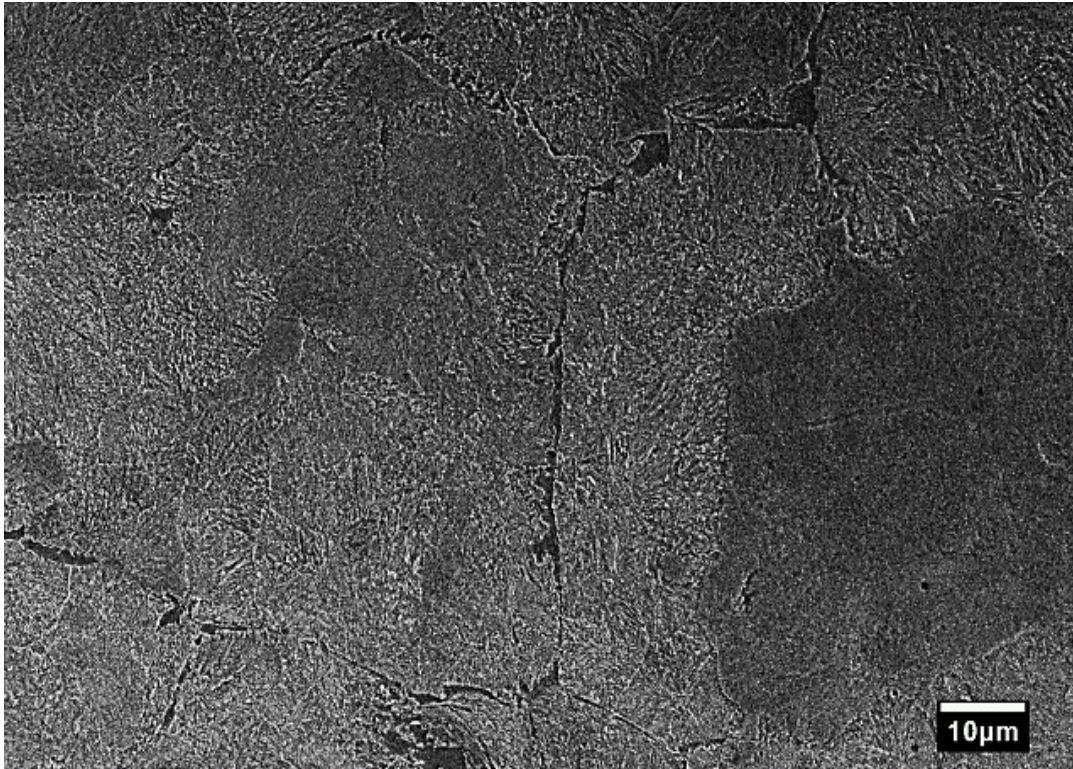


In this work, the interest was focused on the definition of WEL under an abrasive wear on macro-scale. The two grinding conditions allow the analysis of wear parameter in the microstructure transformation.

3.4.2.1 Microstructural Characterization

The rail microstructure consists in fine pearlite colonies (lamellae arrangement of cementite and ferrite) with a lamellar spacing of $0.15 \pm 0.02 \mu\text{m}$ as shown in **Figure 3-34**.

Figure 3-34. Secondary electron micrograph of the microstructure on the interior (bulk) of the pearlite rail



SIMON *et al.* showed that the running band of the rail is under different contact conditions resulting in a variation of surfaces and subsurface morphologies (SIMON *et al.*, 2013). A preliminary analysis was performed in the rail without grinding process and the results are shown as follows.

Figure 3-35 shows the microstructure analysis in the closely layer to the worn surface (red arrows). SEM images with different magnification were presented, highlighting a region with material detachment. In **Figure 3-35a** it was not easy to observe the sub-superficial layer formation i.e. the fine pearlite arrangement is predominant. In **Figure 3-35b**, two areas of interest denominated as A (in the detached material) and B (near to the worn surface) were selected.

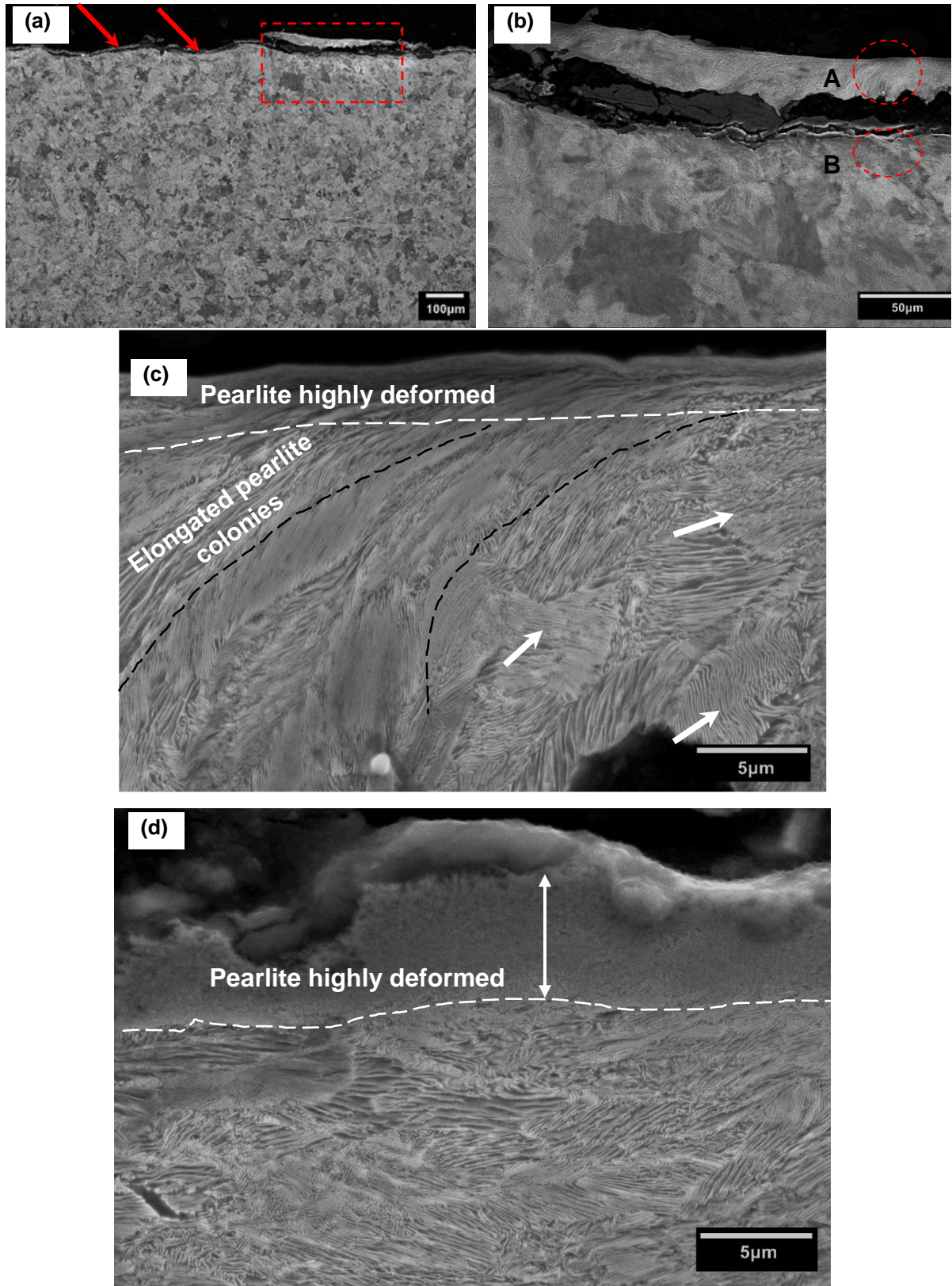
Figure 3-35c shows the formation of a layer characterized by high deformation (white dashed lines) in the topmost surface area. Two types of lamellar features can be observed: (i) the lamellar with multidirectional morphology, indicated by the white arrows; (ii) line lamellar with aligned-like and elongated colonies features, as indicated by the dashed black lines.

In pearlite colonies where structural faults such as curved lamellae can be observed, a certain density of Geometrically Necessary Dislocations (GND) is present to match the observed curvatures. In the case of a eutectoid microstructure strained by the accumulated wheel/rail contacts, those observations show that a misoriented area can be related to cementite lamellae deformation (DYLEWSKI; RISBET; BOUVIER, 2017).

Figure 3-35d corresponds to the section on the surface of the material and shows WEL formation in the nearest region to the surface delimited by the white dashed line. WEL formation is the microstructural phenomenon commonly recognized in the wheel-rail contact. Rolling contact fatigue (RCF) is the dominant damage mechanism in rails. High and repetitive external load, exceeding 1 GPa, leads to formation of surface microstructural alterations, surface crack formation and spallation. (CLAYTON, 1980; DANKS; CLAYTON, 1987; CLAYTON et al., 1999; ZAPATA; JARAMILLO; TORO, 2011).

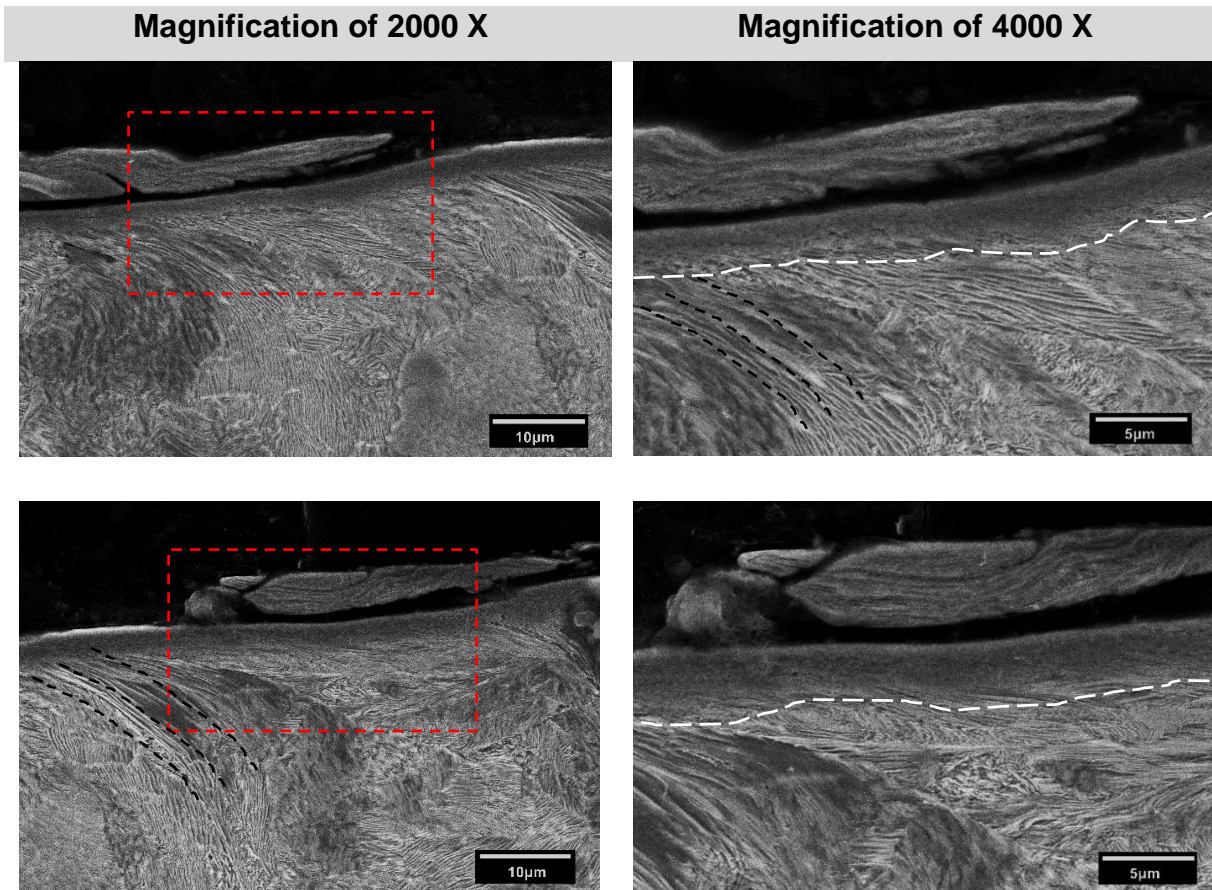
TAKAHASHI in a study about WEL formation in rails claimed the absence of severe plastic deformation in the studied rail, from the observation of unchanged cementite interlamellar distance in the rail surface pearlite and the absence of work-hardened pearlite zone beneath the WEL. A temperature increase in the contact zone wheel-rail was reported, which evidenced the martensitic phase transformation (TAKAHASHI; KAWAKAMI; UEDA, 2010).

Figure 3-35. SEM micrographs showing the microstructure (cross section) of a rail without grinding process in: a) region near to the worn surface, b) material detachment highlighted, c) area A of interest showing a pearlite highly deformed layer and d) area B of in interest



Material detachment and WEL formation were observed along the rail as shown in **Figure 3-36**. For all the analyzed regions it was observed the preferential pearlite colonies aligned in the layer closely to the WEL as indicated by the black lines in the SEM micrographs.

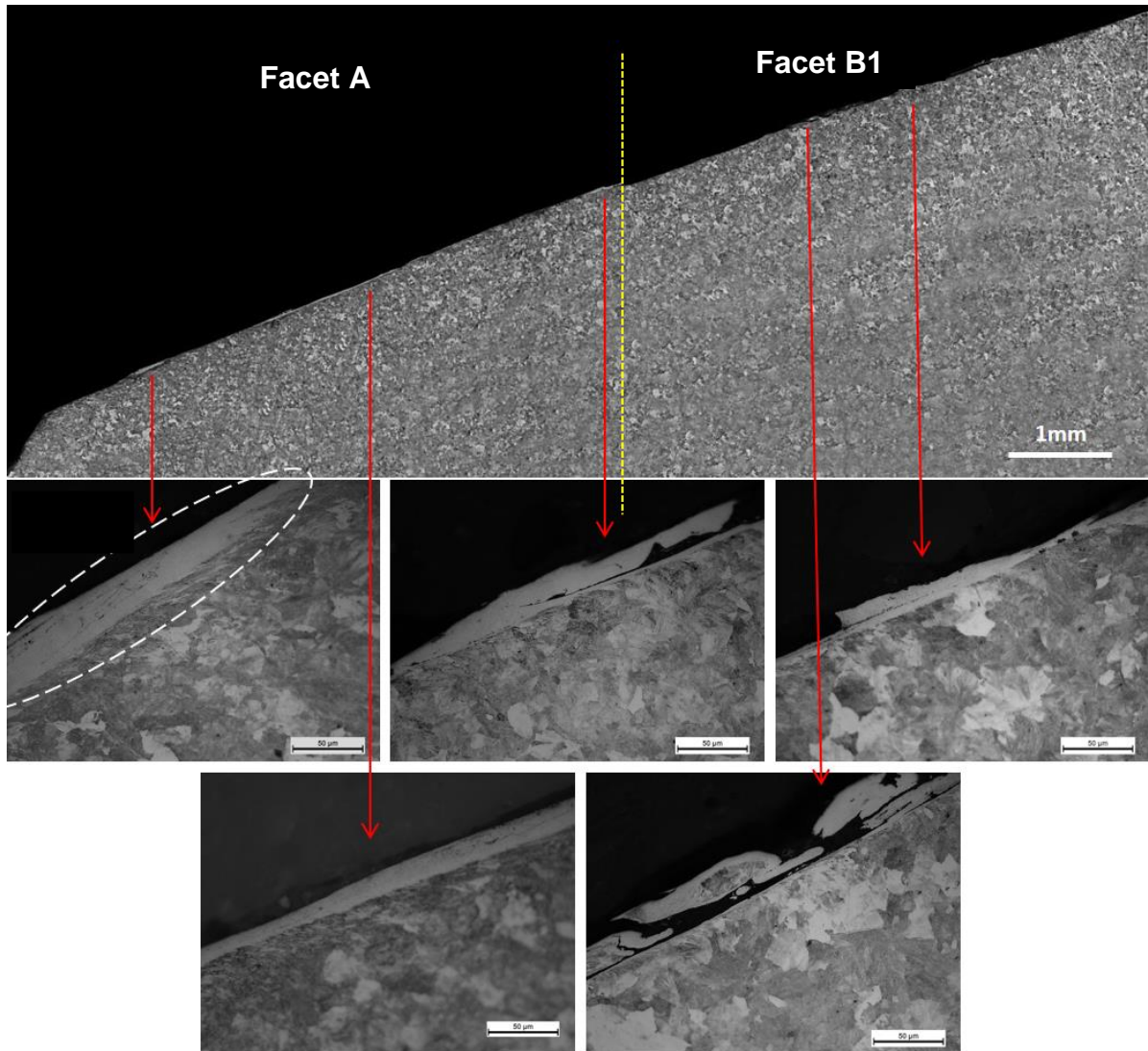
Figure 3-36. SEM micrographs of the rail showing in cross-section the regions with material detachment and WEL formation



3.4.2.2 Microstructural analysis after grinding process

Figure 3-37 shows the Optical Microscopy (MO) micrographs in a general view of the areas of interest. The two facets (A and B1) obtained after the grinding process were observed, corresponding to strip I (follow the **Figure 3-33**). Non-continuous WEL formation was observed along the facets. WEL is commonly recognized as a thin and hard layer, which appears white under light reflection (in OM) after being etched in 2–5% HNO₃ in ethanol (Nital etchant).

Figure 3-37. Optical Microscopy micrographs (OM) from the strip I highlighting facets A and B1 of the rail



A detailed analysis of the microstructure was performed using higher magnification than obtained in OM. The comparison of the microstructure after grinding disc in the nearest region of worn surface is shown in **Figure 3-38-41**. Polished grooves were observed and identified by the white arrows.

Figure 3-38 shows two regions taken from the rail under the first grinding procedure. It was observed the formation of two layer beneath the surface, the white etching layer with a thickness of 30 µm and a severely deformed layer with a thickness of 8 µm. **Figure 3-38a** shows the material detachment and a crack propagation along the WEL (identified by the black arrow). **Figure 3-38b** shows a region with a thin and broken WEL with a severe deformed pearlite. According to SATO *et al.* Cracks initiate at the

surface and propagate along lines of plastic flow and stop within the plastically deformed material (SATO ANDERSON, P.M., RIGNEY, D.A., 1993).

Figure 3-38. Microstructure in cross-section of the facet A in the sample from the rail under the first grinding condition. a) SEM micrograph of a region with WEL formation and material detachment, b) FEG-SEM micrographs of the region with WEL formation and highly deformed microstructure

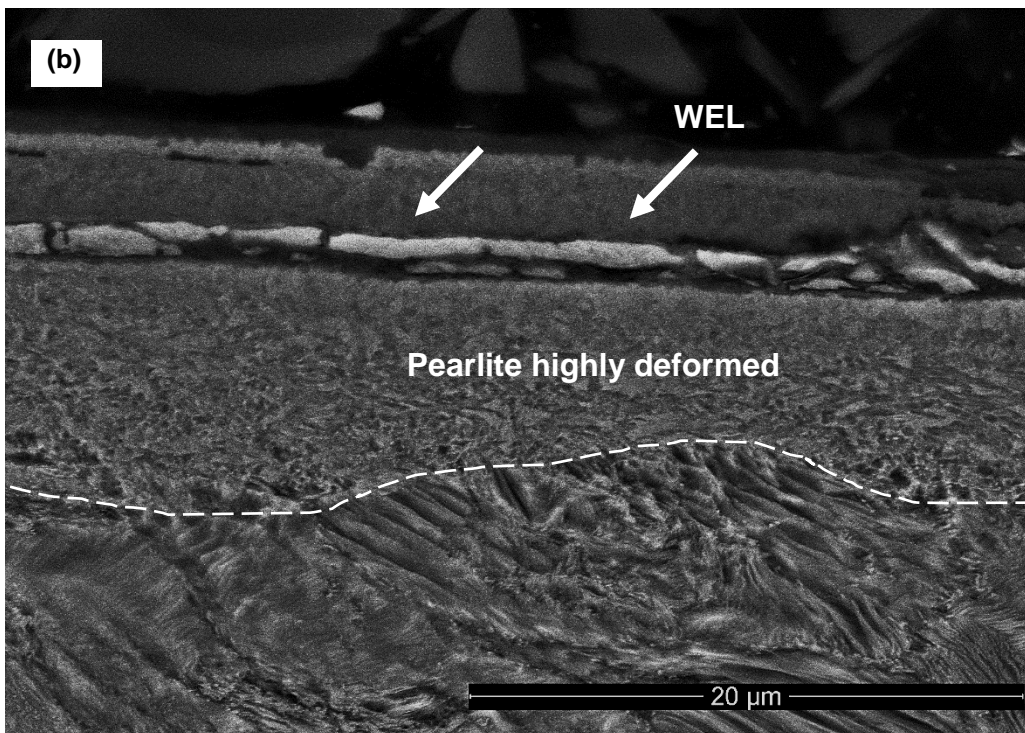
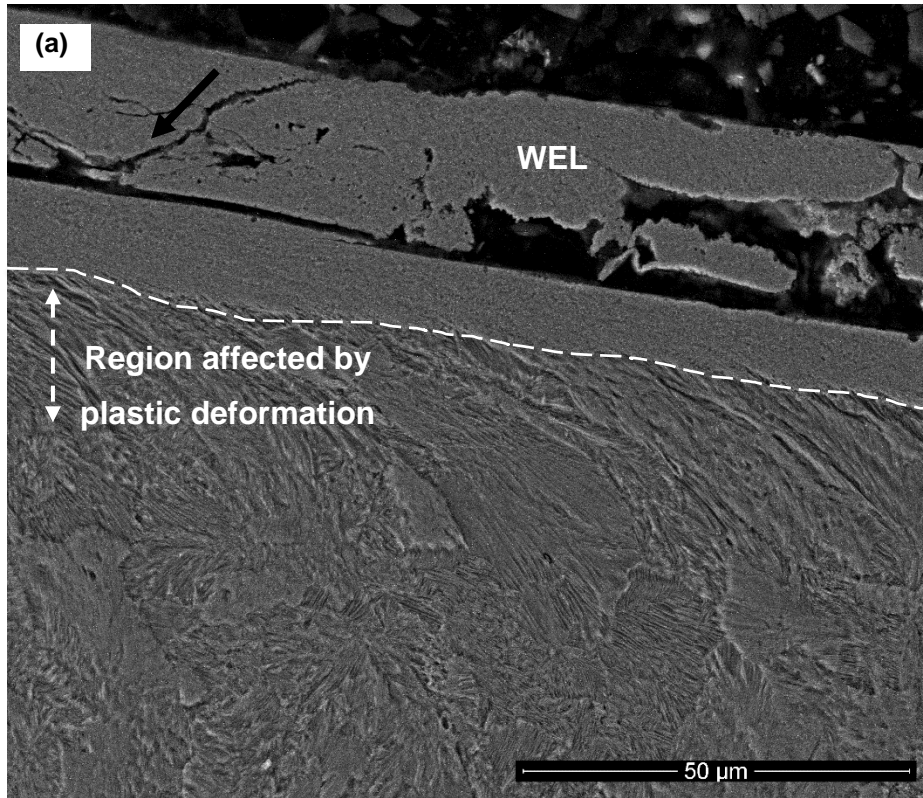
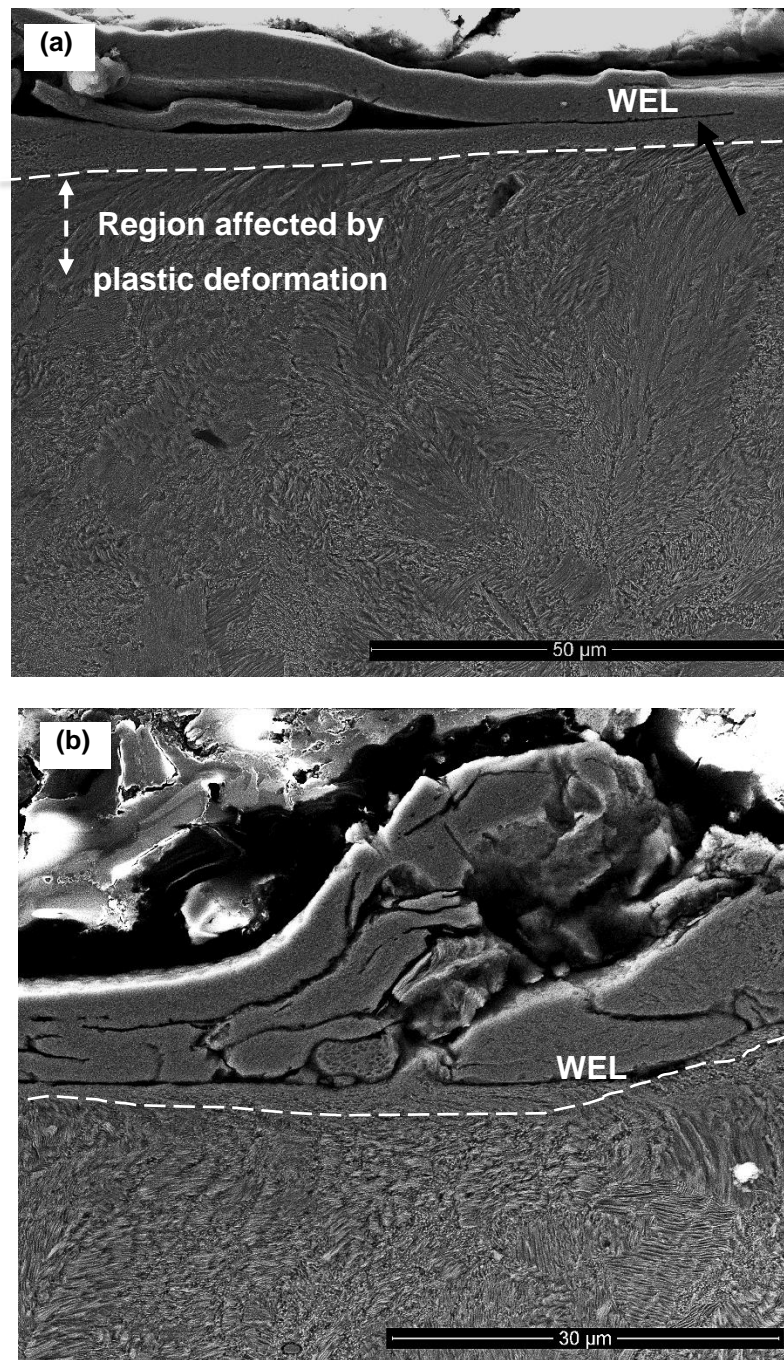


Figure 3-39 shows the microstructure of the closely layer of the surface in the facet A under the second grinding condition. It was identified the WEL formation with a thickness of 35 μm and a microstructure plastic deformation beneath the WEL with a thickness of 5 μm . It was also observed superficial cracks along the WEL in a parallel direction to the worn surface (black arrow in **Figure 3-39a**). **Figure 3-39b** shows massive cracks along the WEL.

Figure 3-39. Secondary electron micrograph of the microstructure (cross-section) in facet A from two regions showing the WEL formation and the deformed layer. The samples were taken from the rail under the second grinding condition



Erro! Fonte de referência não encontrada. shows the microstructure of the rail in the facet B1 under the first rail grinding condition. It was observed an affected region by the contact, characterized by the combination of WEL formation and pearlite severely deformed as indicated by the white arrow in Erro! Fonte de referência não encontrada. **a**. It was also identified an internal crack crossing along the WEL. This region has a thickness of 25 μm . Figure 3-40b shows a region plastically affected characterized by the formation of pearlite colonies with elongated cementite lamellae as indicated by the black box.

Figure 3-40. Secondary electron micrograph of the microstructure (cross-section) in facet B1 of the sample take from the rail under the first grinding condition

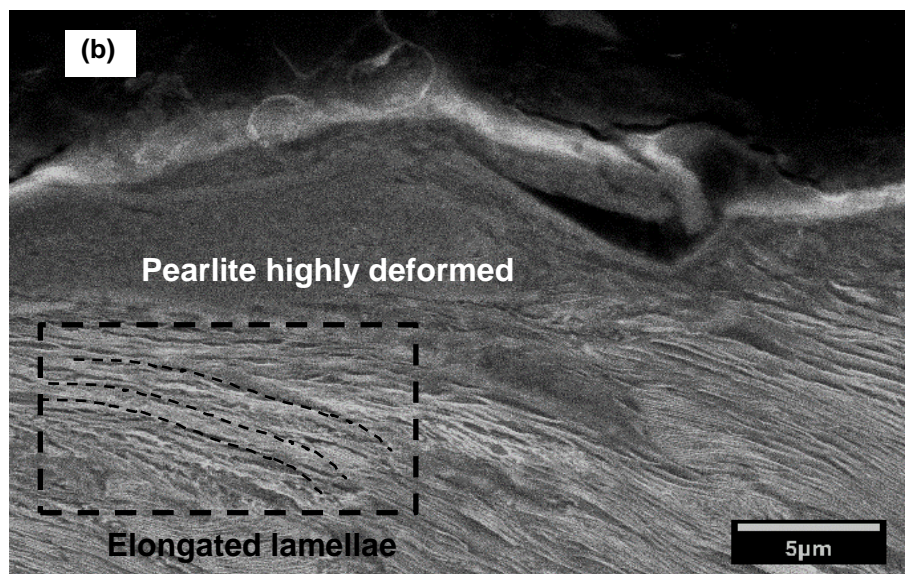
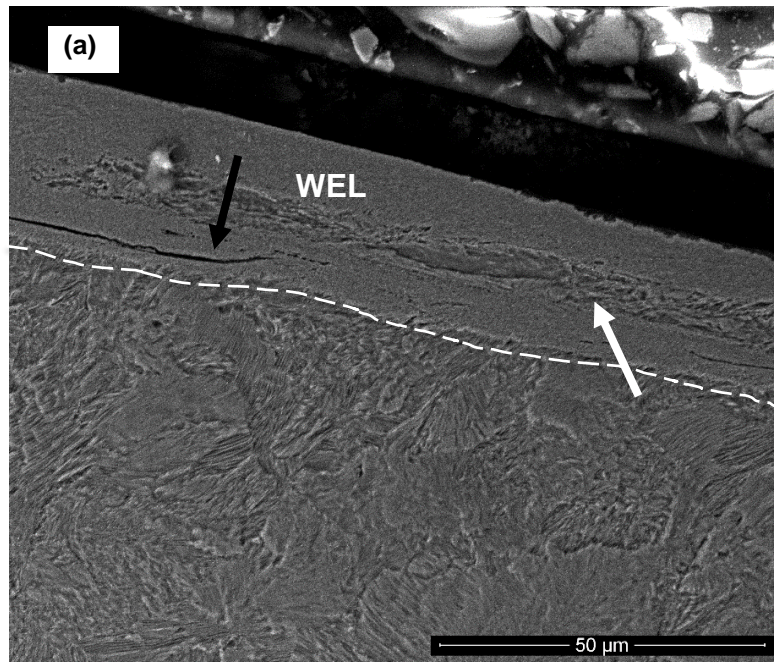
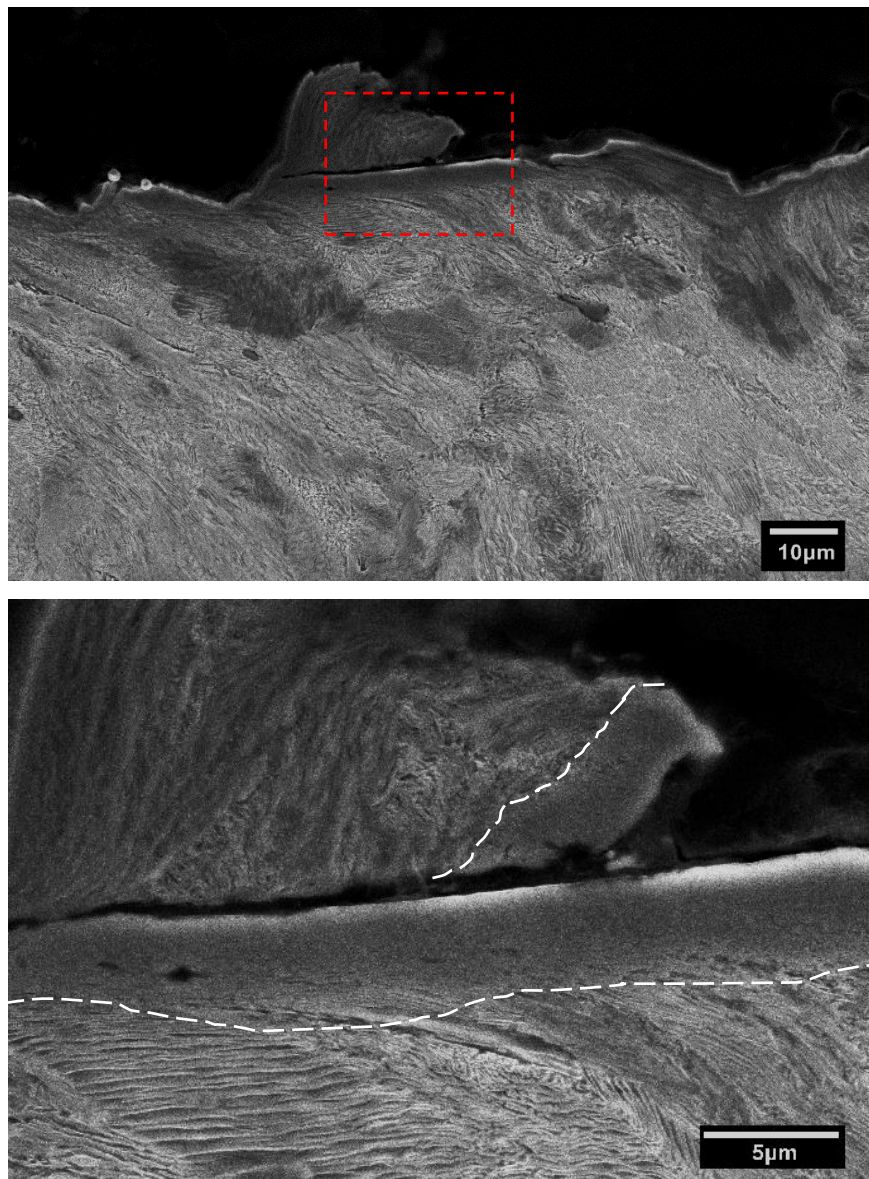


Figure 3-41. Secondary electron micrograph of the microstructure (cross-section) in facet B1 of the sample taken from the rail under the second grinding condition



A continuous and thin WEL formation was identified in the microstructure of both regions of interest (rail surface and detached material). Randomly oriented pearlite colonies were observed below the thin WEL.

KALOUSEK *et al.* after TEM examination of worn surfaces shows microstructural micrograph with a considerable refinement of the interlamellar spacing and a formation of very fine polycrystalline ferrite grains. Diffraction patterns show that a strong possibility of texture formation exists (KALOUSEK; FEGREDO; LAUFER, 1985). The results shown in this analysis are in concordance with the discussion promoted by

DYLEWSKI *et al.* in the tridimensional analysis of the microstructure in worn rails (DYLEWSKI; RISBET; BOUVIER, 2017).

3.4.2.3 Crystallography orientation using EBSD

The EBSD analysis was performed according to the decomposition of the rolling band into transversal strips (**Figure 3-33**). The analysis on rail samples was performed in Rolling Direction (RD). In order to generate orientation maps, a step size of 0.15 μm has been chosen, which is lower than the interlamellar spacing of 0.3–0.35 μm . Only the ferrite phase (body centered cubic system) has been indexed by the analysis. Cementite lamellae can be located by image quality indexation as cementite has a different crystallographic structure (orthorhombic system). In order to analyze crystallography and pearlitic microstructure evolution at the same time, maps showing the crystal direction orientation (IPF) in color and image quality (IQ) in grey scale have been studied.

SEM observations of the microstructure below the worn rail surface have confirmed that the pearlitic microstructure was affected by the grinding process. Elongated and fine pearlite colonies aligned in the rolling direction were observed.

Figure 3-42-43 show facets A and B1 of samples taken from the rail after first grinding disc pass, respectively. A Secondary Electron micrograph was taken from the cross-section microstructure showing the pearlite morphology. Surface cracks initiate and propagate along the oriented lamellar structure. Patches of White Etching Layer (WEL) in which no lamellae can be distinguished have also been observed. Below the rail surface (nearest layer to the worn surface) was not identified the microstructure features due to the microstructure breaking down into smaller grains than the resolution of EBSD method can be analyze or as results of the reduction in band contrast and indexing proportion by severe deformation as discussed by (MEYERS *et al.*, 2003; GEE; MINGARD; ROEBUCK, 2009). The scan in the deeper layer shows both high and low misoriented points corresponding to severely deformed microstructure with a different crystallographic orientation.

The influence of the combination of grinding speed and engine power applied in the grinding disc in the microstructure behavior was established. The sample taken from a

rail with higher linear speed (**Figure 3-43**) shows a higher deformation (below the WEL), representing in a less randomized orientation than samples taken from the first condition (lower grinding speed and higher normal force applied).

In laboratory tests the number of passes show severe deformation below the contact zone. The reduction of the grinding speed results in a higher number of passes of the grinding disc in the same facet. DYLEWSKI *et al.* shows the accumulation in the relationship between the severe plastic strain and the microstructure evolution. In severe condition of contact in the running band, the lamellae are aligned below the rail surface in the direction of shear where severe deformation and fracture of perlite microstructure are found (DYLEWSKI; RISBET; BOUVIER, 2017).

Figure 3-42. EBSD micrographs of the facet A of the sample take from the rail under the first grinding condition

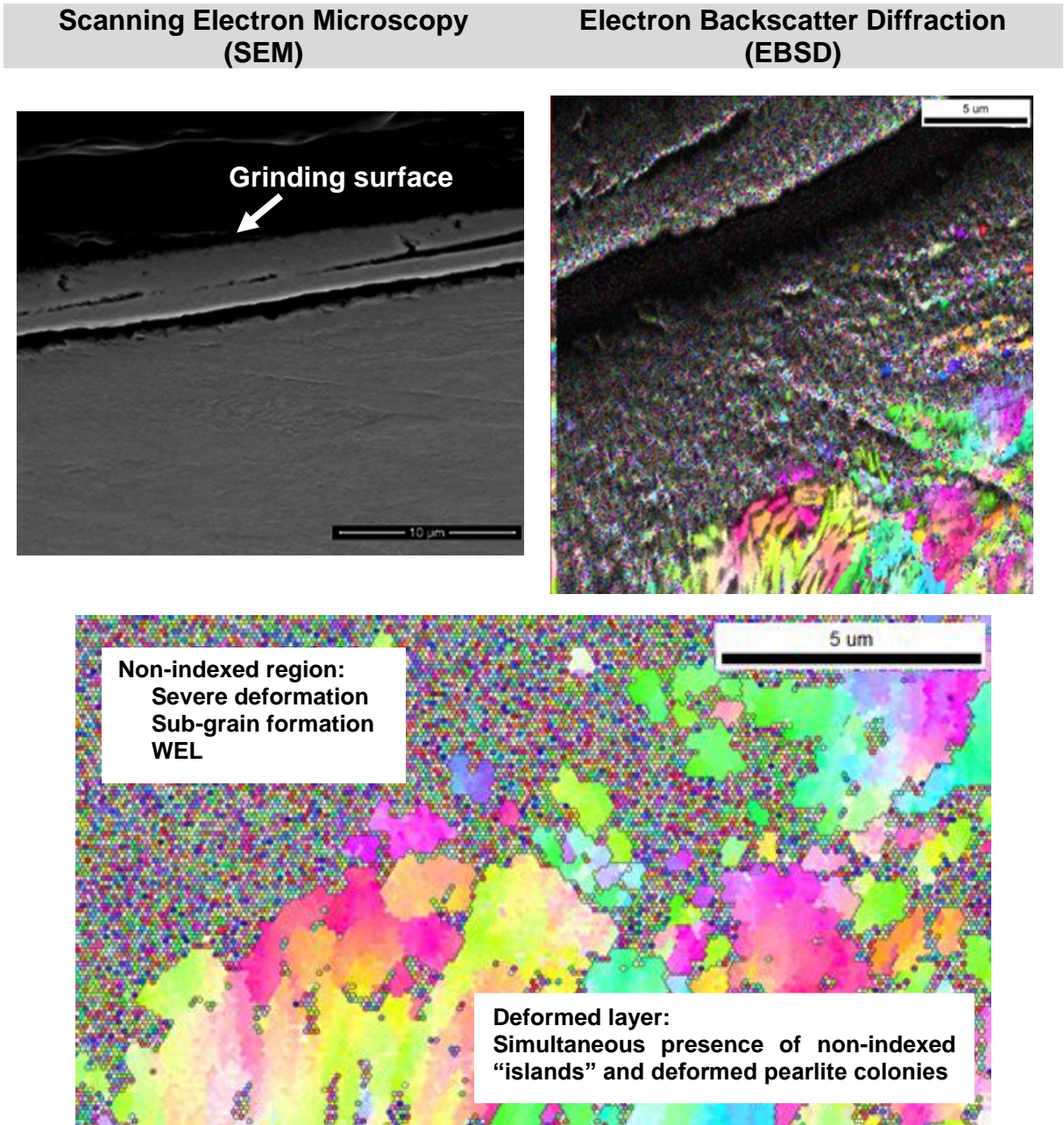
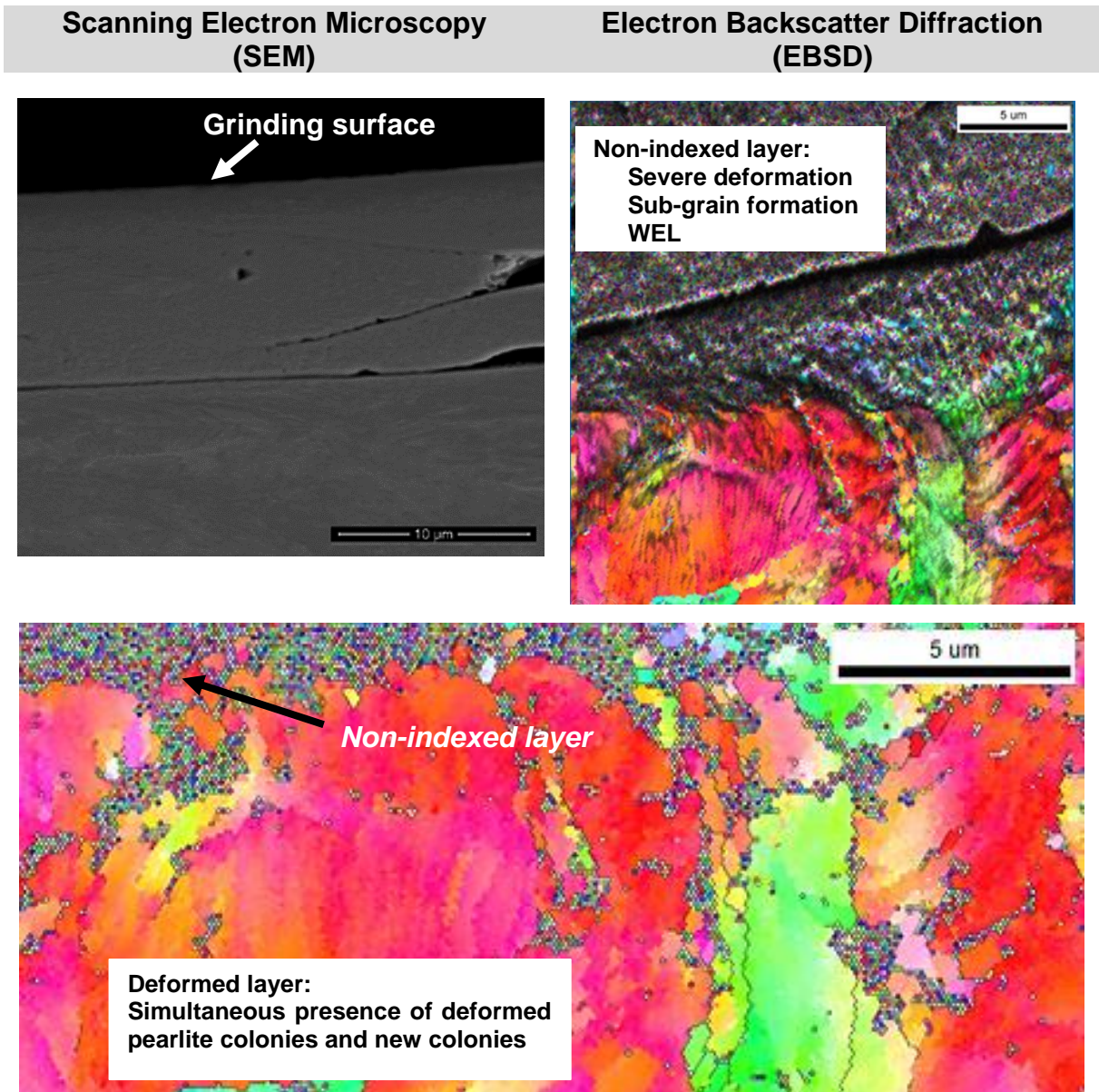


Figure 3-43. EBSD micrographs of the facet B of the sample taken from the rail under the first grinding condition



3.5 CONCLUSION

In this work, the influence of the scratch test (as a controlled abrasive wear) in the deformed layer formation was analyzed. The effect of successive indenter passes on the surface of the multiple deformed layers below the contact zone was studied.

Once defining the rail grinding as a multi-scale scratch test and classifying it as abrasion wear, a comparison of the laboratory results with the influence of rail grinding conditions in the pearlite colonies deformation was carried out.

The conclusions of this study are presented as follows:

Friction Coefficient

- The COF was not sensitive at the test wear conditions in terms of number of passes, showing a slight difference in the average values. In macro scale, statistically significant differences in COF were not determined by the pass conditions. In macro scale a small difference was observed after the first indenter pass, corresponding to 7% higher compared to the subsequent indenter passes.

Work-hardening

- The influence of material work hardening after the first pass cannot be ignored, since the behavior of samples tested in macro scale was similar regardless of the normal load applied.

Microstructure beneath the worn surface

- The microstructure beneath scratch region is characterized by the reduction of the grain size followed by the plastic deformation promoting the lattice distortion and a high density of dislocations in a region at 15 μm from the worn surface for the samples with severely scratch conditions.
- Both factors in the scratch test, the applied normal load and the number of passes increases the thickness of the sub-surface layer thickness affecting especially the transitional layer.
- The prior wear process to the rail grinding promotes the non-continuous WEL formation characterized by two types of lamellar features which can be observed: (i) the lamellar with multidirectional morphology and (ii) line lamellar with aligned-like and elongated colonies features.

- The rail grinding procedure promotes the non-continuous WEL formation and a plastic deformation in the layer below them characterized by pearlite colonies aligned-like and elongated. Grinding speed has influence in the superficial roughness (not discussed in this thesis); while the load applied in the procedure affect the material removal rate.
- The crack formation was identified and initiate at the surface and propagate along lines of plastic flow, rather than normal to the local direction of maximum tensile stress.

Crystallographic orientation

- Deformation resistance of pearlite colonies was clearly dependent on their crystallographic orientations (anisotropic effect). The microstructure observed in the transition regions seems to act as a barrier to the propagation of plastic deformation due to normal load or to the increase in the number of passes.
- The relationship between crystal orientation as presented in IPF, KAM and the TF map require a detailed study. The presumption of colonies undeformed and oriented preferentially at the slip system was not clarified in this work.
- Crystallographic texture can be found in samples tested with the lower normal load (4 N) and its relationship with the number of passes was determined as a function of the reference plane selected. Using the traditional microscopy arrangement (RD) crystallographic texture was found in the less severe condition of passes, while in the TD as a reference plane, a high concentration of pearlite colonies oriented at $\langle 111 \rangle$ was determined.
- The combination of low grinding speed and high load promotes a higher deformed layer formation beneath the patch zone. This configuration produces a less randomized orientation of the pearlite colonies

3.6 REFERENCES

BAKSHI, S.; SHIPWAY, P. H.; BHADESHIA, H.K.D.H. Three-body abrasive wear of fine pearlite, nanostructured bainite and martensite. *Wear*, v. 308, n. 2013, p. 46–53, 2013.

CHEN, H.; ZHANG, C.; LIU, W.; LI, Q.; CHEN, H.; YANG, Z. G.; WENG, Y. Microstructure evolution of a hypereutectoid pearlite steel under rolling-sliding contact loading. *Materials Science and Engineering A*, v. A655, p. 50–59, 2016.

CLAYTON, P. The relations between wear behaviour and basic material properties for pearlitic steels. *Wear*, v. 60, n. 1, Apr. 1980, p. 75–93, 1980.

CLAYTON, P.; SAWLEY, K. J.; BOLTON, P. J.; PELL, G. M. Wear behavior of Bainitic steels. *Wear*, v. 120, n. 1987, p. 199–220, 1999.

DA SILVA, W. M.; COSTA, H. L.; DE MELLO, J. D. B. Transitions in abrasive wear mechanisms: Effect of the superimposition of interactions. *Wear*, v. 271, n. 5–6, p. 977–986, 2011.

DA SILVA, W. M.; DE MELLO, J. D. B. Using parallel scratches to simulate abrasive wear. *Wear*, v. 267, n. 11, p. 1987–1997, 2009.

DANKS, D.; CLAYTON, P. Comparison of the wear process for euctoid steels: field and laboratory tests. *Wear*, v. 120, p. 233–250, 1987.

DELANNAY, L.; JACQUES, P. J.; KALIDINDI, S. R. Finite element modeling of crystal plasticity with grains shaped as truncated octahedrons. *International Journal of Plasticity*, v. 22, n. 10, p. 1879–1898, 2006.

DYLEWSKI, B.; RISBET, M.; BOUVIER, S. The tridimensional gradient of microstructure in worn rails – Experimental characterization of plastic deformation accumulated by RCF. *Wear*, v. 392–393, n. July 2016, p. 50–59, 2017.

FACCO, G. G. Exploring Linear Rake Machining in 316L Austenitic Stainless Steel for Microstructure Scale-Refinement, Grain Boundary Engineering, and Surface Modification. 2013. University of Pittsburg, 2013.

FARGAS, G.; ROA, J. J.; MATEO, A. Influence of pre-existing martensite on the wear resistance of metastable austenitic stainless steels. *Wear*, v. 364, p. 40–47, 2016.

FRANCO, L. A. *Abrasão de ferro fundido cinzento: Aplicação a motores automotivos*. 2015. Tese de doutorado da Escola Politécnica da Universidad de São Paulo, Departamento de Mecânica, 2015.

GEE, M.; MINGARD, K.; ROEBUCK, B. Application of EBSD to the evaluation of plastic deformation in the mechanical testing of WC/Co hardmetal. *International Journal of Refractory Metals and Hard Materials*, v. 27, n. 2, p. 300–312, 2009.

HUMPHREYS, F. J.; M. HATHERLY. Chapter 3. In: *Recrystallization and Related Annealing Phenomena*. p. 67–89, 2004.

KALOUSEK, J.; FEGREDO, D. M.; LAUFER, E. E. The wear resistance and worn metallography of pearlite, bainite and tempered martensite rail steel microstructures of high hardness. *Wear*, v. 105, n. 3, p. 199–222, 1985.

KATO, K. Wear mode transitions. *Scripta Metallurgica*, v. 24, n. c, p. 815–820, 1990.

KOCKS, U. F.; MECKING, H. Physics and phenomenology of strain hardening: The FCC case. *Progress in Materials Science*, v. 48, n. 3, p. 171–273, 2003.

LI, H.; HSU, E.; SZPUNAR, J.; UTSUNOMIYA, H.; SAKAI, T. Deformation mechanism and texture and microstructure evolution during high-speed rolling of AZ31B Mg sheets. *Journal of Materials Science*, v. 43, n. 22, p. 7148–7156, 2008.

LI, Q.; HUANG, X.; HUANG, W. Strain hardening behavior and deformation characteristics of multiphase microstructure in a medium-carbon quenching and partitioning bainitic steel. *Materials Science and Engineering: A*, v. 707, n. 24, p. 199–206, 2017.

LIU, M.; YANG, C. D.; CAO, G. H.; RUSSELL, A. M.; LIU, Y. H.; DONG, X. M.; ZHANG, Z. H. Effect of microstructure and crystallography on sulfide stress cracking in API-5CT-C110 casing steel. *Materials Science and Engineering A*, v. 671, p. 244–253, 2016.

MEYERS, M. A.; XU, Y. B.; XUE, Q.; PÉREZ-PRADO, M. T.; MCNELLEY, T. R. Microstructural evolution in adiabatic shear localization in stainless steel. *Acta Materialia*, v. 51, n. 5, p. 1307–1325, 2003.

OKOLO, B.; PÉREZ-WILLARD, F.; HAWECKER, J.; GERTHSEN, D.; WANNER, A. Focused ion beam study of the effects of shot peening on the subsurface microstructure of normalized pearlitic steel. *Journal of Materials Processing Technology*, v. 183, n. 2–3, p. 160–164, 2007.

PARK, H.-K.; KIM, S.-J.; HAN, H. N.; HAN, C.-H.; HWANG, N.-M. Deformation Feature of Goss Grains in Fe-3%Si Steel Focused on Stored Energy after Cold Rolling. *Materials Transactions*, v. 51, n. 9, p. 1547–1552, 2010.

PEREIRA, J. I.; MACHADO, P. C.; PENAGOS, J. J.; SINATORA, A. Wear characterization from field and laboratory tests of pearlitic steels used for SAG mill liners. *Wear*, v. 376–377, p. 37–45, 2017.

SARMA, G. B.; DAWSON, P. R. Effects of interactions among crystals on the inhomogeneous deformations of polycrystals. *Acta Materialia*, v. 44, n. 5, p. 1937–1953, 1996.

SATO, M.; ANDERSON, P.M.; RIGNEY, D.A., Rolling-sliding behaviour of rail steels. *Wear*, v. 162–164, p. 159–172, 1993.

SATOH, Y.; IWAFUCHI, K. Crystal orientation analysis of running surface of rail damaged by rolling contact. *Wear*, v. 258, n. 7–8, p. 1126–1134, 2005.

SHEN, J. H.; LI, Y. L.; WEI, Q. Statistic derivation of Taylor factors for polycrystalline metals with application to pure magnesium. *Materials Science and Engineering A*, v. 582, p. 270–275, 2013.

SIMON, S.; SAULOT, A.; DAYOT, C.; QUOST, X.; BERTHIER, Y. Tribological characterization of rail squat defects. *Wear*, v. 297, n. 1–2, p. 926–942, 2013.

STEENBERGEN, M. Rolling contact fatigue in relation to rail grinding. *Wear*, v. 356–357, p. 110–121, 2016.

STOUDT, M. R.; LEVINE, L. E.; CREUZIGER, A.; HUBBARD, J. B. The fundamental relationships between grain orientation, deformation-induced surface roughness and strain localization in an aluminum alloy. *Materials Science & Engineering A*, v. 530, p. 107–116, 2011.

TAKAHASHI, J.; KAWAKAMI, K.; UEDA, M. Atom probe tomography analysis of the white etching layer in a rail track surface. *Acta Materialia*, v. 58, n. 10, p. 3602–3612, 2010.

TAKAHASHI, T.; PONGE, D.; RAABE, D. Investigation of orientation gradients in pearlite in hypoeutectoid steel by use of orientation imaging microscopy. *Steel research international*, v. 78, n. 1, p. 38–44, 2007.

TAKAYAMA, Y.; SZPUNAR, J. a. Stored energy and Taylor factor relation in an Al-Mg-Mn alloy sheet worked by continuous cyclic bending. *Materials Transactions*, v. 45, n. 7, p. 2316–2325, 2004.

XU, L.; CLOUGH, S.; HOWARD, P.; STJOHN, D. Laboratory assessment of the effect of white layer on wear resistance for digger teeth. *Wear*, v. 183, n. 94, p. 112–117, 1995.

XU, X.; ZWAAG, S. Van Der; XU, W. A novel multi-pass dual-indenter scratch test to unravel abrasion damage formation in construction steels. *Wear*, v. 322–323, n. 2015, p. 51–60, 2015.

ZAPATA, D.; JARAMILLO, J.; TORO, A. Rolling contact and adhesive wear of bainitic and pearlitic steels in low load regime. *Wear*, v. 271, n. 1–2, p. 393–399, 2011.

ZHANG, H. W.; OHSAKI, S.; MITAO, S.; OHNUMA, M.; HONO, K. Microstructural investigation of white etching layer on pearlite steel rail. *Materials Science and Engineering A*, v. 421, p. 191–199, 2006.

4- ANALYSIS OF THE ROLLING CONTACT FATIGUE (RCF) IN PEARLITIC STEEL UNDER CONDITIONS OF LABORATORY TEST (TWIN-DISC ROLLING CONTACT TRIBOMETER) AND FIELD (WHEEL)

4.1 ABSTRACT

On this chapter, it was analyzed the microstructural transformation in samples taken from a worn railway wheel and compared with the behavior in samples tested in laboratory test under conditions of different number of cycles. The samples tested in the twin-disc tribometer were obtained from a pearlitic rail with hardness of 350 ± 10 HV₁₀. The microstructure deformation beneath the contact was highlighted as the main feature of the material response in both wear conditions. For all samples, the microstructural transformation was characterized by a formation of ultra-fine grains in the region close to the worn surface. A second layer beneath the severe deformation layer is characterized by an interlamellar spacing reduction and elongated pearlite colonies. The work-hardening in both conditions was expressive, being identified an increment of the micro-hardness as a function of the distance with surface. In both conditions the first 100 μ m from the surface suffer the most severe increase of the values, up to 800 HV_{0.1} in samples tested in laboratory and a hardness up to 500 HV_{0.1} in the railway wheel. It was determined the RD // <111> as the main crystallographic orientation in the most severe deformed layer and a randomized orientation in the transitional layer. It was not found a microstructural transformation like austenitic or martensitic formation.

4.2 INTRODUCTION

Railway wheels and rails operate under conditions which generate plastic deformation, rolling contact fatigue with a range sliding and sliding wear at the tribological interface. Investigation of the behavior of wheel/rail materials under different work conditions has been carried out using different equipment configurations such as: full scale, wheel and plate, pin-on-disc and twin-disc rigs.

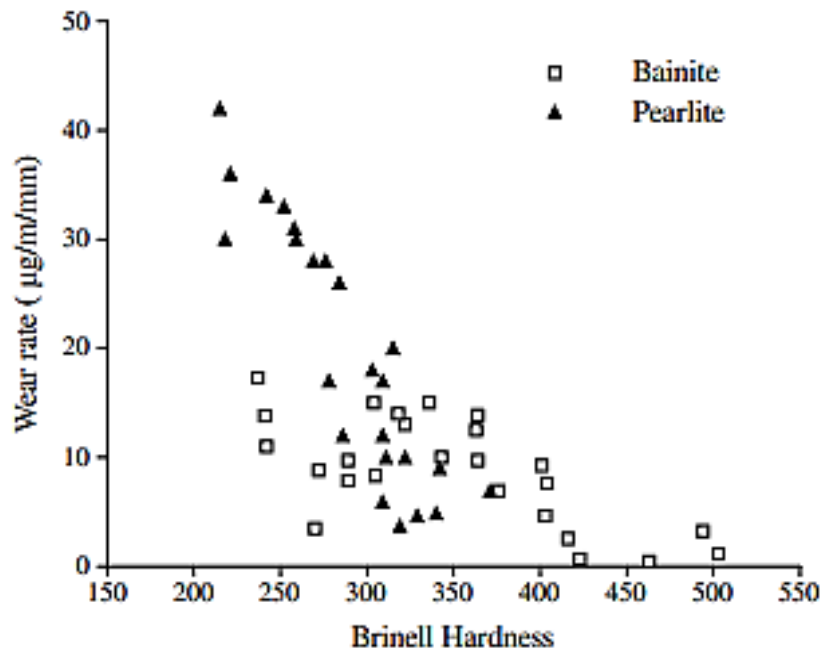
Full scale experiments were performed to evaluate the mechanical and thermal effects in zones under railway flats along the rail (AHLSTROM,1999). Testing using pin-on-disc set up has been carried out in order to understand of the influence of leaves on

adhesion, in full sliding conditions, rather than the rolling-sliding found in a wheel/rail contact (OLOFSSON, 2004).

Once the rolling contact fatigue is of major concern in wheels and rails (BOLTON; CLAYTON, 1984; SADEGHI et al., 2009) the use of twin-disc tribometer to evaluate wheel and rail materials (BEYNON; GARNHAM; SAWLEY, 1996; SATO, M.; ANDERSON, P.M.; RIGNEY, D.A., 1993; ZHU et al., 2018), lubricants (CHEN et al., 2014; L'HOSTIS et al., 2017; PALADUGU; LUCAS; SCOTT HYDE, 2018; ZHU; LYU; OLOFSSON, 2015) and creepage (MAKINO; KATO; HIRAKAWA, 2012; OLOFSSON et al., 2013; ZHU et al., 2018) for instance.

In pure sliding and severe rolling/sliding conditions the improvement in wear resistance with increasing hardness for pearlitic steels is much greater than that for the bainitic steels (CLAYTON; TIN, 1996). **Figure 4-1** shows the strong dependency of the rolling/sliding wear resistance with the bulk hardness in pearlite microstructure, whereas in the case of bainite the wear resistance has a less intense dependence on the hardness.

Figure 4-1 Rolling/sliding wear rate of a few pearlitic and bainitic steels with varying hardness



Adapted from (CLAYTON; TIN, 1996)

For pearlitic rails the increase in wear resistance in twin-disc tests is also perceived in heavy haul, rails there is an increase of high carbon, high hardness rails as stated for

instance at the AAR rail designation (IHHA, 2015). The same effect of increase rolling/sliding wear resistance is also recognized in the wheels. **Table 4-1** shows that class D of pearlitic wheels are harder than the older class C ones. The practical consequence is greater performance of the class D wheels over the class C ones (FREITAS, 2015; THIAGO GOMES VIANA, 2015).

Table 4-1 Steel grade specified by AAR

Specification	Steel grade	Carbon content (%)	Hardness HB
ARR M-107/M-208	Class L	≤ 0.47	197 – 277
	Class A	0.47 – 0.57	255 – 321
	Class B	0.57 – 0.67	302 – 341
	Class C	0.67 – 0.77	321 – 363
	Class D		341 – 415

From (AAR, 2007)

This chapter proceeds with the comparison between the microstructure formation in the subsurface of samples tested using twin-disc machine and in samples taken from areal wheel after the natural wear, in order to obtain a deep understanding of the phenomena involved.

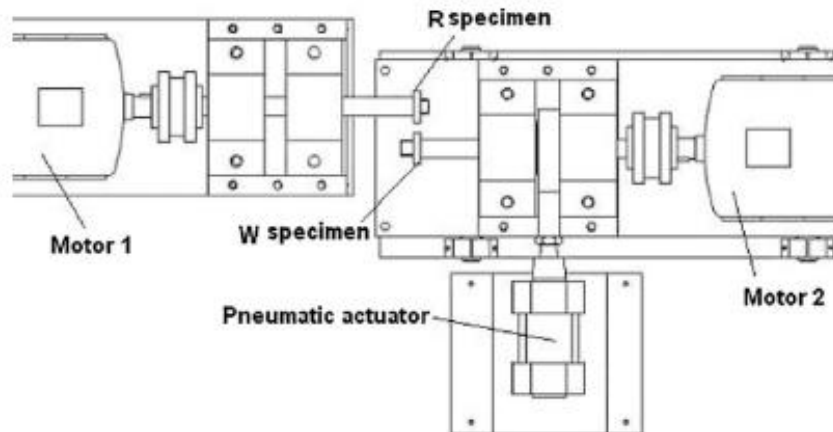
4.3 EXPERIMENTAL PROCEDURE

4.3.1 MATERIALS AND SAMPLE PREPARATION

4.3.1.1 Laboratory test

The samples used in this analysis were obtained from a pearlitic rail with hardness of $350 + 10 \text{ HV}_{10}$. The rolling contact fatigue test was carried out with the twin-disc rolling contact tribometer (**Figure 4-2**). The tester consists of two independent electric motors that control the rotating speeds of two pivoted driving shafts. The slip ratio can be controlled by adjusting the rotational speed of the shafts. Both the wheel and the rail specimens have the same size and shape, and the sizes of the outer diameter and thickness. The initial load was applied while the rail and the wheel specimens were arranged to maintain in line contact, and the rotating velocity of the rail and wheel specimens was adjusted to reach the target slip ratio.

Figure 4-2 Schematics diagram of the twin-disc tribometer



From (ZAPATA; JARAMILLO; TORO, 2011)

Tests conditions

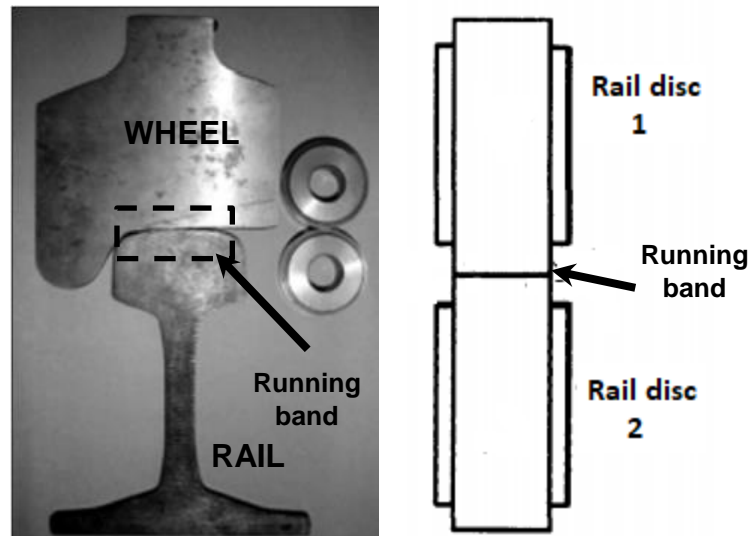
The samples were tested using a nominal disc rotational speed of 400 rpm and a contact pressure of 1.1 GPa. Tests were carried out at slip value of 1 % with a number of cycles between 25.000 to 650.000.

In the conventional arrangement the mounting of the specimen follows the denomination W (wheel) and R (rail). In this case all the specimens were taken from the same sample (rail) and the denomination W and R was used for identification of the samples. Two samples were selected for the analysis corresponding to the opposite conditions (in terms of number of cycles). The sample from the less severe conditions (25.0000 cycles) was denominated as W4 (W: sample correspond to the driving disc and the number 4 correspond to the number of sample). For the most severe conditions (650.000 cycles), the sample W9 was selected. The running band (surface in contact between the two disc) corresponded to a two-flat surface.

4.3.1.2 Wheel-rail contact

Figure 4-3 shows the wheel used in the sample preparation. The analysis was performed in the running band which reported severe plastic deformation and microstructural alteration (indicated by the ditched box).

Figure 4-3 Image of the generic wheel-rail contact and the configuration in the twin-disc tribometer



4.3.2 ANALYSIS OF THE MICROSTRUCTURE BENEATH THE CONTACT ZONE

Microstructural analysis was used with Scanning Electron Microscopy - SEM with different levels of resolution. The FEG (FEI Quanta 450 FEG) and FIB/SEM (FEI - Quanta 3D FEG/FIB microscope) were used as the characterization tools.

The crystallographic orientation analysis was performed with Electron Backscatter Diffraction (EBSD) using IPF map and Taylor Factor (TF) tools in a FEI INSPECT 50 – EDAX microscopy.

Transmission Electron Microscopy was performed in the region close to the surface (in cross section) using a JEOL 3010 microscopy after FIB/SEM sample preparation as follow:

- Deposition of the Pt (2.4 nA – 5 kV)
- Opening of the cavities (30 nA – 30 kV)
- Cleaning/reduction of the lamella (5 nA - 30 kV, 3 nA – 30 kV)
- Fixation of the lamella in the Omniprobe equipment

4.4 RESULTS AND DISCUSSION

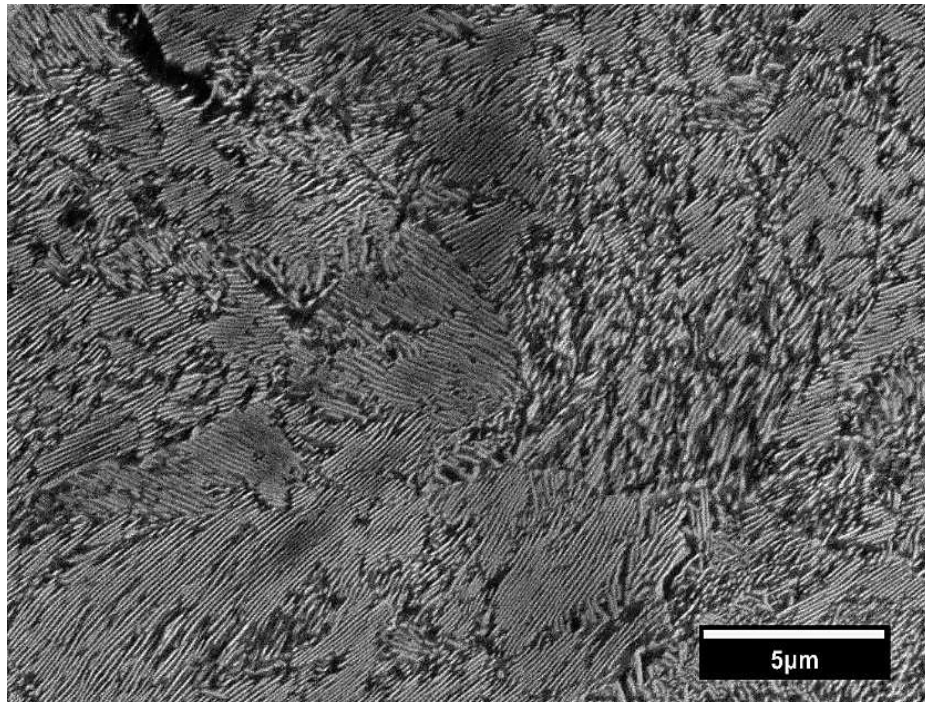
4.4.1 TWIN-DISC ROLLING CONTACT TRIBOMETER

The analysis of the microstructural and surface transformation was carried out in the samples W4 and W9 corresponding with the specimens under 25.000 cycles and 650.000 cycles. The denomination W was used to indicate the position in the tribometer.

4.4.1.1 Microstructural Characterization

Figure 4-4 shows a microstructure of the samples in an undeformed region, characterized by lamellar arrangement of ferrite and cementite, corresponding to a pearlite. A fine interlamellar spacing of $0.14 \pm 0.01 \mu\text{m}$ was measured.

Figure 4-4 A secondary electron SEM image of the undeformed pearlitic microstructure



4.4.1.2 Characterization of the worn surface

Figure 4-5 shows the three regions analyzed from the W4 specimen (25000 cycles). The first image corresponds to the original surface (before tests), showing a surface characterized by the presence of grooves as result of the grinding process (surface preparation). **Figure 4-5b** shows a region located in the transition zone of the contact zone and the original surface. The formation of spalling as RCF defects was observed.

Finally, the worn surface (**Figure 4-5c**) shows large thin metallic flakes according to (BOLTON; CLAYTON, 1984) and can be classified as regime type II in rolling-sliding contact.

Figure 4-5 Secondary Electron micrographs of the W4 surface (25000 cycles). a) Area without contact between discs, b) transition area corresponding with the lateral zones of the contact and c) center of the worn surface

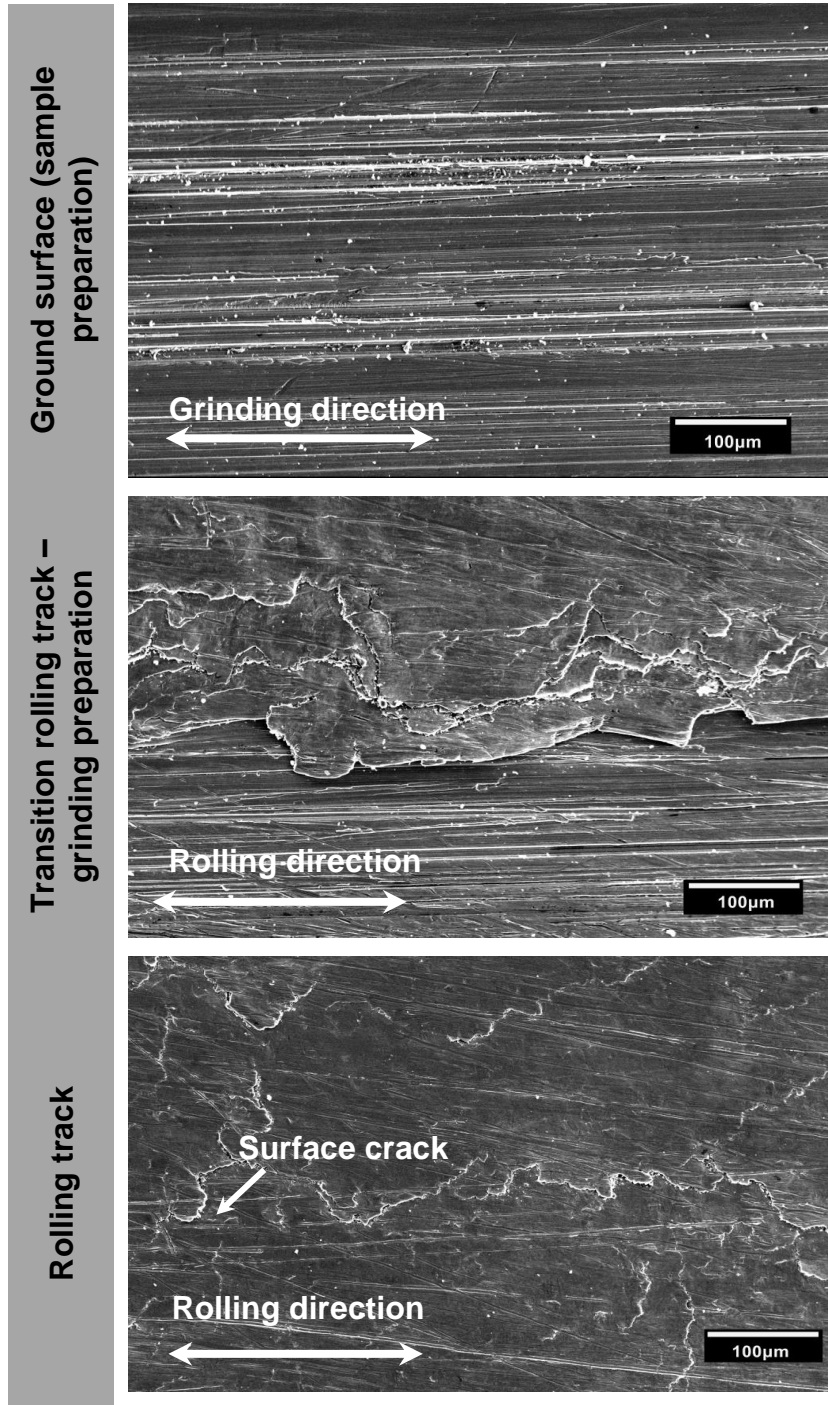
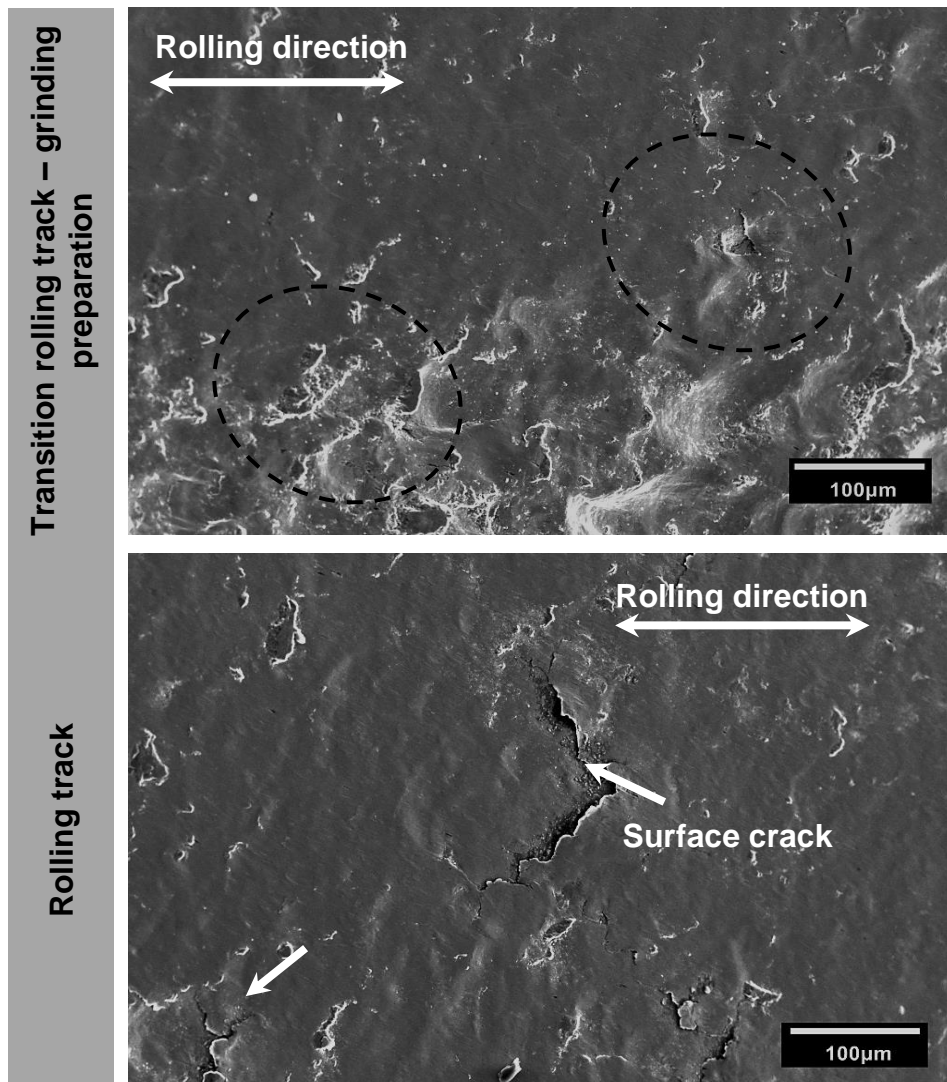


Figure 4-6 shows the surface of the W9 tested in the regions of the interface to rolling track and the grinding surface (sample preparation) and the rolling track. The formation of superficial fatigue cracks was identified, which promotes the spalling (RCF defect).

The surface cracks observed in W4 and W9 are in accordance with the severe wear regime (type III) which produces few cracks associated with manganese sulphide inclusions (BOLTON; CLAYTON, 1984; WANG et al., 2016). ZAPATA *et al.* reported in the analysis of the rolling contact and adhesive wear in low load regime that the ratchetting is the dominant wear micro-mechanism leading to surface fatigue, in samples tested with 2% creepage (ZAPATA; JARAMILLO; TORO, 2011).

Figure 4-6 SEM images of the worn surface from the W9 specimen (650000 cycles)



4.4.1.3 Microstructural characterization beneath the rolling contact

The analysis of the influence of the number of cycles in the behavior of the pearlitic steel under disc-disc contact requires of the study of the sub-superficial transformation (WEL formation) and the crystallographic orientation. In this section, the WEL formation analysis is presented.

4.4.1.3.1 Characterization by Scanning Electron Microscopy

Figure 4-7 shows the microstructure in cross-section of samples tested at 25.000 cycles (W4) using Optical Microscopy (OM). The surface crack observed in the SEM top micrographs was observed with more detail. The WEL formation is observed in the first 50 – 70 μm .

Figure 4-7 OM micrograph of the microstructure in cross section of specimen W4

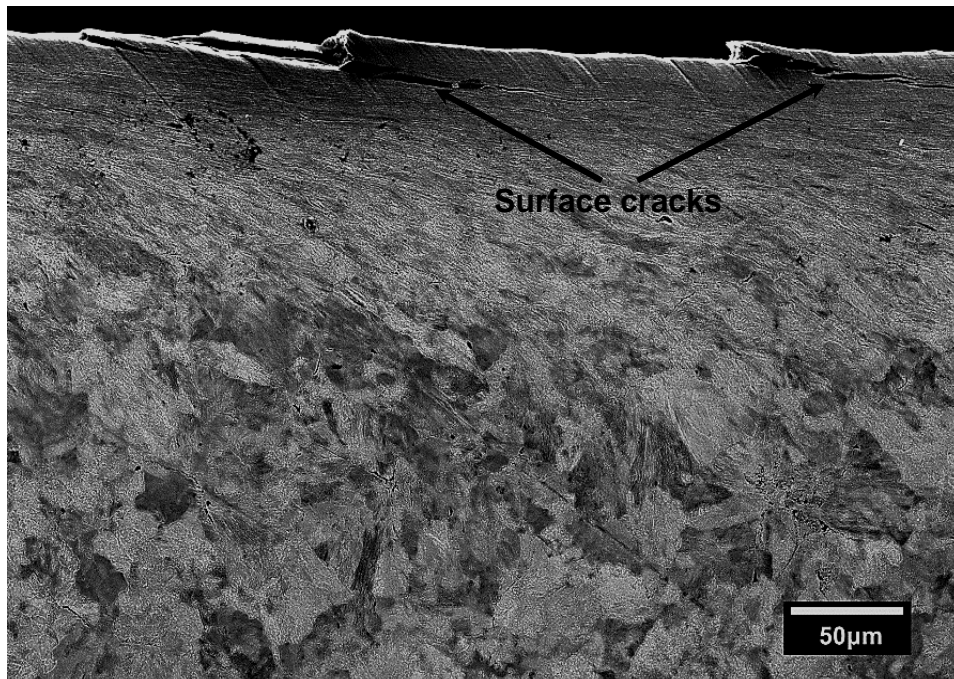


Figure 4-8 shows the microstructure of W4 using a higher resolution than OM. The SEM allows the observation in the nearest region of the worn surface. The micrograph shows the surface cracks identified with the red arrows. The microstructure was divided in two layers denominated A and B according with morphology. The layer A corresponds to the most severe deformed layer which includes the fatigue cracks. On the other hand, the layer B is characterized by the simultaneous presence of deformed

layer (reduction of interlamellar spacing) and pearlite colonies not affected by the stress field evolve during the mechanical loading.

Figure 4-8 SEM micrograph of the microstructure in cross-section showing the sub-surface layers distribution

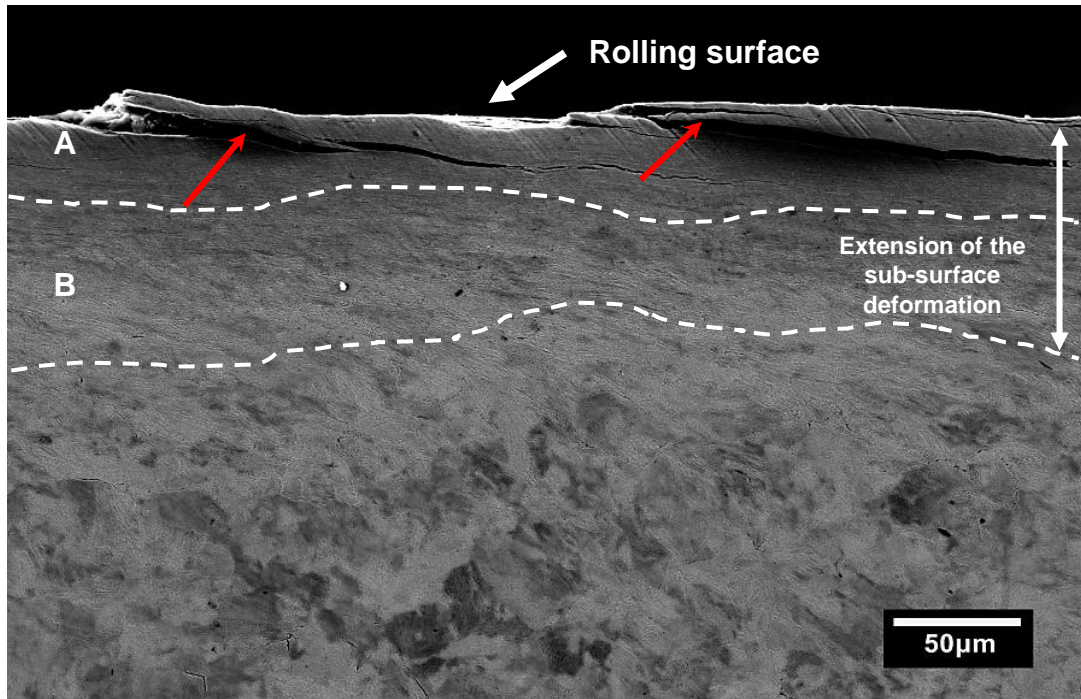


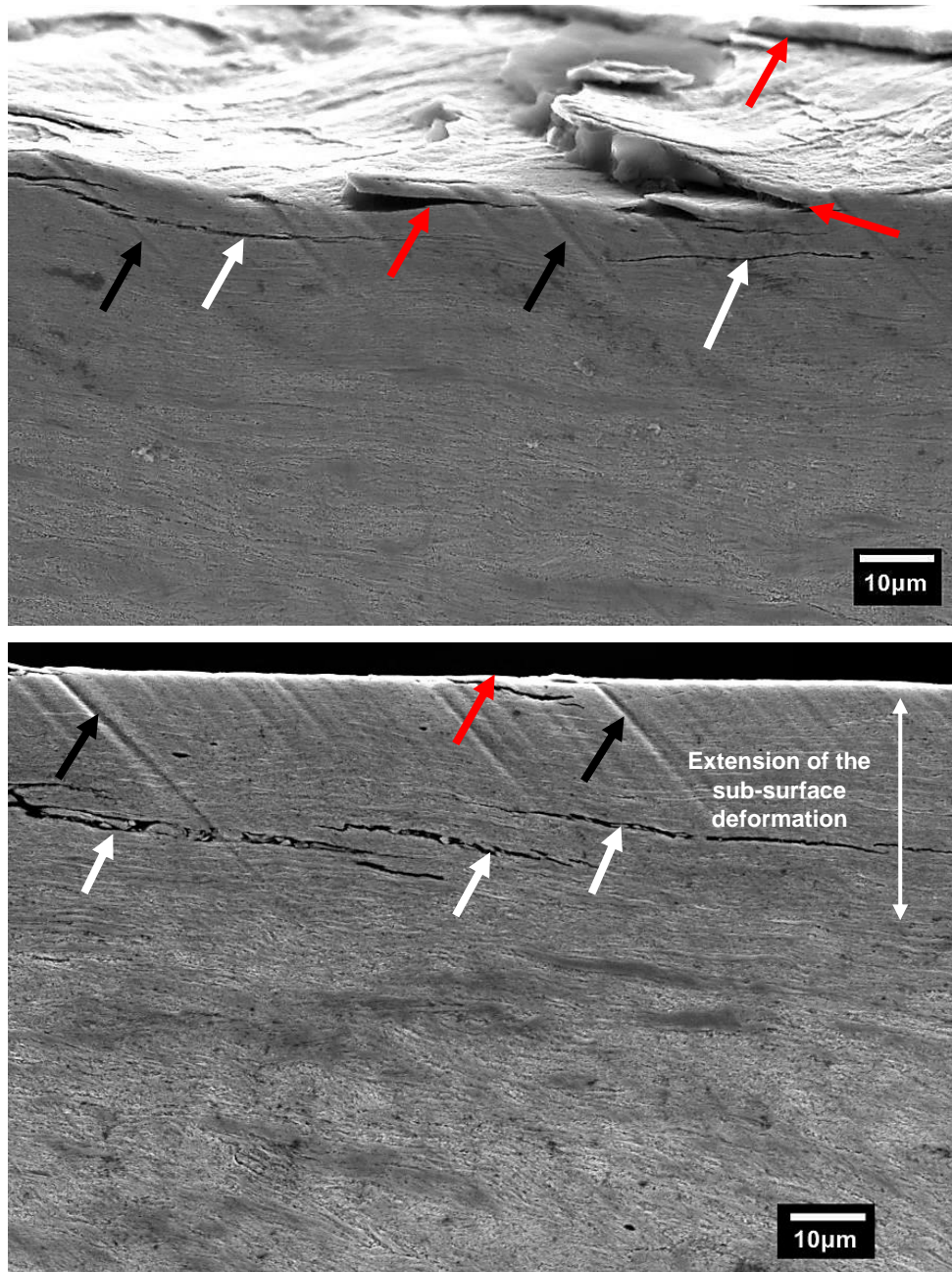
Figure 4-9 shows the microstructure in cross-section using FEG-SEM. Two regions with different surface characteristics are used by the WEL formation characterization. For both regions, the surface cracks are indicated by the red arrows, while aligned cracks with the worn surface are shown by the white arrows. Polishing marks were also observed and are identified by the black arrows. **Figure 4-9a** shows the more severely deformed layer with RCF defects identified as fatigue cracks (spalling). **Figure 4-9b** shows a second region of the sample also characterized by a severe microstructure deformation in the sub-superficial layers. An initial stage of RCF formation was observed on this region identifying by the nucleation of aligned cracks (internal cracks) in the same direction of rolling surface. The cracks are located mostly in the transitional layer.

LEWIS et al. discussed the presence of surface cracks in laboratory tests using levels of slip in the configuration disc-disc. The increase of the severity of the contact (i.e. increment of the slip ratio) promote the propagation of some of these surface cracks to the interior of the material (core) turning up to the running parallel to the wear surface

to tuning up to turning down causing larger chunks of the material to detachment material (LEWIS; DWYER-JOYCE, 2004; BRAGHIN; BRUNI; LEWIS, 2009).

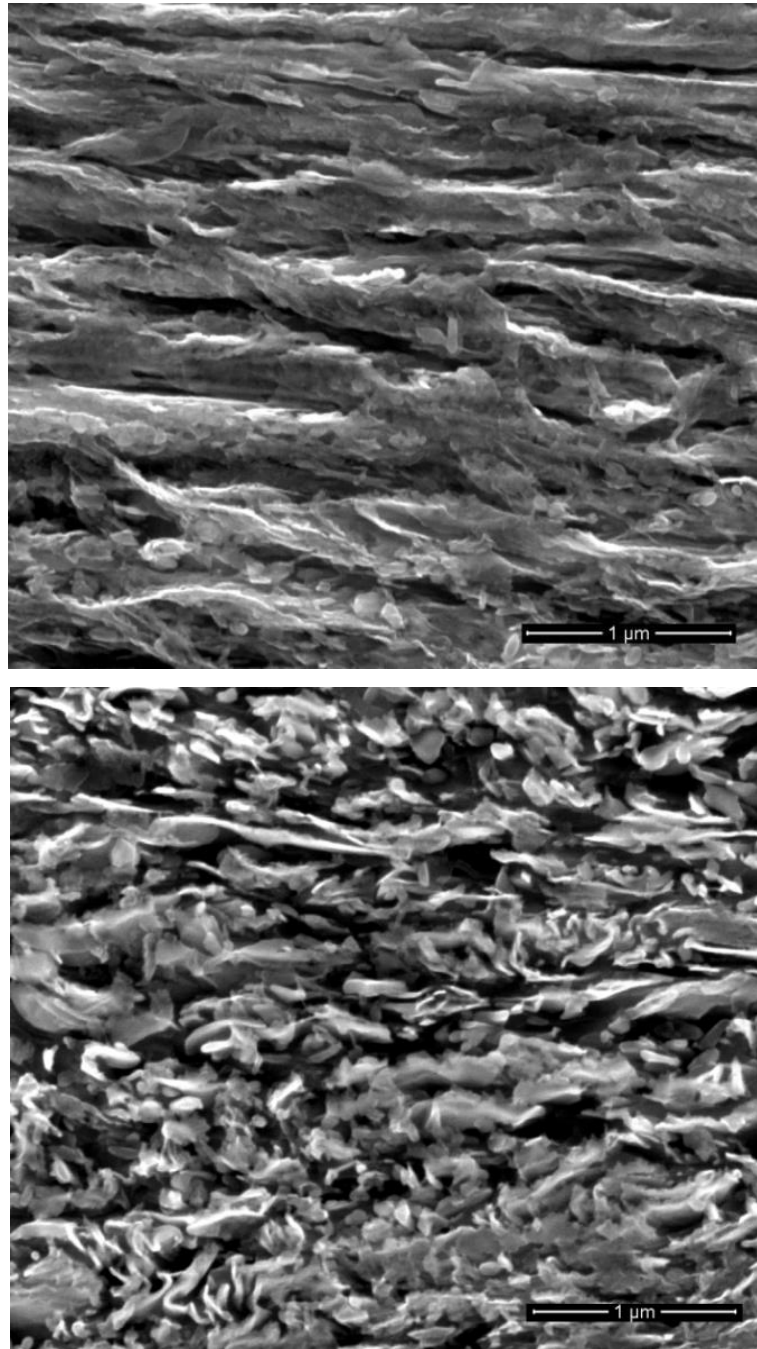
MAKINO *et al.* shows, in the study of the effect of the slip ratio on the RCF, that the number of cycles contributes expressively in the crack growth due to the crack propagation in the depth direction being large (MAKINO; KATO; HIRAKAWA, 2012).

Figure 4-9 FEG-SEM micrographs of the microstructure beneath the rolling band in two regions of the sample highlighting the morphology in the layer A. Sample of interest: 25.0000 cycles (W4)



The lamellar arrangement of pearlite microstructure in a region close to the surface was analyzed using higher magnification in a FEG/SEM microscopy in samples W4 and W9 as shown in **Figure 4-10**. In both conditions, the evidence of the pearlite microstructure was not found, corresponding to a highly deformed microstructure.

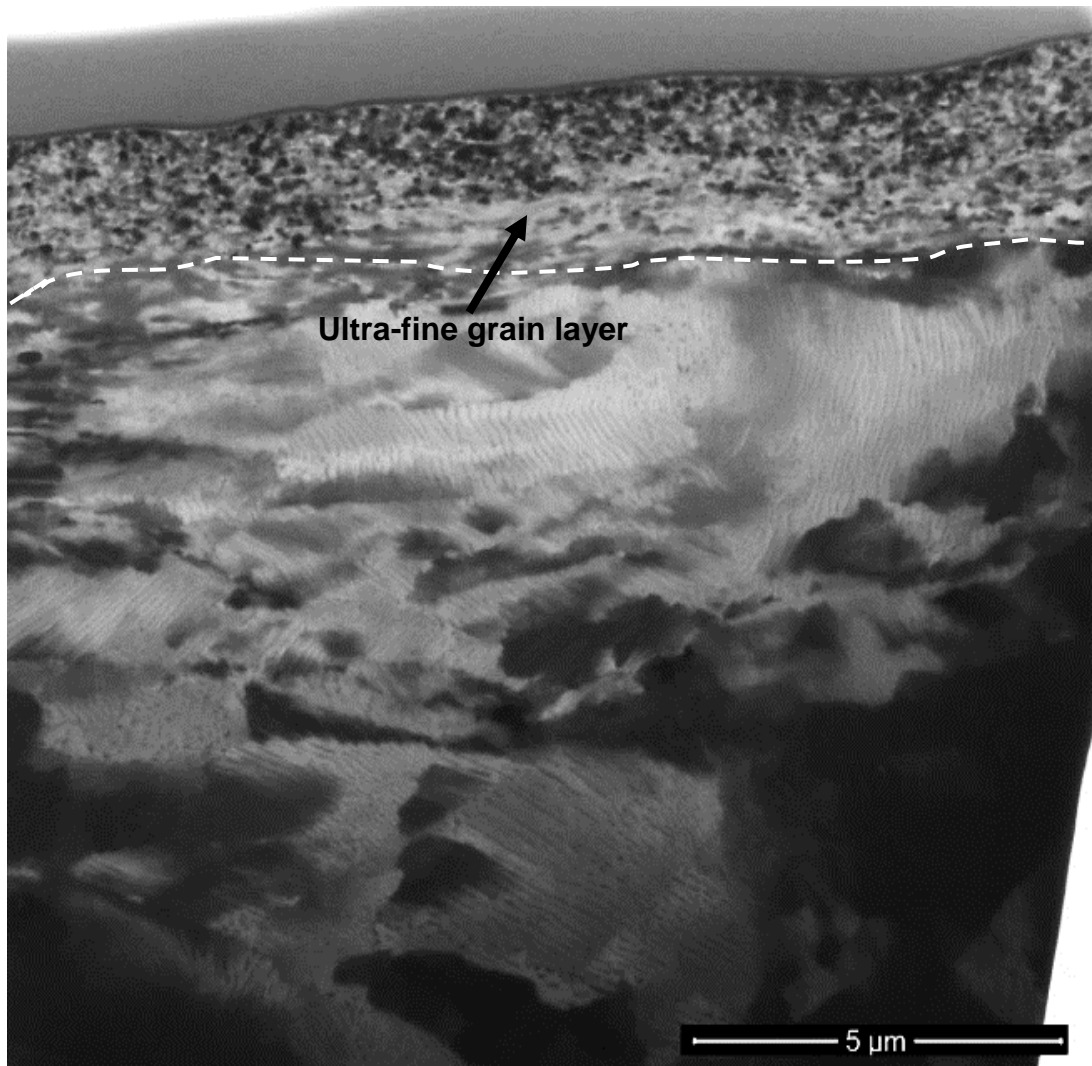
Figure 4-10 FEG-SEM micrographs showing the microstructure transformation in the layer A of samples W4 and W9, respectively.



4.4.1.3.2 Characterization by Focused Ion Beam (FIB-SEM)

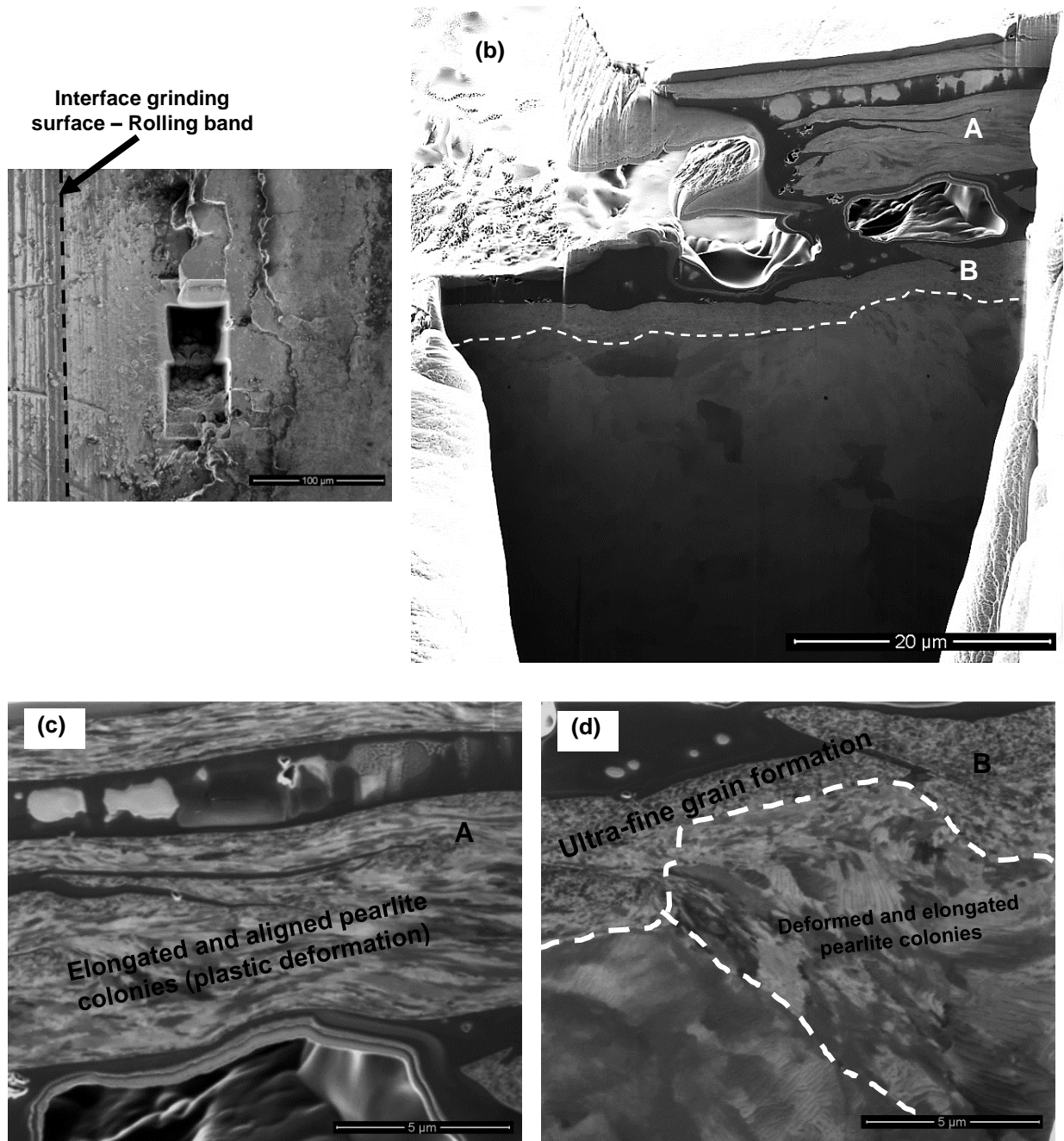
The microstructural analysis in the region below the worn surface was carried out using FIB-SEM. As a preliminary analysis, the microstructure on cross-section of the sample was characterized under grinding conditions (sample preparation) as shown in **Figure 4-11**. An ultra-fine grain layer, according to (LOJKOWSKI; DJAHANBAKHS; BU, 2001) was observed along the sample with 2–3 μm of thickness.

Figure 4-11 FIB-SEM micrograph of the microstructure of the grinding sample (sample preparation for disc-disc contact)



In a sequence, the analysis of the tested samples was carried out. Following the sequence used in the surface characterization, the W4 sample was analyzed in the transition region between the ground surface and the surface affected by the rolling contact as shown in **Figure 4-12**.

Figure 4-12 FIB-SEM micrograph of the microstructure of the W4 in the end of the rolling band (beneath of the material removed from the surface)

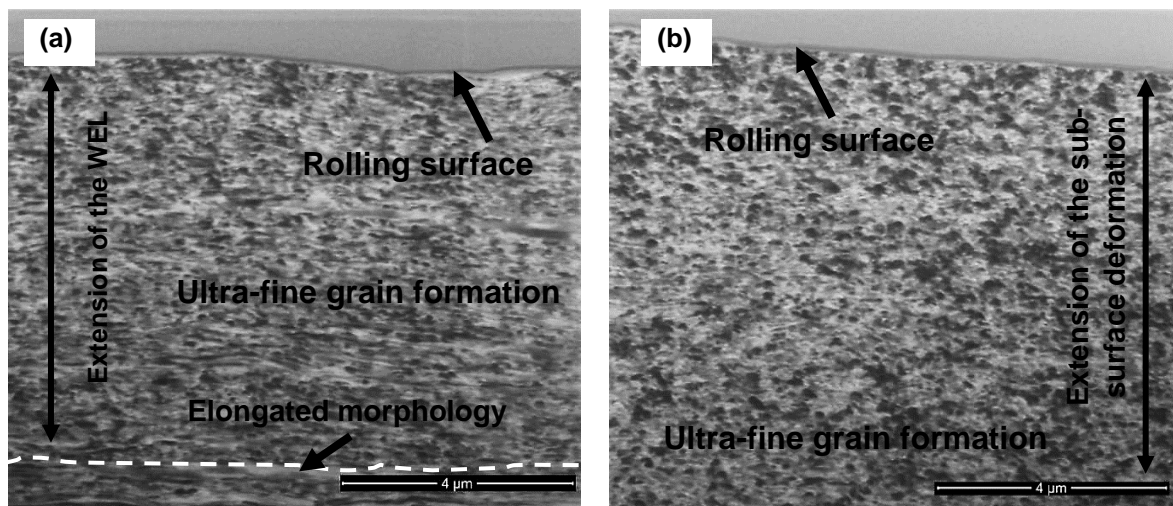


Two types of microstructural transformation were observed beneath worn surface (**Figure 4-12b**). In the rolling contact region, a microstructure was observed characterized by elongated and aligned pearlite colonies, whereas the region closely to the grinding preparation, the microstructure consists in ultra-fine grains. The presence of a transition layer was observed beneath the rolling contact region as indicated in the **Figure 4-12c**.

The worn surface observed in the W4 (in the contact zone) is in accordance with the results obtained by BOLTON and CLAYTON in the analysis of rolling-sliding wear damage in rail. The microstructure transformation can be classified in type I with the surface microstructure consisting of highly deformed ferrite (BOLTON; CLAYTON, 1984). In the deeper layers, a difference in the morphology was observed characterized by the reduction of the ferrite grain size followed by the presence of the transition layer.

The analysis of the microstructure beneath rolling surface in both samples shows a homogeneous WEL formation with characteristics of ultra-fine grain formation. The W4 shows a formation of region with elongated morphology after 8 μm (**Figure 4-13a**). An intermediary layer was not observed in the case of the W9 at the same depth that W4, as shown in **Figure 4-13b**.

Figure 4-13 FIB-SEM micrographs of the microstructure of the sub-superficial layer in W4 and W9

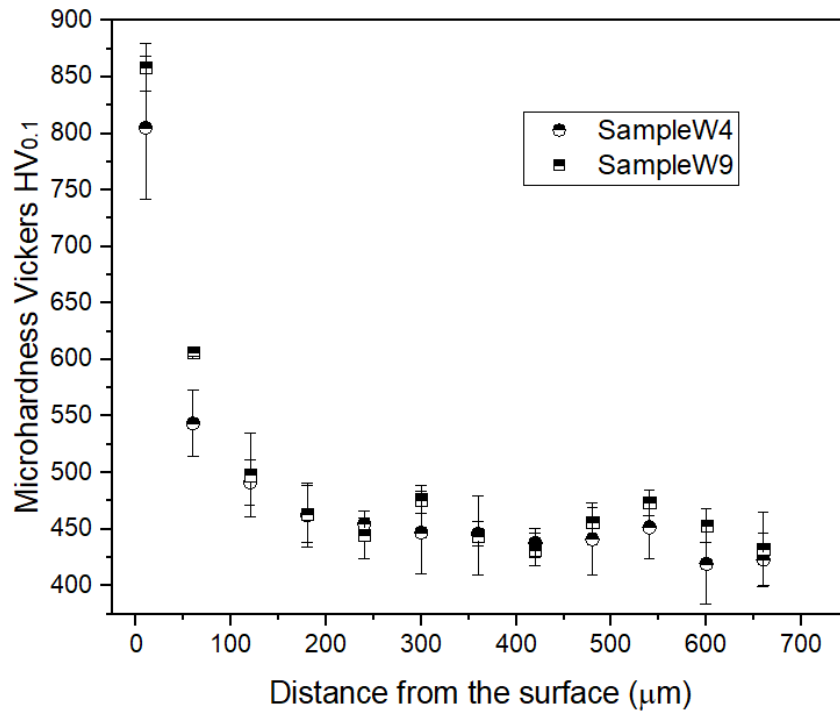
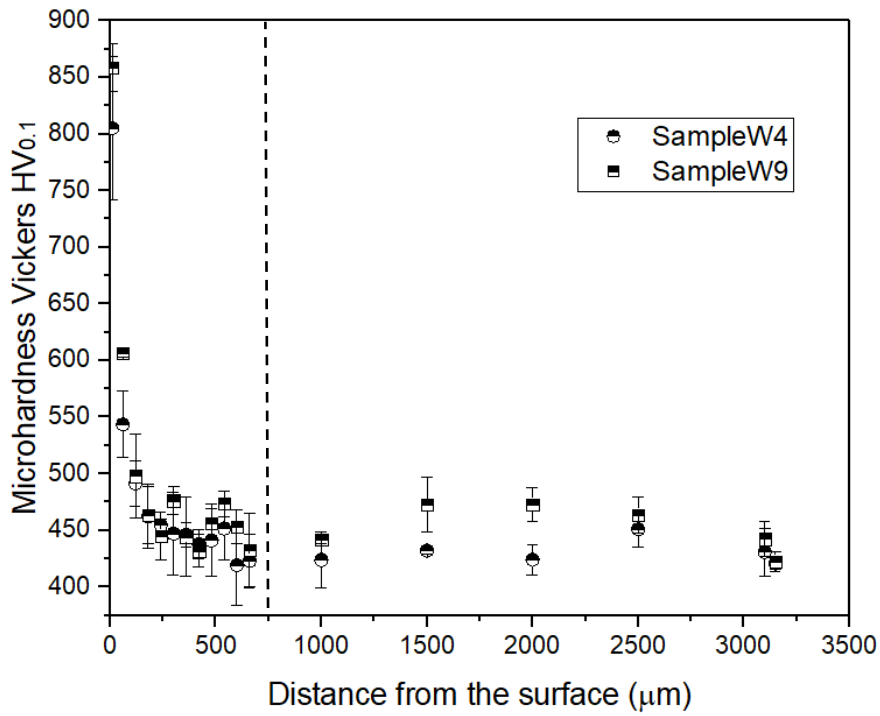


4.4.1.4 Micro-hardness profile analysis

The variation of hardness as a function of depth from the rolling–sliding surface was measured in order to study work-hardening effects and the result are presented in **Figure 4-14**. An increment of the micro-hardness was measured on W4, rising from $430 \pm 10 \text{ HV}_{0.1}$ at 3000 μm from the surface to $800 \pm 52 \text{ HV}_{0.1}$ on the surface. On the other hand, the micro-hardness profile of the W9 shows the increase of the values from $440 \pm 12 \text{ HV}_{0.1}$ at 3000 μm from the surface to $860 \pm 21 \text{ HV}_{0.1}$ on the sub-surface layer.

The thickness of the severe deformed layer was measured for both samples in 100 μm . Stability in the hardness values was observed in the profile after this distance from the surface until 3000 μm (ends of the profile measure) corresponding with 430 - 440 $\text{HV}_{0.1}$, values expressive higher that the initial hardness, 350 $\text{HV}_{0.1}$.

Figure 4-14 Micro-hardness profile of samples after disc-disc test



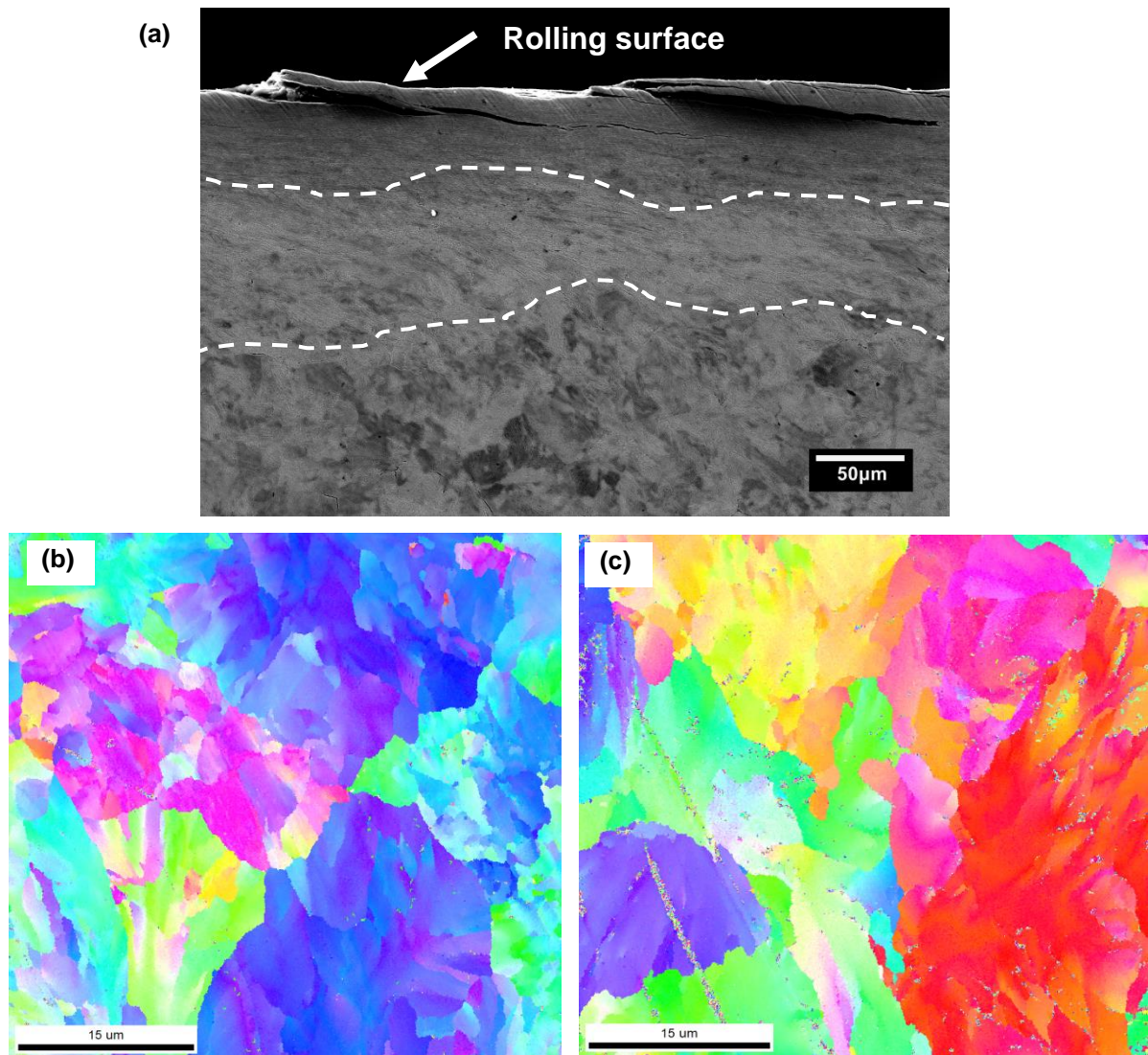
LINZ *et al.* shows that an increment in the number of cycles affects the micro-hardness profile once the plastic deformation is promoted, and this influenced the work hardening (LINZ *et al.*, 2015)

4.4.1.5 Crystallographic orientation analysis by EBSD

The sub-superficial layers designed as layer A and B observed in both samples W4 and W9 (**Figure 4-8**) were analyzed using Electro Backscatter Diffraction – EBSD. The Inverse Pole Frequency (IPF) maps of the W9 sample (severe test conditions) with the RD configuration are shown in **Figure 4-15**. As shown on previous chapters in this thesis, the severe deformed layer was not fully identified (diffraction patterns) by EBSD due to the small grain size (microscopy resolution) and/or the reduction in band contrast and indexing proportion by severe deformation (MEYERS *et al.*, 2003; GEE; MINGARD; ROEBUCK, 2009). For that reason, the analysis was emphasized in the regions near to the severe deformation (down 10 μm in agreement with the analysis FIB-SEM for this sample). For the layer A (**Figure 4-15**) this region corresponds to the border with the beginning of the transitional layer (indicated by the top white dashed line). The crystallographic orientation of the perlite colonies in these conditions was mainly RD // {111} as shown in **Figure 4-15b**. Some alteration in the lattice was observed and identified by the color gradient at the interior of the colonies.

Figure 4-15c shows the crystallographic orientation in the transitional layer (B). A randomized distribution of color was observed, which indicates a smaller tendency to crystallographic texture. This layer corresponds to the region with higher level of mixture between deformed and not affected colonies. TAKAHASHI *et al.* observed the presence of sub-boundaries usually characterized as low angle boundaries. According to the authors, the existence of dislocation inside the pearlite colonies promotes the continuous changes in the orientations (TAKAHASHI; PONGE; RAABE, 2007).

Figure 4-15 Crystallographic orientation of the microstructure beneath the rolling band shows by EBSD. a) SEM micrograph of the microstructure highlighting the layers A and B. IPF maps of specimen W9. a) Layer A and c) layer B

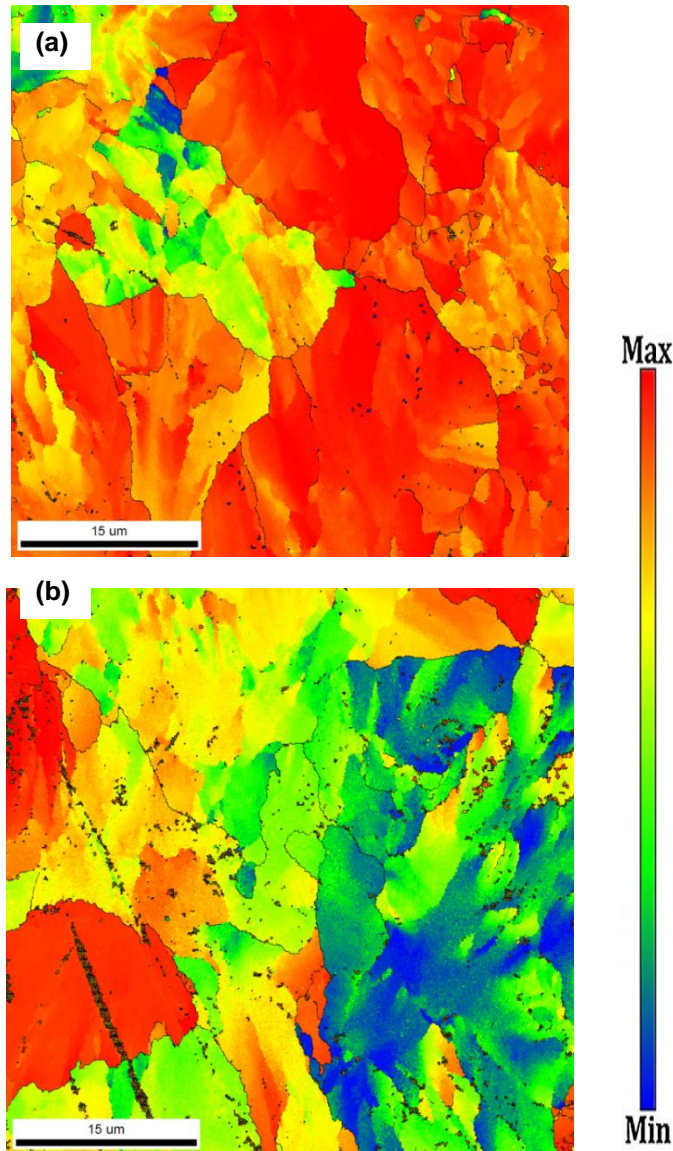


The level of stress induced into the grains in the two regions of interest was analyzed using the Taylor Factor (TF) tool (**Figure 4-16**). The color distribution was obtained using the preferential slip system for BCC metals $\{110\} \langle 111 \rangle$ (DELANNAY; JACQUES; KALIDINDI, 2006). In the region close to the severe deformed layer (A), there is a lower capacity to deform than the region B, being represented by the red color in the most colonies.

TAKAYAMA *et al.* showed that stored energy increases with an increase in the TF in almost all the cases being attributed to the non-homogeneous deformation. Low TF

grains are not difficult to deform and require only a small amount of the total slip on all active slip systems (TAKAYAMA; SZPUNAR, 2004).

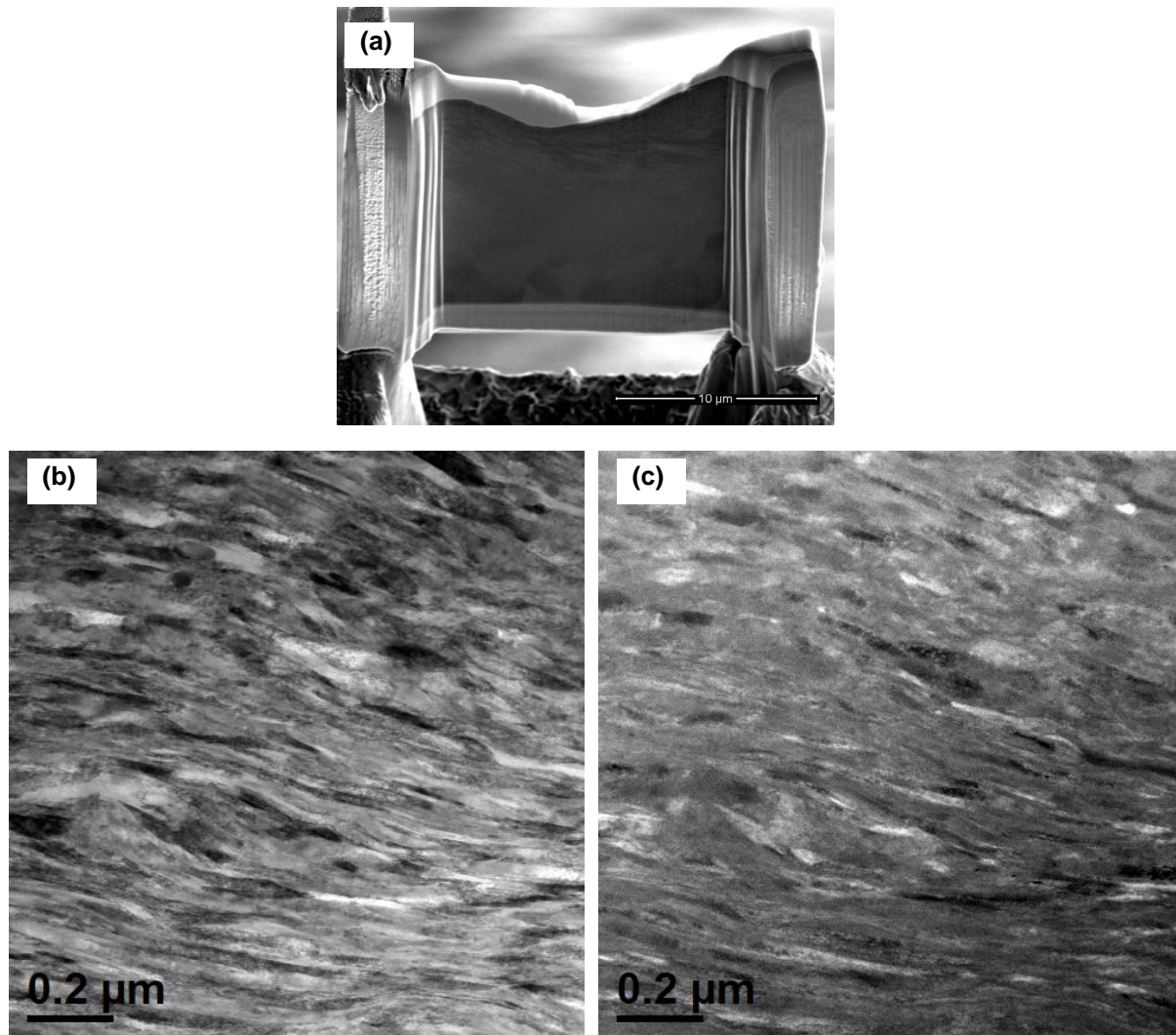
Figure 4-16 Taylor Factor analysis of the W9 specimen in a) layer A and b) layer B



4.4.1.6 Microstructural characterization by Transmission Electron Microscopy

Transmission Electron Microscopy was used for the analysis of the microstructure transformation in W9. For this analysis, the severely deformed layer was selected as region of interest. The lamella used for the analysis was obtained via FIB/SEM microscopy and is shown in **Figure 4-17a**. Micrographs of the microstructure in bright and dark field were obtained, respectively as shown in **Figure 4-17b-c**. At this level of resolutions was possible to establish that even in the ultra-fine region, there is a microstructure with elongated aligned-like features.

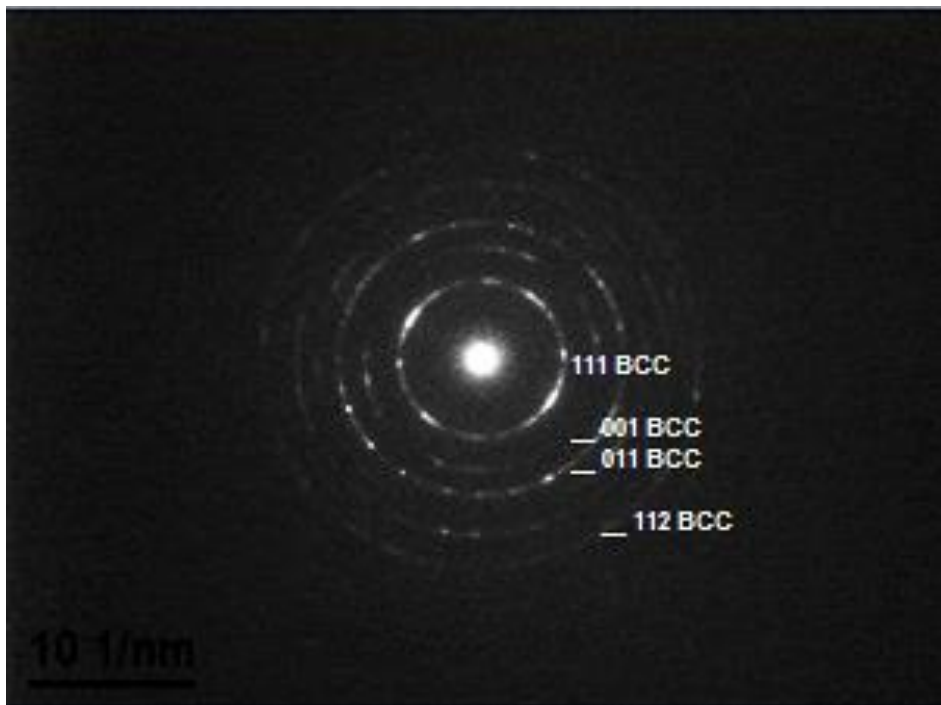
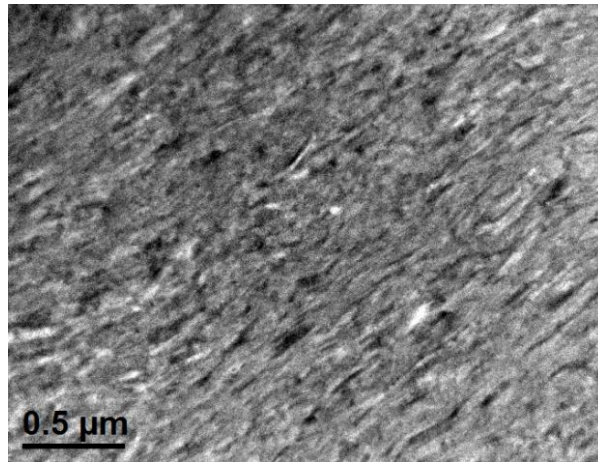
Figure 4-17 Transmission Electron Microscopy image of the samples W. a) Sample preparation, b) Bright field image, c) Dark field image



The HTEM and the electron pattern diffraction (SAED) were obtained in this region as shown in **Figure 4-18**. The SAED pattern shows microstructure composed by polycrystalline ferrite, identified by a not uniform ring patterns as discussed by (KRUMEICK, 2011).

Similar diffraction patterns were observed by ZHANG *et al.* in the study of the WEL formation on pearlite steel rail ((ZHANG *et al.*, 2006) and ZHOU *et al.* in the analysis of the WEL formation during rolling-sliding friction (ZHOU *et al.*, 2016).

Figure 4-18 High resolution - TEM micrograph and SAED diffraction patterns at 100 μm from the worn surface



4.4.2 WHEEL-RAIL CONTACT (CHARACTERIZATION ON FIELD)

The characterization of the microstructural behavior was performed in a sample taken from a worn wheel. The area of interest was selected due severe deformation as indicated in the white box in **Figure 4-19**.

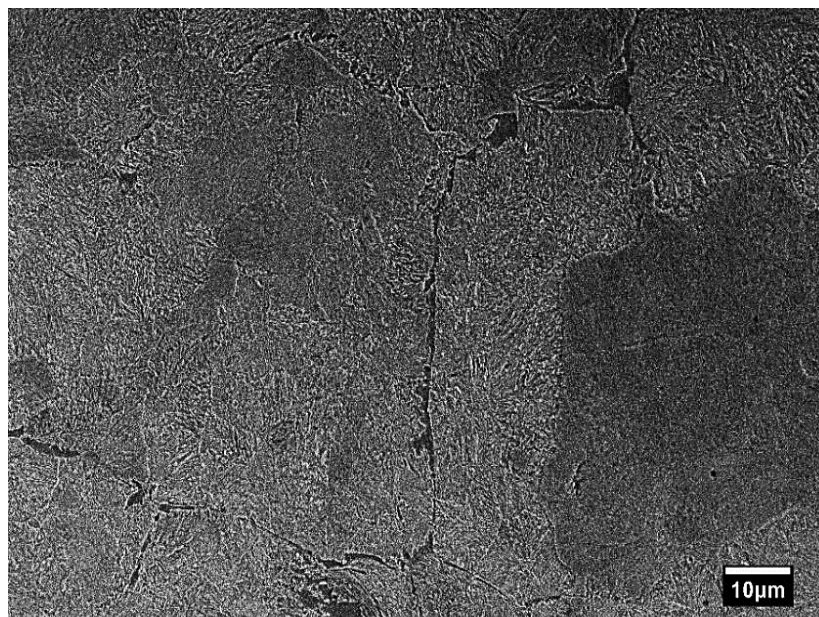
Figure 4-19 Wheel sample used in the microstructural characterization, corresponding with the severely deformed section



4.4.2.1 Microstructural characterization in the initial condition

Figure 4-20 shows the microstructure obtained via SEM in an undeformed region. The microstructure corresponds to lamellar arrangement of ferrite (α -Fe) and cementite (Fe_3C).

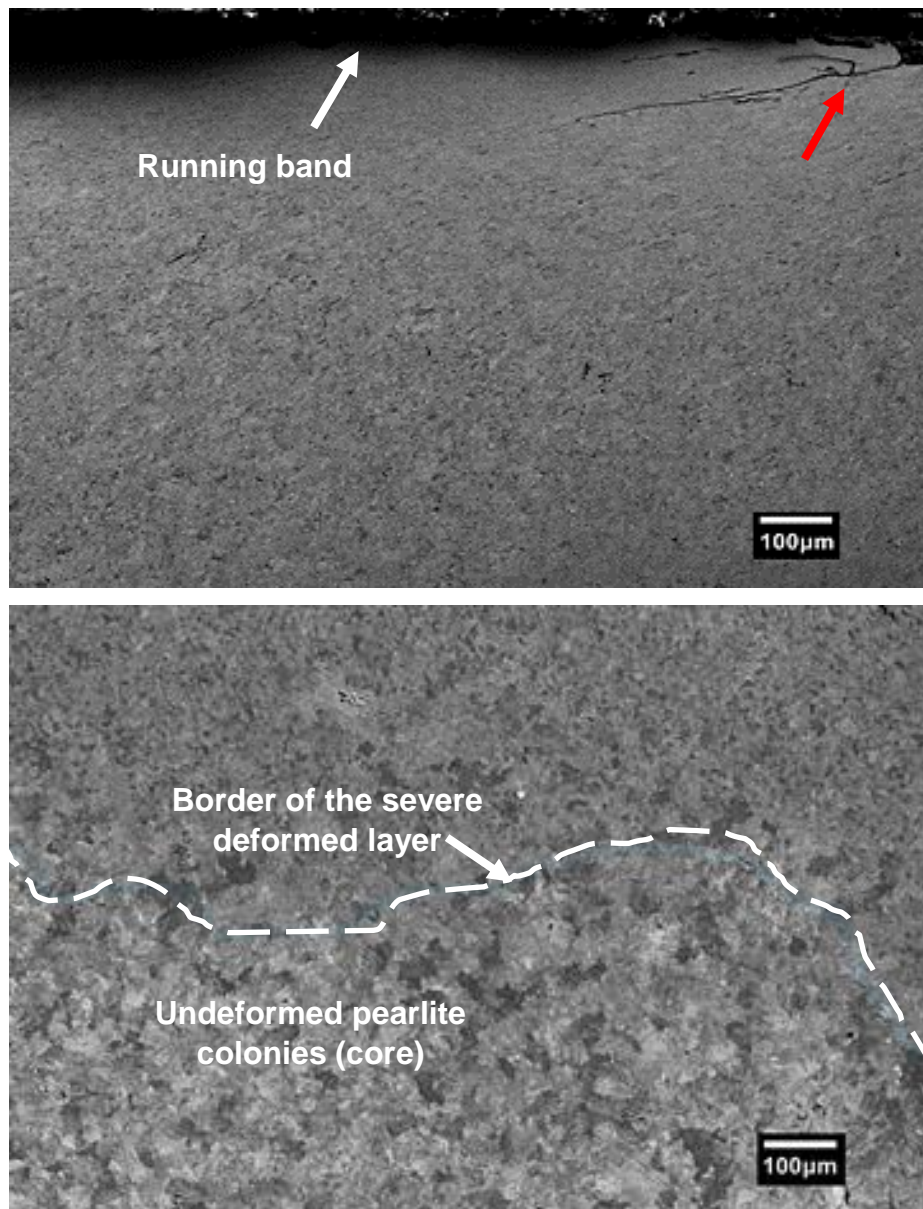
Figure 4-20 A secondary electron SEM image of the undeformed pearlitic microstructure



4.4.2.2 Microstructural characterization of the sub-superficial layer

The microstructural characterization was performed in the contact patch (central region of the running band) as shown in **Figure 4-21a**. Surface cracks formation indicated by the red arrow was observed and its propagation through the deformed layer by the tensile/shear stresses evolved in the contact. In these wear conditions, a thicker deformed layer (up to hundreds of micrometers) was observed. **Figure 4-21b** shows the transition from the severely deformed microstructure and the beginning of the region with features of a combination of deformed and undeformed colonies.

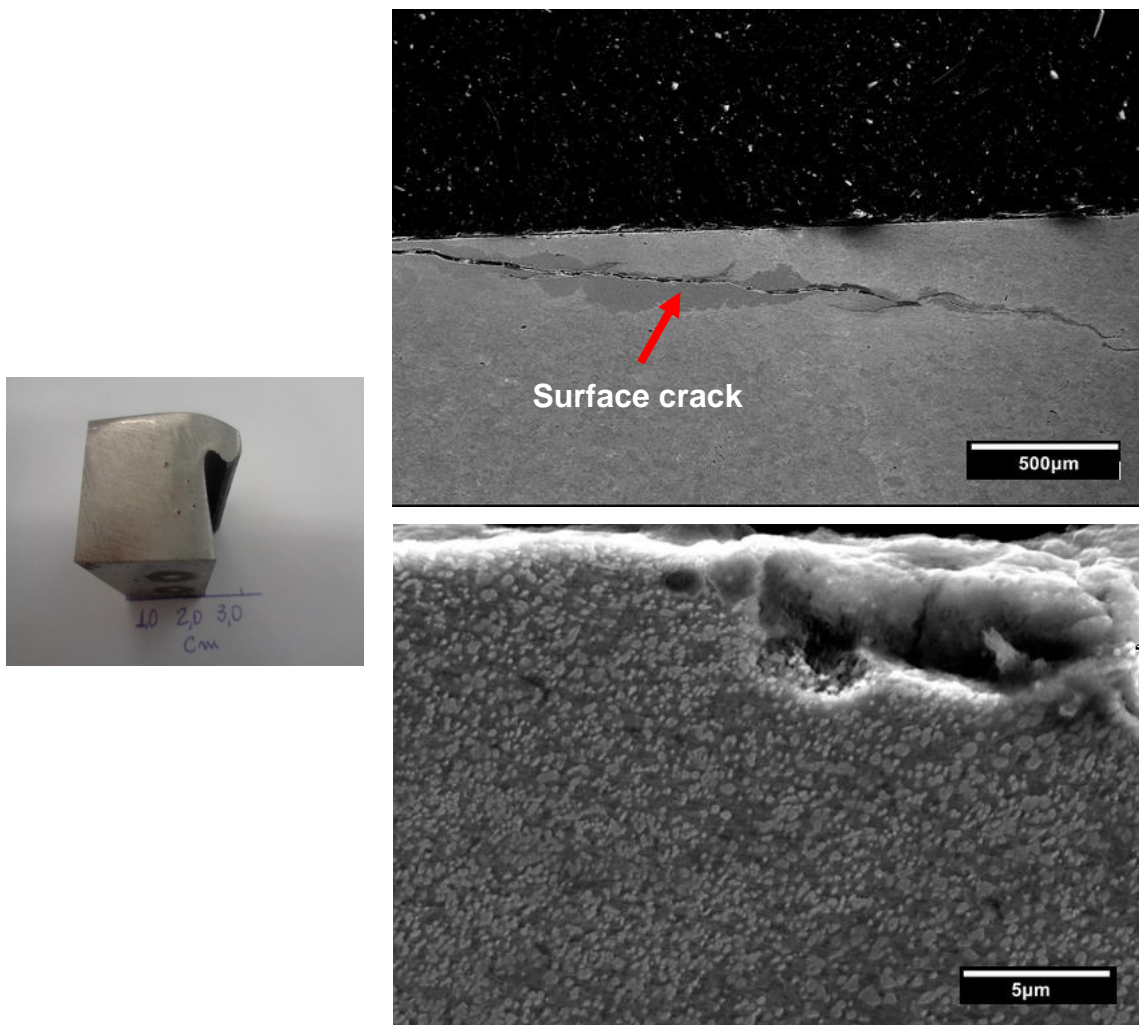
Figure 4-21 Microstructural characterization in cross-section using SEM



CARROL *et al.* describes the cracks growth within the pearlite from the interface with the WEL as the result of plastic deformation and ductility exhaustion of the material (CARROLL; BEYNON, 2007).

A detailed characterization of the deformed layer is presented in **Figure 4-22**. The running band was selected as the area of interest and indicated by the red box. A surface crack was observed propagating through the deformed layer until a depth of 500 μm . In a higher resolution and magnification micrograph (**Figure 4-22**). It was observed that the microstructure is characterized by small cementite formation (**Figure 4-22b**). The IHHA classified the sub-surface-initiated Rolling Contact Fatigue in wheels as shattered “rim defects”, “deep shelling”, “spread rims” and as “subsurface fatigue”. The damage begins with the initiation of a crack some millimeters below the running surface under multiple action of tangential stresses (IHHA, 2015).

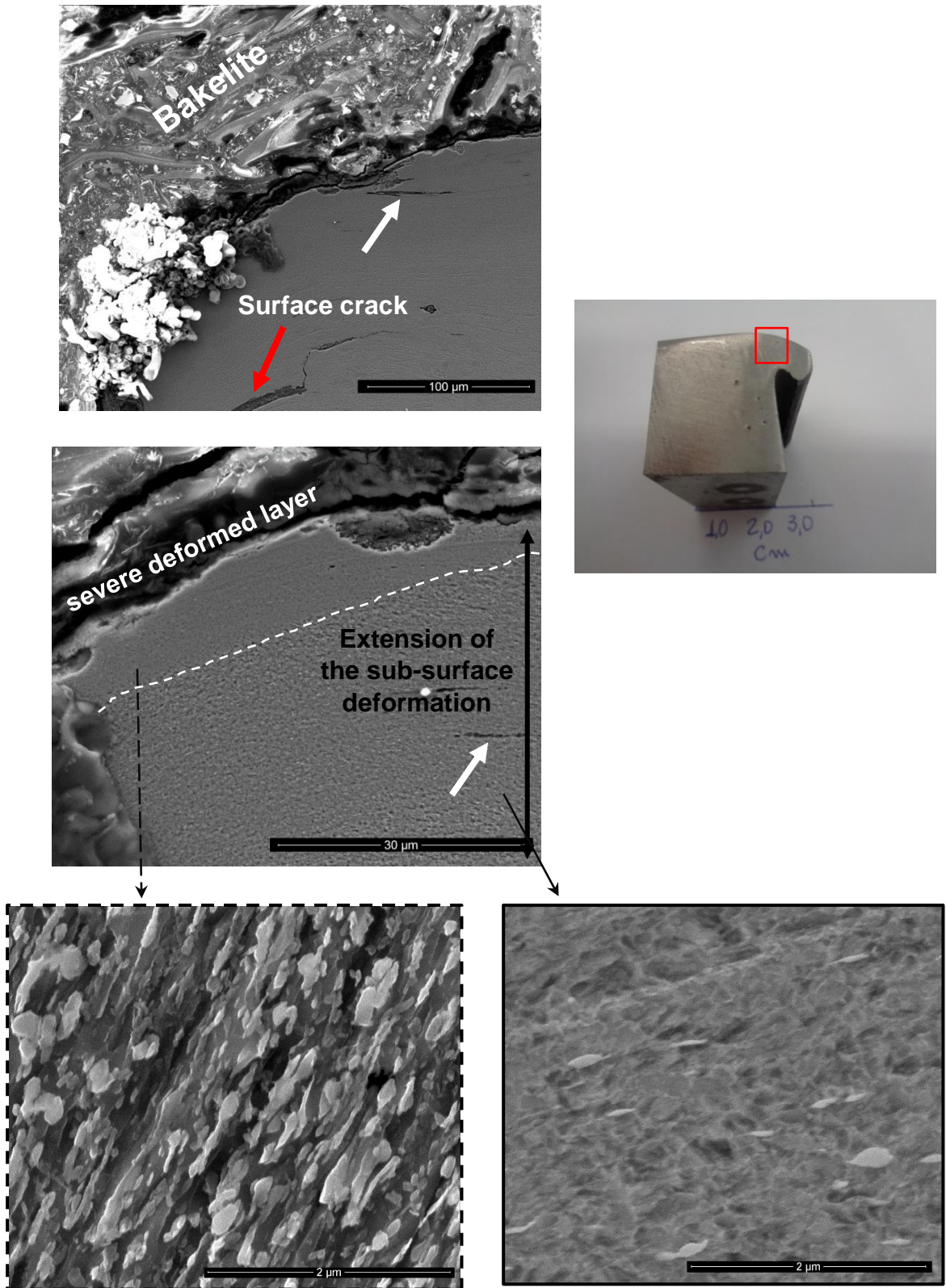
Figure 4-22 FEG-SEM micrographs of the microstructure in cross-section from the deformed layer



The characterization of a second region in the running band which corresponds to a higher deformation is shown in **Figure 4-23** and indicated by the red box. Two sub-superficial deformed layers were identified at 30 μm from the surface; a severely deformed layer (close to the surface) and a layer plastically affected. The SEM micrograph shows a surface defect (RCF) identified by the black dashed box, an internal crack (white arrow) and a surface crack indicated by the red arrow located in the region with severe plastic deformation.

The severely deformed layer consists in breakage cementite, oriented following the running direction. On the other hand, 10 μm from the surface the presence of cementite in the deformed layer was not observed, which can indicate that the carbon dissolution in ferrite to form the supersaturated carbon ferrite takes place. This phenomenon was observed in process of severe plastic deformation (high strains rates condition) when the formation of nanogained structures were demonstrated. UMEMOTO shows the cementite dissolution in the nanocrystalline layer for shot peening, ball milled and ball dropped processes (UMEMOTO, 2003).

Figure 4-23 Microstructural characterization beneath the running band in the more severe region

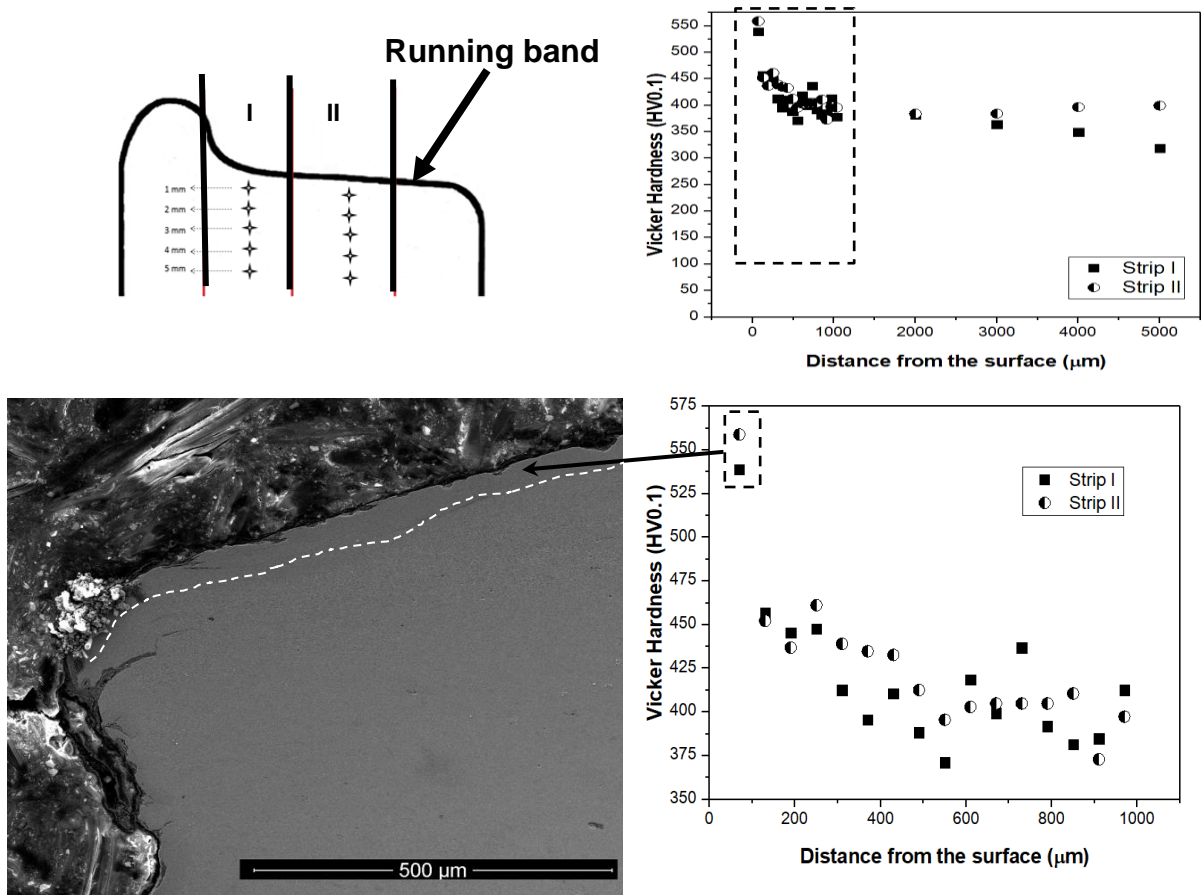


4.4.2.3 Micro-hardness profile determination

As observed in the SEM micrographs presented previously, the pearlite arrangement suffers some alterations due the strain rates in the contact zone, which influenced the microstructural work hardening. **Figure 4-24a** shows the schematic representation of the hardness spots in the microstructure beneath the running band. It also shows the correlation of those values (HV_{0.1}) with the distance of the surface (depth).

In the micro-hardness curve, a stabilization of the values as of 100 μm was observed. In a comparison of the behavior in the two zones of interest, there was not a statistical difference but a tendency of higher work hardening in the strip II, which corresponds to the contact point in the running band with a higher friction coefficient. Friction coefficient is an essential factor in influencing available adhesion. If friction is too high, this can also lead to an excessive wear influenced by the alterations/transformation of the microstructure (LEWIS; OLOFSSON, 2009; OLOFSSON et al., 2013).

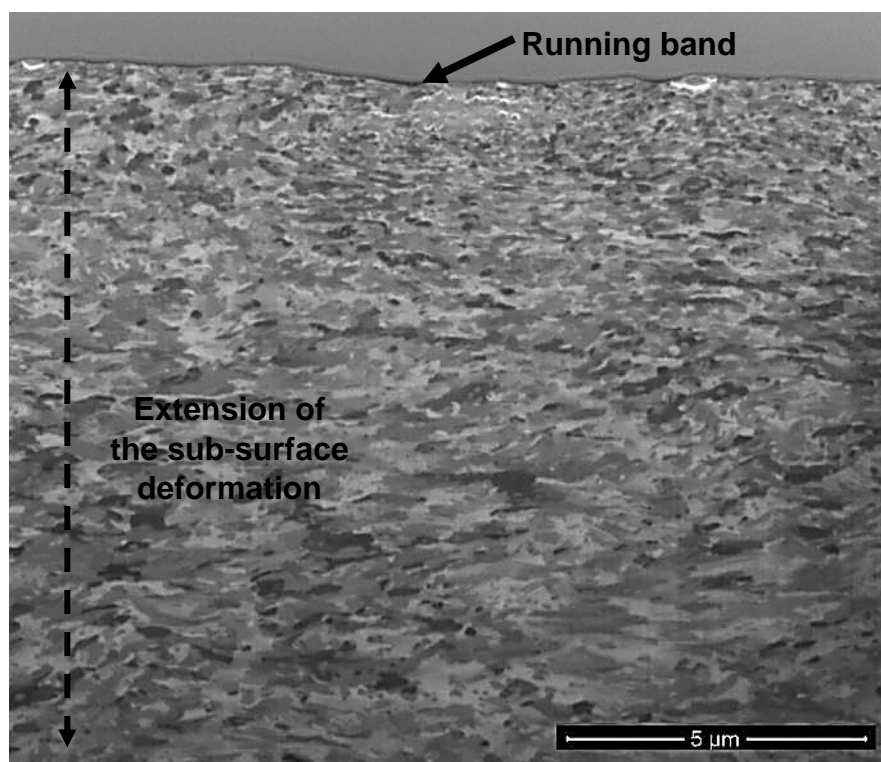
Figure 4-24 Hardness profile of the wheel in the cross-section of the running band (strip II) and severe plastic deformation zone (strip I)



4.4.2.4 Characterization by Focused Ion Beam (FIB-SEM)

The microstructural analysis was continued using FIB-SEM. Strip II was selected as the area of interest. **Figure 4-25** shows the extension of the WEL formation in the first 25 μm from the surface. The microstructure consists in ultra-fine grain (nanostructured) of ferrite and is in agreement with the microstructure transformation observed in the other tribosystems discussed in previous chapters of this thesis describes in the literature (UMEMOTO, 2003; FARGAS; ROA; MATEO, 2016; PEREIRA et al., 2017).

Figure 4-25 FIB-SEM micrograph in the center of the running band



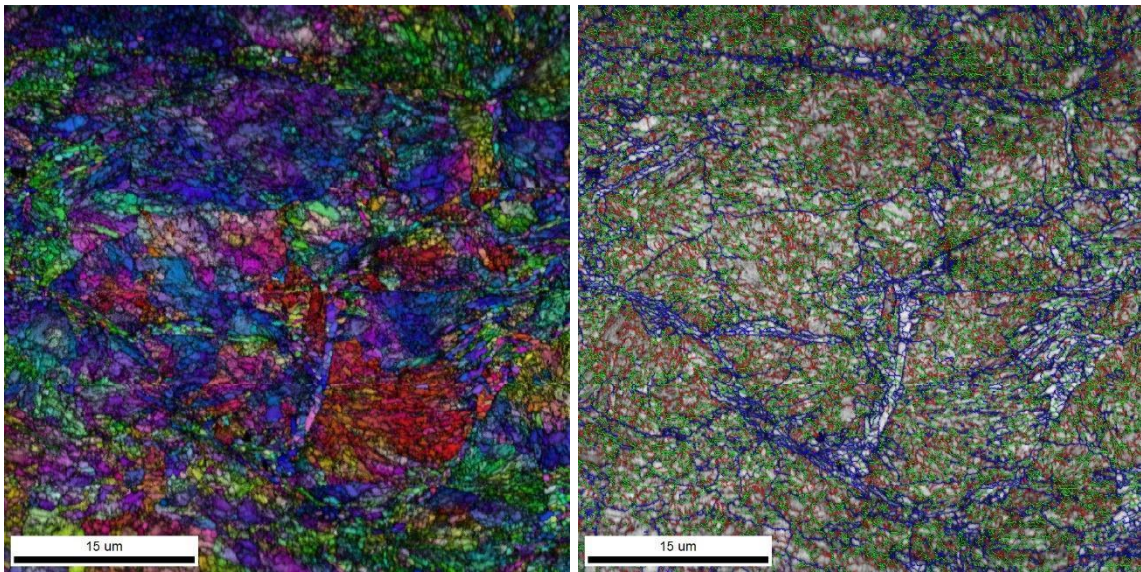
4.4.2.5 Crystallographic orientation analysis by EBSD

The EBSD was carried out using the conventional configuration RD direction (Rolling/Reference direction) as described previously. **Figure 4-26** shows the analysis of IPF and grains boundaries in the strip II (close to the surface).

The IPF map (**Figure 4-26a**) shows significant distortion in the lattice since it represents grains with internal orientation changes indicated by the color profile. The crystals observed in the map are strongly fragmented into very small grains with random orientation. The LAGB distribution observed in **Figure 4-26b** shows the increase of the dislocations density.

LINZ et al discussed that the deformation of grains below the aligned layer was interpreted as an indicator for the amount of shear strain that acts in particular depths below the surface. For the harder pearlitic phase the cementite represents an obstacle for dislocation movement and thus a larger stress increment is needed to take up the same externally imposed strain increment as the ferrite (LINZ et al., 2015).

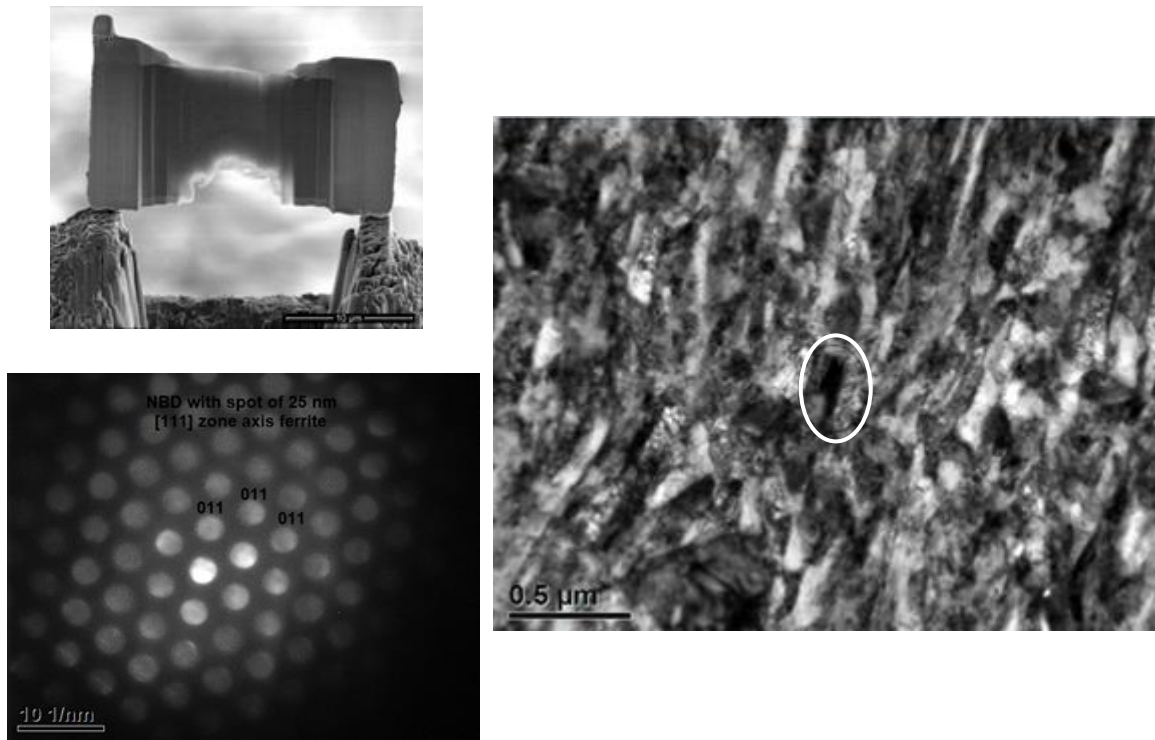
Figure 4-26 Sub-surface EBSD plots after wheel-rail contact, a) inverse pole figure (IPF) , b) pattern quality plot combined with grain boundaries (red lines for LAGBs of 2–5°, green lines for LAGBs of 5 – 15° and blue for > 15° HAGBs)



4.4.2.6 Microstructural characterization by Transmission Electron Microscopy

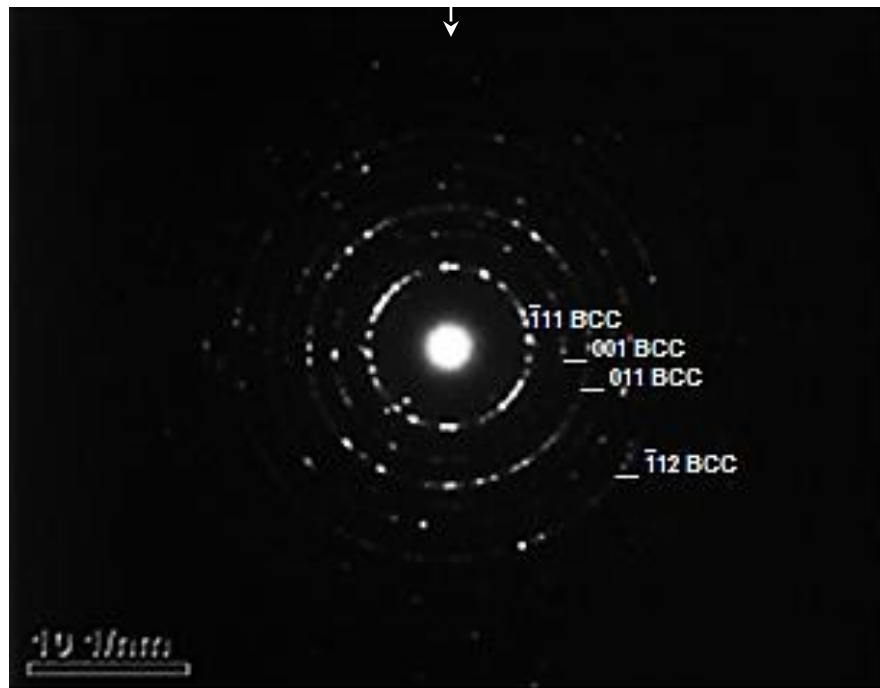
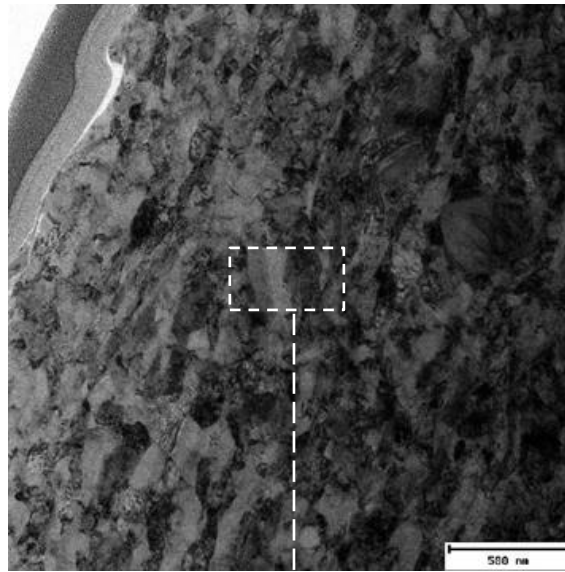
Figure 4-27 shows the TEM micrographs from different positions in the topmost surface. The first selected-area electron diffraction (SAED) pattern identified by the red circle indicates that the microstructure is composed of crystal of ferrite in an axes zone of [111].

Figure 4-27 Transmission Electron Microscopy image of the samples W (disc-disc). a) Sample preparation, b) HRTEM image



A later definition of the SAED patterns identified the polycrystalline ferrite formation characterized by the ring patterns as shown in **Figure 4-28**. The fully random orientation was not observed. No austenite and martensite transformations were observed from the SAED patterns. These results are in contradiction with the observation of PYZALLA and SATOH, who conclude that the WEL was generated by a thermal condition resulting in a microstructural transformation (PYZALLA et al., 2001; SATOH; IWAFUCHI, 2005).

Figure 4-28 High Resolution - TEM micrograph of the deformed layer used by the SAED analysis.
SAED diffraction patterns obtained in different spots



4.5 CONCLUSION

On this chapter, the behavior of pearlitic steel under rolling contact fatigue in controlled conditions (laboratory tests) and field conditions (real-wheel) was analyzed. The WEL formation was highlighted as the main feature of the material response. The conclusions of the characterization by electron microscopy are shown according with features observed in the analysis as follows:

Wear type

- In the laboratory tests, it was defined that the number of cycles was in enough conditions to produce spalling as RCF defect, corresponding to wear type III.

Microstructure beneath the worn surface

- A microstructural transformation was identified for all samples analyzed in the laboratory test, being characterized by the formation of two sub-superficial layers.
- The microstructure of the layer beneath the rolling surface consists in polycrystalline ferrite (ultra-fine grains formation).
- The second layer (called as the transition layer) is characterized by plastic deformation and the combination of deformed and undeformed colonies. The deformed colonies show a reduction of the interlamellar spacing and elongated cementite lamellae.
- The increment of number of cycles promotes the increase of the thickness in the most severe deformation layer (A). For samples tested at 25.000 cycles it was found a layer A with 80 μm of thickness, while increasing to 650.000 cycles this value was 120 μm .
- Crack nucleation was identified on the surface as well as its propagation along the most severe deformed layer, thus promoting the material removal by spalling. The transitional layer is characterized by some internal cracks nucleation propagating in a parallel plane to the rolling-sliding surface.
- In the railway wheel, the microstructure is characterized by the formation of two types of deformed layer in the first 30 μm from the surface. A layer thinner and closer to the surface with approximately 10 μm consists in breakage cementite, aligned in the running direction, while in the micrographs taken in a higher

distance from the surface it was observed a deformed layer characterized by the cementite dissolution in ferrite.

- Cracks nucleation and posteriorly propagation were observed in both layers. The change of geometry in the wheel sample and the plastic deformation resulting by the high strain rate promote more expressive crack propagation.

Work-hardening

- An expressive increase of the microhardness was observed in the samples, corresponding to 400 *Vickers* point from the core to the surface. The first 100 μm from the surface in both samples reported values up to 800 $\text{HV}_{0.1}$ with a stabilization until 3000 μm from the surface at 400 $\text{HV}_{0.1}$.
- The sample take from the railway wheel shows a lower increment of the hardness than observed in the laboratory conditions. In the first 100 μm was reporter a value of hardness up to 500 $\text{HV}_{0.1}$ with the decreasing as function of the distance from the surface. At the next 1000 μm it was observed a stabilization in 400 $\text{HV}_{0.1}$ for the both strips analyzed. This stabilization on the values corresponds with the thickness of the plastic deformed layer (transitional layer) which was reporter in several hundreds of micrometers.

Crystallographic orientation

- In samples analyzed in the laboratory, the layer beneath the surface shows pearlite colonies oriented mainly to RD // $\langle 111 \rangle$ with the presence of the dislocation promoting a small lattice distortion. In the case of the transition layer, a crystallographic texture was not observed.
- In the railway sample, the polycrystalline ferrite formation (ultra-fine grain) was identified with a preferential orientation of RD // $\langle 111 \rangle$. It was not defined microstructural transformation like austenitic or martensitic formation.

4.6 REFERENCES

- AAR. Manual of Standards and Recommended Practices Section C - Part II, 2007.
- BEYNON, J. H.; GARNHAM, J. E.; SAWLEY, K. J. Rolling contact fatigue of three pearlitic rail steels. *Wear*, v. 192, n. 1–2, p. 94–111, 1996.
- BOLTON, P. J.; CLAYTON, P. Rolling-sliding wear damage in rail and tyre steels. *Wear*, v. 93, n. 2, p. 145–165, 1984.
- CHEN, H.; FUKAGAI, S.; SONE, Y.; BAN, T.; NAMURA, A. Assessment of lubricant applied to wheel/rail interface in curves. *Wear*, v. 314, n. 1–2, p. 228–235, 2014.
- FREITAS, I. M. De. Análise de propriedades e mecânica da fratura de rodas ferroviárias microligadas fundidas e forjadas. In: 70º Congresso Anual da ABM, Anais.2015.
- IHHA. Guidelines to Best Practices for Heavy Haul Railway Operations: Management of the Wheel and Rail Interface. Simmons-Boardman Books, IC, 2015.
- L’HOSTIS, B.; MINFRAY, C.; FRÉGONÈSE, M.; VERDU, C.; TER-OVANEISSIAN, B.; VACHER, B.; LE MOGNE, T.; JARNIAS, F.; DA-COSTA D’AMBROS, A. Influence of lubricant formulation on rolling contact fatigue of gears – interaction of lubricant additives with fatigue cracks. *Wear*, v. 382–383, p. 113–122, 2017.
- MAKINO, T.; KATO, T.; HIRAKAWA, K. The effect of slip ratio on the rolling contact fatigue property of railway wheel steel. *International Journal of Fatigue*, v. 36, n. 1, p. 68–79, 2012. Disponível em: <<http://dx.doi.org/10.1016/j.ijfatigue.2011.08.014>>.
- OLOFSSON, U.; ZHU, Y.; ABBASI, S.; LEWIS, R.; LEWIS, S. Tribology of the wheel-rail contact-aspects of wear, particle emission and adhesion. *Vehicle System Dynamics*, v. 51, n. 7, p. 1091–1120, 2013.
- PALADUGU, M.; LUCAS, D. R.; SCOTT HYDE, R. Effect of lubricants on bearing damage in rolling-sliding conditions: Evolution of white etching cracks. *Wear*, v. 398–399, p. 165–177, 2018.

SADEGHI, F.; JALALAHMADI, B.; SLACK, T. S.; RAJE, N.; ARAKERE, N. K. A Review of Rolling Contact Fatigue. *Journal of Tribology*, v. 131, n. 4, p. 41403, 2009.

SATO, M.; ANDERSON, P.M.; RIGNEY, D.A., M. Rolling-sliding behaviour of rail steels. *Wear*, v. 162–164, p. 159–172, 1993.

THIAGO GOMES VIANA. Estudo comparativo do comportamento de aços (trilhos) premium na tenacidade à fratura e na propagação de trinca por fadiga, de aplicação ferroviária. 2015. REDEMAT, 2015.

ZAPATA, D.; JARAMILLO, J.; TORO, A. Rolling contact and adhesive wear of bainitic and pearlitic steels in low load regime. *Wear*, v. 271, n. 1–2, p. 393–399, 2011.

ZHU, W. T.; GUO, L. C.; SHI, L. B.; CAI, Z. B.; LI, Q. L.; LIU, Q. Y.; WANG, W. J. Wear and damage transitions of two kinds of wheel materials in the rolling-sliding contact. *Wear*, v. 398–399, n. October 2017, p. 79–89, 2018.

ZHU, Y.; LYU, Y.; OLOFSSON, U. Mapping the friction between railway wheels and rails focusing on environmental conditions. *Wear*, v. 324–325, p. 122–128, 2015.

5 FINAL DISCUSSION

Even with extensive information in the literature, the nature of the WEL formation has not been successfully described, especially in devices under abrasive wear conditions.

This thesis showed that the sub-microstructures formed in pearlitic steels present similar features regardless of the difference in wear conditions in relevant engineering systems under abrasive wear and Rolling Contact Fatigue (RCF).

5.1 Wear Mechanisms

The worn surface of SAG lifter presents micro-cutting as a dominant abrasion wear mechanism. The massive material detachment observed in some regions follow the progressive plastic deformation and the reduction of interlamellar spacing promoting cracks nucleation.

For samples worn in laboratory tests it was determined that the procedure B, classically recommended by the ASTM Standard G65 (i.e. normal load of 130 N), does not reproduce the wear micro mechanisms observed at the samples of mill SAG. A better simulation of the wear mechanisms observed at the in service worn surface was achieved with applied loads in the range of 200 N to 280 N.

In RCF analysis, the analysis of the worn surface of samples tested at creepage of 1% supported by SEM images shows the formation of long spalling defect with subsequent large thin metallic flakes in the center of the contact (disc-disc). Those results are in agreement with (BOLTON; CLAYTON, 1984; ZAPATA; JARAMILLO; TORO, 2011) and can be classified as regime type I (rolling-sliding contact) corresponding to mild wear regime.

5.2 Microstructure features

This research shows the microstructure deformation for samples under abrasion conditions and the different microstructure features (White Etching Layer formation, severe deformation microstructure) in samples under Rolling Contact Fatigue conditions.

The characterization of the microstructure under abrasion conditions in samples worn in service and after laboratory tests (DSRW) like observed in this thesis, is a

contribution to the discussion promote by the observation of ZHU *et al.* and WANG *et al.* The authors reported contradictory results in terms of WEL formation in laboratory test. The abrasiveness of the process involving abrasion wear does not promote microstructural changes since the process are characterized by the material removal. (XU *et al.*, 1995; WANG *et al.*, 2016; ZHU *et al.*, 2018). The microstructure in the region close to the worn surface is characterized by the formation of two layers according to the level of deformation/transformation of the pearlite.

The microstructural transformation of the severe deformed layer (close to the worn surface) was analyzed via SEM, EBSD and TEM techniques. It was observed that the microstructure is characterized by the formation of ultra-fine grains of ferrite. This result is in agreement with the LOJKOWSKI *et al.* which describe the formation of a WEL as the formation of nanocrystalline α -Fe–C alloy (LOJKOWSKI; DJAHANBAKHS; BU, 2001). This region initiates the process of new grain formation requiring local grain-boundary rotations generating an equiaxed microcrystalline structure, according with MEYERS *et al.* (MEYERS, 2003).

Following the analysis in regions deeper in the sample, a second layer was found, characterized by the combination of deformed and undeformed pearlite colonies. This layer was called the transition layer. A detailed characterization of the layer showed that the influence in the behavior of this kind of materials was pointed out as the original contribution of this work.

In the case of samples tested under RCF and sliding wear conditions, the same stratification of the microstructure morphology found in the abrasive conditions was observed. The severe deformed layer consists in a microstructure characterized by a formation of ultra-fine grain of ferrite. The transition layer is characterized by pearlite colonies with cementite lamellae strain-aligned, small cementite formation and a reduction of the lamellae spacing.

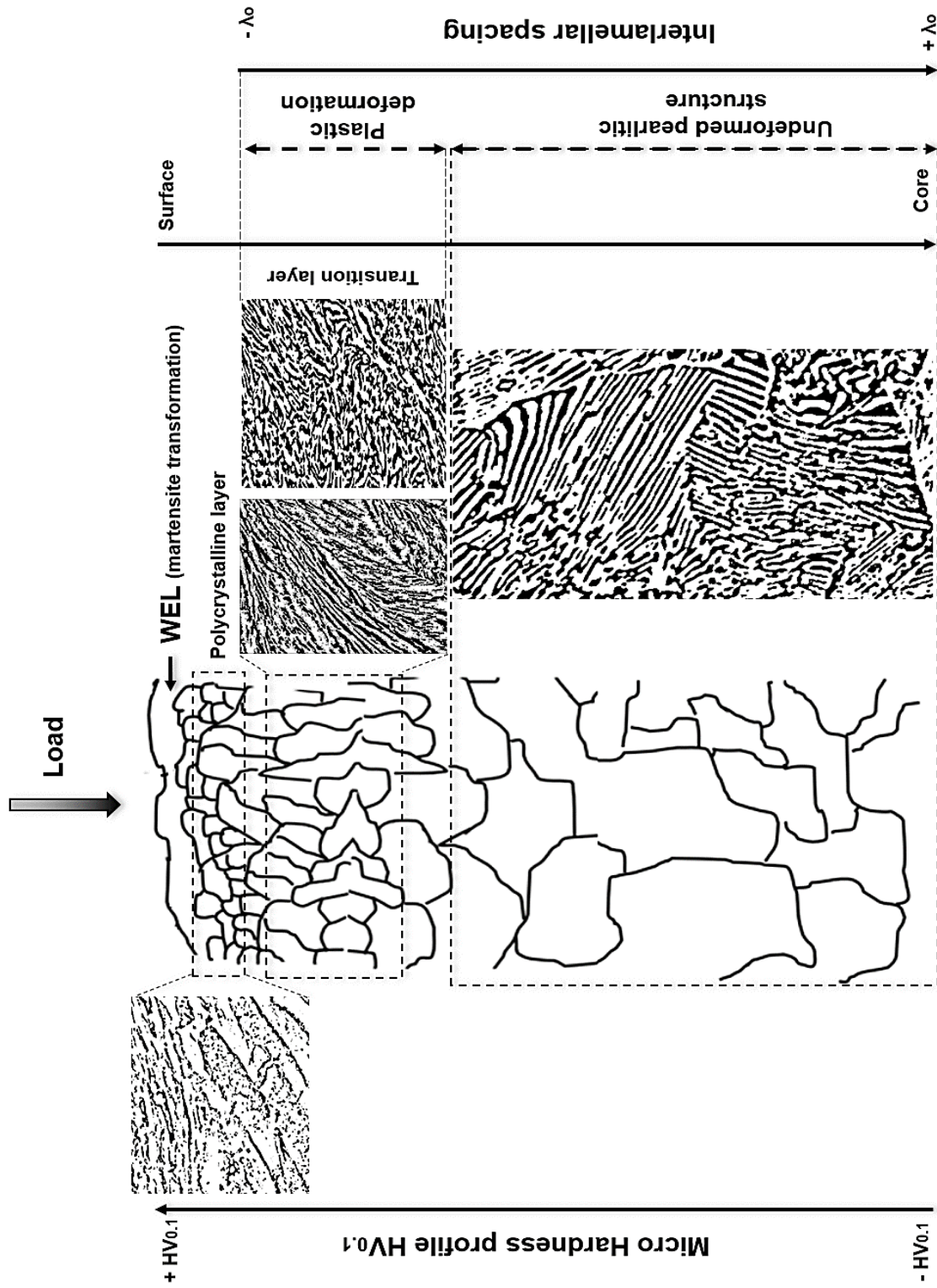
In these samples, the formation of surface cracks was observed, which grows parallel to the contact surface. Cracks initiated and propagated in the highly sheared surface and near-surface disc layers. Crack growth was often associated with planes of weakness, notably flattened manganese sulphide inclusions and grain boundaries (BEYNON; GARNHAM; SAWLEY, 1996; GARNHAM; DAVIS, 2011).

The samples analyzed after the scratch tests and rail grinding procedure show the formation of the several layers beneath the worn surface with particularly microstructural features as follows: In the case of the rail grinding procedure, the region close to the worn surface shows the WEL formation as described by PYZALLA *et al.* and TAKAHASHI *et al.* consisting in the WEL develops due to heating above austenitisation temperature followed by rapid cooling (thermal-martensite) (PYZALLA *et al.*, 2001; TAKAHASHI; KAWAKAMI; UEDA, 2010). Deeper in the sample, the formation of ultra-fine grains was observed, with the same characteristics observed in the samples analyzed in abrasion wear and RCF/sliding wear. A third layer was identified and defined as a plastically affected layer featured by the formation of cementite lamellae strain-aligned and a reduction of the lamellae spacing.

In the case of samples tested by scratch test, the microstructure is characterized by a polycrystalline layer, corresponding to ultra-fine grains of ferrite in the region close to the surface and an interlamellar spacing reduction in the pearlite colonies in the region plastically affected (deeper in the sample).

Erro! Fonte de referência não encontrada. shows the schematic representation of the microstructure in the different layers observed beneath the surface for samples tested in laboratory and analyzed after worn in service.

Figure 5-1 Schematic representation of the microstructural transformation beneath the worn surface



The laboratorial experimentation, the characterization of devices taken from the service and the comparison of the results of those both ranges, allows identifying the following evidences:

1. Concomitant work between plastic deformation of ferrite and the heating of the interface.

According to Moore, the effect of the rise in temperature during the metal rubbing will not (or will unlikely) affect the basic wear mechanism but will affect the surface in different levels: structural changes, increase of rate of diffusion of elements and changes in the mechanical properties of the heated zone (MOORE, 1970).

2. Plastic deformation of ferrite caused the increment of the dislocation density and subsequent carbon atom dissolution.

In the analysis of the substructure formation in pearlitic steels, it was reported that the dislocation movements in ferrite between the cementite control the work hardening. In deformed pearlite, dislocation source activity at cementite-ferrite interfaces was observed even in small strains (~ 0.01), due to elastic incompatibility stresses between cementite and ferrite, which can lead to localized plastic flow in interfaces at stresses lower than the yield stress (KALOUSEK; FEGREDO; LAUFER, 1985; DOLLAR; BERNSTEIN; THOMPSON, 1988; MERCER; HUTCHINGS; BOX, 1989).

GAVRILJUK (2003) calls the attention of two mechanisms of the cementite dissolution proposed (GAVRILJUK, 2003). The first one presented by Gridnev et al. proposed that cementite decomposition is due to the much higher binding energy between carbon interstitials and ferrite dislocations (0.75 eV) as compared to the binding energy of carbon atoms in the cementite lattice (0.40–0.42 eV). Thus, ferrite dislocations near the interface with cementite drag carbon atoms out of the cementite into the ferrite. On the other hand, Languillaume et al. suggested that the destabilization of the cementite promotes the decomposition. The geometrical thinning of cementite lamellae and the creation of slip steps could cause this process during wire drawing, which increases the free energy and the subsequent destabilization (LANGUILLAUME; KAPELSKI; BAUDELET, 1997).

3. Discordance walls and sub-grains structures formation.

The yield strength of pearlite is consistent with the stress necessary to move dislocations in ferrite between two impenetrable cementite walls, which increase with interlamellar spacing refinement leading to strengthening (DOLLAR; BERNSTEIN; THOMPSON, 1988).

According to the literature, the level of deformation influences the recrystallization, i.e. a lower temperature is required for the recrystallization to start with the increment of the deformation (PADILHA; SICILIANO, 2005). The Transmission electronic microscope (TEM) analysis in the most severe deformed layer evidenced the formation of sub-grains structures associated with the stored energy on the deformation process (driving force).

The energy balance in the interface could justify the necessary increment in the load applied for DSRW (150 N up to ASTM Standard G65) to simulate the surface observed in the semi-autogenous mill (SAG).

4. Correlation between the crystallographic orientation and the microstructural transformation

The analysis of EBSD images in the cross section for all conditions shows that the deformation resistance of pearlite colonies was clearly dependent on their crystal orientations (anisotropic effect). The microstructure observed in the transition region seems to act as a barrier to the propagation of plastic deformation.

SATOH and IWAFUCHI used this configuration in the analysis of texture formation in a rail after successive rolling contact. The authors reported a colony reorientation to TD // {111}, thereby referring a crystallography texture. Those results suggest that the crystallographic plane results in small grains which become parallel to the running surface (SATOH; IWAFUCHI, 2005). In this new approach, the relationship between crystal orientation (presented in IPF, KAM and the TF map) require a detailed study. The presumption of colonies undeformed and oriented preferentially at the slip system was not clarified.

The identification of those regions/layers in the sub-microstructure allows the interpretation of the hardness profiles as a function of the depth in the samples,

clarifying the differences in the work-hardening mechanisms. The mechanical property, the dislocation density, distribution and lamellae orientation measurements will provide a detailed picture of the work-hardening mechanisms in a fully pearlitic steel. It was reported that the increase of hardness in the layer close to the surface is controlled by the increment in the number of dislocations, work hardening by grains refinement. The transition layer is controlled by the increment of the dislocations density and the progressive reduction of the interlamellar spacing in the areas localize close to the severe deformed layer. The frictional processes provide the energy required by the cementite dissolution and the recrystallization of the ferrite in the pearlite in the nearest region of the contact zone.

The **Table 5-1** summarize the characteristics identified in the different wear conditions analysis.

Table 5-1 Main characteristics of the samples tested in the different wear conditions

Experimental chapter one	WEAR CHARACTERIZATION OF THE SEMI- AUTOGENOUS GRINDING MILL	1. Wear mechanisms		Cutting and ploughing. Presence of material remove (massive loss mass)
		2. Microstructural analysis beneath the worn surface	Severe deformed layer (close to the surface) Transition layer Core	Polycrystalline layer, characterized by ultra-fine grains of ferrite Deformed pearlite colonies Not plastically affected region (lamellae arrangement)
		3. Detailed microstructural analysis of the transition layer		Combination of deformed and undeformed pearlite colonies Interlamellar spacing reduction in the deformed colonies Crystallographic texture in the direction <111>
		4. Work hardening		Microhardness increment of 80 Vickers points: from 343 ± 13 HV0.1 in the core to 461 ± 22 HV0.1 in the polycrystalline layer
	WEAR CHARACTERIZATION IN DSRW ABRASIVE TEST (LABORATORY RANGE)	1. Wear mechanisms	As a function of the region of interest in the specimens (contact abrasive flow-surface)	Indentation (entrance area) Combination of cutting and ploughing (central area) Combination of indentation and ploughing (exit area)
		2. Microstructural analysis beneath the worn surface	Severe deformed layer (close to the surface) Transition layer Core	Polycrystalline layer, characterized by ultra-fine grains of ferrite Interlamellar spacing reduction Not plastically affected region (lamellae arrangement)
		3. Detailed microstructural analysis of the transition layer		It was not used the EBSD as a characterization technique
		4. Work hardening		It was not measured due the thin region plastically affected

Experimental chapter two	SCRATCH TEST: INFLUENCE OF THE TEST PARAMETERS IN THE WEL FORMATION	1. Wear mechanisms		Changes in the geometrical features: Expressive increase of the depth and width as a function of the applied normal load	
		2. Microstructural analysis beneath the worn surface (groove cross-section)	Severe deformed layer (close to the surface) Transition layer Core	Polycrystalline layer, characterized by ultra-fine grains of ferrite Deformed pearlite colonies Not plastically affected region (lamellae arrangement)	
		3. Detailed microstructural analysis of the transition layer		High dislocation density Interlamellar spacing reduction Crystallographic texture in the direction $\langle 111 \rangle$ The test conditions (applied load and scratch sequence) affect the thickness of the layer	
		4. Work hardening	It was not measured due the thin region plastically affected		
	RAIL GRINDING PROCEDURE: APPLIED MULTI-PASS SCRATCH TEST	1. Wear mechanisms	It was considerate pure abrasion		
		2. Microstructural analysis beneath the worn surface	Severe deformed layer (close to the surface) Transition layer Core	A discontinuous WEL formation Polycrystalline layer, characterized by ultra-fine grains of ferrite Deformed pearlite colonies Not plastically affected region (lamellae arrangement)	
		3. Detailed microstructural analysis of the transition layer		Formation of cementite lamellae strain-aligned with a reduction of the lamellae spacing. The procedure conditions (applied force and grinding speed) do not affect the thickness of the layer Not crystallographic texture was identified	

Experimental chapter three	TWIN-DISC ROLLING CONTACT TRIBOMETER	1. Wear mechanisms	Rolling Contact Fatigue	
		2. Microstructural analysis beneath the worn surface	Severe deformed layer (close to the surface) Transition layer Core	The thickness of the layer is affected by the number of the cycles Identification of surface cracks, growing parallel to the contact surface Polycrystalline layer, characterized by ultra-fine grains of ferrite Deformed pearlite colonies Not plastically affected region (lamellae arrangement)
		3. Detailed microstructural analysis of the transition layer		Interlamellar spacing reduction Crystallographic texture in the direction <111>
		4. Work hardening		Microhardness increment of 410 - 470 Vickers points: from 393 ± 13 HV0.1 in the core to 853 ± 20 HV0.1 for the W9 sample (650.000 cycles) and 810 ± 45 HV0.1 to W4 (25.000 cycles)
	WHEEL-RAIL CONTACT (CHARACTERIZATION ON FIELD)	1. Wear mechanisms	It was not analyzed. The aim of the analysis was the microstructural transformation	
		2. Microstructural analysis beneath the worn surface	Severe deformed layer (close to the surface) Transition layer Core	Identification of surface cracks, growing parallel to the contact surface Polycrystalline layer, characterized by ultra-fine grains of ferrite Deformed pearlite colonies Not plastically affected region (lamellae arrangement)
		3. Detailed microstructural analysis of the transition layer		Interlamellar spacing reduction Crystallographic texture in the direction <111>
		4. Work hardening		Microhardness increment of 190 Vickers point: from 363 ± 13 HV0.1 in the core to 550 ± 15 HV0.1 in the polycrystalline layer

6 COMPLEMENTARY REFERENCES

Aldrich, C. Consumption of steel grinding media in mills – A review. *Minerals Engineering*, v 49, p 77–91, 2013.

BAKSHI, S.; SHIPWAY, P.H.; BHADESHIA, H.K.D.H. Three-body abrasion wear of fine pearlite, nanostructured bainite and martensite, *Wear*, v 308, p 46-53, 2013.

BAKSHI, S.; LEIRO, A.; PRAKASH, B.; BHADESHIA, H.K.D.H. Dry rolling/sliding wear of nanostructured bainite, *Wear*, v 316, p 70-79, 2014.

POWELL, M.; SMIT, I.; RADZISZEWSKI, P.; CLEARY, P.; RATTRAY, B.; KLASGORAN, E.; SHAEFFER, L. The selection and design of mill liners, *Advances in comminution*, p 331-376, 2006.

TALAMINI, B. Finite element estimation of the residual stresses in roller-straightened rail, *Proceedings of IMECE04, Anaheim, California, 2004*.

CHAVES, A. Rodas ferroviárias: Análise, microestrutura e proposta de melhora. Dissertação de mestrado da Escola Politécnica da Universidade de São Paulo, departamento de Engenharia Metalúrgica e de Materiais, 2017.

NISHIKAWA, L. Soldagem de trilhos ferroviários perlíticos: Origem das microestruturas. Dissertação de mestrado da Escola Politécnica da Universidade de São Paulo, departamento de Engenharia Metalúrgica e de Materiais, 2018.

7 CONCLUSIONS

The main and most important conclusions of this work are:

The laboratory tests reproduce the same stratification in terms of microstructure beneath the worn surface. In the case of the DSRW the increase of the normal load applied to 280 N was required by the correlation field-laboratory. This normal load value is above the recommendation found in the ASTM Standard G65 (procedure B) for the test procedure.

The deformed layer, i.e. the sub-superficial layer in all the devices tested in this work shows the same structure in terms of microstructure deformation. The formation of two layers denominated as severely deformed was observed, characterized by the formation of ultra-fine grains of ferrite (dynamic recrystallization) and the transition, which consists in dislocation movement and the combination of deformed colonies (with a reduction of the interlamellar spacing) and undeformed colonies (not plastically affected by the contact). The classical arrangement of a pearlite was identified in the core of the samples.

The features on the surface are determined by the microstructure in the steady state and not by the original microstructure, i.e. in the case of the pearlite, the hardness is determined mainly by the interlamellar spacing, but in the case of deformed microstructures as addressed on this work, the hardness depends on the region of analysis. In the region with predominance of work hardening the hardness is influenced by the increase of the dislocation density but in the region close to the surface, it is simultaneously influenced by the ferrite grain refinement and the work hardening by solid solution of high carbon contents.

The scratch test shows a high quantity of energy release in the indenter tip, i.e. abrasive tip like used as the friction modifier or in the grinding procedure produce a relevant energy in the contact patch. For absolute loads in the order of milinewton, it was possible to observe partial or complete microstructure stratification (layers formation) beneath worn surface.

8 FUTURE WORK

Based on the assumption of the preponderant role of the pearlite microstructure in the determination of the hardness, the typical approach for the control of the hardness consistent in the grains size control (grain refinement) by manufacturing process control or by post treatment like no head rail is identified as the correct way. On the other hand, as observed showed in this work, the work hardening mechanisms is associated with solid solution and grain size, being possible the use of treatment like age-hardening and the control of the internal deformation of the grains by the increase of the deformation ability. To propose alternatives for the increase of the service life of the SAG (lifter and liner), wheels and rails is required.

Deeper and continuous microstructural characterization of the deformed layers using high resolution techniques like Transmission Electron Microscopy once the study presented in this work was performed with a reduced number of samples due to the limitation in the Brazilian research sources.

To continue the development of the EBSD study in samples under abrasive wear conditions once the technique was shown as an important tool for the characterization of the microstructure.

The analysis of the transition layer was performed in a morphological way showing the need to carry out a more detailed experimental study and associate the results with the residual strain. The stress field has a preponderant role in surface fatigue by RCF due the influence in the crack propagation inclination.

The role of the WEL in the increase of the operating lifetime of the railway gains relevance once the rail grinding procedure is used as a maintenance process on the ground. The effect of the rail grinding conditions in the microstructural transformation requires a detailed analysis. Experimental simulation of the grinding process is necessary for the understanding of the nature of the WEL formation.

To expand the study presented in this thesis to single-phase material as the manganese steel used in the manufacturing of devices used in the mining industry like mill liner and crossed (frogs) in the railway.

LIST OF PUBLICATIONS

Journal

PEREIRA, J.I.; TRESSIA, G.; MACHADO, P.C.; FRANCO L.A.; SINATORA, A. Scratch test of pearlitic steels: Influence of normal load and number of passes on the sub-superficial layer formation, **Accepted with revision by Tribology International**, 2017

PEREIRA, J.I.; MACHADO, P.C.; PENAGOS, J.J.; SINATORA, A. Wear characterization from field and laboratory tests of pearlitic steels used for SAG mill liners. *WEAR JCR*, v. 376-377, p. 37-45, 2017.

PENAGOS, J.J.; **PEREIRA, J.I.**; MACHADO, P.C.; ALBERTIN, E.; SINATORA, A. Synergetic effect of niobium and molybdenum on abrasion resistance of high chromium cast irons. *WEAR JCR*, v. 376-377, p. 983-992, 2017.

MACHADO, P.C.; **PEREIRA, J.I.**; PENAGOS, J.J.; YONAMINE, T.; SINATORA, A. The effect of in-service work hardening and crystallographic orientation on the micro-scratch wear of Hadfield steel. *WEAR JCR*, v. 376-377, p. 1064-1073, 2017.

CASTRO, CRISTOVÃO A. FERREIRA; **PEREIRA, J.I.**; MARANHO, OSSIMAR; SILVA, CARLOS HENRIQUE DA. Resistencia al desgaste de materiales de las orugas de tractores después del proceso de recuperación. *Matéria (UFRJ) JCR*, v. 20, p. 08-22, 2015.

CONFERENCE PRESENTATIONS

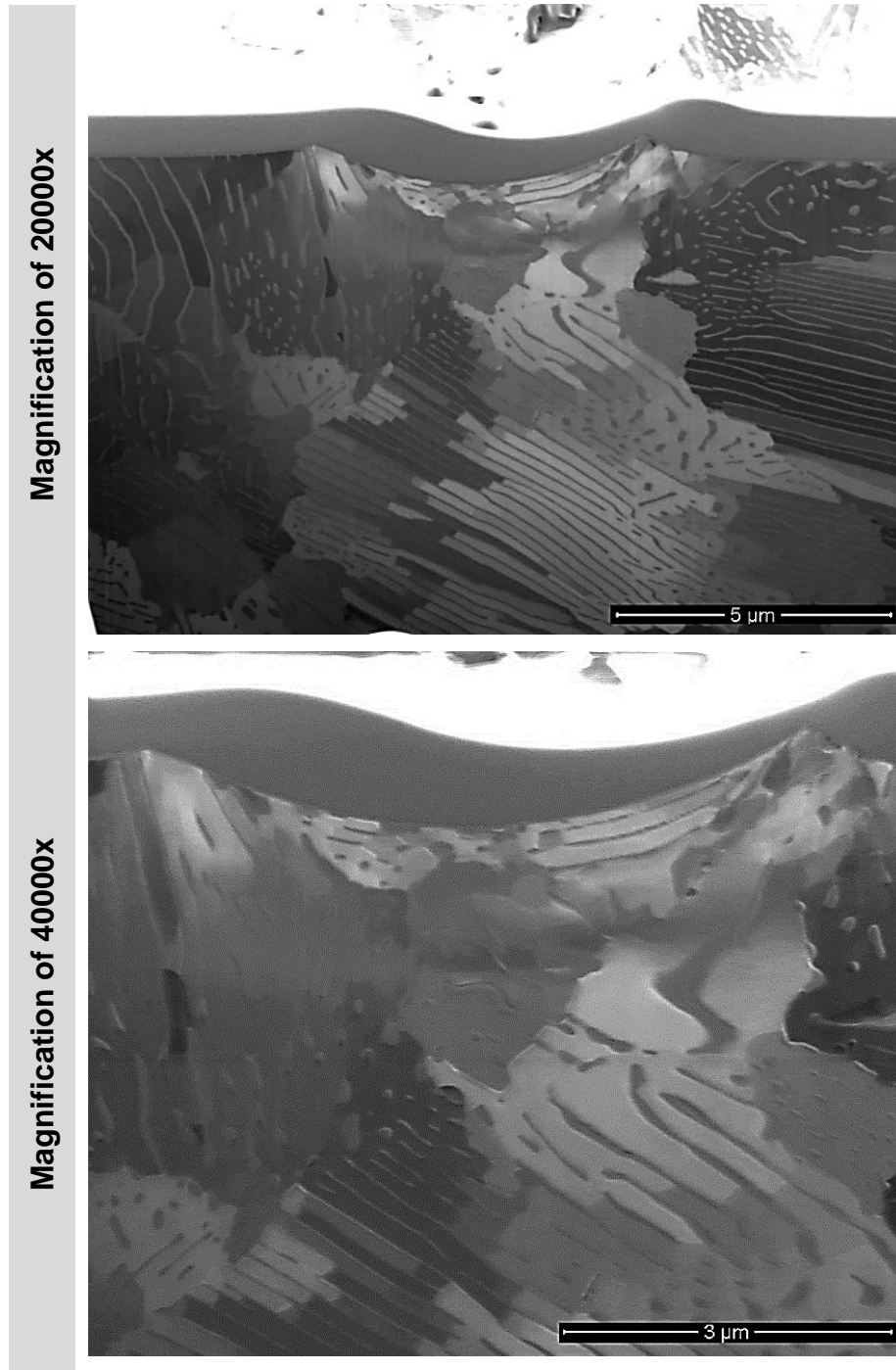
PEREIRA, J.I.; TRESSIA, G.; MACHADO, P.C.; FRANCO L.A.; SINATORA, A. Analysis of ultrafine-grains layer formation after multi-pass scratch tests on pearlitic steel, 44th Leeds-Lyon Symposium on Tribology 2017, Lyon, France. (Poster).

PEREIRA, J.I.; MACHADO, P.C.; PENAGOS, J.J.; SINATORA, A. Wear characterization from field and laboratory tests of pearlitic steels used for SAG mill liners. 2017, 21st International Conference on Wear of Materials 2017, California, USA. (Oral presentation).

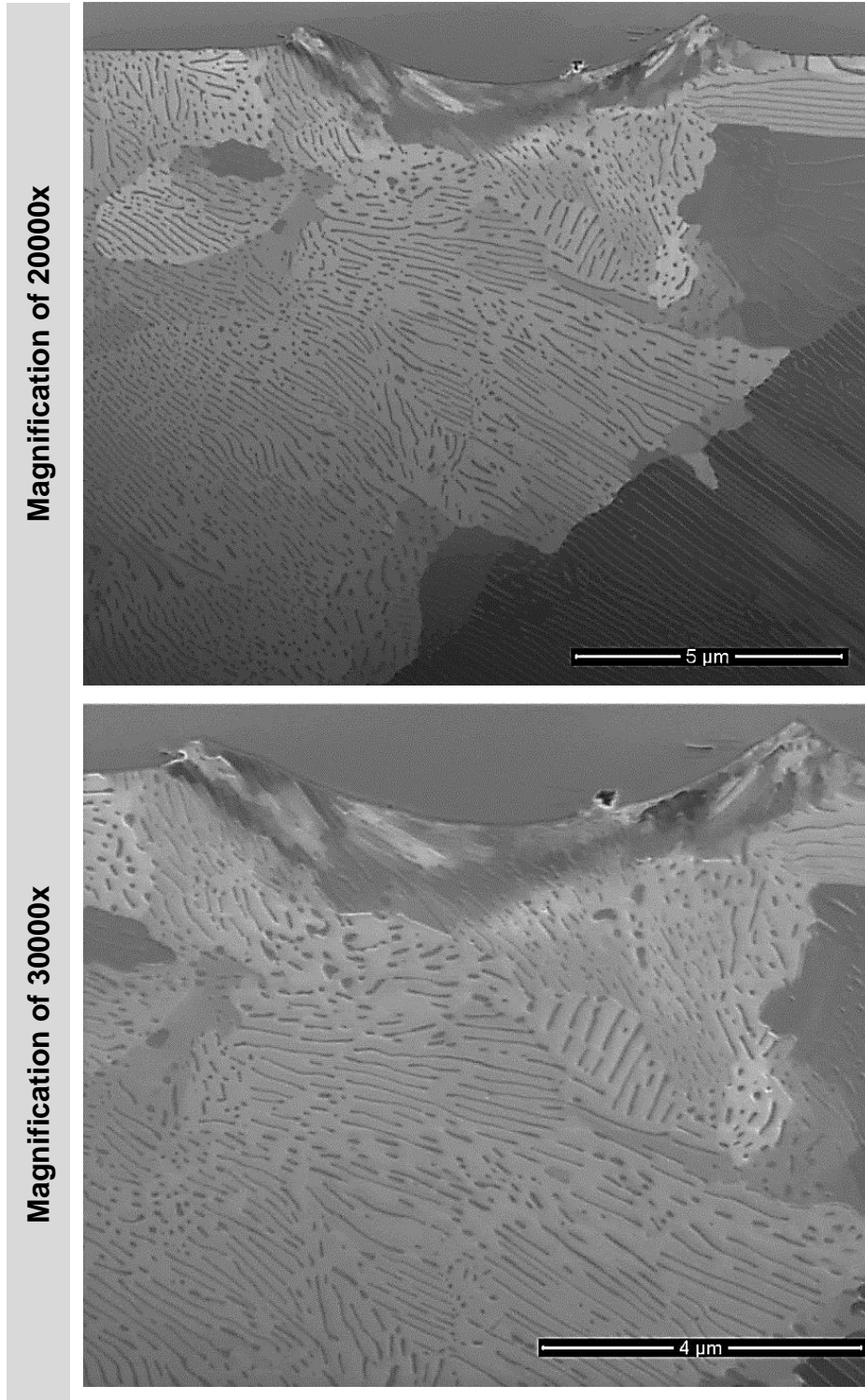
ANNEX

Annex 1 SEM-FIB micrographs of samples tested with scratch test at micro test range (Hysitron tribometer)

Sample tested in two-passes scratch test sequence'



- Sample tested in three-passes scratch test sequence.



- Sample tested in four-passes scratch test sequence.

